

**Quantum Metrology and Many-Body Physics: Pushing the
Frontier of the Optical Lattice Clock**

by

Michael J. Martin

B.S., Harvey Mudd College, 2006

A thesis submitted to the
Faculty of the Graduate School of the
University of Colorado in partial fulfillment
of the requirements for the degree of
Doctor of Philosophy
Department of Physics

2013

This thesis entitled:
Quantum Metrology and Many-Body Physics: Pushing the Frontier of the Optical Lattice Clock
written by Michael J. Martin
has been approved for the Department of Physics

Jun Ye

Ana Maria Rey

Date _____

The final copy of this thesis has been examined by the signatories, and we find that both the content and the form meet acceptable presentation standards of scholarly work in the above mentioned discipline.

Michael J. Martin, (Ph.D., Physics)

Quantum Metrology and Many-Body Physics: Pushing the Frontier of the Optical Lattice Clock

Thesis directed by Prof. Jun Ye

Neutral atom optical standards require the highest levels of laser precision to operate near the limit set by quantum fluctuations. We develop state-of-the-art ultra-stable laser systems to achieve a factor of 10 enhancement in clock measurement precision and additionally demonstrate optical linewidths below 50 mHz. The most stable of these lasers reaches its thermal noise floor of 1×10^{-16} fractional frequency instability, allowing the attainment of near quantum-noise-limited clock operation with single-clock instabilities of $3 \times 10^{-16}/\sqrt{7}$. We utilize this high level of spectral resolution to operate a ^{87}Sr optical lattice clock in a regime in which quantum collisions play a dominant role in the dynamics, enabling the study of quantum many-body physics. With a fractional level of precision of near 1×10^{-16} at 1 s, we clearly resolve the signatures of many-body interactions. We find that the complicated interplay between the p wave-dominated elastic and inelastic interaction processes between lattice-trapped atoms leads to severe lineshape distortion, shifts, and loss of Ramsey fringe contrast. We additionally explore the theoretical prediction that these many-body interactions will modify the quantum fluctuations of the system and we find that in certain parameter regimes the quantum noise distribution exhibits a quadrature dependence. We further present technological advancements that will permit ultra-stable lasers to operate with reduced thermal noise, leading to a potential gain of an additional factor of 10 in stability. This indicates that laser fractional frequency instabilities of 1×10^{-17} are within experimental reach, as is a fully-quantum-limited regime of optical clock operation.

Dedication

To my parents:

For all that you've taught me and for your guidance towards this path.

and

In memory of Don and Jean Martin, who strongly supported my education.

Acknowledgements

I would like to begin by thanking my parents Marie and Rob who have always supported me with their love and kept me on the right track. I would also like to acknowledge my stepmother Caroline, who played a significant role in my life. I would also like to thank my extended family for their support and love. Finally, I thank my new family-in-law, the Donahues and Boyds, for welcoming me with such love and kindness.

My interest in physics began at Corvallis High School, where I was fortunate to take Pat Canan's physics course. Mr. Canan was a constant guide and mentor who spent countless hours of his personal time training myself and friend and classmate Connelly Barnes to pursue a spot on the national physics team. While we didn't make the final cut, this experience prepared me extremely well for the rigors of college and got me hooked on physics.

I am indebted to Harvey Mudd College for giving me the opportunity to attend and for the great education I received. I would like to specifically thank Professors John Townsend, Thomas Donnelly, Richard Haskell, and Peter Saeta. Peter directed my research along with three other students with whom I was fortunate to work: Rachel Kirby, Tristan Sharp, and Shannon Woods.

When I arrived at the University of Colorado for graduate school, I was fortunate to become housemates with a great group of guys, two of whom were JILA physicists. I am grateful for the guidance of both Seth Rittenhouse and Evan Salim, who helped me orient myself as a first-year student in the graduate program and gave me invaluable advice. Evan also introduced me to the better mountain biking trails in the area, and I have enjoyed, in addition to his friendship, biking with him over the years that I have been in graduate school. I would also like to thank other

Boulder-area friends for their support during my time as a graduate student including Nora Matel and Erinn Looney-Triggs.

During my first year at CU, I met Carly Donahue, whom I would later marry. I have enjoyed our journey through graduate school together and I am a much happier person thanks to her; I can't imagine life without her. I am overjoyed that I will soon be joining her in Pasadena and grateful for her patience as I finished my work in Boulder.

When I first joined Jun Ye's group at JILA, I came under the mentorship of graduate student Seth Foreman. Under his direction, I was able to quickly learn the lab technology and get my bearings, all while having a good laugh now and then. I am grateful to Seth for his extremely generous time expenditures and cheerful, skilled tutelage. I also worked closely with Marcio Miranda at that time, and I am grateful for his good-natured assistance and friendship.

Other early co-workers I had the opportunity to work with were Andrew Ludlow, Marty Boyd, Gretchen Campbell, Tanya Zelevinsky, and Thomas Zanon-Willette. Gretchen served as a mentor during her time with us in the lab, and I am very thankful for her good-spirited tutelage and her scientific talent. I am also grateful to Marty for serving as a mentor and friend during our overlap in Jun's group, and he and I worked together on the early details of the JILA-PTB silicon cavity project reported in this thesis. I am also grateful for continued interaction with Andrew Ludlow, now with the NIST Time and Frequency Division.

Over the last 6.5 years I have been privileged to overlap significantly with a lot of great labmates. On the Sr1 experiment, I was very fortunate to work with postdoc Matt Swallows, a talented physicist and good friend. I learned a great deal of physics from Matt through his generous and thoughtful teaching. I always appreciated the fact that Matt was willing to take the time to share his encyclopedic knowledge and discuss (crazy) ideas objectively. Perhaps more importantly, Matt also exemplified the traits of a good scientist and set a standard to which I aspire. Visiting Fellow and collaborator Jan Thomsen has been an amazing co-worker and friend. I have also greatly enjoyed working with another Sr1 teammate, Mike Bishof. Mike is a very talented scientist and I am continually impressed with how easy he makes it all look. Another addition to the Sr team for

a year or so was Craig Benko, who eventually joined the XUV comb project. Craig is very talented and thoughtful, and I am indebted to him for his help with some of the less-than-glamorous aspects of setting up the Big ULE ultrastable laser, which he rendered in good spirits. A visitor to our lab, Yige Lin, worked with us on the Sr1 project and made significant contributions and I'm glad for the time that we had together in the lab. Finally, I have had the pleasure to work with a recent addition to Sr1, Xibo Zhang. Xibo is a very deep thinker and I have enjoyed our scientific discussions. With Mike and Xibo at the helm, I have no doubt that Sr1 is on the right path.

In addition to my Sr1 teammates, I have had the pleasure to work with many talented folks from the Sr2 project. Sebastian Blatt was one of the Sr labmates with whom I have overlapped the longest. I always enjoyed talking to him about physics and I have learned a lot from him. I will miss the *feuerzangenbowle* he would share at holiday parties. Travis Nicholson has also been in the lab nearly as long as I have. I've always enjoyed discussing physics with Travis due to his broad knowledge, and passion. Ben Bloom and I have also overlapped considerably, and I've always appreciated his rigorous approach and thoughtfulness. Newer additions to Sr2 have been Jason Williams and Sara Campbell. Jason has been a wonderful co-worker due to his skill, knowledge, and kindness. Sara is the newest addition to the "Sr gang" and I have no doubt that through her enthusiasm, energy, and talent the long-term success of the Sr projects will be ensured.

I would also like to thank Dylan Yost, Thomas Schibli, Mike Thorpe, Matt Stowe, Mark Yeo, Ben Stuhl, Matt Hummon, Brian Sawyer, Florian Adler, Tom Allison, Arman Cingoz, Steven Moses, and Kevin Cossel for their assistance over the years. Kevin has been particularly generous with his time and energy, and I'm indebted to him for several great suggestions, his technical expertise, and kind assistance on more than one occasion. We've also shared some (somewhat epic) experiences in the wilds of Colorado that I will certainly never forget!

In developing next-generation ultrastable laser systems, I have been very fortunate to work with some amazing people at JILA. It has been a great honor and pleasure for me to work with Jan Hall. Jan is a founder of the field of laser stabilization and has been a driving force in AMO science; his expertise was invaluable for the development of the laser systems reported in this thesis. Jan

was also a most gracious labmate—especially when we were making all sorts of noise and commotion in his (nominally) “quiet room” during the installation of the new laser system. I have greatly enjoyed discussions with Jan ranging from science to life. He is a unique and powerful intellect, not to mention a great person. Mark Notcutt was an early collaborator in designing some of the laser systems reported here, and a long-term leader in the field of laser stabilization. Lisheng Chen was a visitor during one summer, and I learned a lot from him in the months that we worked together. A recent addition to the Ye labs frequency comb and ultrastable laser development team has been postdoc Wei Zhang. Wei has been an amazingly hard-working and good-natured colleague and I am confident that he will realize another order of magnitude in laser stability. Recently, we have begun a collaboration with Markus Aspelmeyer and Garrett Cole to develop new crystalline mirror coatings, the first results of which are reported in this thesis. I’ve greatly enjoyed the opportunity to interact with them both.

The silicon cavity PTB/JILA collaboration has yielded exciting scientific results, and I am also grateful for the opportunity to get to know our colleagues at PTB. I worked very closely with Thomas Kessler and Christian Hagemann on characterizing the silicon cavity. Thomas and Christian were great hosts, and I thank them for their generosity. It was also a great pleasure to work with Fritz Riehle, Uwe Sterr, and Thomas Legero, and I thank them for the great opportunity to participate in the collaboration. Other PTB colleagues with whom I enjoyed discussions are Christian Lisdat, Stephan Falke, Thomas Middelmann, Christian Grebing, Nils Huntemann, Harald Schnatz, Gesine Grosche, Eckhard Peik, Piet Schmidt, Olaf Mandel, and Sana Amairi.

JILA and NIST are full of remarkably talented scientists, and I am grateful for the interactions I have had with other groups. Ana Maria Rey has been a wonderful collaborator and teacher over the years that we have worked with her in trying to understand the intricacies of the inter-atomic interactions within the lattice clock. Murray Holland, Dominic Meiser have driven the development cavity QED-inspired ideas employing Sr. James Thompson and Zilong Chen helped develop the ideas explored in Chapter 6 of this thesis. I would also like to thank Scott Diddams, Jeff Sherman, Tara Fortier, Andrew Ludlow (again), Nathan Lemke, and Chris Oates at the NIST Time and

Frequency Division.

I have also benefitted from interactions with visiting scientists over the years. Professor Long-Sheng Ma has been a recurring and cherished visitor. I have always been amazed by his subtle and remarkably apt questions regarding our experiments. During Roe Ozeri's visit, we first began to discuss the possibility of the atomic spectrum analyzer (Chapter 6). I also enjoyed Rana Adhikari's visit to our lab, and thank him for fruitful discussions. Ingmar Hartl, Axel Ruehl, and Martin Fermann have taught me much of what I know about Yb:fiber lasers.

I would additionally like to thank the JILA personnel who have been so instrumental (pun intended) in making everything work. From the instrument shop Kim Hagen, Hans Green, Tracy Keep, Tom Foote, Todd Asnicar, David Alchenberger, Ariel Paul, and Blaine Horner have all played central roles in helping construct apparatus that are central to our experiments. I am specifically indebted to Kim, Hans, and Todd for their great work in helping me construct the "Big ULE" system. From the electronics shop, I have greatly benefitted from the assistance and skill of Terry Brown, James Fung-a-Fat, Mike Whitmore, Carl Sauer, David Tegart, and Paul Beckingham. Terry, especially, has shown great patience in answering any questions I might have. I would also like to thank Diane Moreland for her assistance over the years.

Finally, I would like to thank my advisor, teacher, and guide over these last 6.5 years, Jun Ye. It should be clear from the list of scientists and coworkers whom I have thanked above that Jun runs a dynamic, productive, and talented group at the cutting edge of many fields within atomic, molecular, and optical science. He is a remarkable scientist and I always marvel at his ability to successfully guide so many different projects to such high levels of success. He is also a kind and generous person, which is mirrored in the lab atmosphere. For Jun's commitment to his students' success I am extremely grateful.

My thanks to all! -MJM, 4/19/2013

Contents

Chapter

1	Introduction	1
1.1	Historical discussion	1
1.2	Precision spectroscopy and atomic clocks	2
1.2.1	Ultrastable lasers in optical clocks	6
1.3	Characterizing the stability of clocks	7
1.4	Performance of neutral-atom clocks	8
1.5	Frequency combs	9
1.6	Beyond timekeeping: Clocks in modern physics	11
1.7	Overview of this thesis	12
2	The ^{87}Sr optical lattice clock	13
2.1	Introduction	13
2.2	Narrow-line laser cooling	15
2.3	Lattice dipole trapping	17
2.3.1	Atomic polarizability calculation	18
2.3.2	One-dimensional optical lattice	24
2.4	Experimental apparatus	25
2.4.1	Laser cooling at 461 nm	28
2.4.2	Narrow line cooling with ^{87}Sr	30

2.4.3	Optical dipole trap and clock spectroscopy: experimental configuration . . .	36
2.4.4	Atom state detection and measurement	40
2.5	Lattice spectroscopy	40
2.5.1	Lattice spectroscopy: experimental	45
2.6	Limits to atom-laser coherence due to photon scattering	48
2.6.1	Kramers-Heisenberg formula	49
2.7	<i>In situ</i> thermometry and cooling	55
2.8	Systematic uncertainty	57
2.8.1	Blackbody radiation	60
2.9	Quantum projection noise and the Dick effect	61
3	Thermal noise in optical interferometers	67
3.1	Introduction	67
3.2	Thermo-mechanical noise in physical systems	68
3.2.1	Fluctuation-dissipation theorem and Levin’s “direct approach”	70
3.2.2	Brownian motion in optical cavities	73
3.3	Thermodynamic noise	77
3.3.1	Substrate thermoelastic noise	78
3.3.2	Coating thermo-optic noise	79
3.4	Total thermal noise contribution to cavity frequency stability	81
3.4.1	Examples of thermal noise floor	82
3.5	Conclusion	83
4	High-precision laser stabilization with optical cavities	90
4.1	Introduction	90
4.2	Review of optical cavities	92
4.2.1	Measuring Finesse	95
4.2.2	Pound-Drever-Hall Locking	99

4.2.3	Sources of lock error	103
4.2.4	Choice of EOM crystal	104
4.2.5	Active control of residual amplitude modulation	107
4.3	Mechanical design of optical reference cavities	109
4.3.1	Vibration sensitivity	109
4.4	Designing two ultrastable lasers for the 10^{-16} level performance	111
4.4.1	Design of the “Big ULE” cavity	111
4.4.2	Design of the “JILA cavity”	118
4.4.3	Mesh size effect	121
4.4.4	Thermo-mechanical perturbations	122
4.5	A near quantum-limited lattice clock	126
4.5.1	Experimental details of the Big ULE	126
4.5.2	Verification of thermal-noise limited performance	131
4.5.3	High stability for rapid systematic evaluation	131
4.5.4	Clock comparison	134
4.6	PTB Si cavity and JILA cavity intercomparison	138
4.7	Crystalline mirrors	144
4.8	Frequency comb development: bridging spectral gaps coherently	148
4.8.1	Ultra-broadband Yb:fiber comb	149
4.8.2	Ultimate limits of comb performance	151
4.9	Outlook and conclusion	154
5	The optical lattice clock as a quantum many-body system	156
5.1	Atomic collisions at ultracold temperatures	156
5.1.1	Partial wave treatment of atomic interactions	157
5.1.2	Considerations for clock shifts	159
5.2	First observations of cold-collisions in an optical lattice clock	160

5.2.1	An s -wave collisional mechanism in a spin-polarized ^{87}Sr lattice clock	162
5.3	Treatment of the clock shift in a many-body framework	164
5.3.1	Second quantization	165
5.3.2	Many-body Hamiltonian	166
5.3.3	Writing the many-body Hamiltonian with spin operators	169
5.3.4	Adding the atom-laser interaction	172
5.4	S -wave model	172
5.4.1	Concluding remarks regarding s -wave interactions	176
5.5	New experimental evidence for p -wave interactions	177
5.5.1	Inelastic loss	177
5.5.2	Lineshape distortion and loss of Ramsey fringe contrast	181
5.6	p -wave many-body model	186
5.6.1	Collective model	186
5.6.2	The collective model and density shifts in a 2D optical lattice	189
5.7	Mean-field and perturbative tests of the many-body dynamics	189
5.7.1	Perturbative tests of the many-body Hamiltonian	190
5.7.2	Mean-field solution of the collective model	192
5.7.3	Density shift in the mean field limit	193
5.7.4	Measuring the density shift with a Ramsey interrogation scheme	194
5.7.5	Describing spectroscopic lineshapes with the mean-field model	199
5.8	Beyond mean-field effects	203
5.8.1	Perturbative corrections to the spin model	204
5.8.2	Truncated Wigner approximation	205
5.8.3	Ramsey fringe contrast decay	207
5.8.4	Quadrature-dependent noise measurement	210
5.9	Conclusion	214

6	Measuring laser noise via quantum state manipulation	217
6.1	Introduction to the general formalism	217
6.2	Limit of infinitely short pulses	220
6.2.1	Computing variances from the sensitivity function	221
6.2.2	Computing the variance	222
6.2.3	Computing the Allan variance	224
6.2.4	The sensitivity function $R(f)$ and experimental results	225
6.3	Adding the effects of frequency noise during the pulses	227
6.3.1	Sensitivity function for Rabi spectroscopy	234
6.4	Mapping the laser spectrum: multi-echo sequences	235
6.5	Conclusion	237
7	Conclusion	239
7.1	Summary of key results	239
7.2	Outlook	240
	Bibliography	244
	Appendix	
A	Coherent atom-light interactions	264
A.1	Derivation of the Hamiltonian	264
A.2	Time evolution operator for lineshape calculation	266
A.2.1	Rabi lineshape	266
A.2.2	Ramsey lineshape	267
A.2.3	Dick sensitivity function for Rabi spectroscopy	269
A.2.4	Dick sensitivity function for Ramsey spectroscopy	270

B	Calculating the dipole moments from measured atomic lifetimes	272
C	Spherical tensor treatment of the light shift	276
D	The s - and p -wave interaction overlap integrals	280
E	Site occupancy distribution	283
E.1	Sites with n	283
E.2	Linearity of the density shift and average occupancy	285

Tables

Table

1.1	Common Allan variances.	7
2.1	Upper states used in calculating the polarizability of the 1S_0 and 3P_0 clock states. . .	23
2.2	Scattering rates from 3P_0 into the 3P fine structure manifold and 1S_0 Rayleigh scattering at the magic wavelength.	53
2.3	Systematic frequency shifts and their uncertainties for the ^{87}Sr frequency standard (as in Refs. [1, 2]).	58
3.1	Summary of the parameters used in the text.	75
3.2	Mechanical properties of typical optical materials.	75
3.3	Thermal and thermo-optic/optical properties of common optical materials at room temperature and at 1064 nm.	81
4.1	Zero-crossing sensitivities obtained from the finite element modeling.	121

Figures

Figure

1.1	Coherent atom-light interaction	3
1.2	Ramsey and Rabi spectroscopy.	4
1.3	Schematic diagram of a frequency standard.	5
1.4	Graphical depiction of the sampling method employed to calculate the Allan deviation of a continuous measurement.	8
1.5	Frequency comb and optical clocks.	10
2.1	Strontium level diagram	14
2.2	Polarizability of the 1S_0 and 3P_0 clock states.	24
2.3	Experimental apparatus for trapping ultracold ^{87}Sr	27
2.4	Hyperfine structure of the $5s5p^1P_1$ and $5s5p^3P_1$ levels	29
2.5	Schematic depiction of the 689 nm MOT for the $F = 9/2 \rightarrow F = 11/2$ transition. . .	31
2.6	Ratio of σ^\pm absorption as a function of ground state magnetic sublevel, m_g	32
2.7	Field gradient programming	34
2.8	Clock operation with stretched nuclear spin states for first-order Zeeman insensitivity	36
2.9	Optical lattice dipole trap and clock laser pathway	37
2.10	The clock laser delivery system	39
2.11	Atomic state detection scheme	41
2.12	Spectroscopy in a one-dimensional optical lattice	43

2.13 Spectroscopic resolution of longitudinal and radial sidebands in a 1D optical lattice potential	44
2.14 Spectroscopic lineshape obtained with Rabi spectroscopy performed on the $^1S_0 \rightarrow ^3P_0$ clock transition at 429 THz.	45
2.15 Rabi flopping as a probe of the spread in Rabi frequency.	46
2.16 Raman scattering rate as a function of wavelength	51
2.17 Rayleigh scattering rate as a function of wavelength	52
2.18 Experimental measurement of optical pumping due to lattice scattering.	54
2.19 Temperature extraction and effect of additional cooling	56
2.20 Two-dimensional lattice geometry	59
2.21 Ramsey and Rabi lineshapes compared for quantum projection noise calculation. . .	62
2.22 Fourier and time-domain representation of the Dick sensitivity function and its implications for reaching quantum-limited clock performance.	64
3.1 Modified Hooke's law system.	69
3.2 Schematic of the relevant optical components for calculating the thermal noise of an optical cavity.	73
3.3 Thermal noise of cavity A with $\text{SiO}_2/\text{Ta}_2\text{O}_5$ mirrors.	84
3.4 Thermal noise of cavity A with GaAs/AlGaAs mirrors.	85
3.5 Thermal noise of cavity A with GaAs/AlGaAs mirrors and a half-wave cap.	86
3.6 Thermal noise of cavity B with $\text{SiO}_2/\text{Ta}_2\text{O}_5$ mirrors, $T = 124$ K.	87
3.7 Thermal noise of cavity B with GaAs/AlGaAs mirrors, $T = 124$ K.	88
3.8 Thermal noise of cavity B with GaAs/AlGaAs mirrors and an additional half-wave cap, $T = 124$ K.	89
4.1 Schematic of an optical cavity in the standing wave configuration.	93
4.2 Reflection coefficient and corresponding phase shift of the reflected light incident upon an optical cavity.	95

4.3	Measurement of cavity photon storage lifetime.	97
4.4	Measurement of photon storage time with a swept-frequency optical field.	99
4.5	Pound-Drever-Hall sidebands and error signal.	101
4.6	LiNbO ₃ and ADP modulator configurations.	105
4.7	Experimental setup for active control of residual amplitude modulation (RAM) in a waveguide electro-optic modulator.	107
4.8	Experimental demonstration of reduced residual amplitude modulation (RAM) . . .	108
4.9	The finite element model considered for the “Big ULE” cavity.	112
4.10	Two dimensional planar fits to offset (a) and tilt (b) as a function of z and d	114
4.11	The Big ULE cavity and Zerodur support structure.	115
4.12	The double-layer vacuum system for the Big ULE.	116
4.13	The Big ULE cavity with its new Zerodur glass support structure. The cavity rests upon Viton hemispheres (not shown).	117
4.14	The JILA cavity design and vacuum system.	119
4.15	FEA simulation of the “JILA cavity.”	120
4.16	Effect of mesh size on the FEA-predicted mirror displacement.	122
4.17	Temperature dependence of coefficients of thermal expansion (CTEs) of common cavity spacer and substrate materials.	123
4.18	Deformation of mixed-material optical cavities	124
4.19	Net coefficient of thermal expansion for the Big ULE assuming a spacer T_0 of 15.4° C.125	
4.20	Two-stage Pound-Drever-Hall (PDH) locking for laser stabilization with the Big ULE.128	
4.21	Effect of the sound-proof box on the optical frequency spectrum.	130
4.22	Demonstration of a thermal-noise limited laser at fractional instability of 1×10^{-16} from 1–1000 s.	132
4.23	Ultra-narrow Rabi lineshapes demonstrating 3-s optical-atomic coherence.	133
4.24	Stability of interleaved measurements for systematic evaluation with Rabi pulse du- ration of 500 ms.	135

4.25	Clock comparison scheme.	136
4.26	Clock comparison Allan deviations and pulse timing.	137
4.27	The silicon cavity.	139
4.28	Direct optical beat between the JILA cavity-stabilized laser and the Si cavity-stabilized laser.	140
4.29	Modified Allan deviation of the stabilities extrapolated via the three-cornered-hat analysis.	141
4.30	Crystalline mirror and cavity.	145
4.31	Comb frequency-transfer and stability of a laser locked to the cavity employing GaAs/AlGaAs crystalline mirrors.	146
4.32	Spectrum of the ultra-broadband Yb:fiber comb and optical beats.	149
4.33	Spectrum of broadened Yb oscillator and relevant beat notes at 698 nm and 1.54 μm	150
4.34	Experimental test of the intrinsic limits of the an optical frequency comb.	153
5.1	First observation of a density shift with a spin-polarized ^{87}Sr lattice clock.	161
5.2	Harmonic approximation compared to the true radial profile of the trap.	168
5.3	Interaction motional eigenstates within a single trap site.	169
5.4	Two-particle illustration of the s -wave shift mechanism.	173
5.5	Two-particle lineshapes with s -wave interaction energy. (a) $U_{12}^- = 0$ (b) $U_{12}^- = 1\Omega$ (c) $U_{12}^- = 2\Omega$ (d) $U_{12}^- = 5\Omega$	174
5.6	The s -wave density shift and the strongly interacting regime.	176
5.7	Atom loss as a function of lattice hold time.	178
5.8	Two-body loss coefficient γ_{ee} for spin polarized ^{87}Sr in $^3\text{P}_0$ $ F = 9/2, m_F = +9/2\rangle$	180
5.9	Broadened lineshape with 1 s atom-light interaction time.	181
5.10	Low density lineshape vs. high density lineshape with lattice depth consistent with $\nu_z = 80$ kHz.	182

5.11	Narrow line scan (1 s probe time) with 40% typical lattice power and a sample temperature of 1 μK .	183
5.12	Comparison of two lineshapes taken under similar atom number conditions of $N_{\text{tot}} \simeq 5000$.	184
5.13	Ramsey fringes contrast and two body-loss.	185
5.14	Visual depiction of the collective model.	187
5.15	Temperature dependence of the p -wave interaction energies and their thermal distribution.	190
5.16	Spectroscopy of the clock transition in the linear response regime with pulse area fixed to $\theta = 0.2\pi$.	191
5.17	Effect of two-body losses on the density shift measurement for two test cases, with $\chi = 2\pi \times 0.2$ Hz, $C = -0.3\chi$, and $\Gamma_{ee} = 2\pi \times 0.07$ Hz.	195
5.18	Timing sequence and example of inter-sequence excitation fraction measurement.	197
5.19	Measured Ramsey shift as a function of the scaled excitation fraction \bar{f} .	198
5.20	Lineshape (red circles) and normalized total atom number (black circles) as a function of detuning and for decreasing $\bar{\Omega} \simeq \pi/t_R$.	200
5.21	Lineshape as a function of experimental parameters.	202
5.22	Interaction effects visible at the sub-Hz energy scale.	203
5.23	Ramsey contrast decay measurement scheme and the failure of mean-field model.	206
5.24	Ramsey fringe contrast decay vs. initial pulse area.	208
5.25	Effect of the $(S^z)^3$ term on the Ramsey fringe contrast.	209
5.26	Spin noise measurement sequence.	211
5.27	Bloch sphere evolution as a function of dark time for $N_{\text{tot}} = 20$.	212
5.28	Spin noise vs. rotation quadrature.	215
5.29	Magnified spin noise vs. rotation quadrature.	216
6.1	The spin echo sequence being considered.	219

6.2	The sensitivity function, $r(t)$ of a four-pulse echo sequence in the limit of infinitely short π -pulses.	221
6.3	Diagnosing the laser spectrum with spectroscopy.	226
6.4	The time-domain sensitivity function $r(t)$ for the echo sequence with 80 ms duration and 20 ms π -pulses.	230
6.5	Verification of improved laser noise spectrum with a spin echo sequence.	232
6.6	Overview of the sensitivity functions $ R(f) ^2$ for increasing echo pulse number.	233
6.7	Linear scale plots of the Fourier-space sensitivity functions.	235
6.8	Multi-pulse extrapolation of laser noise spectrum.	236
6.9	Dick effect-limited laser performance with the newly evaluated laser spectrum.	238
A.1	Rabi spectroscopy lineshape.	267
A.2	Ramsey spectroscopy lineshape.	268
A.3	Rabi and Ramsey sensitivity functions.	270
D.1	s - and p -wave mode-dependent interaction strength coefficients.	282
E.1	Lattice loading from the red MOT and longitudinal distribution.	284
E.2	Distribution of site occupancies.	285
E.3	Average site occupancy as a function of total atom number.	286

Chapter 1

Introduction

Many of the tools that are crucial for optical atomic clocks and high-precision optical spectroscopy played a prominent role in 20th century physics. Likewise, the development of both microwave and optical frequency standards has been an important driving force in quantum measurement and atomic, molecular, and optical science. The technology utilized in today's state-of-the-art optical frequency standards has spurred numerous new research directions, including optical frequency combs, ultrastable optical interferometers, and interacting quantum gases. Here we provide an introduction to optical frequency standards, their key components, and metrics for evaluating their performance.

1.1 Historical discussion

Precision spectroscopy has played a foundational role in our understanding of modern physics. Radio-frequency spectroscopy enabled early measurements of nuclear magnetic moments [3, 4], the Lamb shift in atomic hydrogen [5], and the accurate determination on an anomalous electron g -factor [6]. These measurements each represent experimental milestones that spurred theoretical development in atomic and nuclear physics as well as quantum optics and quantum electrodynamics. The pioneering work of Norman Ramsey in developing the method of separated oscillatory fields [7] set the stage for the development of radio frequency (RF) frequency standards by enabling the accurate and precise determination of resonances in atomic beams. The Cs fountain clocks that define the SI second today operate using Ramsey's scheme, and the precise RF clocks flying aboard

GPS satellites have fundamentally changed the way much of the world navigates.

With the invention of the laser [8], the field of laser-based optical spectroscopy was born, allowing optical measurement of fundamental quantities, such as the Lamb shift [9, 10]. Furthermore, optical analogues of the Ramsey separated fields technique were demonstrated in the optical domain [11, 12], representing the first demonstrations of coherent optical spectroscopy and setting the stage for high resolution spectroscopy of narrow optical transitions in molecules, atoms, and ions.

The advent of laser cooling and trapping [13, 14, 15, 16, 17, 18, 19] represents another groundbreaking milestone for modern science and has opened up the quantum world to direct laboratory exploration and manipulation. With laser-cooled atoms and ions, coherence times for optical (e.g., [20, 21, 22]) and microwave (e.g., [23]) spectroscopy were dramatically improved. The long coherence times were a direct contributor to the success of frequency standards based on laser cooled atoms and ions that emerged from this work, and directly enabled the most precise and accurate clocks in existence today.

1.2 Precision spectroscopy and atomic clocks

The physical basis for precision spectroscopy and atomic timekeeping is the relationship between energy and frequency, given by Plank's famous equation relating the frequency of photon to its energy

$$\Delta E = h\nu, \tag{1.1}$$

where ΔE is the energy between the ground and excited clock states (g and e , respectively), h is Planck's constant and ν is the transition frequency (i.e., the frequency of the absorbed or emitted radiation). Optical and microwave transitions between metastable states in ions and atoms make good frequency references because they are based on quantum systems whose transition frequencies depend very directly on the fundamental laws of nature, and should be perfectly reproducible from one realization to another. In many cases, g is the energetic ground state of the atom or ion,

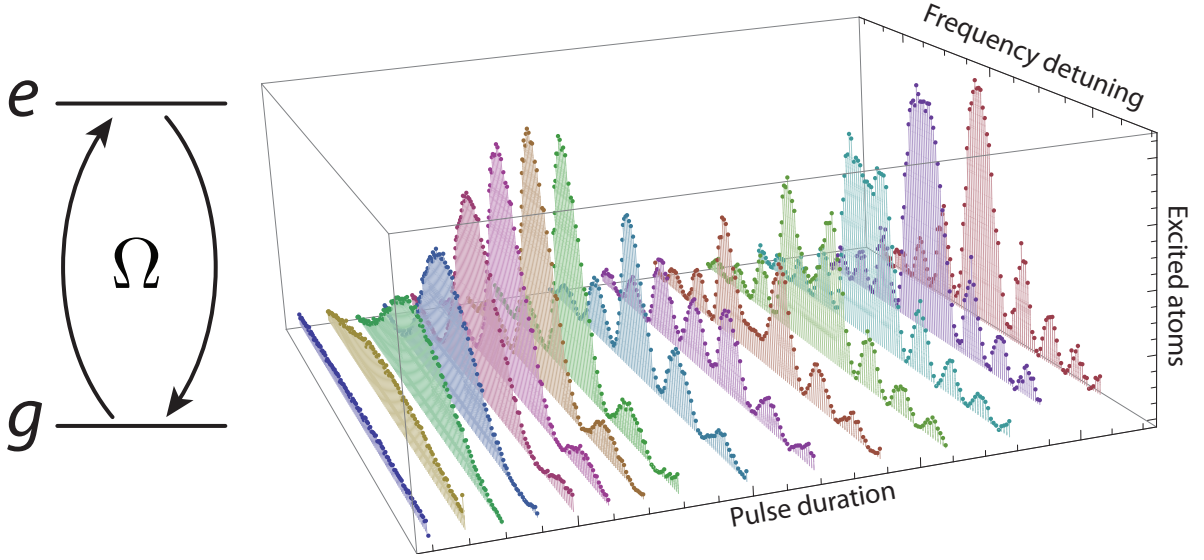


Figure 1.1: Coherent spectroscopy in a ^{87}Sr optical lattice clock. The atomic population undergoes a series of collapses and revivals as a function of laser detuning and pulse duration, demonstrating a coherent regime of spectroscopy.

while e is a highly metastable, excited state whose natural lifetime exceeds all experimentally relevant timescales. As a result, the techniques of coherent spectroscopy, as first developed by I. I. Rabi and N. H. Ramsey for nuclear magnetic resonance measurements, are still utilized today, from RF frequencies to ultraviolet optical frequencies. Figure 1.1 depicts an example of coherent spectroscopy using lattice-trapped and spin-polarized ^{87}Sr —the ^{87}Sr optical lattice clock that is the subject of this thesis. In Chapter 2 we provide a complete description of the ^{87}Sr optical lattice clock. Briefly, an ultrastable laser is tuned such that the photon energy is nearly matched to ΔE and the pulse is applied for a given duration. The duration is chosen such that the maximum population transfer occurs on resonance for a given coupling strength between the laser and atom called the “Rabi frequency.” For an electric dipole-allowed transition, the Rabi frequency Ω is given by

$$\Omega = \langle g | \hat{\mathbf{d}} \cdot \mathbf{E}_0 | e \rangle / \hbar, \quad (1.2)$$

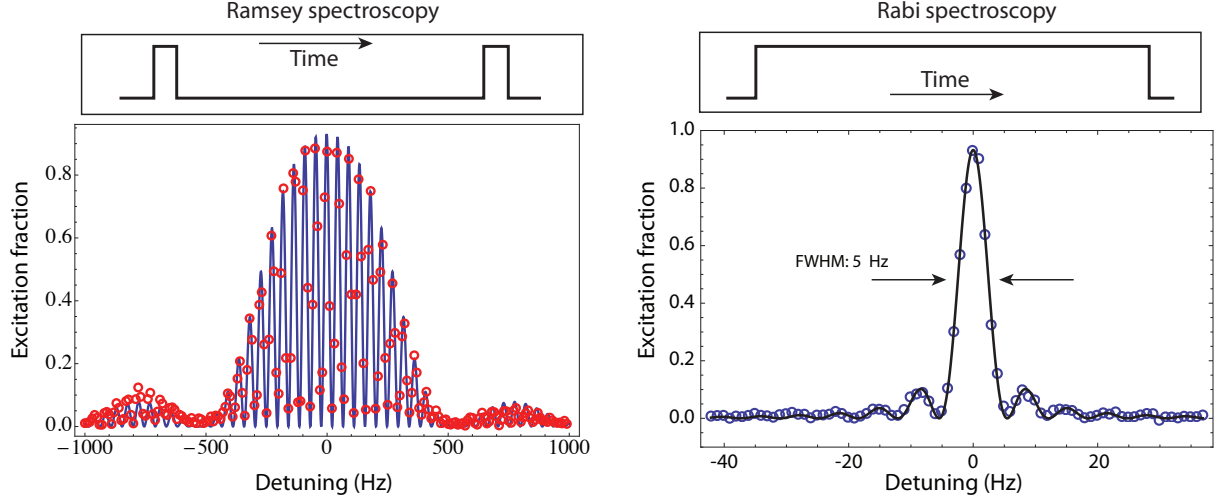


Figure 1.2: Spectroscopic lineshapes obtained via Ramsey and Rabi spectroscopy in a ^{87}Sr lattice clock. Both techniques are utilized in optical clocks. The temporal width of the features in both Ramsey and Rabi spectroscopy are inversely proportional to the total spectroscopy time. For the Rabi spectroscopy lineshape shown at right, the probe time was 160 ms, corresponding to an expected frequency full-width at half-maximum (FWHM) of 5 Hz.

where $\hat{\mathbf{d}}$ is the dipole operator $\hat{\mathbf{d}} \equiv e\hat{\mathbf{r}}$, e is the electron charge, and $\hat{\mathbf{r}}$ is the position operator. Here \mathbf{E}_0 is the amplitude of the laser electric field. As can be seen in Fig. 1.1, the population of atoms in e undergoes periodic collapses and revivals depending on the laser detuning from resonance, and the duration the pulse is applied. This is the hallmark of coherent spectroscopy; the atom-field coupling is the relevant part of the interaction, while spontaneous emission occurs so infrequently that it does not play a large role in the dynamics of the population evolution. Figure 1.2 shows an example of each Rabi and Ramsey spectroscopy utilized in the ^{87}Sr optical lattice clock. The fit lineshapes represent the ideal case of an isolated two-level system and are derived in Appendix A.

In order to consider a given ultranarrow resonance in an atom or ion a good candidate for a frequency standard, the transition of interest should exhibit strong immunity to external perturbations, such as magnetic fields. Additionally, atoms or ions serving as optical standards are typically trapped sufficiently tightly that problems such as Doppler broadening and recoil shifts can be mitigated by the tight trap.¹ These traps consist of RF Paul traps for ions [24] and

¹ In RF frequency standards, the effect of recoil is negligible and the Doppler effect is vastly reduced.

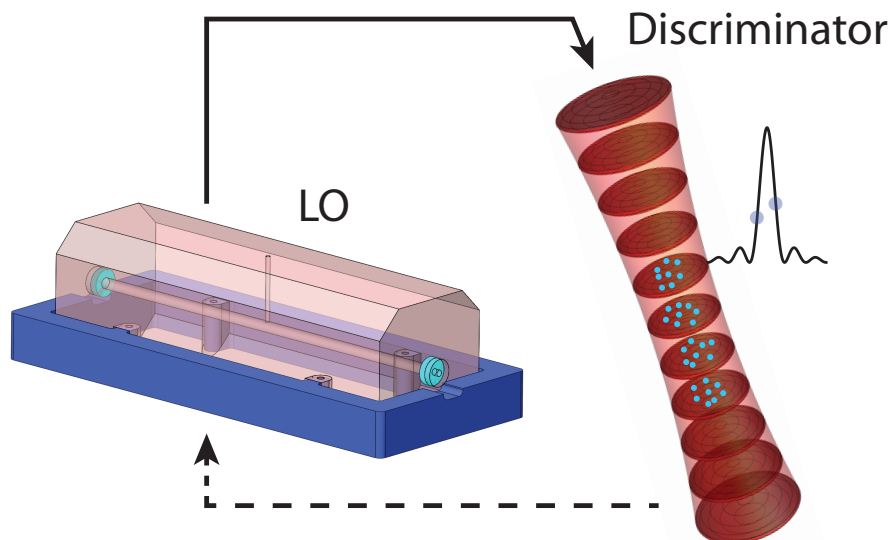


Figure 1.3: Schematic diagram of a frequency standard. The local oscillator (LO) probes the atomic system used as a frequency reference (solid line). The information gained from this measurement is used to correct the LO frequency such that it is actively locked to atomic transition.

engineered, standing-wave optical dipole traps at the “magic-wavelength” for neutral atom optical clocks [25, 26], also known as optical lattices. In addition to these general considerations, the transition used for the clock must be sufficiently narrow to provide a sharp frequency discrimination signal. This last condition is met by using multiply forbidden transitions in the clock atoms or ions, resulting in extremely long excited state lifetimes (in some cases > 100 s) and correspondingly very narrow resonance linewidths.

Atomic clocks of all types (microwave, optical trapped ion, and optical neutral atom) all rely on the same principle of operation. An oscillator with good short-term stability, the local oscillator (LO), is used to interrogate a transition in the ion or atomic ensemble as shown in Figure 1.3. The LO very precisely probes the transition, and the information is then used to correct the LO such that it is maintained on resonance.

Optical atomic clocks have now reached unprecedented levels of stability and accuracy. At the forefront of accuracy, a clock located at the National Institute of Standards and Technology

(NIST), based on a single aluminum ion and probed via quantum logic spectroscopy now has a fractional frequency uncertainty of 8.6×10^{-18} [27]. A second clock based on a mercury ion, also at NIST, is at the 2×10^{-17} fractional frequency uncertainty level [28]. Additionally, a Sr^+ ion operated by the National Research Council of Canada has recently attained an uncertainty of 2.2×10^{-17} [29]. Finally we note that the PTB Yb^+ ion clock has reached an uncertainty of 7.1×10^{-17} [30]. These remarkable advances in ion-based clocks are followed closely by a new class of optical clocks based on ensembles of ultracold neutral atoms held tightly in optical lattices. The most accurate at the level of 1×10^{-16} fractional uncertainty [31, 32, 33, 34], with the ^{87}Sr lattice clock currently the most accurate of the neutral atom-based clocks. The Sr lattice clock also has the best record of international agreement in measurements against the Cs primary frequency standard of any optical standard [35, 34].

1.2.1 Ultrastable lasers in optical clocks

Central to the performance of any frequency standard is the stability of its local oscillator. The task of the local oscillator is twofold: it must probe the reference transition in the quantum reference while introducing minimal noise through an aliasing process known as the Dick effect [36, 37], and it must act as a “flywheel” to maintain the short- to medium-term stability of the frequency reference. These two considerations alone have spurred massive development efforts in ultrastable lasers for use with optical standards (e.g., [38, 39, 40, 41, 42, 43]), which stand the most to gain from improvements in the local oscillator.

From a broader standpoint, optical interferometers are found at the heart of many diverse experiments that perform the highest-precision laser-based measurements, from quantum mechanical to cosmological scales. Chapter 3 explores key limitations to optical interferometers: the detrimental thermal coupling to the environment arises as a direct consequence of mechanical losses in the interferometer substrates and coatings, which in turn limit laser stability. Chapter 4 specifically discusses the development of three ultrastable laser systems for use with optical clocks, including the construction of an ultrastable laser with fractional instability at 1×10^{-16} from 1–1000 s and

Noise type	$G_\nu(f)$	$\sigma_y^2(\tau)$
White	h_0	$\frac{h_0}{2\tau}$
Flicker	$h_{-1}f^{-1}$	$2 \log 2h_{-1}$
Random walk	$h_{-2}f^{-2}$	$\frac{2\pi^2 h_{-2}\tau}{3}$

Table 1.1: Common Allan variances for different noise spectra (as in [45]).

a linewidth as low as 26 mHz.

1.3 Characterizing the stability of clocks

Forming metrics for the stability of atomic clocks is important in order to characterize their performance. By **performance** we mean “how long does it take to make a measurement with a given statistical uncertainty.” This question is distinct from, but related to, the clock uncertainty. **Systematic uncertainty**, by contrast, characterizes the absolute (dis)agreement we expect between two systems due to our limited knowledge of perturbing effects that introduce subtle, systematic differences in the operating conditions of each clock. Ultimately, it is these effects that limit the accuracy of a frequency standard.

In order to characterize the performance of a frequency standard, the most common and widely-used metric is the Allan deviation [44]. The Allan deviation is a procedure to characterize the time-dependence of the noise in a string of frequency measurements. Unlike the standard deviation, which can become divergent for certain noise spectra, the Allan deviation can characterize data described by a wider range of underlying noise processes [45]. For a continuous measurement, the Allan deviation is defined as

$$\sigma_y^2(\tau) = \frac{1}{\nu_0^2} \left\langle \frac{(\bar{\nu}_{i+1} - \bar{\nu}_i)^2}{2} \right\rangle. \quad (1.3)$$

Here, each quantity $\bar{\nu}_i$ etc. is averaged over the time interval τ at the i th such time interval, as illustrated in Fig. 1.4. Equation 1.3 represents the expected value of the pair deviation for a given continuous measurement when it is averaged in bins with width τ .

The power of Eq. 1.3 is that it allows easy identification of the underlying noise process. Table 1.1 shows the behavior of the Allan deviation for different types of underlying frequency noise

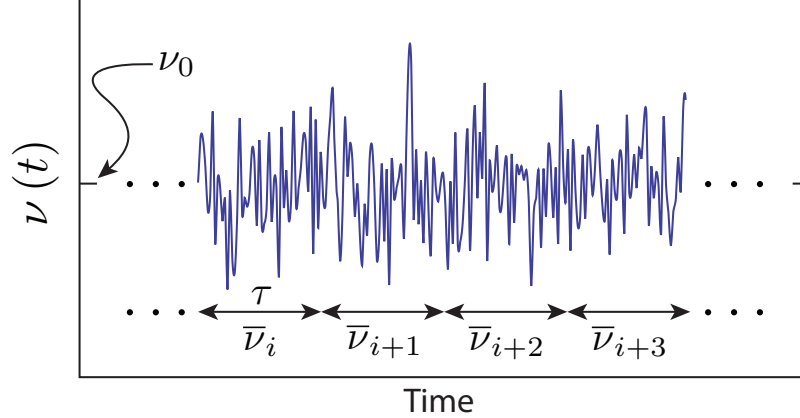


Figure 1.4: Graphical depiction of the sampling method employed to calculate the Allan deviation of a continuous measurement. Here, the data is averaged in bins of time-width τ . The data is centered around frequency ν_0 .

(see, e.g., [45]), where $G_\nu(f)$ is the single-sided frequency noise power spectral density. For example, one can easily distinguish between noise spectra of the type $G_\nu(f) = h_\alpha f^\alpha$ for $\alpha \in \{0, -1, -2\}$. Here $G_\nu(f)$ is the one-sided power spectral density of frequency fluctuations. Throughout this thesis we will use $G_\xi(f)$ for one-sided spectral densities and $S_\xi(f)$ for two-sided spectral densities of an arbitrary quantity ξ (e.g., frequency, phase, position, electric field, etc.). In Chapter 6 we will discuss the Allan deviation and its relation to frequency noise spectrum more thoroughly, and elucidate the relationship between atomic spin observables and the local oscillator frequency noise power spectral density.

1.4 Performance of neutral-atom clocks

While the accuracy of single ion-based clocks is extraordinary, there is a compelling reason to pursue in parallel standards based upon ensembles of atoms: signal to noise. Roughly speaking, making N parallel measurements versus one single measurement should yield a \sqrt{N} enhancement of the signal to noise ratio (SNR). The \sqrt{N} -dependence of the noise—which allows the corresponding SNR gain of \sqrt{N} —is known as quantum projection noise [46] (discussed in detail in Chapter 2). The quantum projection noise-limited stability of an optical atomic clock based on a quantity, N ,

of quantum references (neutral atoms or ions) is given by [47, 48]

$$\sigma_y(\tau) = \frac{\chi}{\pi Q \sqrt{N}} \sqrt{\frac{T_c}{\tau}}. \quad (1.4)$$

Here, χ is a constant of order unity that accounts for the details of spectroscopy and fraction of atoms excited, and Q is the fractional line quality factor, which for optical standards can be $> 10^{14}$, and is one of the key motivating factors for their development. For even modest input parameters, an instability of $\sigma_y(\tau) < 10^{-16}/\sqrt{\tau/1 \text{ s}}$ is possible.

Until recently, no neutral atom-based optical standards were able to achieve quantum limited performance due to broadband laser noise, which ends up contaminating the clock correction signal through the Dick effect (discussed in Chapter 2). In Chapter 4 we will describe development of a next generation ultrastable laser local oscillator for the ^{87}Sr clock, which has allowed the ^{87}Sr clock to operate in the near-quantum limited regime. This development represents an important milestone in the history of optical standards.

1.5 Frequency combs

Femtosecond laser-based optical frequency combs are important tools for optical metrology and have revolutionized the field [49, 50]. With laser media ranging from bulk Ti:Sapphire and optical fibers to microtoroidal resonators, the frequency comb revolution shows no signs of slowing down. The spectral coverage of frequency combs has been demonstrated to span the mid-IR to the vacuum ultraviolet [51, 52, 53].

At the heart of a comb's utility is the equation that describes the optical frequency of a given mode, ν_n , as

$$\nu_n = n f_{\text{rep}} + f_0. \quad (1.5)$$

Here, $f_{\text{rep}} = 1/\tau$ is the comb pulse repetition rate, where τ is the time between successive pulses. f_0 is the carrier envelope offset frequency which arises due to the fact that the group and phase velocities inside the laser cavity are different and is related to the pulse-to-pulse carrier envelope

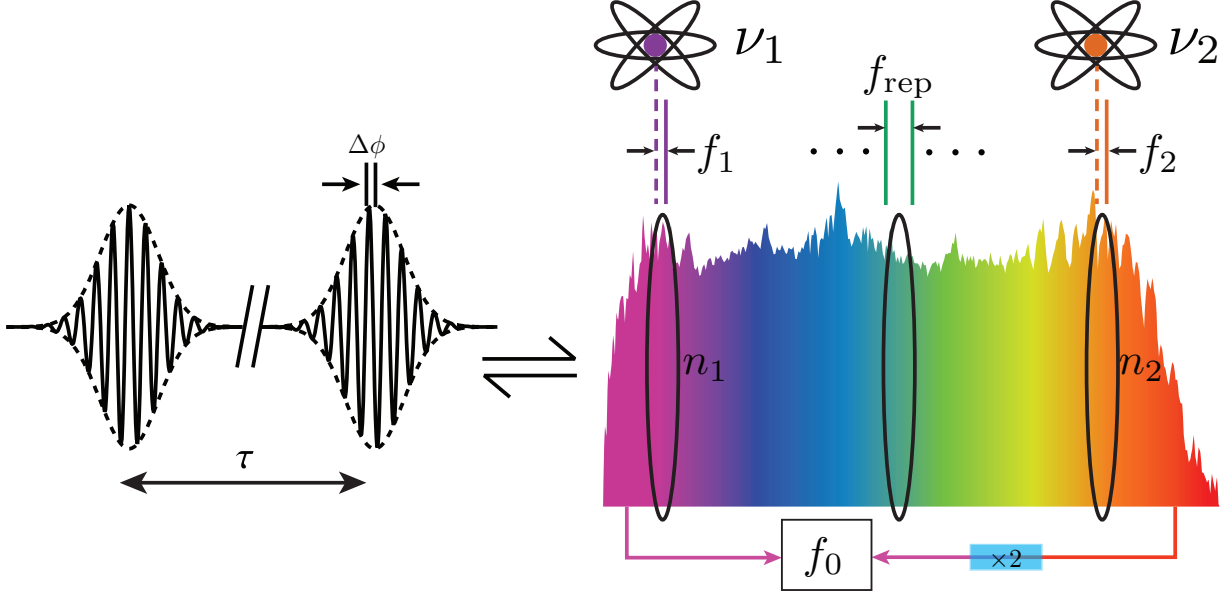


Figure 1.5: Frequency comb and optical clocks. The time-domain picture at left leads to a frequency-domain spectrum of evenly spaced spectral components or “teeth.” Here, a fully stabilized frequency comb is depicted comparing two optical clocks at disparate optical frequencies. By measuring the RF beats, f_1 and f_2 , the two optical frequencies can be compared. By measuring the comb repetition rate, f_{rep} , an absolute determination of the optical frequencies ν_1 and ν_2 can be made.

phase slippage ($\Delta\phi$ in Figure 1.5) by

$$f_0 = \Delta\phi f_{\text{rep}} / (2\pi). \quad (1.6)$$

In principle, f_{rep} and f_0 are the comb’s only degrees of freedom when describing the frequency of a given “tooth” in the frequency domain.

Figure 1.5 depicts a frequency comb as utilized in the direct comparison of optical clocks, or in the absolute frequency measurement of a clock (see, e.g., [1] for an absolute frequency measurement of ^{87}Sr utilizing an optical frequency comb). By locking a frequency comb to an optical source and stabilizing f_0 by the self-referencing technique [54, 50], the comb degrees of freedom are completely constrained and directly related to the optical phase of the reference laser. By making a heterodyne beat with a second laser, the phase of the two optical sources can be directly compared (Figure 1.5b), often across > 100 THz of spectral bandwidth [55, 56]. This technique can be

used to compare optical atomic clocks based upon different atomic species to constrain the drift of fundamental constants [28], and also allows optical frequencies to be measured against primary frequency standards with sub-Hz accuracy [57, 1, 32, 33, 30, 34]. Paired with frequency combs, phase-stabilized fiber links [58, 59, 60] allow frequency comparisons of clocks hundreds of kilometers removed and separated by hundreds of THz of bandwidth.

Even at the single-clock level, frequency combs will remain relevant and perhaps even play a more direct role in clock operation as local oscillator ultrastable lasers are developed over a broad spectral range. We will briefly discuss ongoing development of frequency combs to connect lasers hundreds of THz apart and to support the ^{87}Sr optical lattice clock in Chapter 4. In Chapters 3 and 4, we will see some of the motivating factors for developing ultrastable lasers in the $1.5\ \mu\text{m}$ region to connect lasers in the near-IR wavelength region to visible wavelengths.

1.6 Beyond timekeeping: Clocks in modern physics

Because they represent some of the most precise measuring device ever built, optical clocks are important tools for modern science. Due to their high precision and accuracy, optical clocks are the ideal devices for measuring spatio-temporal variations in the laws of physics, such as testing for gravitational coupling to fundamental constants in tests of local position invariance, and the time invariance of the fundamental constants of nature [61, 35, 34]. Another application of ultra-precise clocks is geodesy. A clock's sensitivity to the gravitational redshift allows it to be an extremely sensitive probe to differences in the earth's gravitational potential due to the gravitational redshift effect [62]. However, clocks employing many particles are also interesting systems in and of themselves from a quantum measurement perspective. Equation 1.4 is valid for uncorrelated atoms, but in the case that the atoms were maximally entangled (i.e., spin squeezed), the instability would be lower by approximately an additional factor of \sqrt{N} [63].

Many body quantum systems comprised of quantum gases of atoms [64, 65, 66, 67, 68, 69] and molecules [70, 71, 72] show promise for realizing novel quantum phases of matters and for the simulation of intractably complex condensed matter analogues. Alkaline-earth atoms possess

$SU(N)$ symmetry in the nuclear spin degrees of freedom, which could facilitate frustrated quantum magnetic models [73, 74, 75, 76]. Even “open” quantum systems subject to inelastic losses can enable new opportunities for studying quantum entanglement [77]. Chapter 5 explores many-body interactions between atoms in the ^{87}Sr optical lattice clock, where spin correlations emerge as a consequence of collective elastic and inelastic p -wave interactions. The correlations manifest themselves in the decay of Ramsey fringe contrast and as quadrature-dependent quantum noise in the effective spin degree of freedom encoded in the $^1\text{S}_0$ and $^3\text{P}_0$ clock states.

1.7 Overview of this thesis

This thesis describes the development and implementation of ultrastable lasers for spectroscopy in a ^{87}Sr lattice clock, and for exploring the many-body nature of the interactions between ^{87}Sr in a one-dimensional optical lattice. We demonstrate a 10-fold improvement in clock stability over any previous optical clock system, either ion- or neutral atom-based, allowing a 100-fold reduction in the time required for evaluating systematic effects. In Chapter 2, we describe the optical lattice clock system used in this work. Chapter 3 explores thermal noise in optical interferometers—a key limitation in developing stable lasers with performance at the 10^{-16} level. Chapter 4 describes the design and implementation of ultrastable laser systems. Chapter 5 explores the many-body nature of the optical lattice clock, utilizing the 10-fold improved stability of the next-generation local oscillator laser. Chapter 6 describes a theoretical framework and experimental demonstration of utilizing the optical clock as a frequency discriminator by utilizing pulse sequences, allowing unprecedented precision for characterizing the broadband noise of a single ultrastable laser system.

Chapter 2

The ^{87}Sr optical lattice clock

The Sr lattice clock was the first optical lattice clock to be developed, and is now by far the most prolific and well-characterized neutral atom optical frequency standard. This fact is reflected in its acceptance as a secondary representation of the second by the *Bureau International des Poids et Mesures* (BIPM) and the strong record of international agreement of the optical frequency of the $^1\text{S}_0 \rightarrow ^3\text{P}_0$ clock transition in ^{87}Sr . In this chapter, we review the properties that enable ^{87}Sr to be a successful optical lattice clock, the experimental apparatus utilized in the JILA ^{87}Sr lattice clock, and key limitations to both stability and uncertainty.

2.1 Introduction

The features that make Sr an interesting and productive species for wide-ranging studies in ultracold quantum gases also make it a highly suitable candidate for an optical clock. In the 1990s, the first experiments to laser cool Sr were performed, and were motivated by the novelty of the $J = 0$ ground state and the potential for precision spectroscopy [78, 79]. As seen from the level structure diagram in Fig. 2.1, strontium possesses two transitions from the $^1\text{S}_0$ ground state that are suitable for laser cooling: the broad $^1\text{S}_0 \rightarrow ^1\text{P}_1$ permits magneto-optical traps (MOTs) with $> 10^9$ atoms at temperatures at the level of 1 mK (which was used in the initial laser-cooling experiments), and the narrow $^1\text{S}_0 \rightarrow ^3\text{P}_1$ transition permitting a quantum-limited minimum temperature of ~ 250 nK [80]. Furthermore, the lowest-lying state of the triplet manifold is metastable with an estimated lifetime of ~ 100 s, for ^{87}Sr , whereas in ^{88}Sr , the transition lifetime is estimated at nearly 6000 years

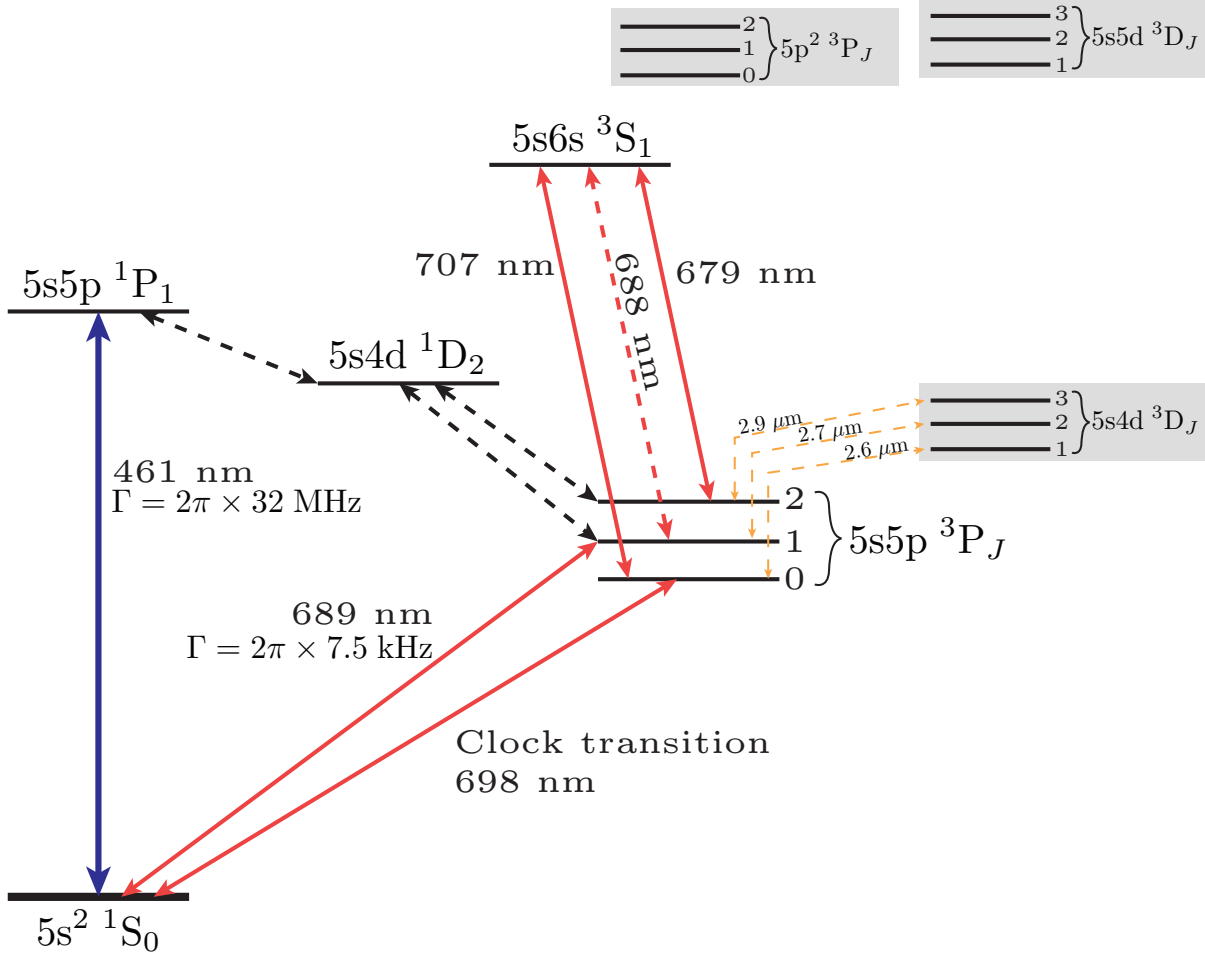


Figure 2.1: Strontium level diagram. Solid lines indicate laser-driven transitions. The dashed black lines are the problematic decay processes from the MOT at 461 nm that must be closed via optical pumping at 679 nm and 707 nm. The grey boxed transitions indicate the manifolds of primary relevance for the 3P_0 polarizability at the lattice wavelength and also the DC polarizability. Details of these states are given in the main text.

[81]! In both isotopes, therefore, this level can truly be considered metastable, and is thus the $^1S_0 \rightarrow ^3P_0$ transition is suitable for ultra-high precision optical spectroscopy and forms the basis of the strontium lattice clock. Finally, the alkaline earth-like level structure of the triplet and singlet manifolds possess sufficient complexity such that they support “magic wavelengths” for the 1S_0 and 3P_0 states, and this was a key component of the first lattice clock proposal based on the $^1S_0 \rightarrow ^3P_0$ transition [82].

In a magic-wavelength trap, the AC stark shift of a probe or dipole trapping optical field perturbs each state equally [26]. Within the context of precision spectroscopy, the presence of a magic wavelength permits the construction of an optical dipole where the transition between the metastable clock states is unperturbed by the trapping field. This permits a very elegant conceptual simplification of the dynamics of an atom in a magic-wavelength dipole trap. We consider the coherent superposition

$$|\psi\rangle = \alpha|g, \mathbf{n}\rangle + \beta|e, \mathbf{n}\rangle. \quad (2.1)$$

Here, g represents the 1S_0 ground state, e represents the 3P_0 metastable state and $\mathbf{n} \equiv \{n_x, n_y, n_z\}$ labels the motional state of the atom in a three-dimensional harmonic trap. At exactly the magic wavelength, the motional and electronic quantum states are decoupled, so that we may instead write Eq. 2.1 as

$$|\psi\rangle = (\alpha|g\rangle + \beta|e\rangle) \otimes |\mathbf{n}\rangle. \quad (2.2)$$

The success of the clock based on the $^1S_0 \rightarrow ^3P_0$ transition relies directly on the decoupling of the motional and electronic degrees of freedom, such that the spectra obtained in the lattice clock are free from AC Stark shifts or broadening as a result of thermally-distributed motion of the atoms.

This Chapter describes in detail the apparatus used to cool ^{87}Sr into a magic-wavelength optical lattice dipole trap. We will explore the details of the magic wavelength trapping including limitations due to lattice photon scattering. Details regarding the ultrastable clock laser are given later, in Chapter 4. In Chapter 4 we also demonstrate operation of the clock in a near-quantum-limited regime.

2.2 Narrow-line laser cooling

As mentioned in the previous discussion, one feature of the level structure of Sr that makes it appealing for use in an optical standard, as well as for quantum gas research, is the presence of the narrow $^1S_0 \rightarrow ^3P_1$ transition. In fact, the exploration of narrow-line cooling in Sr and other Alkaline earth/Alkaline earth-like atoms represents an important milestone in the history of laser

cooling. To date, $\Delta J = 1$ intercombination transitions (i.e. the $^1S_0 \rightarrow ^3P_1$ transition) have been utilized to trap and cool a large array of species and isotopes of alkaline earth and alkaline earth-like atoms. Examples include Sr [83, 84, 85], Calcium ([86]), and Ytterbium [87]. Due to the breakdown of LS-coupling towards jj -coupling in heavier atoms [88], the intercombination transitions coupling in Mercury [89, 90] and Radium [91] are well suited for single-stage laser cooling, and have been used for this purpose, but are too broad to be considered narrow-line cooling transitions. In this section, we briefly describe some of the important features of narrow-line laser cooling.

The expression “narrow line cooling” is typically used to denote a laser-cooling on a cycling transition for which the recoil frequency shift of the transition, given by

$$\omega_{\text{rec}} = \frac{\hbar\omega_a^2}{2mc^2}, \quad (2.3)$$

where ω_a is the optical transition angular frequency and m is the atomic mass, is comparable to the linewidth of the transition that is utilized for cooling. In the case of Strontium, the narrow $^1S_0 \rightarrow ^3P_1$ transition is a nearly ideal transition for laser cooling. For Sr, $\omega_{\text{rec}}/(2\pi) = 4.8$ kHz and is thus comparable to the 7.5 kHz natural linewidth of the $^1S_0 \rightarrow ^3P_1$ transition. In a sense, this is the ideal situation. For laser cooling on transitions where $\omega_{\text{rec}} \lesssim \Gamma$, the minimum temperature is expected to be in the quantum-limited regime set by the recoil energy [92],

$$k_B T = \hbar\omega_{\text{rec}}. \quad (2.4)$$

At the same time, the peak force of the cooling beams, given by $F_{\text{max}} = \hbar k \Gamma / 2$ and which determines the velocity capture range, must be large enough to provide robust trapping. Thus, there is no real benefit to performing traditional optical molasses laser cooling on a transition for which $\Gamma \ll \omega_{\text{rec}}$ with respect to a transition for which $\Gamma \simeq \omega_{\text{rec}}$. Specifically, in narrow-line MOTs, F_{max} can be dangerously close to the force exerted by gravity, mg . In the case of strontium, where $\Gamma = 2\pi \times 7.5$ kHz, $F_{\text{max}} \simeq 16 \times mg$ [85], allowing the atoms to be trapped against gravity. In Calcium, for example, where the $^1S_0 \rightarrow ^3P_1$ transition has $\Gamma = 2 \times 10^3$ 1/s, F_{max} is only $1.5 \times mg$, necessitating the use of an optical quenching technique to artificially increase Γ [86].

The nearly ideal parameters of the Sr $^1S_0 \rightarrow ^3P_1$ led to successes in laser cooling with this transition, yielding temperatures as low as ~ 250 nK [80] and in-MOT phase-space densities of ~ 0.1 [93]. Further work to overcome the detrimental effect of photon rescattering has recently led to the production of a directly laser-cooled Bose-Einstein condensate (BEC) [94] in ^{84}Sr , a technique that shows great promise in creating a continuous source of BEC (i.e., a continuous atom laser) and facilitating other quantum gas experiments that benefit from fast repetition.

2.3 Lattice dipole trapping

Trapping and manipulating neutral atoms with intense light fields is a well-established and extremely powerful technique [95, 96]. In contrast to magnetic trapping, optical dipole traps can produce intricate trapping potentials with sub-wavelength precision, the most prolific of which are optical lattices. In an optical lattice, the interference of two or more several phase coherent laser beams (or a single retro reflected beam) can give rise to periodic light patterns in one, two, and three dimensions. Among other uses, the use of such highly periodic potentials can aid quantum simulation of condensed matter systems [97], and serve as a test bed for exploring quantum phase transitions [64, 98], frustrated quantum systems [99], quantum Hall physics [100], and quantum gases and polar molecules in reduced dimensionality [101, 71]—and this is only to name a few.

In the context of optical lattice clocks, the periodicity of the potential is actually not a necessary, or even desired feature. Rather, the interferometric nature of the optical trapping field allows extremely tight local trapping potentials, with trapping frequencies $\gtrsim 100$ kHz easily accessible. This in turn enables spectroscopy in the Lamb-Dicke regime [102, 103, 104], where the recoil energy is much less than the harmonic oscillator zero-point energy of the trap. In the Lamb-Dicke regime, Doppler broadening effects are well-resolved from the unperturbed carrier transition, while the recoil momentum is absorbed by the trapping field (we will return to the topic of Lamb-Dicke confinement in Section 2.5). This is an essential requirement for a precise optical atomic clock,

given that Doppler broadening of an atomic transition is (see e.g., [88])

$$\frac{\Delta\nu}{\nu} = \sqrt{\frac{8k_B T \log 2}{mc^2}}, \quad (2.5)$$

which corresponds to $\Delta\nu/\nu \simeq 1 \times 10^{-10}$ for ^{87}Sr at $1 \mu\text{K}$, corresponding to a Doppler-broadened linewidth of 30 kHz. Of course, Doppler-free spectroscopy techniques have existed since nearly the advent of the laser. For instance, Doppler-free Ramsey [11, 12] and Ramsey-Bordé spectroscopy can be performed on narrow-line transitions within atomic beams and MOTs [105, 106], allowing sub-kHz features to be observed [20] and forming the basis of the calcium neutral-atom standard [107]. However, the natural linewidths of highly forbidden atomic transitions in Alkaline-earths, such as the $\sim 1 \text{ mHz}$ $^1\text{S}_0 \rightarrow ^3\text{P}_0$ transition in ^{87}Sr are still many orders of magnitude below the best linewidths achieved with free-space Doppler-free techniques, such as Ramsey Bordé spectroscopy. The role of the optical lattice then is not just to remove the effects of Doppler broadening and the potential systematics associated with Doppler-free Ramsey-Bordé spectroscopy, but to enter a regime where a large fraction of the atoms can be sufficiently localized to be probed at the one-second timescale.

2.3.1 Atomic polarizability calculation

In general, the utility of dipole trapping as a scientific technique lies in the favorable scaling of scattered radiation, which causes heating and decoherence, to the total depth of the trapping potential. If we consider an isolated resonance in the rotating wave approximation, and for detunings small compared to the transition's optical frequency, the ratio of scattered radiation to the dipole potential is [96],

$$\hbar\Gamma = \frac{\gamma}{\Delta}U. \quad (2.6)$$

where Γ is the rate of scattered radiation, γ is the decay rate of the atomic transition considered, Δ is the trapping laser detuning ($\Delta \equiv \omega_L - \omega_a$), and U is the induced dipole potential. We note that although Eq. 2.6 is utilized quite frequently to estimate the photon scattering rate in optical lattice clocks, where often $|\Delta| \sim \omega_a$, the expression given in Eq. 2.6 fails badly because it does not

take into account the wavelength-dependence of the density of states for the scattered photon and Fermi Golden Rule energy scaling, nor does it include the counter-rotating term if we do not make the rotating wave approximation. Including both these effects for a two-level system yields [96]

$$\hbar\Gamma = U \left(\frac{\omega_L}{\omega_a} \right)^3 \left(\frac{\gamma}{\Delta} - \frac{\gamma}{\omega_L + \omega_a} \right), \quad (2.7)$$

which can yield fairly accurate results for the ground state scattering of ^{87}Sr , where the $^1\text{P}_1$ level dominates the scattering. We also note that, while U is straightforward to calculate for a simple two-level system, there are regimes where no single atomic resonance dominates and thus determining U requires summing over many atomic levels. The significance of Eqs. 2.6 and 2.7 is that the ratio of trapping strength (good) to rate of photon scattering (bad) gets better and better as the detuning is moved farther away from resonance. This is the motivation behind the far off-resonance trap [95]. We will study the limitations to the Sr lattice clock due to photon scattering in Section 2.6.

To accurately calculate the trapping potential for a general system, where the two-level approximation does not necessarily apply, we begin by considering a monochromatic optical field with a spatial amplitude dependence such that

$$\mathbf{E}(\mathbf{r}, t) = \frac{1}{2}\mathbf{E}_0(\mathbf{r})e^{-i\omega t} + \frac{1}{2}\mathbf{E}_0^*(\mathbf{r})e^{i\omega t}. \quad (2.8)$$

The term $\mathbf{E}_0(\mathbf{r})$ can further be expressed as

$$\mathbf{E}_0(\mathbf{r}) = \boldsymbol{\varepsilon}E_0(\mathbf{r}), \quad (2.9)$$

where $\boldsymbol{\varepsilon}$ and $E_0(\mathbf{r})$ are the field polarization and amplitude, respectively. Both of these quantities are complex. For a monochromatic plane wave with linear polarization, Eq. A.1 reduces to the familiar expression $\mathbf{E}(\mathbf{r}, t) = \boldsymbol{\varepsilon}E_0 \cos(kx - \omega t)$.

For the electric field given in Eq. A.1, the dipole trapping potential is given by

$$U(\mathbf{r}) = -\frac{1}{2}\alpha(\boldsymbol{\varepsilon}) \langle |\mathbf{E}(\mathbf{r}, \mathbf{t})|^2 \rangle = -\frac{1}{4}\alpha(\boldsymbol{\varepsilon}) |E_0(\mathbf{r})|^2 \quad (2.10)$$

Here the $\langle \dots \rangle$ represents a time average over an optical cycle so that α is defined with respect to the mean square electric field. This allows consistency with the definition in the case of a dc electric field [88].

The polarizability is found from second-order perturbation theory [88, 108] as

$$\alpha(\varepsilon) = 2 \sum_k \frac{\omega_{ik} \left| \langle \phi_i | \varepsilon \cdot \hat{\mathbf{d}} | \phi_k \rangle \right|^2}{\hbar (\omega_{ik}^2 - \omega^2)}. \quad (2.11)$$

Here, the polarizability is determined by summing over all dipole-allowed upper states, $\{\phi_k\}$ where \mathbf{d} is the dipole operator that connects the atomic level of interest, ϕ_i to upper atomic levels that are responsible for the induced dipole moment. Here, ω_{ik} is the frequency difference between the state ϕ_i and the states $\{\phi_k\}$. The dependence on the light polarization follows fundamentally from the tensorial nature of the polarizability operator. In fact, we can write $\alpha(\varepsilon) = \varepsilon_\mu^* \varepsilon_\nu \alpha_{\mu\nu}$ (repeated indices are summed), where $\alpha_{\mu\nu}$ is the polarizability tensor. As with any cartesian tensor operator, we can decompose α_{ij} into a spherical tensor basis, which will allow us to make some general statements about the light- and atom-polarization dependence of the polarizability. Thus, as it is written, Eq. 2.11 does not cast the polarizability in its most useful form.

2.3.1.1 Scalar, vector, and tensor light shifts

While Eq. 2.11 is perfectly valid for calculating the dipole trapping potential and light shifts, the tensorial nature of the polarizability is not apparent, nor can we make any qualitative statements regarding its behavior. It is the goal of this section to summarize the most useful results regarding the polarizability tensor. Specifically, we can write [109]

$$U(\mathbf{r}) = -E_\mu^{(-)} E_\nu^{(+)} \alpha_{\mu\nu} \quad (2.12)$$

where

$$\alpha_{\mu\nu} = 2 \sum_k \frac{\omega_{ik} \langle \phi_i | \hat{d}_\mu | \phi_k \rangle \langle \phi_k | \hat{d}_\nu | \phi_i \rangle}{\hbar (\omega_{ik}^2 - \omega^2)}. \quad (2.13)$$

The electric field is now expressed with slightly different parameters such that $\mathbf{E}^{(+)} \equiv \mathbf{E}_0(\mathbf{r})/2 = [\mathbf{E}^{(-)}]^*$. In Appendix C, we follow the approach of [108, 109] to reduce the tensorial $\alpha_{\mu\nu}$ into

contributions of irreducible spherical tensors to derive the standard expression for scalar, vector, and tensor light shifts (see, eg, [110])

$$\alpha(\boldsymbol{\varepsilon}) = \alpha_s + i\alpha_v(\boldsymbol{\varepsilon} \times \boldsymbol{\varepsilon}^*) \cdot \mathbf{e}_z \frac{m}{F} + \alpha_t \frac{(3|\boldsymbol{\varepsilon} \cdot \mathbf{e}_z|^2 - 1)}{2} \left[\frac{3m^2 - F(F+1)}{F(2F-1)} \right]. \quad (2.14)$$

Here, we have introduced α_s , α_v , and α_t , the ‘‘scalar’’, ‘‘vector’’, and ‘‘tensor’’ polarizabilities, respectively. In terms of the reduced matrix elements, the polarizabilities are [108, 109]

$$\alpha_s(\omega) = \sum_{n'F'} \frac{2\omega_{nF \rightarrow n'F'} \left| \langle nF || \hat{\mathbf{d}} || n'F' \rangle \right|^2}{3\hbar(\omega_{nF \rightarrow n'F'}^2 - \omega^2)} \simeq \sum_{n'J'} \frac{2\omega_{nJ \rightarrow n'J'} \left| \langle nJ || \hat{\mathbf{d}} || n'J' \rangle \right|^2}{3\hbar(\omega_{nJ \rightarrow n'J'}^2 - \omega^2)}, \quad (2.15)$$

$$\alpha_v(\omega) = \sum_{n'F'} (-1)^{F+F'+1} \sqrt{\frac{6F(2F+1)}{(F+1)}} \begin{Bmatrix} 1 & 1 & 1 \\ F & F & F' \end{Bmatrix} \frac{\omega_{nF \rightarrow n'F'} \left| \langle nF || \hat{\mathbf{d}} || n'F' \rangle \right|^2}{\hbar(\omega_{nF \rightarrow n'F'}^2 - \omega^2)}, \quad (2.16)$$

$$\alpha_t(\omega) = \sum_{n'F'} (-1)^{F+F'} \sqrt{\frac{40F(2F-1)(2F+1)}{(1+F)(2F+3)}} \begin{Bmatrix} 1 & 1 & 2 \\ F & F & F' \end{Bmatrix} \frac{\omega_{nF \rightarrow n'F'} \left| \langle nF || \hat{\mathbf{d}} || n'F' \rangle \right|^2}{\hbar(\omega_{nF \rightarrow n'F'}^2 - \omega^2)}. \quad (2.17)$$

We can relate the reduced matrix element $\langle F || \hat{\mathbf{d}} || F' \rangle$ to $\langle J || \hat{\mathbf{d}} || J' \rangle$ by [111, 108, 109]

$$\langle F || \hat{\mathbf{d}} || F' \rangle = \langle J || \hat{\mathbf{d}} || J' \rangle \sqrt{(2F'+1)(2J+1)} (-1)^{F'+J+I+1} \begin{Bmatrix} J & J' & 1 \\ F' & F & I \end{Bmatrix}. \quad (2.18)$$

Here, the terms in curly brackets are the Wigner 6- j symbols and $\omega_{nF \rightarrow n'F'}$ is the transition frequency between the state with quantum numbers n and F to the state with quantum numbers n' and F' . In Appendix B, we describe the procedure for relating the reduced matrix elements $\langle J || \hat{\mathbf{d}} || J' \rangle$ and $\langle F || \hat{\mathbf{d}} || F' \rangle$ to transition lifetimes commonly reported in the literature.

There are several special cases worth considering for α_v and α_t . The first interesting scenario is the case where $F = 0$, which describes the clock states for ^{88}Sr . Here, it is immediately clear that $\alpha_v = 0$ and $\alpha_t = 0$. This matches the intuitive picture of an $F = 0$ as a state devoid of a specific orientation—not to mention that there are no m_F levels, rendering the very notion of a vector or tensor shift invalid. The second case is very similar, but more relevant for this work. This is the case where $J = 0$ but there is nuclear spin I , such that $F = I$. If we insert the result of Eq. C.26 for $\langle F || \hat{\mathbf{d}} || F' \rangle$ into Eqs. C.23–C.25 and perform the sum over F' for any J' value, we get

a number that is very nearly zero for α_v and α_t as long as the laser detuning is much larger than the hyperfine splitting. If we ignore the hyperfine splitting completely, then the result for α_v and α_t is identically zero. Finally, the last case of interest, and one that is relevant for the ^{171}Yb clock [32], is the case¹ where $F = 1/2$ and $J = 0$. Here we see that $\alpha_t = 0$. Again, this makes intuitive and pragmatic sense because with only two m_F levels, the concept of a tensor shift is ill-defined.

Finally, it is worth mentioning that, due to the hyperfine state mixing between the $^3\text{P}_0$ clock state and the $^3\text{P}_1$ and $^1\text{P}_1$ states, the clock state does acquire a small but finite vector and tensor shift. These quantities have been theoretically explored [112] and thoroughly measured by the SYRTE Sr lattice clock group [110]. As seen in Eq. 2.14, as long as the light polarization is controlled with respect to the quantization axis, these shifts can be removed by including them in the definition of the magic wavelength, or by a post-correction, and should pose no threat to clock accuracies below 10^{-17} [110].

2.3.1.2 Numerical results for Sr

The $^1\text{S}_0$ and $^3\text{P}_0$ clock states of ^{87}Sr both have $J = 0$, thus based on the discussion of the previous section the polarizability should only have a contribution for α_s . Ignoring hyperfine structure, it is straightforward to calculate α_s for both the $^1\text{S}_0$ and $^3\text{P}_0$ states from Eqs. C.23 and C.26 (see appendix B) as

$$\alpha_{3\text{P}_0}(\omega) = 2\pi\epsilon_0\hbar c^3 \sum_{n',J'} \frac{\omega_{nF \rightarrow n'F'} A_T(n', J')}{\tilde{\omega}_{n',J'}^3 (\omega_{nF \rightarrow n'F'}^2 - \omega^2)} \frac{(2L' + 1)}{3} \quad (2.19)$$

$$\alpha_{1\text{S}_0} = 6\pi\epsilon_0\hbar c^3 \sum_{n',J'} \frac{A_T(n', J')}{\omega_{nF \rightarrow n'F'}^2 (\omega_{nF \rightarrow n'F'}^2 - \omega^2)}. \quad (2.20)$$

Here, $A_T(n', J')$ is the total decay rate of the excited state labelled by quantum numbers n' and J' , where n' is shorthand for the electronic configuration and J' is the total angular momentum (for all dipole-allowed transitions from the clock states, $J' = 1$); and $\tilde{\omega}_{n',J'}$ is an effective transition

¹ This instance is seemingly covered by the $J = 0$ rule, which precludes both vector and tensor shifts. It turns out the origin of the vector and tensor shifts in the clock state arises from hyperfine-induced state mixing between levels of like F [112]. Thus, for the case of $J = 0$, $F = 1/2$, the statement that there is no tensor shift is a rigorous one, while the statement that for $J = 0$ levels $\alpha_v = \alpha_t = 0$ is not.

States used for 3P_0 scattering rate calculation		
State	A-coefficient	Detuning from 3P_0
5s6s 3S_1	8.5*	2.773*
5s7s 3S_1	1.75*	4.356*
5s8s 3S_1	0.822	4.984
5s9s 3S_1	0.453	5.303
5s10s 3S_1	0.277	5.487
5s4d 3D_1	0.0345	0.724
5s5d 3D_1	6.1	3.899
5s6d 3D_1	2.67	4.781
5s7d 3D_1	1.42	5.192
5s8d 3D_1	0.851	5.419
5s9d 3D_1	0.551	5.59
5p5p 3P_1	12.7	3.982
States used for 1S_0 polarizability		
State	A-coefficient	Detuning from 1S_0
5s5p 1P_1	19.05	4.08998
5s6p 1P_1	0.186	6.42732
5s7p 1P_1	0.319	7.33361
4d5p 1P_1	1.2	7.76074
5s8p 1P_1	1.49	7.76074
5s9p 1P_1	1.16	8.0039
5s10p 1P_1	0.76	8.16695
5s11p 1P_1	0.488	8.28212

Table 2.1: Upper states used in calculating the polarizability of the 1S_0 and 3P_0 clock states. The Einstein A-coefficient is given in units of 10^7 1/s, and the detuning is given in units of 10^{15} rad/s (i.e., $10^{-15} \times \Delta\omega$, where $\Delta\omega$ is the transition frequency). The numerical values are obtained from [112] and references therein, with the exception of the data marked with an asterisk, which is from [113].

frequency from the upper state connecting to 3P_1 that takes into account the relativistic correction due to the fine structure energy splitting within the 3P manifold. This latter correction is derived in Appendix B. With these particularly simple expressions for the $J = 0$ clock states, we calculate the polarizability employing the decay rates of a subset of the upper-lying states, given by the values in Table 2.1. The results of this calculation are shown in Fig. 2.2. As expected from several calculations and measurements spanning the history of the Sr clock’s development, we find a magic wavelength in the vicinity of 813 nm, where the discrepancy between experiment arises from an incomplete knowledge of the transition rates and also the fact that we do not treat continuum

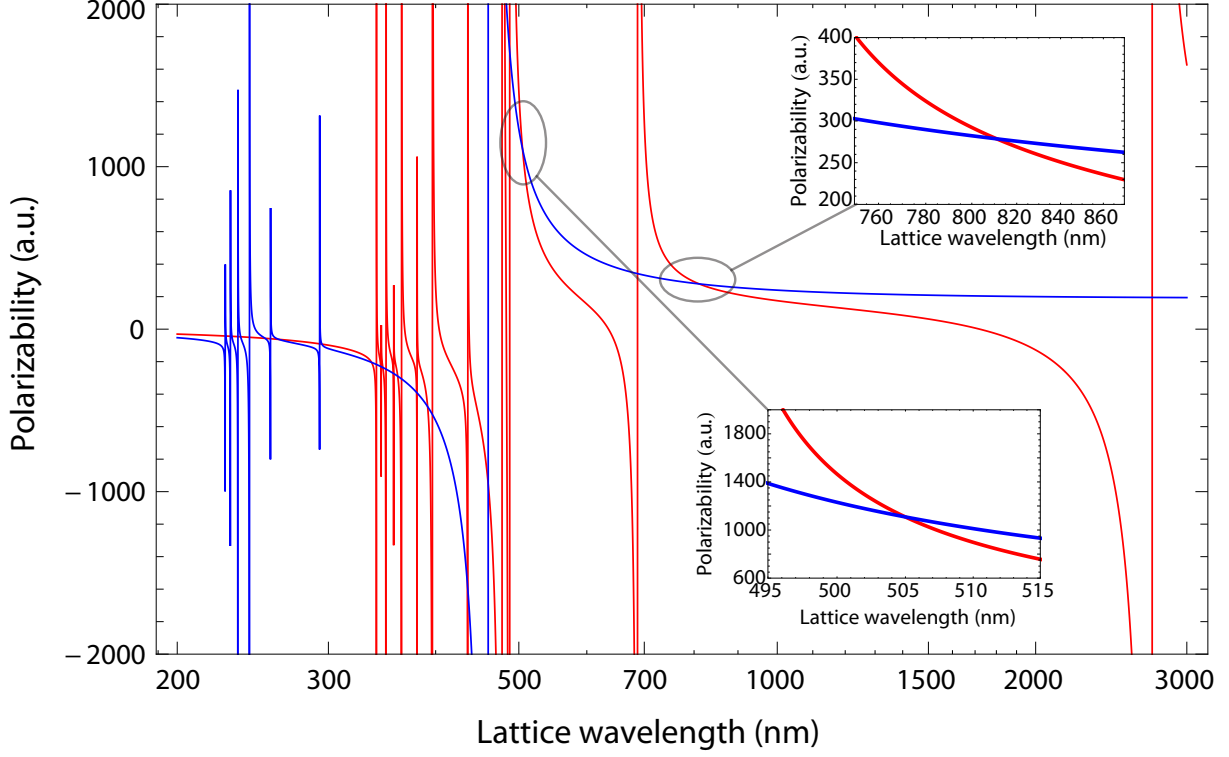


Figure 2.2: Polarizability of the 1S_0 (blue line) and 3P_0 (red line) clock states in atomic units (a.u.). The insets show two regions where the polarizabilities of the 1S_0 and 3P_0 clock states are matched.

states in this calculation [114, 115]. Interestingly, another magic wavelength crossing occurs in the vicinity of 505 nm. As conveyed qualitatively by Eq. 2.6, one might expect that using this as a lattice wavelength would lead to unacceptably large lattice scattering. We will treat photon scattering from the lattice in Section 2.6. Surprisingly, we find that the magic wavelength at 505 nm will have acceptable scattering rates for an equivalent trapping frequency, indicating that this may be an interesting magic wavelength for use with relatively low-power optical sources.

2.3.2 One-dimensional optical lattice

Now that we have calculated the polarizabilities, we consider the specific case of a one-dimensional optical lattice formed by a retro-reflected laser beam. We consider a focused input

beam with electric field amplitude profile

$$E^{\text{in}}(\mathbf{r}; t) = \frac{1}{2} E_0^{\text{in}}(r_{\perp}) e^{-ikz - i\omega t} + \text{c.c.} \quad (2.21)$$

with the radially-dependent amplitude

$$E_0^{\text{in}}(r_{\perp}) = \sqrt{\frac{4P_0}{\pi\epsilon_0 c w_0^2}} e^{-r_{\perp}^2/w_0^2}, \quad (2.22)$$

where P_0 is the total input power. If the beam is perfectly retro-reflected to the same focus, the electric field profile will be

$$E(\mathbf{r}; t) = \frac{1}{2} [2 \cos(kz) E_0^{\text{in}}(r_{\perp})] e^{-i\omega t} + \text{c.c.} \quad (2.23)$$

and thus according to Eq. 2.10 the lattice potential will be

$$U(\mathbf{r}) = -\alpha \cos^2(kz) |E_0^{\text{in}}(r_{\perp})|^2. \quad (2.24)$$

If we expand the potential along the z -direction at $r_{\perp} = 0$ we can treat the potential as a harmonic oscillator. The longitudinal trap frequency associated with this profile is easily found to be [112]

$$\nu_z = \frac{1}{2\pi w_0 \lambda} \sqrt{\frac{32\pi\alpha P_0}{c\epsilon_0 M}} = \frac{1}{\lambda} \sqrt{\frac{\alpha I_{\text{peak}}}{\epsilon_0 c M}}. \quad (2.25)$$

where $I_{\text{peak}} = 2\epsilon_0 c |E_0^{\text{in}}(0)|^2 = 8P_0/(\pi w^2)$. Similarly, the trap frequency associated with the radial confinement is given by

$$\nu_r = \frac{1}{2\pi w_0^2} \sqrt{\frac{16\alpha P_0}{\pi\epsilon_0 c M}} = \frac{1}{2\pi w_0} \sqrt{\frac{2\alpha I_{\text{peak}}}{\epsilon_0 c M}}. \quad (2.26)$$

We find that at 813.428 nm, the calculated Sr clock-state polarizability is 2.8×10^2 a.u. (a.u. stands for atomic units of polarizability, 1 a.u. = $4\pi\epsilon_0 a_0^3$). For $\nu_z = 80$ kHz, $I_{\text{peak}} = 3.4 \times 10^4$ W/cm² corresponding to $P_0 = 140$ mW for $w_0 = 32$ μ m, which is beam waist utilized in the experiment (we describe the lattice setup in Section 2.4.3 and the details of lattice spectroscopy in Section 2.5).

2.4 Experimental apparatus

The experimental apparatus used in this work has been extensively described elsewhere [112, 114, 80]. For completeness, we describe the essential details here. The vacuum system used to cool

and trap ^{87}Sr is shown in Fig. 2.3. An effusive oven loaded with high-purity strontium is operated at a maximum temperature of 575°C .² Earlier measurements of the beam flux indicated a beam flux of 3×10^{11} atoms/s [80]. We measure similar loading rates and MOT sizes, so we estimate that our current flux is also consistent with this number despite the fact that the oven has been disassembled and reloaded in the intervening decade. As depicted in Fig. 2.3, a rotary feedthrough actuates a cylindrical atomic beam shutter, which can be used to extinguish the atomic beam during operation of the experiment if desired. Interestingly, we observe no detrimental effect due to the atomic beam except that it leads to an additional background signal that must be subtracted.

A total of three 40 L/s ion pumps maintain a pressure estimated in the low 10^{-10} Torr level in the main chamber. This represents a four-fold improvement from the previously-reported experimental design [112, 114, 80], as indicated by in-trap lifetime measurements. The main improvement permitting these significantly lower pressures is the addition of a secondary differential pumping tube. In the original experiment, there was a single differential pumping tube, separating the oven from the main chamber, and permitting an order of magnitude difference in the pressures. With the addition of the second differential pumping region, we maintain an almost two order of magnitude difference between the oven and main chamber, for a vacuum-limited trap lifetime of 8 s [116].

A pair of Anti-Helmholtz coils (not pictured in Fig. 2.3) are placed so that the axial field direction is oriented vertically. They are capable of producing an axial field gradient of 50 G/cm for an input current of approximately 60 A. The current in these coils is servo-controlled and capable of being switched at ms timescales. This fast and precise control is utilized to perform programmed field-ramps for different stages of optical cooling. Small Helmholtz coil pairs oriented along the H1, H2 directions as labeled in Fig. 2.3 (horizontal direction 1 and 2, respectively) provide fine tuning to null stray fields in the horizontal plane. A third Helmholtz coil pair in the vertical direction (V) provides fine-tuning of the magnetic field in that direction.

During operation of the experiment, stray magnetic fields are nulled to < 10 mG by coils in

² The nozzle (front) part of the oven is operated at 575°C , while the back end of the oven is maintained at 365°C . This ensures that the nozzle region does not accumulate Sr and clog.

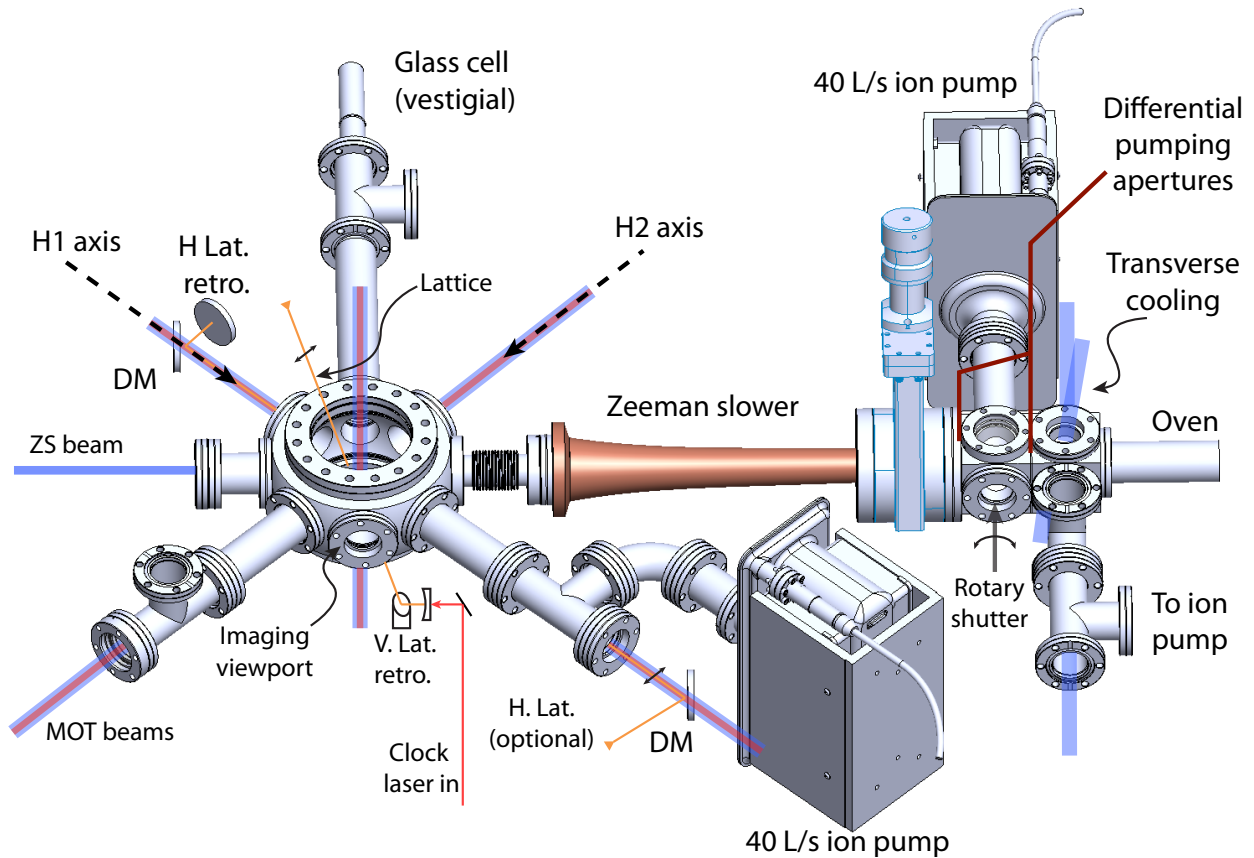


Figure 2.3: Experimental apparatus for trapping ultracold ^{87}Sr . A collimated atomic beam is emitted from the oven region and is subsequently transversally cooled by transverse cooling beams and slowed by a Zeeman slower (ZS). A MOT is formed in the octagonal main chamber (anti-Helmholtz coils not depicted). A total of three 40 L/s ion pumps are attached to the apparatus (pump located nearest the oven is not pictured), and each pump is separated from the others by a differential pumping tube, supporting a nearly two orders of magnitude difference in the oven vacuum pressure with respect to the main chamber. The optical lattice enters from the top viewport with an angle of approximately 19° with respect to gravity and is retroreflected after passing through the top and bottom viewports of the chamber. The lattice polarization is aligned along the H2 axis. Dichroic mirrors (DM) in the H1-axis MOT arms permit a secondary horizontal optical lattice to be overlapped with the vertical lattice.

the H1 and V directions. A residual field of ~ 500 mG is applied along H2 for spectroscopy, while a smaller field of (~ 100 mG) is applied for an optical pumping phase to spin-polarize the atoms if desired. As a result, H2 is the *de facto* quantization axis in the experiment.

Optical access is provided at several locations. Immediately after the oven nozzle, a cube with $2\frac{3}{4}$ " flanges provides access for transverse cooling beams. The next location in the apparatus with

significant optical access is the main chamber itself, which is octagonal in shape (in fact, it is called a “spherical octagon” by the manufacturer, Kimball Physics). Here, two large 6” flange-mounted viewports allow a wide range of optical access from the top and bottom of the chamber. The top viewport serves multiple functions, including providing optical access for fluorescence detection, the optical lattice, and MOT beams. Almost all of the sides of the octagon also have 2 3/4” flange-mounted viewport, utilized for the mot beams and optical imaging, as in Fig. 2.3. The viewport labelled “imaging viewport” in Fig. 2.3 provides access for an amplified CCD camera. All viewports are anti-reflection coated for visible wavelengths.

The trapping and cooling of ^{87}Sr is performed using two transitions for laser cooling. The atomic cloud is directly cooled into a far off resonance optical lattice comprising a standing wave of laser light at 813 nm. To avoid uncontrolled vector and tensor light shifts—which will be further described later—the dipole trap polarization is aligned with H2 with a high extinction-ratio polarizer ($\sim 10^4$). The first transition for laser cooling is the $^1\text{S}_0 \rightarrow ^1\text{P}_1$ transition at 461 nm, which is used for both slowing the beam and trapping and cooling ^{87}Sr in a magneto-optical trap (MOT). The second transition employed is the narrow $^1\text{S}_0 \rightarrow ^3\text{P}_1$ intercombination transition, which permits direct laser cooling to sub μK temperatures. These stages of laser cooling and trapping are described in detail in the next sections.

2.4.1 Laser cooling at 461 nm

The first stage of laser cooling is performed on the broad $^1\text{S}_0 \rightarrow ^1\text{P}_1$ transition, which is shown in Fig. 2.1 and the hyperfine structure of which is shown in Fig. 2.4. We note that the presence of hyperfine structure in ^{87}Sr complicates the cooling dynamics, and can lead to sub-Doppler cooling [117]. In clock operation, we use the first-stage 461 nm MOT to quickly accumulate $\sim 2 \times 10^5$ atoms in 500 ms. This quantity is approximately 10% of the maximum ^{87}Sr 461 nm MOT peak atom number.

The laser light utilized for the 461 nm MOT is derived via second harmonic generation. An external-cavity laser diode (ECDL) seeds a tapered amplifier, which provides approximately 1.6 W

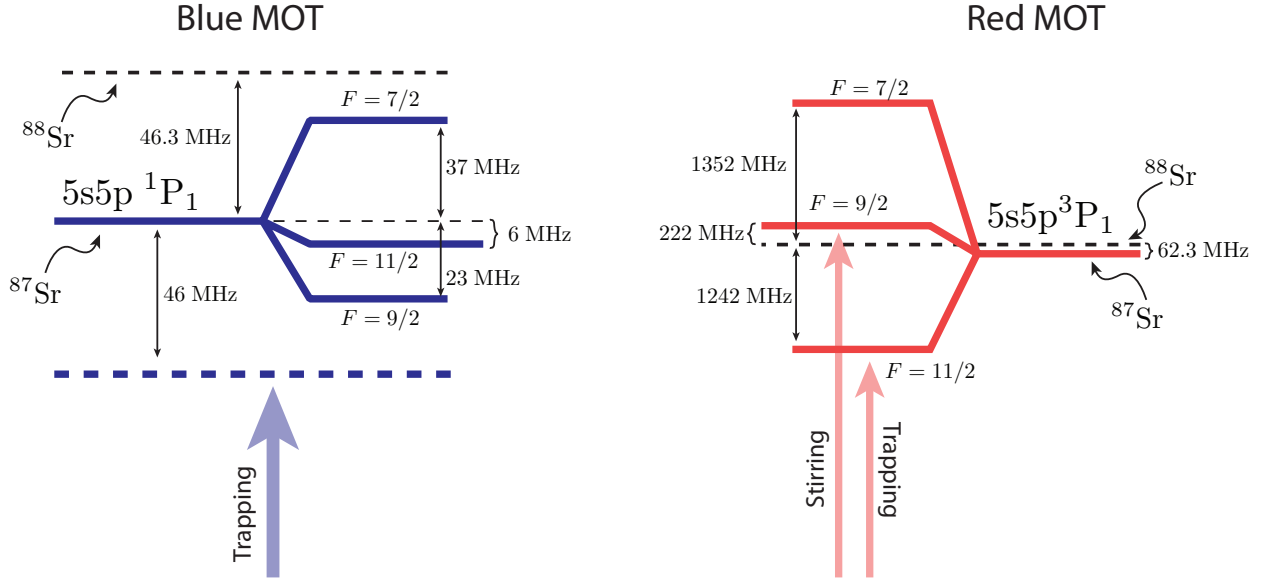


Figure 2.4: Hyperfine structure of the $5s5p^1P_1$ and $5s5p^3P_1$ levels.

of power at 922 nm. After being spatially filtered via a single-mode fiber, approximately 350 mW of power at 922 nm is delivered to two separate doubling cavities employing KNbO_3 crystals. Phase matching is achieved via temperature, with an operating temperature of approximately 150°C . Details can be found in Refs. [112, 114]. Each cavity produces approximately 150 mW of power at 461, which is utilized for slowing, cooling, and trapping with the $^1S_0 \rightarrow ^1P_1$ transition, as described below.

After exiting the oven, the atoms are cooled transversally by elliptical beams tuned 10 MHz below the $^1S_0 \rightarrow ^1P_1$ $F = 11/2$ (Fig. 2.3). After the transverse cooling stage, they are subsequently slowed in a Zeeman slower with a peak field of 600 G, optical power of ~ 60 mW, and detuning of -1030 MHz below the $^1S_0 \rightarrow ^1P_1$ $F = 11/2$ transition. Finally, upon reaching the main chamber the atoms are collected in a MOT operating on the $^1S_0 \rightarrow ^1P_1$ transition. The horizontal MOT beams have ~ 3 cm diameter and the horizontal beams have 8 mW of power, while the vertical beam has 3 mW of power. The field gradient utilized for the $^1S_0 \rightarrow ^1P_1$ MOT (AKA “blue mot”) is 50 G/cm in the vertical direction.

While the $^1S_0 \rightarrow ^1P_1$ transition is nearly closed, as shown in Fig. 2.1, there is a decay pathway

to the metastable 3P_2 level. In order to maintain efficient MOT operation, the 3P_2 level must be repumped by a separate laser at 679 nm connecting the $5s5s\ ^3P_2$ and $5s6s\ ^3S_1$ levels. Due to the fact that the $5s6s\ ^3S_1$ level employed in the repump scheme can in turn decay to the metastable 3P_0 state, an additional repump laser must be utilized to cycle these atoms out of 3P_0 , again via $5s6s\ ^3S_1$. Since the hyperfine manifolds of the $5s5s\ ^3P_2$ and $5s6s\ ^3S_1$ are quite large, we scan the repump lasers so that all the hyperfine levels are reached by a single laser. Finally, in order to prevent dark states from forming, the repump lasers are propagated along both the H1 and V MOT axes. Ultimately, the repumps make a huge difference, with a factor of ~ 40 improvement in the observed fluorescence, and an order of magnitude increase in the MOT lifetime.

2.4.2 Narrow line cooling with ^{87}Sr

A significant body of literature exists that explores the qualitative differences and challenges of laser cooling ^{87}Sr as opposed to its bosonic counterpart, ^{88}Sr [118, 112, 114]. Here we briefly summarize some of the key differences and describe the experimental methods used to cool and trap ^{87}Sr on the $^1S_0 \rightarrow ^3P_1$ transition.

2.4.2.1 The ^{87}Sr 689 nm MOT: principle of operation

In ^{88}Sr , the narrow line cooling transition is an ideal $J = 0 \rightarrow J = 1$ cycling transition, which allows the MOT to operate very efficiently. In the case of ^{87}Sr , with nuclear spin $I = 9/2$, one must consider the hyperfine levels of the 3P_1 level, with quantum number $F \in \{7/2, 9/2, 11/2\}$. At first glance, it might seem straightforward to operate the MOT on the $^1S_0 (F = 9/2) \rightarrow ^3P_0 (F = 11/2)$ transition. However there is a large disparity between the ground state g -factor of $g_S = -6 \times 10^{-4} \simeq 0$ and the excited state g -factors of $g_{7/2} = -1/3$, $g_{9/2} = 2/33$, and $g_{11/2} = 3/11$ [118, 112]. This means that the Zeeman shift in an applied magnetic field is almost exclusively restricted to the excited state manifold. This has two important implications for the MOT operated on the $^1S_0 \rightarrow ^3P_1$ $F = 11/2$ transition. First, the differential Zeeman shift of the ^{87}Sr $^1S_0 \rightarrow ^3P_1$ ($F = 11/2$) transition, as depicted in Fig. 2.5, has significant implications for MOT operation. To simplify

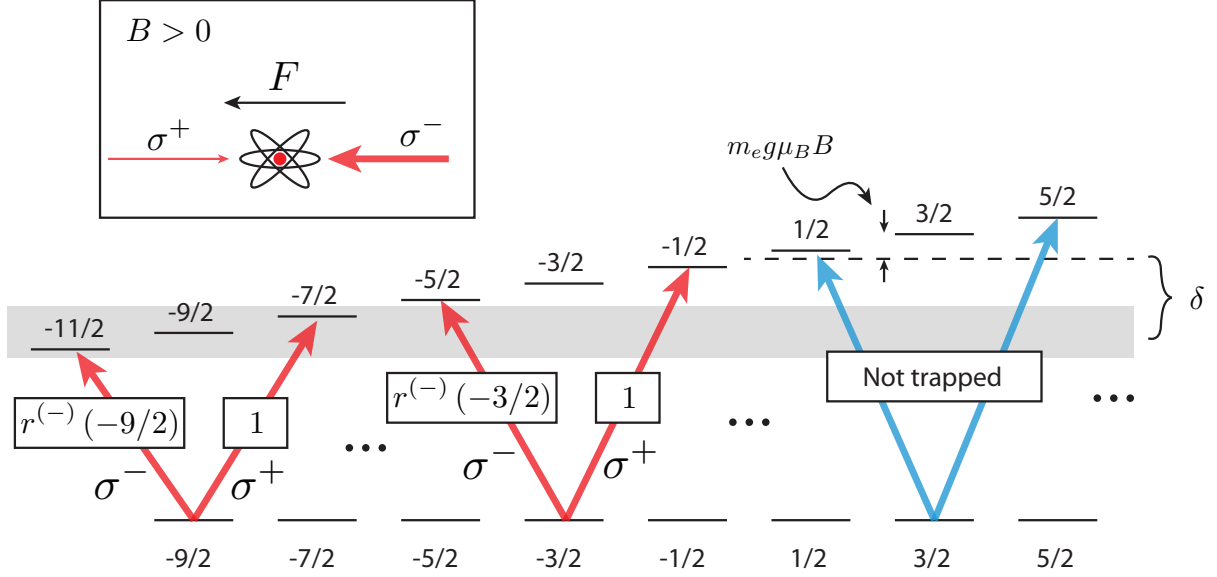


Figure 2.5: Schematic depiction of the 689 nm MOT for the $F = 9/2 \rightarrow F = 11/2$ transition. Due to the absence of an electronic magnetic moment in the ground state, several m_F sublevels are not trapped. The relative σ^+/σ^- transition strengths play a role in optical pumping and maintaining the MOT restoring force as well.

the discussion, we consider only one MOT axis. For a cooling laser detuned below the zero-field resonance with detuning δ , if the motion of the atom brings it into a region of the MOT with $B > 0$, there are a large number of ground-state m_F levels that are not trapped (specifically $m_F \geq 3/2$). This is because the increasing magnetic field will tune the Zeeman shift in the “wrong” direction for these states, and they will sail away without scattering any photons. An example of such a non-trapped state is depicted with blue arrows in Fig. 2.5. An identical effect prevents the states with $m_F \leq -3/2$ in the region with $B < 0$ from being trapped (assuming we use the same definition of quantization axis as before).

A second important implication of the $^{87}\text{Sr } 1\text{S}_0 \rightarrow 3\text{P}_1$ ($F = 11/2$) Zeeman structure arises when the atom is brought into resonance by the Zeeman shift. As depicted for the $m_F = -9/2$ state in Fig. 2.5, **both** σ^+ and σ^- transitions are allowed. An immediate concern is that the position dependent light force could be artificially small or even nullified by scattering photons from both MOT beams. However, it turns out that the Wigner-Eckart theorem effectively eliminates this

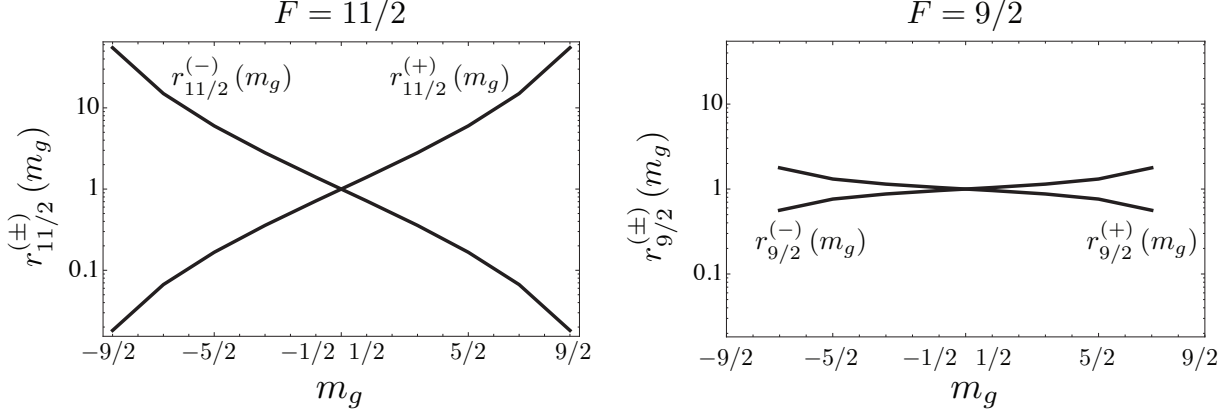


Figure 2.6: Ratio of σ^\pm absorption as a function of ground state magnetic sublevel, m_g .

concern [118]. We can write the ratio of transition probabilities for a σ^- transition with respect to a σ^+ transition for a general $F \rightarrow F + 1$ transition as

$$r_{F+1}^{(-)}(m_g) = \frac{|\langle F, m_g; 1, -1 | F + 1, m_g - 1 \rangle|^2}{|\langle F, m_g; 1, 1 | F + 1, m_g + 1 \rangle|^2} = \frac{(2 + F - m_g)! (F + m_g)!}{(2 + F + m_g)! (F - m_g)!} \quad (2.27)$$

Similarly, $r_{F+1}^{(+)}(m_g)$ is defined as the ratio of σ^+ to σ^- transitions, and is related to $r_{F+1}^{(-)}(m_g)$ simply as $r_{F+1}^{(+)}(m_g) = 1/r_{F+1}^{(-)}(m_g)$. Both $r_{F+1}^{(-)}(m_g)$ and $r_{F+1}^{(+)}(m_g)$ are plotted with respect to m_g in Fig. 2.6. Remarkably, for the situation in Fig. 2.5 with $B > 0$ and $m_g = -9/2$ the ratio of “good” σ^- photons absorbed to “bad” σ^+ photons absorbed is 55 : 1. As seen from Fig. 2.6, if a state is trappable, the ratio of “good” absorptions to “bad” absorptions is greater than unity. Furthermore, we can expect that as a result, the atom will be quickly pumped to the stretched state, which causes the ratio to be maximized.

As we’ve seen, nature already provided one built-in solution to multi-level alkaline earth atoms to permit their trapping, in that the relative transition strengths play an essential role in ensuring the MOT operates stably. However, the first complication that we briefly discussed, namely that there are untrapped ground state m_g levels, requires more direct intervention. The technique developed by the Sr group at U. Tokyo was to utilize a second laser, termed the “stirring laser” [118]. In contrast to the trapping laser, which operates on the $F = 9/2 \rightarrow F = 11/2$ transition, the

stirring laser operates on the $F = 9/2 \rightarrow F = 9/2$ transition. The effect of this second laser is to randomize the ground state m_g distribution so that trappable m_g states are occupied.

The $F = 9/2 \rightarrow F = 9/2$ transition is ideal as a “stirring” transition for two reasons. The first is that the g -factor is much smaller for the $F = 9/2$ level meaning that a near resonant laser will scatter over a larger range of magnetic field. Secondly, and unlike the $F = 9/2 \rightarrow F = 11/2$ transition, the ratio of σ^+ absorptions to σ^- absorptions is fairly uniform. To quantify this, we can define $r_F^{(\pm)}(m_g)$ as in Eq. 2.27. This quantity is plotted in Fig. 2.6, and it is clear that there is very little variation with m_g , meaning that the atoms are indeed efficiently stirred through the ground state m_g manifold, and also that the pumping slightly favors moving atoms away from the untrappable m_g levels.

2.4.2.2 The ^{87}Sr 689 nm MOT: experimental details

To operate the 689 nm MOT, we employ two cooling lasers whose use was motivated above: the “trapping” laser and the “stirring” laser. These two systems are phase locked with variable frequency offset from a master laser, with linewidth of ~ 500 Hz and whose central frequency is locked to the $^{88}\text{Sr } ^1\text{S}_0 \rightarrow ^3\text{P}_1$ ($m = 0 \rightarrow m = 0$) transition via a Doppler-free spectrometer based on a heat-pipe vapor cell with 25 mTorr of Ar buffer gas, which keeps the Sr from coating the windows. Details can be found in [80, 112, 114]. As depicted in Fig. 2.4, the trapping and stirring lasers’ frequencies are chosen such that they are near-resonant with the $F = 11/2$ and $F = 9/2$ hyperfine states, respectively.

In order to enable efficient transfer from the 461 nm MOT into the 689 nm MOT, three distinct MOT phases of the 689 nm MOT are utilized. In the first stage, the trapping and stirring lasers are modulated with a few MHz bandwidth. The modulation parameters are chosen such that the spectrum extends from just below resonance with the $9/2 \rightarrow 9/2$ and $9/2 \rightarrow 11/2$ transitions, to several MHz below. The modulation is chosen to provide good overlap with the Doppler profile of the atoms after being pre-cooled in the 461 nm MOT, with final temperatures of ~ 1 mK.

In the initial broadband phase of the red MOT, the field gradient is reduced from the 50 G/cm

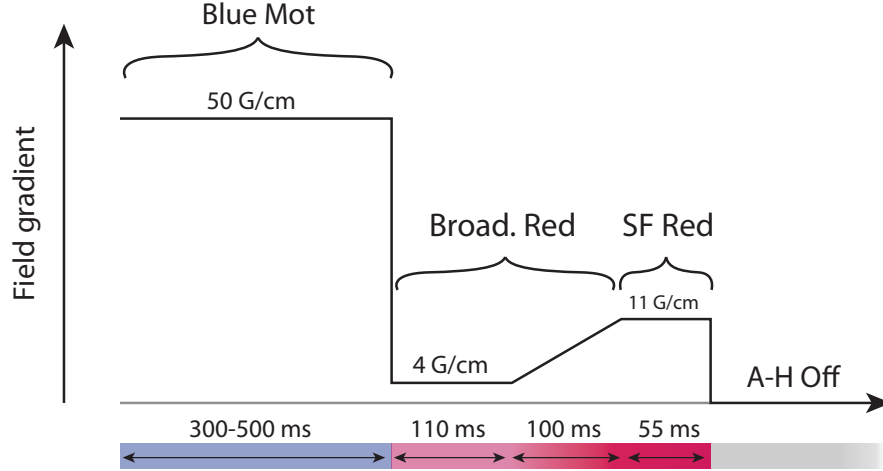


Figure 2.7: Field gradient programming during the three MOT stages: 461 nm (blue) MOT, broadband red MOT, and single-frequency (SF) red. After the single-frequency red mot, the anti-Helmholtz (A-H) coils are turned off to prepare the system for optical pumping and spectroscopy.

employed in the 461 nm MOT, to ~ 4 G/cm. This provides good spatial overlap, or mode-matching, between the blue MOT atomic density distribution and the broadband red MOT. Subsequently, the field is ramped to ~ 11 G/cm over 100 ms. The ramp compresses the MOT in all three spatial dimensions. When the field gradient reaches 11 G/cm, the broadband frequency modulation is switched off, and both the trapping and stirring laser are tuned near resonance, to form the final stage of MOT cooling, the single frequency red MOT. This field ramping procedure and MOT stages are depicted in Fig. 2.7.

The transfer efficiency from the blue MOT is approximately 15%, and results in a sample of atoms with μK temperatures. When the atoms are cooled in the presence of the optical lattice, an additional fraction of the atoms in the red MOT are cooled into the lattice. Due to poor spatial mode-matching between the optical lattice and the red MOT density distribution, the transfer efficiency between the lattice and red MOT is also approximately 15%. Ultimately, we can load approximately $N_{\text{tot}} = 5000$ ^{87}Sr atoms into ~ 100 lattice sites. The distribution of population in the lattice sites is derived in Appendix F, and on average, atoms share lattice site with ~ 20 other

atoms for $N_{\text{tot}} = 5000$.

2.4.2.3 Nuclear spin-polarizing for spectroscopy

The final step prior to clock spectroscopy on the lattice-trapped sample is to nuclear spin-polarize the ^{87}Sr so that a single m_F level is occupied. This serves two purposes: first it prepares an ensemble of identical fermionic ^{87}Sr atoms, meaning that collisional interactions due to the s -wave channel should be suppressed or completely eliminated, which is important for clock accuracy. We will discuss the collisional interaction in detail in Chapter 5. Second, spin-polarized atoms all contribute to the useful spectroscopy signal utilized to operate the clock.

As a consequence of the differential g -factor between the clock ground and excited states, the clock transition possesses a small magnetic field sensitivity, even for m_F preserving transitions between $^1\text{S}_0$ and $^3\text{P}_0$ are resolvable in a few hundred mG magnetic bias field. Specifically, there is a Zeeman shift between the clock states given by [119]

$$\Delta\nu_{\pi} = -\delta g m_F \mu_0 B / h, \quad (2.28)$$

where δg is the differential g -factor, μ_0 is the Bohr magneton, and the subscript π indicates that the formula is for non- m_f changing transitions (“ π ” transitions). The quantity $-\delta g \mu_0 / h = 108.4(4)$ Hz/G [119]. In order to clearly resolve each nuclear spin sublevel via clock spectroscopy, a ~ 500 mG field is applied during spectroscopy.

In order to prepare the atoms in the single nuclear spin state, we employ optical pumping on the $^1\text{S}_0 \rightarrow ^3\text{P}_1$ $F = 9/2 \rightarrow F = 9/2$ transition with circularly polarized light (both σ^+ and σ^- orientations) along a bias field applied along H2, which is the same axis as the bias field applied during clock spectroscopy. During the polarizing, a small bias field of ~ 100 mG is applied to define a quantization axis. A liquid crystal wave plate allows us freedom to switch between σ^+ and σ^- polarization. This freedom to switch polarization is important for removing 1st-order sensitivity to magnetic fields; by alternating between $m_F = +9/2$ and $m_F = -9/2$ states, the average of the two transition frequencies, as indicated by Eq. 2.28, will be first-order insensitive to magnetic fields [31].

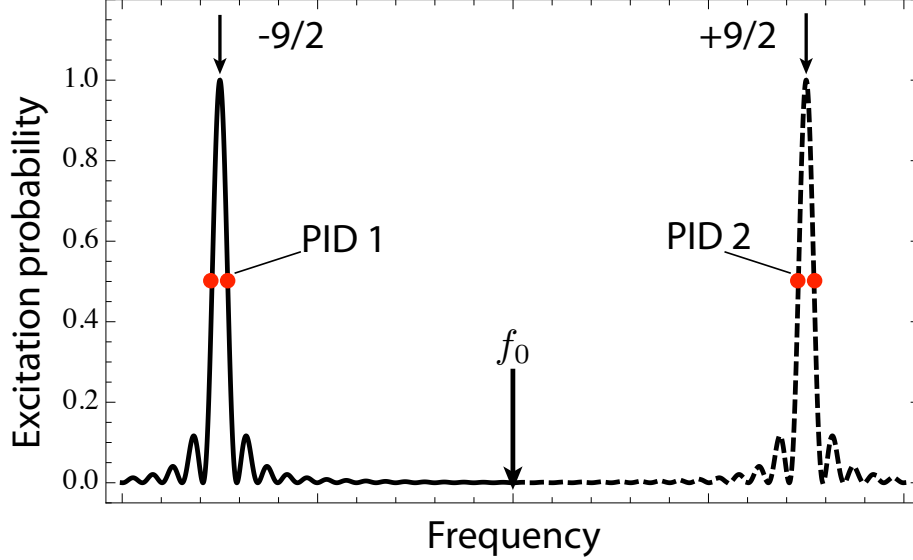


Figure 2.8: Clock operation with stretched nuclear spin states for first-order Zeeman insensitivity. Two independent locks are averaged to find the linear Zeeman shift-free center frequency, f_0 .

Figure 2.8 shows the principle of operation for the dual-spin clock operation. Two independent PID locks—one for $m_F = +9/2$ and the other for $m_F = -9/2$ —are used to extrapolate the linear Zeeman shift-free center frequency, f_0 .

2.4.3 Optical dipole trap and clock spectroscopy: experimental configuration

As described in the previous section, the atoms are directly cooled from the 689 nm MOT into the optical lattice, for which the basic principle of operation was described in Section 2.3. Here we describe the experimental apparatus utilized to create the optical lattice trapping potential.

The lattice optical dipole trap potential is formed by a Gaussian beam retro-reflected upon itself, such that the foci of the input beam and retro-reflected beam coincide. As depicted in Fig. 2.9, the input lattice beam is focused to a $1/e^2$ radius of $32 \mu\text{m}$ by an input lens with focal length of 14 cm such that the beam waist lies at approximately the geometric center of the main chamber. The lattice beam then passes out through the bottom viewport after which it is folded onto a curved retro-reflector mirror with 20 cm radius of curvature. The longitudinal position of

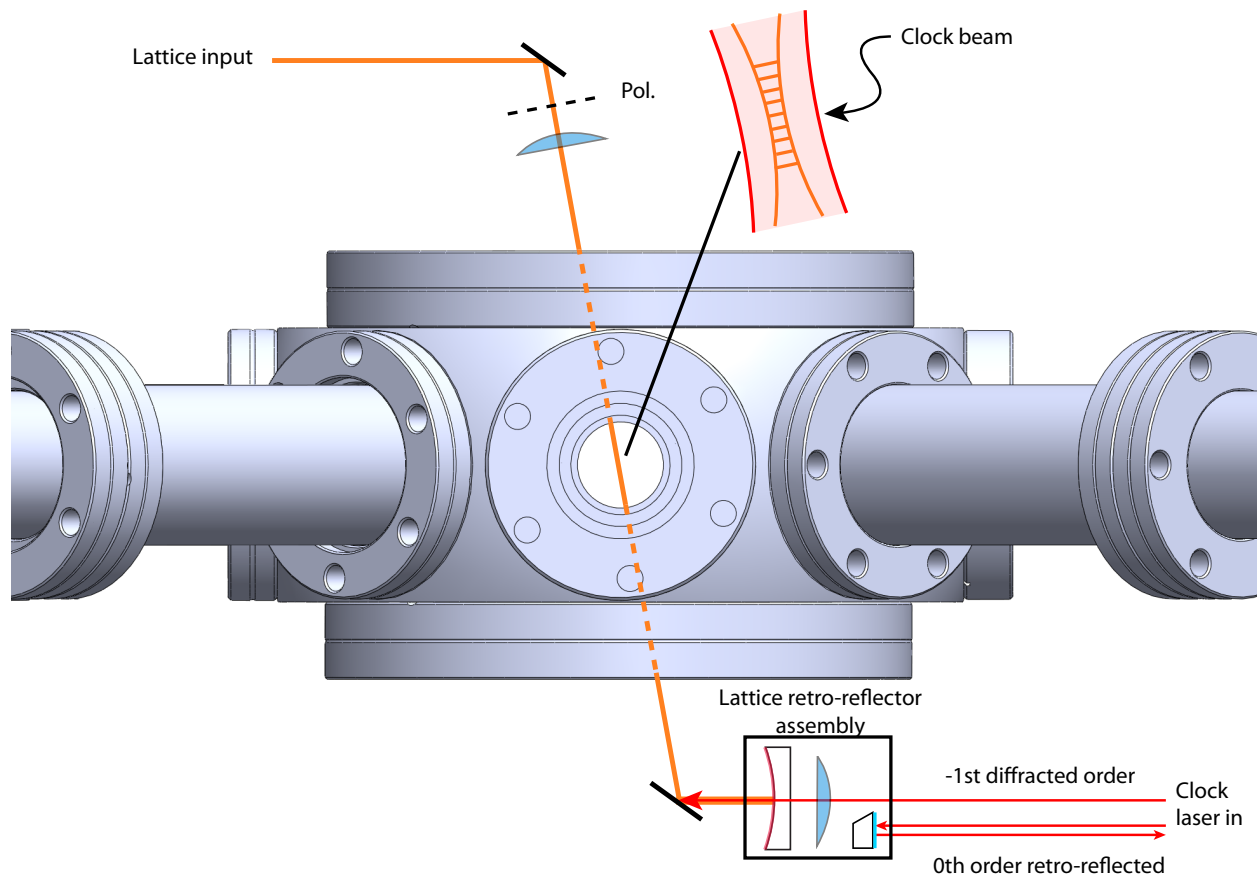


Figure 2.9: Optical lattice dipole trap and clock laser pathway. The lattice is approximately 19° from vertical. The focusing lens has a focal length of 14 cm and the radius of curvature of the retro-reflector is 20 cm.

the mirror is translatable, and its position and orientation are chosen such that a maximum of the lattice light is back-coupled into the single-mode from which the lattice beam originates.

The lattice light is produced by an amplified external cavity laser diode. Approximately 35–40 mW derived from a Littrow-configuration laser diode are injected into a tapered amplifier (Eagleyard EYP-TPA-0808), which produces 800 mW of output power. The output of the tapered amplifier is spectrally filtered with a ~ 1 nm spectral bandwidth interference filter. An optional filter cavity with Finesse ~ 100 can further spectrally filter the output of the tapered amplifier

chip. These precautions are taken because tapered amplifier chips are known to possess amplified spontaneous emission (ASE) spectral pedestals. This uncontrolled Stark shift due to these pedestals has been recognized as an important effect to be controlled in lattice clocks [34]. To date, all published systematic evaluations of the JILA ^{87}Sr lattice clock uncertainty were performed with a Ti:Sapphire laser, which will not suffer from an ASE problem.

In order to perform clock spectroscopy, the clock laser light is injected through the lattice retro-reflector with 99% transmission. A focusing lens ensures that the clock laser is concentrated at the atoms, while the waist of the clock light is kept several times larger than the lattice waist, thus ensuring that inhomogeneities due to the k -vector spread of a tight focus are minimized (discussed more fully in Section 2.5).

2.4.3.1 Clock laser path and RF phase chirp cancellation

The clock laser light is derived from an ultrastable laser system in a separate room, which we describe in Chapter 4. This separate room was chosen for its temperature stability, acoustic noise levels, and relative calm, from which the name “Jan’s quiet room” is derived. The clock laser light is delivered to the “distribution center” (Fig. 2.10). In the distribution center, the clock laser light is amplified by injection locking a second diode with $\sim 500 \mu\text{W}$ of optical power. The output power of the injection system is around 35 mW, which provides ample power for multiple experiments, as well as interface with a femtosecond frequency comb.

After exiting the distribution center, a fiber delivers clock laser light near the experimental chamber. An acousto-optic modulator (AOM) provides the frequency shift for scanning the clock laser onto the atomic resonance, as shown in Fig. 2.10. The delivery of pulsed light to the atoms that is free from switching transients and phase chirp errors is a challenging problem [120]. As shown schematically in Fig. 2.9, care is taken to cancel phase shifts due to RF-induced heating of the AOM, by referencing the light for the fiber noise cancellation system [121] through the AOM, using the 0th-order diffracted light. In this way, the fiber noise cancellation system is always engaged, yet samples approximately the same optical path deviations as the -1st diffracted order, which is

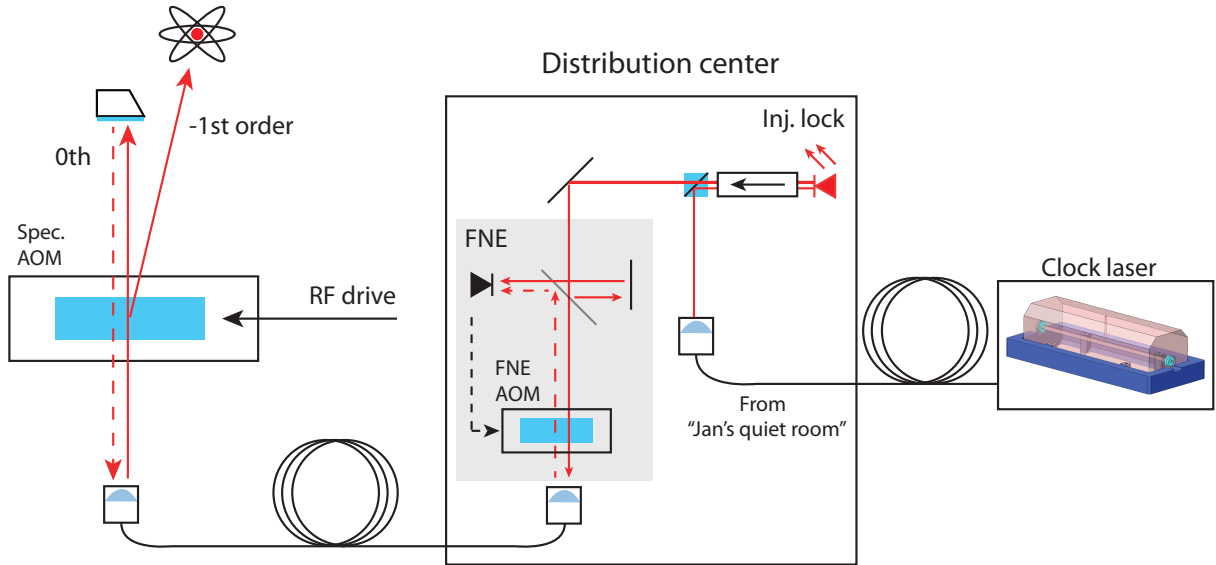


Figure 2.10: The clock laser delivery system. The ultrastable laser is operated in a separate room and is delivered via noise-cancelled fiber to the distribution center. In the distribution center, $\sim 500 \mu\text{W}$ of clock laser light are used to injection lock a laser diode. A second “fiber noise eater” (FNE) system ensures that the light is faithfully delivered to the atoms. Importantly, the effect of RF-heating of the spectroscopy acousto-optic modulator (AOM) is mitigated by including it in the fiber noise cancellation loop.

used for spectroscopy. We have tested that phase chirp-induced frequency shifts can be reduced to $-3(8)$ mHz, corresponding to a fractional frequency shift of $-0.7(2) \times 10^{-17}$ with the AOM diffracting at $\sim 50\%$ efficiency (corresponding to ~ 1 W RF drive) and with short 10 ms pulses. We expect that reducing the RF drive and elongating the clock pulses, as typically utilized in clock operation, can further reduce this shift by an order of magnitude. The 10 ms pulse duration was specifically chosen to emphasize the effect, and an experimentally relevant “cooling off” period of 1 s was used between cycles. In contrast, we measure a large phase chirp when the fiber noise cancellation plane is moved before the AOM, thus the cancellation pathway does not “see” the phase chirp. In this case, the frequency shift was measured at $-129(14)$ mHz, corresponding to a fractional frequency shift of $3.0(3) \times 10^{-16}$. This indicates that an active cancellation or characterization of the AOM phase chirp is indeed necessary for a high-accuracy clock.

2.4.4 Atom state detection and measurement

In order to detect the fraction of atoms in the metastable clock state, a series of fluorescence measurements are performed. As depicted in Fig. 2.11, the first step in the detection process is to count the number of ground state atoms, N_g . This is achieved by measuring the fluorescence from a strong probe beam that completely overlaps the lattice-trapped atoms and is retro-reflected, so that each atom cycles many times before being lost. The power in the probe beam is ~ 30 mW, which is enough to strongly saturate the transition. On average, we collect $\gtrsim 6$ useful photons per atom in the trap in a photo-multiplier tube (PMT). This quantity already includes the PMT quantum efficiency. The effect of the probe is to completely remove the lattice-trapped ground state population. We then repump the excited state atoms to the ground state using the 707 nm and 679 nm repumping transitions. The ground state population is again counted, but represents the number of atoms that were in the excited state, N_e . In between the measurements of N_g and N_e , a third fluorescence measurement characterizes the signal background, N_{bg} , so that N_e and N_g are accurate representations of the lattice-trapped populations. The fraction of atoms in the excited state can then be calculated from N_e , N_g , and N_{bg} as

$$f_{\text{exc}} = \frac{N_e - N_{\text{bg}}}{N_e + N_g - 2N_{\text{bg}}}. \quad (2.29)$$

2.5 Lattice spectroscopy

The precision of the ^{87}Sr optical lattice clock arises from the pairing of an ultrastable laser with sub-Hz linewidth, with an extremely narrow optical transition, whose fundamental limit is the natural linewidth of ^{87}Sr . However, in order to realize the potential of such a precise spectroscopy system, interaction times between the atoms and probing optical field must be at the 1 s timescale. While it might be possible to envision a multi-pulse Ramsey-Bordé optical fountain clock, there are systematics such as the wave-front curvature of the beams leading to first-order Doppler shifts, that will limit the ultimate accuracy of this technique [107, 122], not to mention that the apparatus for 1 s interrogation would be quite large and complex.

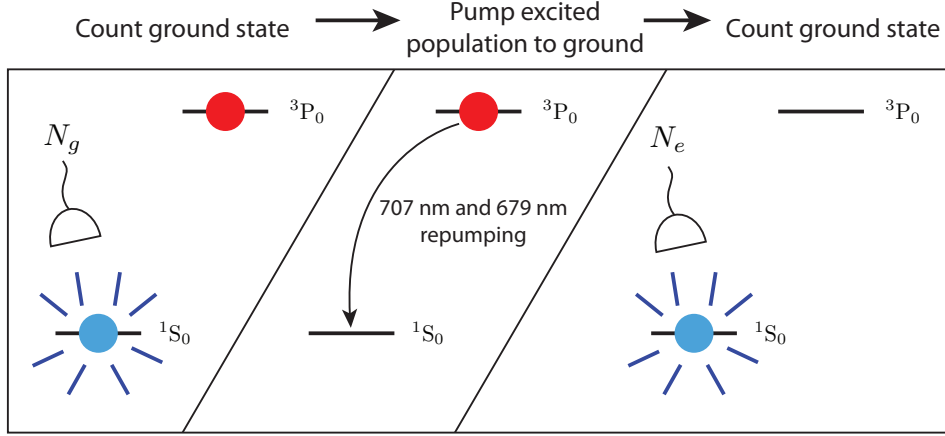


Figure 2.11: Atomic state detection scheme. After the atoms are placed in a superposition of 1S_0 and 3P_0 by the clock laser, the state detection proceeds in three steps: (1) the ground state population is counted (2) the excited state population is moved to 1S_0 via repumping and (3) the ground state population is again counted.

A better way to realize long-term optical and atomic coherence times is to strongly localize the atoms. This technique was used to demonstrate recoil-free optical spectroscopy [103] and subsequent record-breaking line- Q ($Q \equiv \Delta\nu/\nu$) with a single trapped Hg^+ ion, tightly localized in a quadrupole trap [22]. In fact, the Hg^+ ion was so localized, that the characteristic length scale of its thermal motion was much less than the wavelength of the spectroscopy laser. This regime of spectroscopy is known as the Lamb-Dicke regime, where the characteristic energy scale of the confining potential is larger than the photon recoil energy.

During free-space spectroscopy, conservation of momentum requires that as an atom absorbs a photon, it receives an impulse of $\hbar\mathbf{k}$, resulting in a shift of the frequency of

$$E_r = \hbar\omega_r = \frac{(\hbar k)^2}{2m}, \quad (2.30)$$

where ω_r is the recoil frequency, $k = \lambda/(2\pi)$ and m is the mass of the atom. In general, when a quantum emitter/absorber is more localized than a wavelength of light, its absorption spectrum will be strongly modified. For example, a bound atom or ion with quantized motional eigenstates (e.g. harmonic oscillator eigenstates) can only emit or absorb between initial and final quantized eigenstates, leading to a quantized energy spectrum. Early demonstrations of recoil-free spec-

troscopy were performed with Mössbauer spectroscopy, where the recoil momentum is absorbed by the crystalline lattice of the absorbing or emitting material [123] and can lead to extremely high line $Q \simeq 10^{15}$ [124], which has only recently been matched by the ^{87}Sr lattice clock reported in this thesis with a Q of 9×10^{14} [125].

Optical lattices used in optical lattice clocks play an analogous role to the crystal lattice in Mössbauer spectroscopy in the sense that they can tightly localize the atoms and also absorb the recoil momentum. We consider the case where the optical potential is harmonic, such that

$$V(x, y, z) = \frac{1}{2}m\omega_x x^2 + \frac{1}{2}m\omega_y y^2 + \frac{1}{2}m\omega_z z^2, \quad (2.31)$$

where $\omega_x = \omega_y = 2\pi\nu_r$, $\omega_z = 2\pi\nu_z$, and $\nu_z(\nu_r)$ is the longitudinal (radial) trapping frequency given by Eq. 2.25 (Eq. 2.26). In a one-dimensional optical lattice, as depicted in Fig. 2.12, $\omega_z \gg \omega_x \simeq \omega_y$. The corresponding motional eigenstates of the system are the harmonic oscillator energy eigenstates, which we label as $|\vec{n}\rangle \equiv |n_x\rangle|n_y\rangle|n_z\rangle$. These will be discussed in detail in Chapter 5.

When performing spectroscopy in a trap with motional eigenstates given by $|\vec{n}\rangle$, there are two classes of laser-driven transitions possible. The first is where the motional states are left unchanged, such that $|\vec{n}\rangle \rightarrow |\vec{n}\rangle$ and is referred to as the carrier transition. The second class of transition is where one or more motional quantum numbers are changed such that $|\vec{n}\rangle \rightarrow |\vec{n}'\rangle$, and is referred to as a sideband transition. The simplest and most experimentally relevant cases are the carrier transition and the sideband transitions for which a harmonic oscillator level is changed by one vibrational quanta, as depicted in Fig. 2.12. Fig. 2.13 shows the measured sideband transitions with respect to the carrier transition in both the radial and longitudinal directions. In this way, we are able to quantify our trap frequencies fairly accurately, which in turn gives us precise knowledge of the harmonic potential in which the atoms sit.

The motional states of an atom in a harmonic trap will also affect its interaction with a radiation field. The relevant dipole moment for a general transition in a quantized trap is given by [15]

$$\mathbf{d}_{\vec{n}\vec{n}'} = \langle \vec{n} | e^{i\mathbf{k}\cdot\hat{\mathbf{r}}} | \vec{n}' \rangle \langle g | \hat{\mathbf{d}} | e \rangle. \quad (2.32)$$

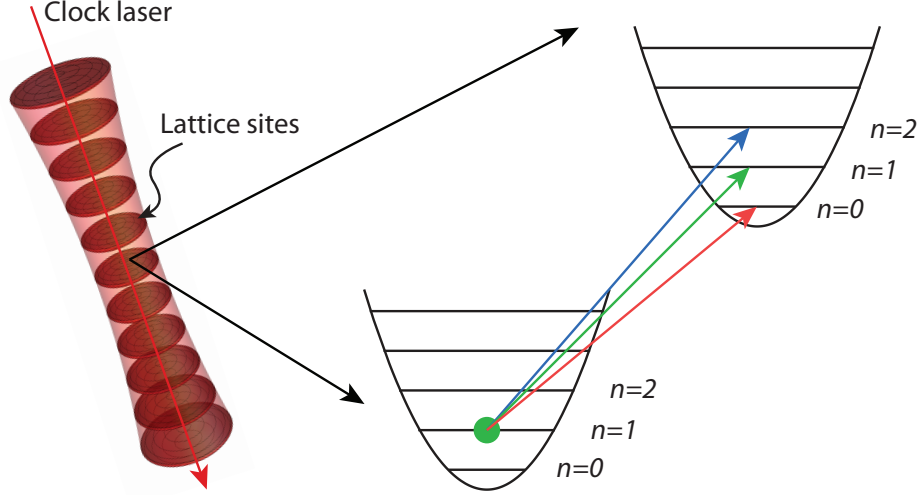


Figure 2.12: Spectroscopy in a one-dimensional optical lattice. The clock probe beam is aligned along the lattice propagation axis. The frequency of the transition is modified according to the change in motional quanta. A blue sideband transition excites an additional motional quanta, while the red sideband transition de-excites a motional quanta.

As a result, we can write the mode-dependent Rabi frequency as a function of the bare Rabi frequency $\Omega_0 \equiv \langle g | \mathbf{E} \cdot \hat{\mathbf{d}} | e \rangle / \hbar$ as [15, 126]

$$\Omega_{\vec{n}\vec{n}'} = \Omega_0 \langle \vec{n} | e^{i\mathbf{k} \cdot \hat{\mathbf{r}}} | \vec{n}' \rangle = \Omega_0 \prod_j e^{-\eta_j^2/2} \sqrt{\frac{n_j^<}{(n_j^< + \Delta n_j)!}} (i\eta_j)^{\Delta n_j} L_{n_j^<}^{\Delta n_j}(\eta_j^2). \quad (2.33)$$

Here, $j \in \{x, y, z\}$, $\Delta n_j = |n'_j - n_j|$, $n_j^<$ is the lesser of n_j and n'_j , and η_j is the Lamb-Dicke parameter in the j th direction. Specifically, the Lamb-Dicke parameter is defined as

$$\eta_j = k_j a_j / \sqrt{2} \quad (2.34)$$

where a_j is the characteristic length for the j th harmonic degree of freedom $a_j = \sqrt{\hbar / (m\omega_j)}$. Finally, k_j is simply the probe k -vector projection along the j th direction.

As clearly seen from Eq. 2.34, the Lamb-Dicke parameter scales as the ratio of the harmonic confinement length to the wavelength of the probe light. One general statement is that if $\eta_j \ll 1$, the Rabi frequency for an n_j changing transition is suppressed relative to the carrier by a factor of

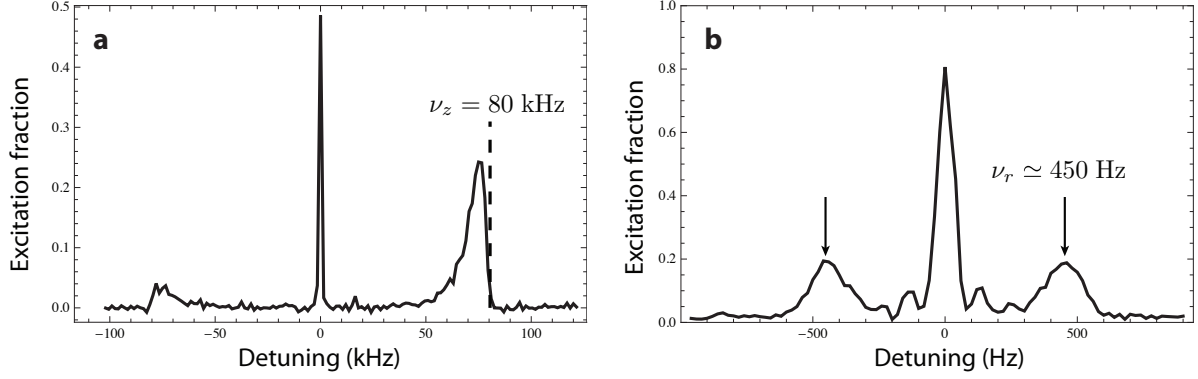


Figure 2.13: Spectroscopic resolution of longitudinal and radial sidebands in a 1D optical lattice potential. (a) The laser frequency is scanned over 100 kHz on either side of the carrier transition, revealing $\Delta n_z = \pm 1$ sideband transitions. The asymmetric shape of the sidebands arises from coupling between the radial and longitudinal optical potential. (b) Radial sidebands with $\Delta n_r = \pm 1$. In order to excite the radial sideband transition, the clock laser was misaligned from the lattice by $\Delta\theta \simeq 10$ mrad.

$\eta_j^{\Delta n_j}$. Furthermore, in the case where $\vec{n} = \vec{n}'$, Eq. 2.34 simplifies significantly, such that

$$\Omega_{\vec{n}} = \Omega_0 \prod_j e^{-\eta_j^2/2} L_{n_j}(\eta_j^2) \simeq \Omega_0 \prod_j 1 - (n_j + 1) \eta_j^2, \quad (2.35)$$

where the final approximation is valid in the limit $\eta_j^2 \ll 1$. Equation 2.35 demonstrates a dependence of the Rabi frequency on $|\vec{n}\rangle$. In general, for a one-dimensional lattice, the optimal situation is to align the spectroscopy laser along z (the axis of strong confinement) to minimize radial sideband excitation and Rabi frequency inhomogeneity.

One final detail to address is the effect of tunneling on lattice spectroscopy. Tunneling in an optical lattice can give rise to frequency shifts and line broadening due to the band structure of the lattice [127, 128]. In order to circumvent this problem, it was prescribed to work in an accelerated frame, achieved by tilting the lattice so that a component of gravity lies along the standing wave. In the so-called Wannier-Stark ladder, tunneling effects are effectively detuned by the ~ 1 kHz energy detuning between adjacent sites due to the effect of gravity [127].

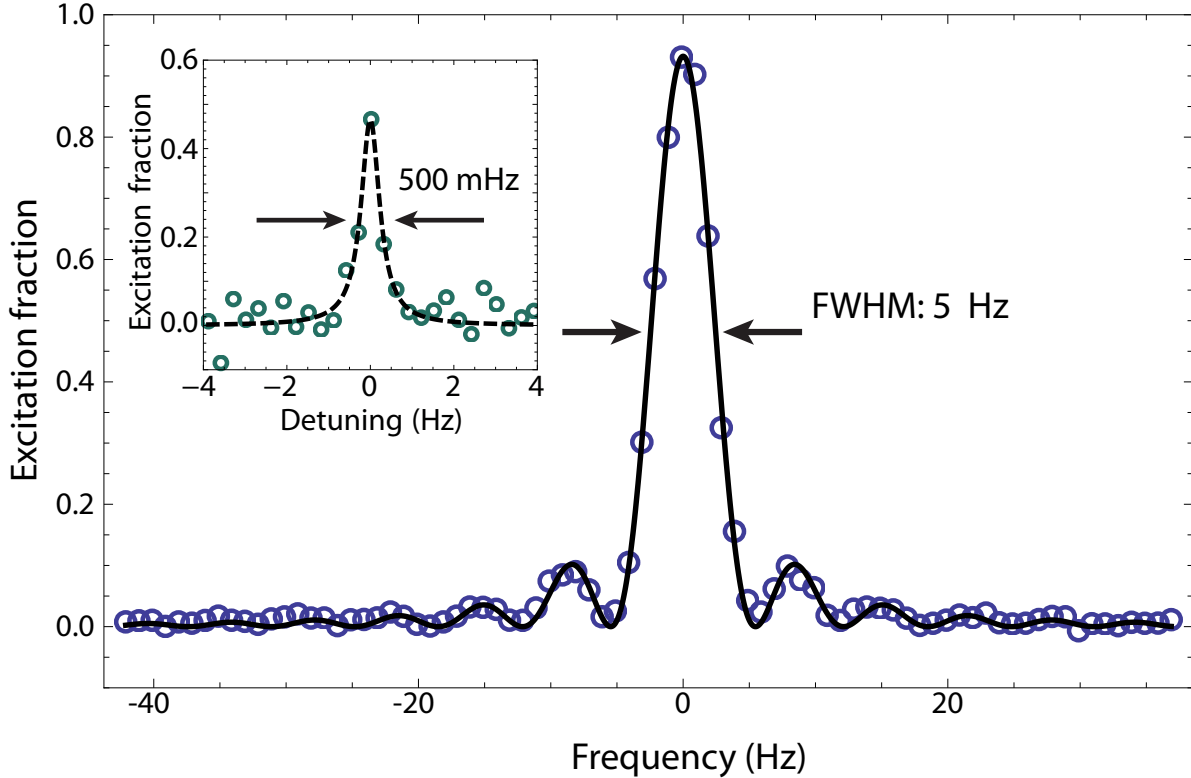


Figure 2.14: Spectroscopic lineshape obtained with Rabi spectroscopy performed on the $^1S_0 \rightarrow ^3P_0$ clock transition at 429 THz with a π -pulse time of $T_{\text{pulse}} = 160$ ms. **Inset:** High-resolution scan taken with $T_{\text{pulse}} = 3$ s. Both scans were taken without any averaging. The ultra-high resolution of these lineshapes is enabled by the clock laser described in Chapter 4.

2.5.1 Lattice spectroscopy: experimental

When performing spectroscopy on the lattice-trapped atoms, the three main parameters of relevance are the duration of the clock pulse(s), the number of clock pulses applied, and the intensity of the clock laser beam. The most common form of spectroscopy employed is Rabi spectroscopy. As seen from the preceding discussion, care must be taken to make sure that the clock probe beam is well-aligned with the optical lattice so that the atoms are well within the Lamb-Dicke regime. Ideally, for the 1D optical lattice, the clock probe has no projection along the x or y directions, such that $\eta_x = \eta_y = 0$. In principle, there are small deviations from this due to a beam misalignments, such that, e.g., $\eta_x = k \sin(\theta) a_x$. Here, typical misalignments are at the few mrad level.

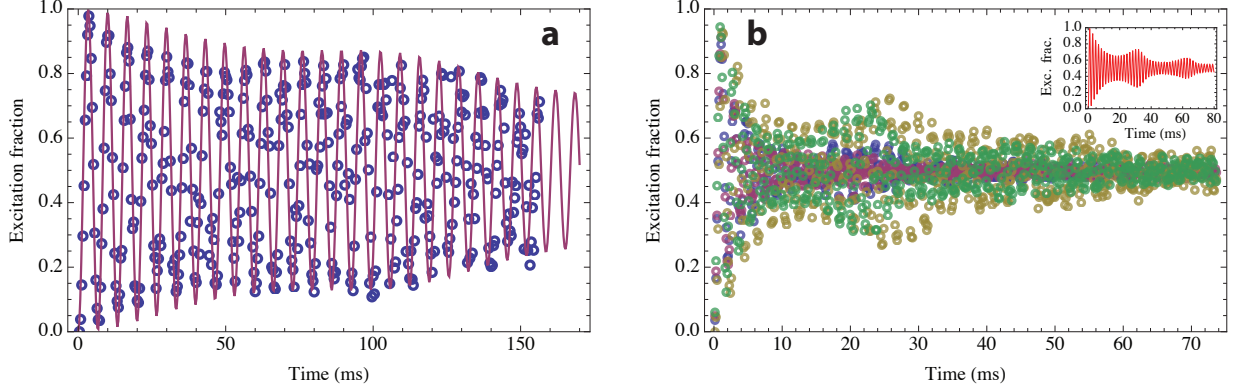


Figure 2.15: Rabi flopping as a probe of the spread in Rabi frequency. (a) Rabi flopping with a longitudinally cooled ($T_z = 1.5 \mu\text{K}$) and radially hot ($T_r = 3.0 \mu\text{K}$) sample. The circles are experimentally recorded data and yield an effective misalignment of 2.5 mrad, resulting in $\Delta\Omega/\Omega = 0.02$ (b) Series of Rabi flopping curves taken with $T_z \simeq T_r \simeq 4 \mu\text{K}$. The extrapolated effective misalignment varied from 3 mrad to 8 mrad ($\Delta\Omega/\Omega$ between 0.06 and 0.11.) **Inset:** Theory curve for the best-aligned case.

Clock spectroscopy is performed by sending a pulse or pulses of clock laser light onto the atoms along the z axis—the direction along which the atoms are strongly confined by the lattice. In the case of Rabi spectroscopy, the applied pulse is chosen such that the Rabi frequency satisfies

$$\Omega T_{\text{pulse}} = \pi. \quad (2.36)$$

This results in unity excitation probability on resonance. After the pulse is applied, the excited state fraction of the atoms is detected as described in Section 2.4.4. An example of a Rabi lineshape with $\tau = 160$ ms is shown in Fig. 2.14. The full-width at half-max (FWHM) of the rabi lineshape is related to T_{pulse} by $\Delta\nu_{\text{FWHM}} \simeq 0.8/T_{\text{pulse}}$, resulting in a 5 Hz FWHM for the 160 ms pulse duration depicted in Fig. 2.14. The theoretical lineshapes and details of both Rabi and Ramsey spectroscopy are discussed in Appendix 1.

In order to experimentally measure the \vec{n} -dependence of the Rabi frequency, we performed several experiments. With our best alignment at $T_r = 3 \mu\text{K}$ and $T_z = 1.5 \mu\text{K}$ (temperature along the longitudinal and radial directions, respectively), we measured very long Rabi coherence, as a function of the number of on-resonance Rabi “flops” (i.e. excitation cycles $|g\rangle \rightarrow |e\rangle \rightarrow \dots$, where

the population returns to the ground state). In order to provide a theoretical fit for the data, we calculate a Boltzmann-weighted sum of different evolution frequencies, whose n -dependence is given by Eq. 2.35a. We assume a fixed misalignment between the clock probe, which is assumed to be a perfect plane wave, and the lattice. The data for the cold, well-aligned case, is shown in Fig. 2.15. The theoretical fit indicates that the effective misalignment is as small as 2.5 mrad, and that for these conditions, the RMS spread of Rabi frequencies $\Delta\Omega$ is about 2%. This is a significant improvement over previously reported results from our group [112, 114]. At hotter temperatures, we measure much faster decay due to the larger number of motional states that are populated. We took numerous traces, as shown in Fig. 2.15b, with varying misalignment. Again, at the optimal alignment, we find an effective misalignment of 3 mrad, while the most severe misalignment shown here is only about 8 mrad. As seen from the figure, probe misalignments are most visible at hotter temperatures, and we used this to our advantage when trying to optimize alignment between the probe and the lattice.

While the agreement between the theory and the data shown in Fig. 2.15 is qualitatively quite good, there are minor discrepancies. There are several reasons for this. The first is that 2-body inelastic losses can affect the evolution of the atomic coherence at longer times (we describe the inelastic losses in detail in Chapter 5). A second reason is that we assume that the only wavefront misalignment between the lattice and the clock probe is due to an angular misalignment. In fact, the probe itself is focused, and the act of focusing the clock probe results in a Gaussian spread of wave-vectors \mathbf{k} . It can be shown that for a probe with $1/e^2$ intensity radius w_0 , the mode-dependence of the Rabi frequencies is

$$\frac{\Omega_{\vec{n}}}{\Omega_0} = \pi w_0^2 e^{-\eta_z^2/2} L_{n_z}(\eta_z^2) \int df_x df_y e^{-\pi^2(f_x^2+f_y^2)(w_0^2+a_x^2)} L_{n_x}(2\pi^2 f_x a_x^2) L_{n_y}(2\pi^2 f_y a_y^2). \quad (2.37)$$

A more complete description of the sidebands would include this effect as well, but for all practical purposes the measured $\Delta\Omega/\Omega \simeq 0.02$ is more than sufficient for high-precision spectroscopy, and we choose to characterize the misalignment as an “effective” one.

2.6 Limits to atom-laser coherence due to photon scattering

The question as to whether optical-atomic coherence in an optical lattice suffers due to photon scattering is of central concern for optical frequency standards employing optical lattices. In the case of Sr, some estimates have placed the scattering rate as high as ~ 3 Hz for a lattice depth of $\sim 100 E_{\text{rec}}$ [129], which would already have negative consequences for the clock and precision spectroscopy reported in this thesis. It is the purpose of this section to calculate the rate of photon scattering from the two clock states.

We begin by noting that the question of decoherence due to light scatter is a nuanced one, primarily because there are two scattering processes that can occur. The first type of light scattering is Rayleigh scattering, where a photon is scattered from the lattice beam but the internal state of the atom does not change. In a recent study of a qubit formed by the ground-state spin of a Be^+ ion, it was found that even if the Rayleigh scattering rates of the two qubit states were matched, the relative sign of the Rayleigh scattering amplitude was the important quantity for the decoherence of the qubit [130]. In a magic wavelength lattice, the AC polarizability and the Rayleigh scattering rate are intimately linked, as it is the induced dipole that both allows the atom to be trapped and that causes Rayleigh scattering.

The second kind of scattering is Raman scattering. Here, the “color” of the absorbed photon and the emitted photon are different, implying that the internal state of the atom has been changed. In the case of Sr, the only Raman scattering processes that are relevant are $^3\text{P}_0 \rightarrow ^3\text{P}_1$ and $^3\text{P}_0 \rightarrow ^3\text{P}_2$. Of these two, it is the first process that is harmful for the coherence of the clock state, since the $^3\text{P}_1$ state can decay back to the ground state. Thus, this process can be considered as a modification of the clock state lifetime due to a small but finite optical pumping from the lattice. The $^3\text{P}_0 \rightarrow ^3\text{P}_2$ simply appears as loss from the excited clock state, and thus should not significantly affect the coherence.

2.6.1 Kramers-Heisenberg formula

In order to calculate all the relevant scattering rates, we begin with the Kramers-Heisenberg formula³ which describes the cross section for scattering between two internal states of an atom—labelled by a and b and connected via an intermediate state j —as [88]

$$\frac{d\sigma}{d\Omega} = r_0^2 \omega \omega'^3 \frac{m^2}{\hbar^2 e^4} \left| \sum_j \left[\frac{(\hat{\epsilon}' \cdot \mathbf{d}_{bj})(\hat{\epsilon} \cdot \mathbf{d}_{ja})}{\omega_{ja} - \omega} + \frac{(\hat{\epsilon} \cdot \mathbf{d}_{bj})(\hat{\epsilon}' \cdot \mathbf{d}_{ja})}{\omega_{ja} + \omega'} \right] \right|^2. \quad (2.38)$$

Here, r_0 is the “classical electron radius” and is given by $r_0 = e^2/(4\pi\epsilon_0 mc^2)$; ω' is the wavelength of the (energy conserving) scattered radiation; $\hat{\epsilon}$ and $\hat{\epsilon}'$ are the polarizations of the incoming and scattered photons, respectively; and ω_{ja} is the complex transition frequency between states a and n , given by

$$\omega_{ja} = \omega_j - \omega_a + iA_{T,j}/2, \quad (2.39)$$

where $A_{T,j}$ is the Einstein A-coefficient of the excited state j (inverse the excited state lifetime). When $a = b$ we have Rayleigh scattering, and $\omega = \omega'$. When a and b differ, we have Raman scattering, and ω' differs from ω to conserve energy. Here, j is a shorthand notation for all possible intermediate states connected by the dipole operator. The dipole matrix elements, are given by, e.g.,

$$\mathbf{d}_{ja} = \langle j | e\hat{\mathbf{r}} | a \rangle, \quad (2.40)$$

where a , b , and j are shorthand for a specific state, with each described by a term symbol $^S L_J$, electronic configuration, and angular momentum projection, m_J . Since we consider the clock states, the initial and final states a and b are restricted to be $\in \{5s^2 \ ^1S_0, 5s5p \ ^3P_0, 5s5p \ ^3P_1, 5s5p \ ^3P_2\}$. To determine the photon scattering rate, we multiply the cross section by the incoming photon flux such that

$$\frac{d\gamma}{d\Omega}(\hat{\epsilon}, \hat{\epsilon}') = \frac{I}{\hbar\omega} \times \frac{d\sigma}{d\Omega} \quad (2.41)$$

$$= \frac{I\omega'^3}{(4\pi\epsilon_0)^2 c^4 \hbar^3} \left| \sum_j \left[\frac{(\hat{\epsilon}' \cdot \mathbf{d}_{bj})(\hat{\epsilon} \cdot \mathbf{d}_{ja})}{\omega_{ja} - \omega} + \frac{(\hat{\epsilon} \cdot \mathbf{d}_{bj})(\hat{\epsilon}' \cdot \mathbf{d}_{ja})}{\omega_{ja} + \omega'} \right] \right|^2. \quad (2.42)$$

³ A good derivation of this formula is found in [131]

The interpretation of $d\gamma/d\Omega$ is photons scattered per second into a solid angle $d\Omega$. This quantity depends on the incoming intensity.

At first glance, Eq. 2.42 looks fairly intractable. After all, we want the total scatter rate given by the integral over 4π of solid angle, namely

$$\gamma = \int \frac{d\gamma}{d\Omega} (\hat{\varepsilon}, \hat{\varepsilon}') d\Omega. \quad (2.43)$$

However, we can modify Eq. 2.42 to look more reasonable. Focusing on the sum, we note that

$$\begin{aligned} \sum_j \left[\frac{(\hat{\varepsilon}' \cdot \mathbf{d}_{bj})(\hat{\varepsilon} \cdot \mathbf{d}_{ja})}{\omega_{ja} - \omega} + \frac{(\hat{\varepsilon} \cdot \mathbf{d}_{bj})(\hat{\varepsilon}' \cdot \mathbf{d}_{ja})}{\omega_{ja} + \omega'} \right] &= \hat{\varepsilon}' \cdot \sum_j \left[\frac{(\mathbf{d}_{bj})(\hat{\varepsilon} \cdot \mathbf{d}_{ja})}{\omega_{ja} - \omega} + \frac{(\hat{\varepsilon} \cdot \mathbf{d}_{bj})(\mathbf{d}_{ja})}{\omega_{ja} + \omega'} \right] \\ &\equiv \hat{\varepsilon}' \cdot \mathbf{D}. \end{aligned} \quad (2.44)$$

The term \mathbf{D} (no subscript) can be thought of as a net induced dipole for the scattered radiation. Now the angular integral can be performed, and we must also sum over the two final polarization states which we label as $\hat{\varepsilon}'_1(\mathbf{n})$ and $\hat{\varepsilon}'_2(\mathbf{n})$. This can be written as

$$\frac{I\omega'^3}{(4\pi\epsilon_0)^2 c^4 \hbar^3} \int d\Omega \left[|\hat{\varepsilon}'_1(\mathbf{n}) \cdot \mathbf{D}|^2 + |\hat{\varepsilon}'_2(\mathbf{n}) \cdot \mathbf{D}|^2 \right]. \quad (2.45)$$

It turns out that the integral in Eq. 2.45 is exactly the same equation that appears in the treatment of spontaneous emission (see problem 4.2 of Ref. [88]), and the final result for γ is given by

$$\gamma = \frac{I\omega'^3}{(4\pi\epsilon_0)^2 c^4 \hbar^3} \left(\frac{8\pi}{3} |\mathbf{D}|^2 \right), \quad (2.46)$$

where the term in parentheses is the evaluated integral of Eq. 2.45 and \mathbf{D} is defined as

$$\mathbf{D} \equiv \sum_j \left[\frac{\mathbf{d}_{bj}(\hat{\varepsilon} \cdot \mathbf{d}_{ja})}{\omega_{ja} - \omega} + \frac{\mathbf{d}_{ja}(\hat{\varepsilon} \cdot \mathbf{d}_{bj})}{\omega_{ja} + \omega'} \right]. \quad (2.47)$$

We proceed by noting that in Eq. 2.46, we have a simple expression that depends on $|\mathbf{D}|^2$, which is defined in Eq. 2.47. The meaning of $|\mathbf{D}|^2$ is simply

$$|\mathbf{D}|^2 = |D_x|^2 + |D_y|^2 + |D_z|^2 = \sum_{q=-1}^1 |D_q|^2$$

Here, D_q is given by

$$D_q = \sum_j \left[\langle b|e r_q|j \rangle \frac{(\hat{\varepsilon} \cdot \mathbf{d}_{ja})}{\omega_{ja} - \omega} + \langle j|e r_q|a \rangle \frac{(\hat{\varepsilon} \cdot \mathbf{d}_{bj})}{\omega_{ja} + \omega'} \right]. \quad (2.48)$$

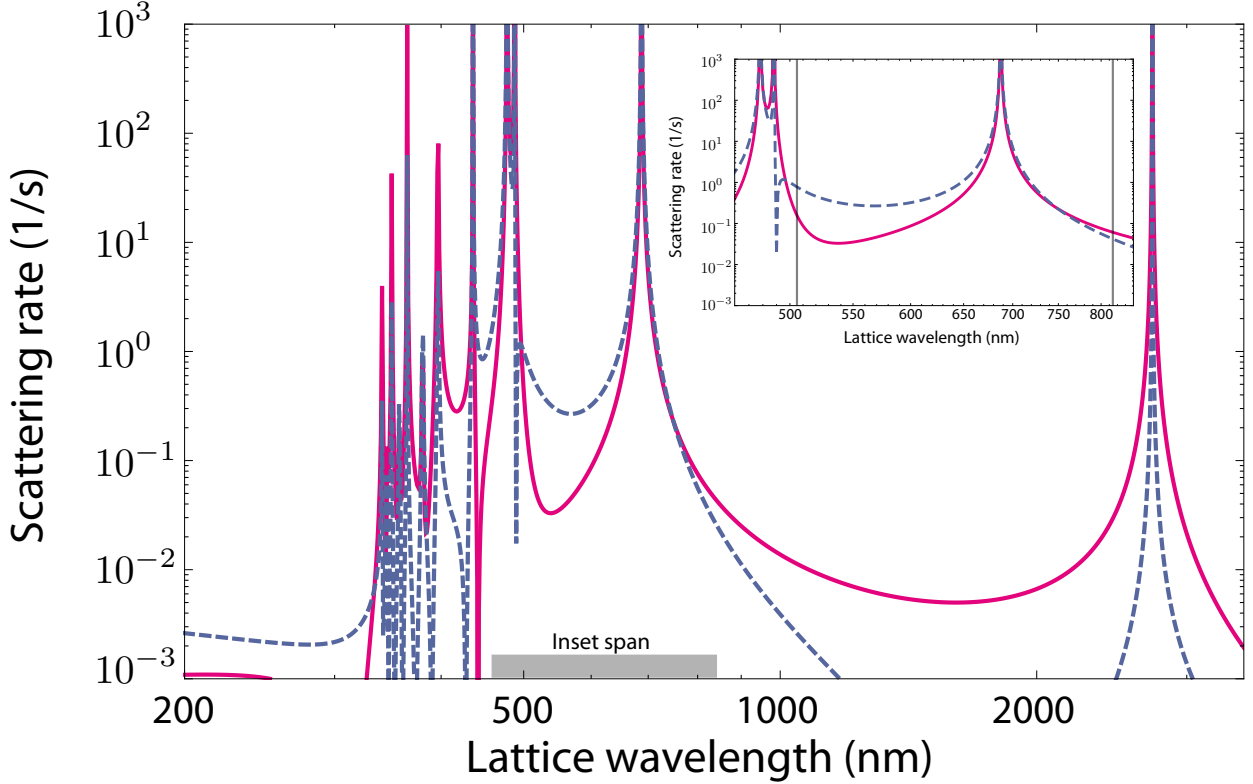


Figure 2.16: Raman scattering rate as a function of wavelength for scattering from 3P_0 into 3P_1 (solid), and 3P_2 (dashed). The lattice peak intensity is $3.4 \times 10^4 \text{ W/cm}^2$, corresponding to $\nu_z = 80 \text{ kHz}$ for an 813.428 nm lattice. The inset (span indicated by a grey bar) shows a detailed view of two magic wavelengths, including the 813 nm magic wavelength used for clock operation.

At this point, if we assume linear polarization of the input beam (lattice), there is a natural choice of quantization axis that simplifies things even more. If we choose the quantization axis to be along the direction of the lattice polarization (also realized in the experiment, conveniently) then Eq. 2.49 becomes

$$D_q = \sum_j \left[\langle b | e \hat{r}_q | j \rangle \frac{\langle j | e \hat{r}_0 | a \rangle}{\omega_{ja} - \omega} + \langle j | e \hat{r}_q | a \rangle \frac{\langle b | e \hat{r}_0 | j \rangle}{\omega_{ja} + \omega'} \right]. \quad (2.49)$$

At this point we can use Eq. 2.46 along with Eqs. 2.48 and 2.49 and the treatment in Appendix B to calculate the scattering rate for a lattice frequency ω and scattered photon frequency ω' . In this calculation, the sum over intermediate states n is carried out for the states given in Table 2.1 for scattering from 3P_0 and 1S_0 .

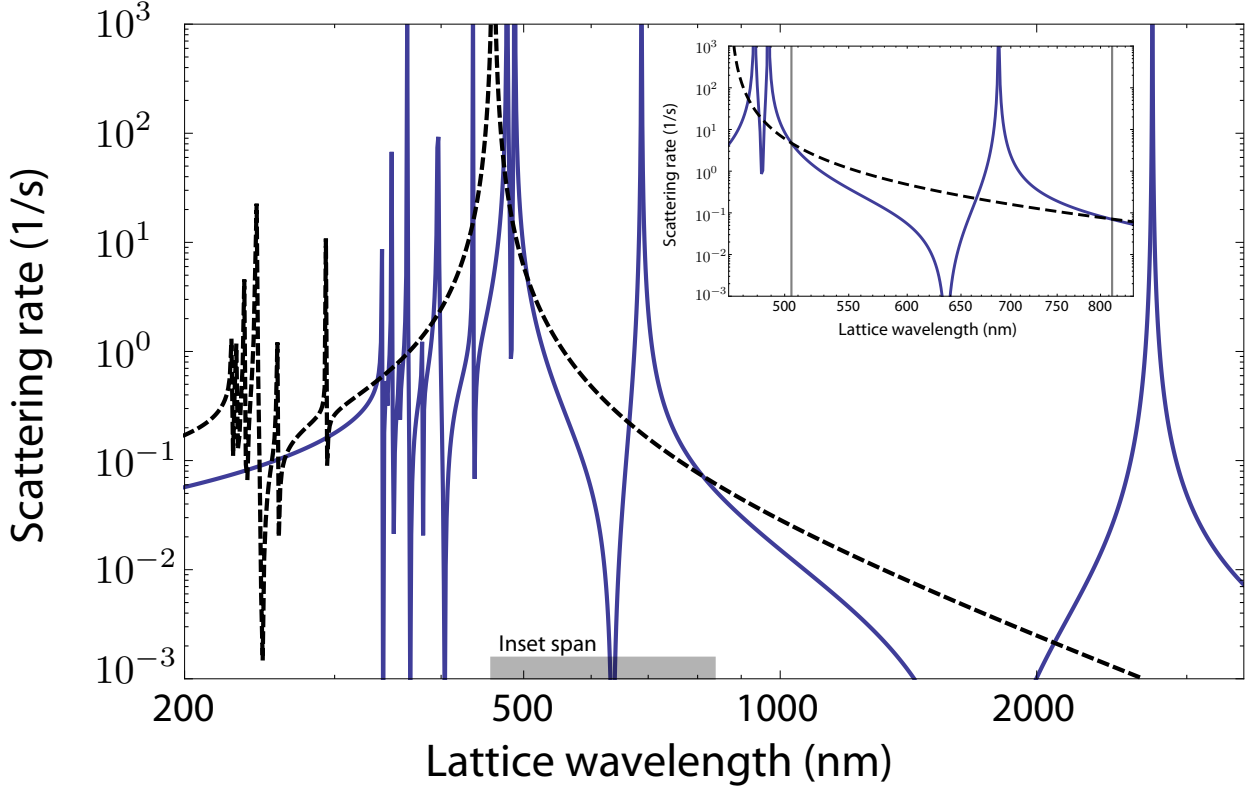


Figure 2.17: Rayleigh scattering rate as a function of wavelength for 3P_0 (solid) and 1S_0 (dashed). The lattice peak intensity is 3.4×10^4 W/cm 2 , corresponding to $\nu_z = 80$ kHz for a lattice at 813.428 nm. As before, the inset (span indicated again by a grey bar) shows a detailed view of two magic wavelengths, including the 813 nm magic wavelength used for clock operation. Note that the Rayleigh scattering rate is the same at the magic wavelength, as expected.

Finally, we extrapolate the lattice laser intensity, I , from the observed sideband frequencies. For the purposes of this work, we assume that the atoms are at the very bottom of the wells, such that they are subject to the maximum lattice intensity. In principle, the finite temperature of the sample will reduce the average intensity seen by the atoms, and the fractional reduction is approximately the same as the ratio of the atomic temperature to the trap depth.

As presented previously, we assume a lattice intensity profile given by

$$I(x, y, z) = \frac{8P_0}{\pi w^2(x, y, z)} e^{-2r^2/w^2(x, y, z)} \cos^2(kz), \quad (2.50)$$

where P_0 is the power of a single beam. The longitudinal trap frequency associated with this profile

Results at 813.428 nm.	
${}^3\text{P}_0 \rightarrow {}^3\text{P}_0$	$7.3 \times 10^{-2} \times (\nu_z/80 \text{ kHz})^2$ [1/s]
${}^3\text{P}_0 \rightarrow {}^3\text{P}_1$	$6.4 \times 10^{-2} \times (\nu_z/80 \text{ kHz})^2$ [1/s]
${}^3\text{P}_0 \rightarrow {}^3\text{P}_2$	$4.4 \times 10^{-2} \times (\nu_z/80 \text{ kHz})^2$ [1/s]
${}^1\text{S}_0 \rightarrow {}^1\text{S}_0$	$7.3 \times 10^{-2} \times (\nu_z/80 \text{ kHz})^2$ [1/s]
Results at 505 nm.	
${}^3\text{P}_0 \rightarrow {}^3\text{P}_0$	$4.9 \times (\nu_z/260 \text{ kHz})^2$ [1/s]
${}^3\text{P}_0 \rightarrow {}^3\text{P}_1$	$1.7 \times 10^{-1} \times (\nu_z/260 \text{ kHz})^2$ [1/s]
${}^3\text{P}_0 \rightarrow {}^3\text{P}_2$	$8.2 \times 10^{-1} \times (\nu_z/260 \text{ kHz})^2$ [1/s]
${}^1\text{S}_0 \rightarrow {}^1\text{S}_0$	$4.9 \times (\nu_z/260 \text{ kHz})^2$ [1/s]

Table 2.2: Scattering rates from ${}^3\text{P}_0$ into the ${}^3\text{P}$ fine structure manifold and ${}^1\text{S}_0$ Rayleigh scattering at the magic wavelength. The Rayleigh rates agree at the magic wavelengths, as expected. The Raman process ${}^3\text{P}_0 \rightarrow {}^3\text{P}_1$ is expected to be the most detrimental to clock coherence. In all relevant conditions at both magic wavelengths we find that this rate is well below 1 Hz.

is given by

$$\nu_z = \frac{1}{2\pi w_0 \lambda} \sqrt{\frac{32\pi\alpha P_0}{c\epsilon_0 M}} = \frac{1}{\lambda} \sqrt{\frac{\alpha I_{\text{peak}}}{c\epsilon_0 M}} \quad (2.51)$$

where $I_{\text{peak}} = 8P_0/(\pi w^2)$. For $\nu_z = 80$ kHz, $I_{\text{peak}} = 3.4 \times 10^4$ W/cm² corresponding to $P_0 = 140$ mW. Using this value for intensity, we find the scattering rate into the ${}^3\text{P}$ fine structure manifold from ${}^3\text{P}_0$ as a function of wavelength as shown in Fig. 2.16., while the comparison of the Rayleigh rates of scattering out of ${}^1\text{S}_0$ and ${}^3\text{P}_0$ is shown in Fig. 2.17. It is important to note that no saturation effects are taken into account, so only the far-off resonant segments of this plot are valid for such high intensity.

2.6.1.1 Numerical values and experimental confirmation

The wavelengths of greatest practical importance are the magic wavelengths near 813 nm and 505 nm. For both these magic wavelengths, we tabulate the scattering rates for a lattice depth corresponding to $\nu_z \simeq 80$ kHz with $\lambda_{\text{lat}} = 813.428$ nm, which corresponds to 140 mW input power and a lattice depth of $130 E_r$ (22 μ K). In order to calculate the scattering rate at 505 nm, we simply assume the same input power (140 mW), but due to the difference in wavelength and polarizability, ν_z is significantly larger than for the lattice formed with the equivalent power at

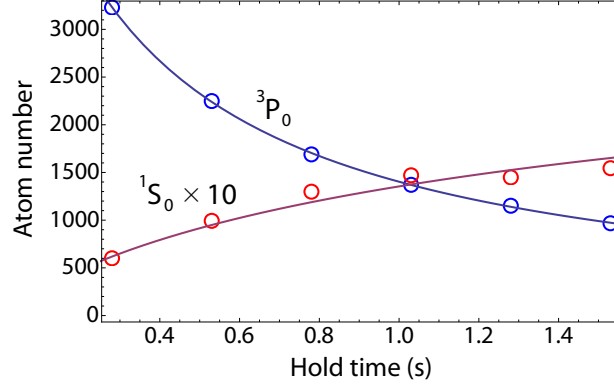


Figure 2.18: Experimental measurement of optical pumping due to lattice scattering. The extrapolated $^3P_0 \rightarrow ^1S_0$ decay rate is due to the both spontaneous decay and optical pumping due to Raman scattering of lattice photons in addition to spontaneous emission from the metastable clock state.

813 nm. In Table 2.2, we summarize the result of the scattering rate for 140 mW input power. The rate will scale with the total input power, and we show the scaling as a function of trap frequency. We note that for 80 kHz sidebands at 505 nm, only 15 mW of optical power are required and all scattering rates—especially the Raman rates—are small. Thus, we anticipate that a lattice at this wavelength could be an intriguing possibility, especially for applications requiring low power consumption. Finally, we note that an important modification must be considered when the ensemble average of the scattering rate is desired; instead of using the I_{peak} obtained by inverting Eq. 2.51, it is necessary to find the RMS intensity averaged over the thermal density-distribution of the atoms. This effect roughly scales as the ratio of the total trap depth to $k_B T_r$ and $k_B T_z$. For $T_z = T_r = 3.5 \mu\text{K}$, the average scattering rate is 70% of the peak scattering rate given in Table 2.2.

In order to test the accuracy of the scattering rate calculation, we performed a measurement of the 1S_0 population as a function of hold time of the lattice. In order to initialize the system, we first excited close to 100% of the atoms to the 3P_0 state with a clock pulse and subsequently removed residual ground-state atoms by using the 461 nm probe beam as a method to “blow-away” ground state atoms. We observed that the ground state population grew at a rate proportional to the excited state population. Due to the effects of two-body inelastic collisions between 3P_0

atoms (described in Chapter 5), the excited state population also decayed while the ground state population was being populated due to $^3P_0 \rightarrow ^3P_1$ Raman scattering, and we took this effect into account. By fitting the rate of accumulation in 1S_0 , we were able to extrapolate that the atoms in 3P_0 were decaying with $\Gamma_{e \rightarrow g} = 5.0(5) \times 10^{-2}$ 1/s. We expect this to be consistent with the temperature corrected $^3P_0 \rightarrow ^3P_1$ Raman rate in Table 2.2, of $\Gamma_{e \rightarrow g}^{\text{Raman}} = 4.4 \times 10^{-2}$ 1/s. Interestingly, while there is fairly good agreement between these numbers, there is one effect that we have not taken into account: the natural lifetime of ^{87}Sr due to spontaneous emission. The $^3P_0 \rightarrow ^1S_0$ natural decay rate has been calculated as $\Gamma_{e \rightarrow g}^{\text{Spont}} = 9(3) \times 10^{-3}$ 1/s, and thus there is good agreement between the predicted $\Gamma_{e \rightarrow g}^{\text{Spont}} + \Gamma_{e \rightarrow g}^{\text{Raman}} = 5.3(3) \times 10^{-2}$ 1/s and the measured $\Gamma_{e \rightarrow g} = 5.0(5) \times 10^{-2}$ 1/s.

Finally, we note that this general technique of measuring decay to 1S_0 should permit an accurate evaluation of the ^{87}Sr natural lifetime. By measuring the optical pumping rate as a function of lattice intensity, the zero-intensity decay rate could be extrapolated, representing a measurement of the natural lifetime. This measurement would benefit from the fact that its analysis will not depend heavily upon the details of the scattering rate calculation.

2.7 *In situ* thermometry and cooling

As described in the previous section, the atomic temperature can have direct and noticeable impact on degree of dephasing between atoms during the laser excitation process. As we will see in Chapter 5, knowledge of and control of excitation inhomogeneity is important for characterizing density-dependent frequency shifts. Furthermore, the atomic density itself is dependent on the temperature, which is also important for characterizing density-dependent effects. In this section, we describe the techniques used for measuring the temperature of the atomic sample in the longitudinal direction (T_z) and in the radial direction (T_r), as well as additional cooling we can perform on the lattice-trapped atoms.

In order to extract T_z , the red and blue longitudinal sidebands are compared in size. Since atoms with $n_z = 0$ cannot lose any further motional quanta, atoms in the longitudinal ground do

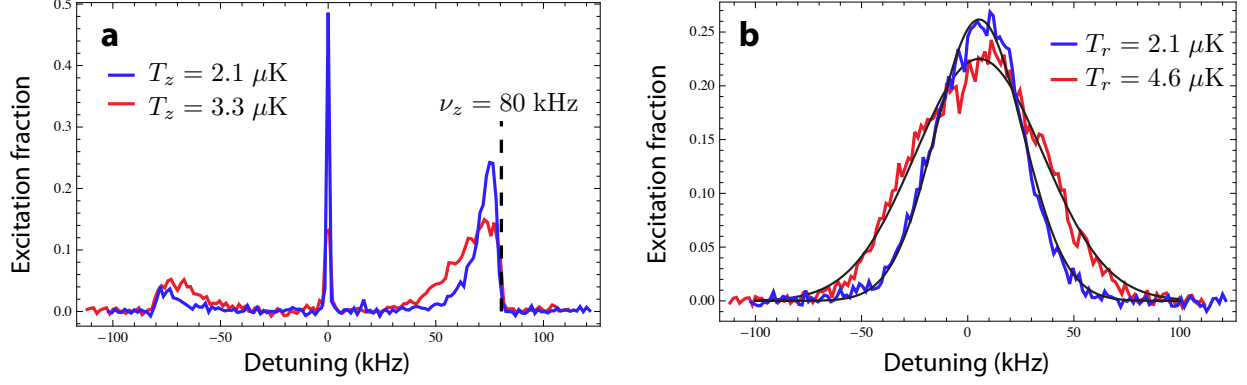


Figure 2.19: Temperature extraction and effect of additional cooling. (a) Uncooled (red) and cooled (blue) longitudinal sideband structure. (b) Uncooled (red) and cooled (blue) Doppler-broadened clock transition. The black line is a Gaussian fit to each temperature condition.

not contribute to the red sideband, thus creating a temperature-dependent asymmetry between the red and blue sidebands. This is in contrast to the other motional states with $n_z > 0$ that contribute to each sideband equally⁴. It can be shown that the ratio of the sideband areas is related to the temperature as [126]

$$\frac{\sigma_{\text{red}}^{\text{total}}}{\sigma_{\text{blue}}^{\text{total}}} = 1 - \frac{e^{-E_0/(k_B T_z)}}{\sum_{n_z=0} e^{-E_{n_z}/(k_B T_z)}}. \quad (2.52)$$

Here, the sum is taken over the approximate number of bound states in the longitudinal direction, which is approximately 6 for a typical 80 kHz lattice. The mode dependent energy, E_{n_z} , includes the effects of quartic distortion of the $\cos^2(kz)$ potential and is given by [126]

$$E_{n_z} = h\nu_z \left(n_z + \frac{1}{2} \right) - \frac{\nu_{\text{rec}}}{2} (n_z^2 + n_z + 1), \quad (2.53)$$

where $\nu_{\text{rec}} = \omega_{\text{rec}}/(2\pi)$, where ω_{rec} is the recoil frequency as defined by Eq. 2.30. In order to find T_z , we simply numerically solve Eq. 2.52 for T_z .

The technique we employ to find T_r is more straightforward. A secondary clock laser beam pathway along the H2 axis (see Fig. 2.3) probes the lattice-trapped atoms along the weakly-confined axis, resulting in a Doppler-broadened transition profile. We fit the doppler width of the profile

⁴ From Eq. 2.33 it might be expected that there would be an asymmetry between the excitations of each sideband. Experimentally, we utilize pulses that “over-drive” the transition, meaning that the excitation saturates to a constant value due to the dephasing explored in the previous section

using a Gaussian distribution $P_e(\nu) \propto \exp[-(\nu - \nu_0)^2 / (2\sigma)]$ where [88]

$$\sigma = \nu_0 \sqrt{\frac{k_B T}{m c^2}}. \quad (2.54)$$

Typical values for the frequency width σ are 15–30 kHz, representing temperatures in the 1–4 μK range.

In order to reduce the temperature of the lattice-trapped ^{87}Sr , we employ two techniques. In order to cool the longitudinal temperature, we employ additional cooling on the lattice-trapped, spin-polarized sample using MOT on the $^1\text{S}_0 \rightarrow ^3\text{P}_1$, $F = 9/2 \rightarrow F = 11/2$ transition, and whose frequency is tuned to optimize the longitudinal temperature. During this sideband cooling stage, the optical pumping beam and bias magnetic field used in the spin-polarizing procedure are left on, ensuring that the atoms cycle primarily on the $m_F = 9/2 \rightarrow m_F = 11/2$ transition and do not depolarize. Since the optical pumping beam (along H2) and the MOT beam along this same axis compete, we must disable this MOT beam pathway during the cooling. In order to cool the atoms in the polarizing transverse dimension, we optionally apply an additional cooling beam along the imaging axis, which cools the atoms transversally along that axis. Figure 2.19 shows the effect of these extra cooling steps on the measured T_z and T_r .

2.8 Systematic uncertainty

The ^{87}Sr optical lattice clock was the first neutral atom standard to surpass the Cs primary frequency standard in its reported systematic uncertainty. In a series of measurements in 2007–2008, we characterized many relevant clock systematics of the Sr lattice clock below the 10^{-16} optical lattice clock by comparing the ^{87}Sr clock frequency with the NIST Ca clock [31]. The comparison was facilitated by the use of an ultrastable octave spanning frequency comb [132] in order to connect the ^{87}Sr clock frequency to a transfer laser at 1064 nm. The transfer laser was transmitted through a noise-cancelled ~ 3.5 km fiber to NIST [55] where a second frequency comb allowed comparison with the Ca clock, which served as a stable reference at intermediate timescales. Due to slow drifts in the Ca clock, data was typically taken in an interleaved fashion, with 100 seconds per

Contributor	Correction (10^{-16})	Uncertainty (10^{-16})
Lattice Stark (scalar/tensor)	-6.5	0.5
Hyperpolarizability (lattice)	0.1	0.1
BBR Stark	54.0	1.0
AC Stark (probe)	0.2	0.1
1 st order Zeeman	0.2	0.2
2 nd order Zeeman	0.36	0.04
Density	3.8	0.5
Line pulling	0	0.2
Servo error	0	0.5
2 nd order Doppler	0	$\ll 0.01$
Systematic total	52.1	1.36

Table 2.3: Systematic frequency shifts and their uncertainties for the ^{87}Sr frequency standard (as in Refs. [1, 2]). The largest contributor to clock uncertainty, the black-body radiation (BBR) shift, is marked in red.

condition (e.g., high-density vs. low-density operation). The net result of the evaluation is shown in Table 2.3. Using the same fiber for microwave frequency transfer, we measured the ^{87}Sr lattice clock against the NIST F1 primary frequency standard, and obtained [1]

$$\nu_{\text{Sr}} = 429,228,004,229,873.65(37) \text{ Hz.} \quad (2.55)$$

We note that this value is in good agreement with all previous and subsequent measurements [133, 33, 134, 34].

In the intervening four years, the optical lattice setup was changed from an injection-locked Ti:sapphire system to an all-solid state one. Additional improvements to the lattice were made at that time, allowing better overlap between the input and retro-reflected lattice beams, thus increasing the longitudinal trap frequency from ~ 40 kHz, to ~ 80 kHz. This change greatly facilitated the collisional physics studied in Chapter 5 of this thesis, but will require a re-evaluation of systematics. However, as we show in Chapter 4, a new ultrastable laser system permits evaluation of a systematic through interleaved measurement (as utilized in [135]) on a very rapid timescale. In contrast to the result presented in [135], where data records spanning several weeks were required for systematic evaluation at the 1×10^{-17} level, the new laser system presented in Chapter 4 of this thesis allows for similar measurement precision to be obtained in 30 minutes. Thus, one could

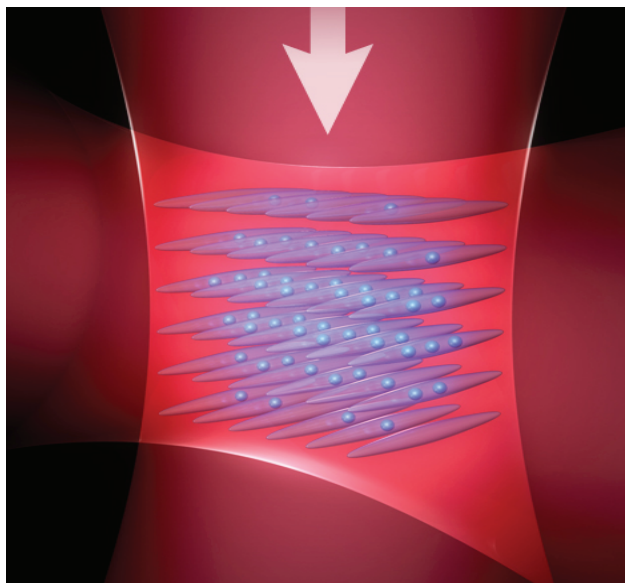


Figure 2.20: Two-dimensional lattice geometry. Here, the single-site occupancies are mainly restricted to zero, one, or two atoms.

envison doing a complete clock systematic evaluation at the 10^{-17} level in one day if averaging time were the only impediment to such a measurement!

As will be shown in Chapter 5, a high-density lattice clock does not make the best frequency reference due to the strong interactions between atoms in the optical lattice. The current experimental configuration is best suited for experimental studies of collisional physics due to the high operating density. However, we have still been able to evaluate the density shift to the low 2.4×10^{-17} fractional frequency uncertainty in the current experimental configuration with a reduced operating atom number of $N_{\text{tot}} = 1000$. In the meantime, a second ^{87}Sr clock under development at JILA employs a much lower-density operating condition by utilizing a buildup cavity for the lattice, allowing a large reduction of density. This second system has been able to demonstrate a density shift uncertainty for operation with 1000 atoms of 8×10^{-19} [43].

A second approach to reducing the density shift that we employed was to confine the atoms in a 2D lattice, depicted schematically in Fig. 2.21. Here, a reduction of the density shift to the 1×10^{-17} was observed, which was made possible primarily by the single-site occupancy combined

with strong interactions for the particles in doubly- and triply- occupied sites [135]. The additional operational complexity of the 2D lattice is not favorable for robust clock operation, but this work was an important demonstration of methods for reducing density shifts by reducing the chance an atom resides in a multiply-occupied site. A three-dimensional lattice would be a natural extension of this technique, and we note that 3D lattice geometries have also been realized with bosonic ^{88}Sr [136]. For the remainder of this thesis, we restrict ourselves to the one-dimensional lattice geometry. In this configuration, the single site occupancies are large enough to constitute quantum many-body systems, and we study them in this context in Chapter 5.

We note that a significant exploration of all lattice-induced shifts has been presented in [110], where effects such as hyperpolarizability (two-photon-induced stark shifts which scale with lattice intensity as I^2) and shifts due to magnetic dipole and electric quadrupole transitions [137], which scale as \sqrt{I} . The conclusion of Ref. [110] is that lattice systematics can be controlled at below the 1×10^{-17} level for the lattice depths we employ in the clock.

2.8.1 Blackbody radiation

As seen from the systematic uncertainties listed in table 2.3, black-body radiation is the largest contributor the ^{87}Sr clock uncertainty (highlighted in red), and this is the case for all ^{87}Sr lattice clocks currently at the 1×10^{-16} uncertainty level [31, 33, 34]. The frequency shift arises due to room-temperature radiation coupling to the AC-polarizability of the clock states. To first order, however, the black body radiation (BBR) depends primarily on the DC polarizability of the clock states as [138, 139, 115]

$$h\Delta\nu_{\text{BBR}} = -\frac{1}{2}\langle E^2 \rangle_T \Delta\alpha(0) [1 + \eta(T)]. \quad (2.56)$$

Here, $\langle E^2 \rangle_T = (8.319 \text{ V/cm})^2 (T/300 \text{ K})^4$ is the average squared electric field magnitude for a given temperature; $\Delta\alpha(0) = \alpha_e(0) - \alpha_g(0)$ is the differential DC polarizability, where $\alpha_e(0)$ and $\alpha_g(0)$ are defined in Eqs. 2.19 and 2.20, respectively; and $\eta(T)$ is the dynamic correction, which takes into account shifts due to corrections beyond the DC polarizability. Until recently, lack

of knowledge of several oscillator strengths utilized for the calculation of $\alpha_e(0)$ had limited the theoretical uncertainty of the room-temperature BBR correction at 7×10^{-17} [140].

Two experiments have successfully measured $\Delta\alpha(0)$ in Yb [139] and Sr [115] optical lattice clocks. In the case of Sr, a discrepancy between the theoretical Sr blackbody frequency correction calculated in Ref. [138] and the measured value was discovered by Middelmann *et al.* [115]. The discrepancy amounts to an additional fractional frequency correction of -1.8×10^{-16} at 300 K. Additional theoretical work has resolved the discrepancy [141], indicating the measured values should supersede the original calculation. For Sr, the measurements of Middelmann *et al.* indicate $\Delta\alpha = 4.07865(11) \times 10^{-39} \text{ C m}^2/\text{V}$, resulting in a static BBR shift of $-\frac{1}{2\hbar}\langle E^2 \rangle_T \Delta\alpha(0) = -2.130186(60) \times \left(\frac{T}{300 \text{ K}}\right)^4 \text{ Hz}$. Additionally, Refs. [115] and [141] agree regarding the contribution of the dynamic polarizabilities to the frequency shift as $-\frac{1}{2\hbar}\langle E^2 \rangle_T \Delta\alpha(0) \eta(T) = -0.1477(23) \times \left(\frac{T}{300 \text{ K}}\right)^6 \text{ Hz}$ (Middelmann *et al.*, [115]) and $-0.1492(16) \times (T/300)^6 \text{ Hz}$ (Safronova *et al.*, [141]).

The measurements have essentially eliminated the systematic uncertainty associated with knowledge of the static polarizability of Sr. However, the total BBR uncertainty quoted in Table 2.3 includes two contributions: the now-irrelevant uncertainty in $\Delta\alpha(0)$ and the uncertainty in the BBR environment experienced by the atoms. The latter effect still contributes the largest and most difficult-to-characterize systematic shift to the ^{87}Sr lattice clock. A 1 K uncertainty in the temperature induces a 7×10^{-17} systematic effect. This reflects the unfortunate fact that Sr has the largest BBR shift coefficient of all lattice clock atomic species. Future work will undoubtedly focus on providing a well-characterized, or possibly cryogenic [142] environment for the lattice-trapped atoms.

2.9 Quantum projection noise and the Dick effect

One of the strongest motivating factors for developing optical lattice clocks is the potential for extremely high stability due to the large signal-to-noise ratio provided by the parallel interrogation of $> 10^3$ atoms. For a clock operated at average excitation fraction given by p , the number of atoms

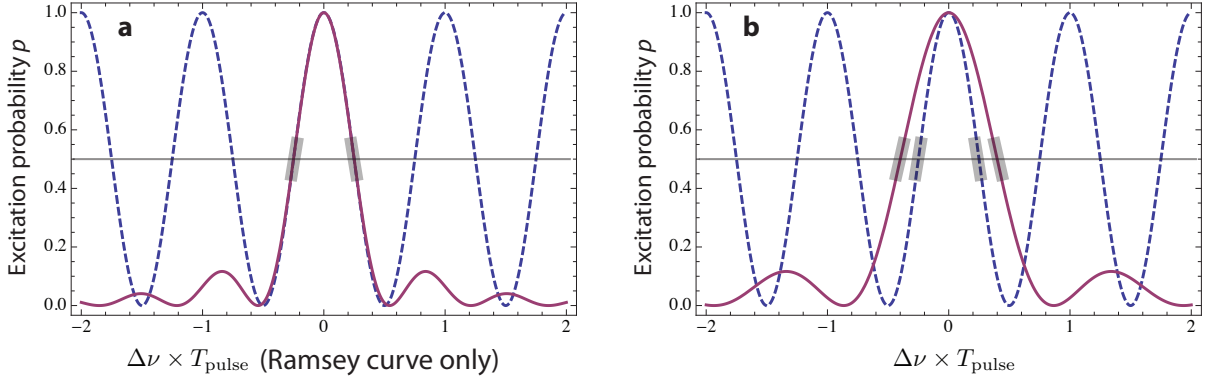


Figure 2.21: Ramsey (dashed) and Rabi (solid) lineshapes compared for quantum projection noise calculation. (a) Here, the ratio of Rabi to Ramsey pulse times is 1.6, such that the full width at half maximum (FWHM) of the Rabi and Ramsey lineshapes are equivalent. In this scenario, the slope at $p = 0.5$ is nearly identical. (b) T_{pulse} is the same for both traces. For a given T_{pulse} , the FWHM of the Ramsey lineshape is a factor of $\simeq 1.6$ narrower.

found in the excited state follows a binomial distribution, assuming the atoms are uncorrelated (i.e., the system is not spin-squeezed). It then follows that the variance of the measured excitation fraction, (see Eq. 2.29) is

$$\delta f_{\text{exc}}^2 \equiv \text{Var}[f_{\text{exc}}] = \frac{p(1-p)}{N}. \quad (2.57)$$

This relationship between the noise and the total atom number is known as quantum projection noise. In fact, measuring quantum projection noise is the method we employ to calibrate the constant of proportionality between our fluorescence detection and the actual total number of atoms in the lattice.

Equation 2.57 is a key result for noise in optical lattice clocks: as the number of atoms increases the noise decreases. However, this is only part of the story. One must convert the atomic noise into frequency noise by use of the spectroscopic lineshape. Typically, clocks are operated with $p = 0.5$, as depicted in Fig. 2.21, where the slope of the excitation probability with respect to frequency is maximized. From the analytic shapes of the Rabi and Ramsey lineshapes, it can be

shown that

$$\sigma_y^{\text{Rabi}}(\tau) \simeq \frac{\Delta\nu^{\text{Rabi}}}{3.03\nu_0\sqrt{N_{\text{tot}}}} \sqrt{\frac{T_{\text{cycle}}}{\tau}}, \quad (2.58)$$

$$\sigma_y^{\text{Ramsey}}(\tau) = \frac{\Delta\nu^{\text{Ramsey}}}{\pi\nu_0\sqrt{N_{\text{tot}}}} \sqrt{\frac{T_{\text{cycle}}}{\tau}}, \quad (2.59)$$

where T_{cycle} is the experimental cycle time, ν_0 is the frequency of the transition, and $\Delta\nu^{\text{Rabi}}$ ($\Delta\nu^{\text{Ramsey}}$) is the FWHM of the spectroscopic feature used for feedback. $\Delta\nu^{\text{Rabi}}$ and $\Delta\nu^{\text{Ramsey}}$ are given by

$$\Delta\nu^{\text{Rabi}} \simeq 0.80/T_{\text{pulse}}, \quad (2.60)$$

$$\Delta\nu^{\text{Ramsey}} = 1/(2T_{\text{dark}}), \quad (2.61)$$

where T_{dark} is the Ramsey free evolution time. Thus, even for a modest spectroscopy time of 200 ms and only $N_{\text{tot}} = 1000$, quantum-projection noise limited clock operation is still $1 \times 10^{-16}/\sqrt{\tau/1 \text{ s}}$ for Rabi spectroscopy.

One roadblock to benefiting from the SNR afforded by thousands of atoms is broadband laser noise, which ends up contaminating the error signal through the Dick effect. The Dick effect is a process through which a periodic clock interrogation with spectroscopic dead time writes noise onto the correction signal, degrading long term stability [36, 143]. For example, for every 1 s of time per clock interrogation cycle a neutral atom system might spend cooling and trapping atoms in an optical lattice, the time during which spectroscopy is performed might only be 100 ms. Thus, there is an inevitable dead time between spectroscopy sequences, resulting in a periodic sampling of the laser phase noise, and leading to aliasing of higher-frequency laser noise, deteriorating the stability.

Specifically, it can be shown that the Dick effect-limited Allan deviation due to the aliasing mechanism is given by [37]

$$\sigma_y^2(\tau) = \frac{1}{\tau} \sum_{m=1}^{\infty} \frac{|R(m/T_c)|^2 G_\nu(m/T_c)}{|R(0)|^2 \nu_0^2}. \quad (2.62)$$

Here T_c is the clock cycle time, including both atom loading and spectroscopy time; $R(f)$ is given

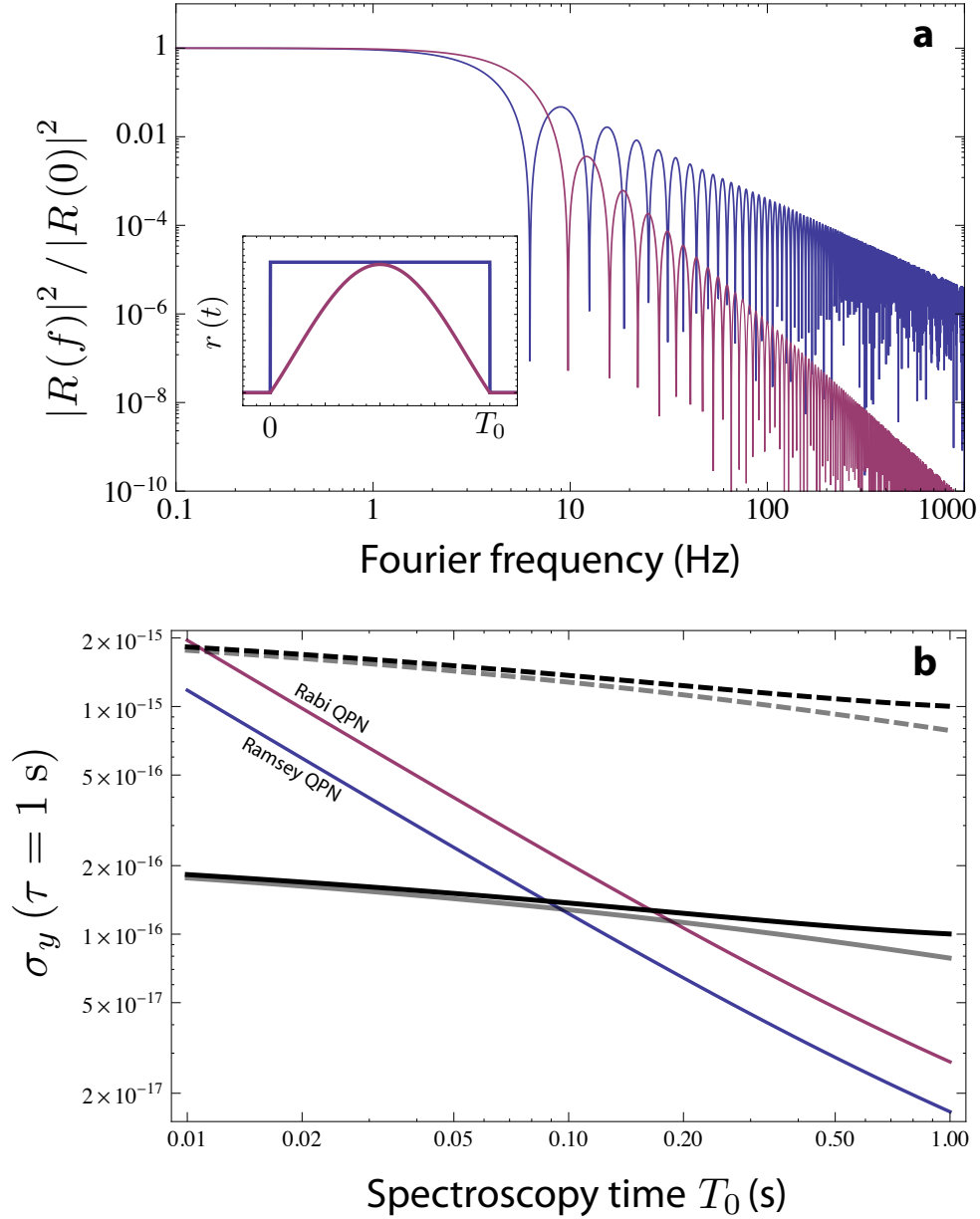


Figure 2.22: Fourier and time-domain representation of the Dick sensitivity function and its implications for reaching quantum-limited clock performance. (a) Fourier sensitivity for Rabi (red) and Ramsey (blue) corresponding to the sensitivity functions shown in the inset. Here the time T_0 corresponds to T_{pulse} (T_{dark}) in the case of Rabi (Ramsey) spectroscopy. For the frequency-domain plots, $T_0 = 200 \text{ ms}$. (b) Here, the loading time is 1 s, such that the cycle time $T_c = 1 + T_0$. We plot the quantum projection noise-limited instability for $N_{\text{tot}} = 1000$ for both Rabi and Ramsey spectroscopy (red and blue, respectively) and the Dick-limited instability for lasers with $\sigma_y(\tau) = 10^{-15}$ (dashed black/grey) and $\sigma_y(\tau) = 10^{-16}$ (solid black/grey). The black (grey) lines are using the Rabi (Ramsey) Dick sensitivity function to calculate the Dick-limited performance. In all cases the instability has been extrapolated to 1 s, so that $\sigma(\tau) = \sigma(1) / \sqrt{\tau/1 \text{ s}}$.

by

$$R(f) = \mathcal{F}[r(t)], \quad (2.63)$$

where $\mathcal{F}[\dots]$ is the Fourier transform operation; and $G_\nu(f)$ is the laser frequency noise power spectral density. The function $r(t)$ describes the spectroscopic sensitivity to a phase shift in the local oscillator laser and is defined through [36]

$$\delta f_{\text{exc}} = \frac{1}{2} \int_0^{T_0} dt \Delta\omega(t) r(t), \quad (2.64)$$

where $\Delta\omega(t)$ is time varying laser detuning (i.e., noise) and δf_{exc} is a fluctuation about the expected excitation fraction due to laser noise. The upper limit of the integral is simply the duration of the spectroscopy, which is assumed to start at $t = 0$. We will return to a detailed discussion of sensitivity functions in Chapter 6. For the moment it is sufficient to give $g(t)$ for Ramsey and Rabi spectroscopy. The Rabi sensitivity function is given by

$$r^{\text{Rabi}}(t) = - \left(\frac{\Delta_0 \Omega_0^2}{\Omega^3} \right) \left\{ \sin(\Omega t) - \sin\left(\pi \frac{\Omega}{\Omega_0}\right) + \sin\left[\frac{\Omega}{\Omega_0}(\pi - t\Omega_0)\right] \right\}, \quad (2.65)$$

where generalized Rabi frequency Ω is related to the bare Rabi frequency Ω_0 by $\Omega = \sqrt{\Omega_0^2 + \Delta_0^2}$, and Δ_0 is a static laser detuning from the transition chosen so that $p = 0.5$. The Ramsey sensitivity function is given by

$$r^{\text{Ramsey}}(t) \simeq \text{rect}\left[\frac{t}{T_{\text{dark}}} - 1/2\right]. \quad (2.66)$$

A derivation of Eq. 2.65 is given in Appendix A. In Chapter 6, we additionally show that Eq. 2.66 is a simple case of the class of sensitivity functions that arise from spin-echo sequences with fast $\pi/2$ - and π -pulses. Figure 2.22a shows the time and frequency-domain behavior of these functions. Figure 2.22b shows the implications of the Dick effect on the long-term stability of an optical frequency standard. Here, two different flicker-noise limited local oscillator spectra are considered, representing a laser with $\sigma_y(\tau) = 1 \times 10^{-15}$, as originally used in the ^{87}Sr lattice clock [40], and a laser with $\sigma_y(\tau) = 1 \times 10^{-16}$, which is the thermal noise floor of the ultrastable laser reported in this thesis and described in Chapter 4. As seen from Fig. 2.22, only the laser with $\sigma_y(\tau) = 1 \times 10^{-16}$

is not limited by the Dick effect over wide range of spectroscopy times, and furthermore the overall clock performance is better by an order of magnitude. Here, flicker noise is chosen because it corresponds to the frequency noise caused by thermal noise in optical interferometers, and is the subject of the next chapter.

As the preceding discussion indicates, laser stability is a crucial aspect of an optical atomic clock. Through the Dick effect, the stability of the local oscillator laser always impacts the stability of the clock. Furthermore, the short term stability of lasers greatly impacts the amount of time required to make systematic evaluations via interleaved measurements. Here, a factor of 10 improvement in laser stability yields a 100-fold reduction of the measurement time necessary, reducing month-long measurement campaigns to mere hours. In the next two chapters, we explore some challenges to improving laser stability, and present three separate laser systems that perform at or near the 1×10^{-16} level of instability.

Chapter 3

Thermal noise in optical interferometers

The goal of this chapter is to introduce the concepts of thermally-driven noise in (opto)-mechanical systems in a qualitative manner; we then proceed into detailed equations that describe noise in optical interferometers. A careful consideration of the sources of noise is necessary for developing state of the art ultrastable lasers, and we use the detailed formalism summarized here to motivate current highly successful optical cavity designs, as well as potential future ultrastable laser systems with instability at the level of 1×10^{-17} .

3.1 Introduction

Optical interferometers are found at the heart of experiments that probe the physical world, from quantum mechanical [144, 145, 146] to cosmological scales [147]. As introduced in Chapter 2, cavity-stabilized lasers are essential components of the most precise optical atomic clocks [43] and their performance directly impacts the ultimate stability of clocks employing thousands of atoms. The mechanism that currently sets the stability limit for interferometers—from μm to km length scales—is detrimental thermal coupling to the environment. This coupling is a direct consequence of mechanical losses in the interferometer substrates and coatings and causes a mechanical displacement which directly impacts the optical phase. In the case of Fabry-Pérot interferometer-based laser stabilization, the length stability of the interferometer directly impacts the frequency noise of the stabilized laser, leading to frequency noise that is directly proportional to the fractional length

change of the interferometer as¹

$$\frac{\Delta\nu}{\nu} = -\frac{\Delta L}{L}. \quad (3.1)$$

Here, L is the length of the Fabry-Pérot interferometer and ν is the central frequency of the laser stabilized to it.

In this chapter, we describe the mechanism by which both Brownian noise and thermodynamical temperature fluctuations in the interferometer components become effective length fluctuations of optical interferometers. We emphasized that understanding these mechanisms is important for designs which mitigate the effect of thermal noise. We also describe a second thermal noise mechanism that arises due to statistical temperature fluctuations in the bulk of optical substrates and coatings. This in turn will also drive length changes in the interferometer through thermal expansion and the thermo-optic effect. In Chapter 4 we will extensively discuss systems developed utilizing these insights.

3.2 Thermo-mechanical noise in physical systems

According to the fluctuation-dissipation theorem, the thermally-driven displacement fluctuations of a system are directly proportional to the admittance of the system such that the single-sided displacement power spectral density for any mechanical degree of freedom with dissipations is [148, 149, 150, 151]

$$G_x(f) = \frac{k_B T |\Re[Y(f)]|}{\pi^2 f^2}. \quad (3.2)$$

Here, $\Re[Y(f)]$ is the real part of the systems complex admittance, which is defined as

$$Y(f) = V(f)/F(f), \quad (3.3)$$

where $V(f)$ is the velocity response to an applied force $F(f)$ in the Fourier domain.

Since $G_x(f)$ depends directly on $Y(f)$, the displacement noise in a system depends directly on the type of mechanical damping model that is employed. In the case of bulk mechanical samples,

¹ In Chapter 4 we rigorously derive the relationship.

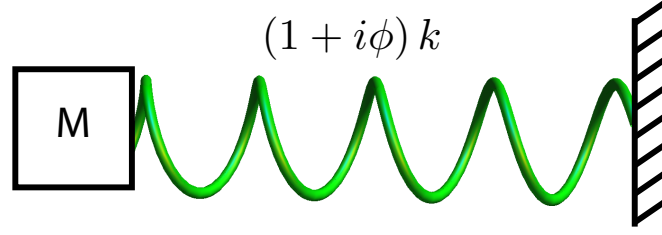


Figure 3.1: Modified Hooke’s law system. Here the addition of the loss angle ϕ creates a displacement-dependent dissipation such that the energy dissipated in one period of motion is $2\pi\phi$ and thus $Q = 1/\phi$.

such as mirror substrates and optical coatings, a type of damping called “internal damping” applies, which can be thought of as a modification of Hooke’s law such that [150]

$$F(f) = -(1 + i\phi)kX(f). \quad (3.4)$$

Here, ϕ is the loss angle, which parameterizes the energy dissipated in the material. It is straightforward to show that the fraction of energy dissipated in a cycle is $2\pi\phi$, such that $Q = 1/\phi$, where Q is the material quality factor.

Equation 3.4 represents the simple case where we consider one mechanical degree of freedom. For the mass on a spring depicted in Fig. 3.1, it is easily shown that

$$Y(f) = \frac{2\pi if}{(1 + i\phi)k - m(2\pi f)^2}. \quad (3.5)$$

In the low-frequency limit, where $2\pi f \ll \sqrt{k/m}$ and $\phi \ll 1$, $\Re[Y(f)] \rightarrow 2\pi f\phi/k$ and thus for the simple mass-on-a-spring system considered in Fig. 3.1,

$$G_x(f) \rightarrow \frac{2k_B T}{\pi f} \left(\frac{\phi}{k} \right). \quad (3.6)$$

In Eq. 3.6 lie all of the essential considerations for a mechanical system driven by Brownian noise: the low-frequency limit of the noise is $1/f$ in its frequency dependence, it is proportional to the loss angle ϕ (and thus inversely proportional to Q) and T , and it is inversely proportional to the material stiffness k .

While the case of a mass on a spring is instructive for building a basic understanding of thermally driven fluctuations in a mechanical system with one degree of freedom, the components

of optical systems, such as mirrors, are much more complicated. The mechanical displacement of a bulk object such as a mirror can be decomposed into normal modes, each of which are effective degrees of freedom with a generalized displacement amplitude. Early attempts to apply the fluctuation-dissipation theorem of Eq. 3.2 to such systems relied upon a decomposition into these normal modes, whose frequencies were numerically calculated [152]. In this approach, the beam profile is weighted by the normal mode displacement amplitude to properly evaluate the optical phase shift due to a given mode. In general, this sum-over-modes method should work, but it is computationally intensive and converges slowly [152, 151]. To solve these issues a new approach was developed, and is the subject of the next section.

3.2.1 Fluctuation-dissipation theorem and Levin’s “direct approach”

In 1997, Levin published a landmark work describing a new approach to calculating the effect of Brownian motion on the stability of optical interferometers [151]. At the heart of this method lies the use of a generalized coordinate. It can be shown that the quantity which affects the optical phase of a reflected beam with electric field amplitude profile $E(x, y) \propto \psi_{ij}(x, y)$ at the mirror’s surface is [152]

$$\Delta\phi = \int |\psi_{ij}(x, y)|^2 \mathbf{k} \cdot \vec{u}_S(x, y) dx dy. \quad (3.7)$$

Here $\Delta\phi$ indicates the resulting optical phase shift cause by $\vec{u}_S(x, y)$ (and is distinct from the loss angle ϕ), the mirror displacement evaluated at the mirror surface; and \mathbf{k} is the laser propagation wave-vector with $|\mathbf{k}| = 2\pi/\lambda$. It is assumed that the laser is propagating in the z -directions. The mode profile is normalized such that

$$\int \psi_{ij}(x, y) \psi_{kl}^*(x, y) dx dy = \delta_{ik} \delta_{jl}, \quad (3.8)$$

where δ is the Kroeneker delta. The indices i and j could in principle label Laguerre-Gauss modes for the case of a spherical mirror resonator, or other solutions to the paraxial Helmholtz equation for other types of boundary conditions (e.g. the case of conical or Mesa beams [153]). For the remainder of this Thesis, we will consider only Gaussian beams (i.e. the TEM00 mode of a spherical-mirror

optical resonator), as these are the lowest-order stable solution in a resonator formed by spherical mirrors, such that

$$|\psi(x, y)|^2 = |\psi_{00}(x, y)|^2 = \frac{2}{\pi w(z)} e^{-2(x^2+y^2)/w(z)}, \quad (3.9)$$

where $w(z)$ is the beam waist at the mirror under consideration.

The phase shift $\Delta\phi$ of Eq. 3.7 can be used to define an effective displacement—essentially the mirror displacement weighted by the beam intensity profile—as

$$x = \Delta\phi / |\mathbf{k}|. \quad (3.10)$$

Thus, even though the mirror itself is a complicated object with many relevant degrees of freedom, it is thus possible to reduce this to a single relevant coordinate, x , via Eq. 3.10.

Levin's technique allows direct computation of the displacement of this coordinate via the fluctuation-dissipation theorem. The whole point of the calculation is to calculate the behavior of $\Re[Y(f)]$ at frequencies well below the lowest-frequency resonant mode. However, it is not clear what the generalized force should be with respect to the generalized coordinate. The approach that Levin developed was to define a generalized force via a pressure of the form

$$\mathbf{P}(x, y; t) = F_0 |\psi_{ij}(x, y)|^2 \cos(2\pi ft) \mathbf{e}_z. \quad (3.11)$$

Here, f is the Fourier frequency of the oscillating pressure. In this way, the total hamiltonian for the generalized force and generalized displacement is

$$H = -F_0 \cos(2\pi ft) \int |\psi_{ij}(x, y)|^2 \mathbf{e}_z \cdot \vec{u}_S(x, y) = -F_0 \cos(2\pi ft) x \quad (3.12)$$

which shows that the generalized force enters the Hamiltonian as in the case where only a single mechanical degree of freedom was considered.

The next step of Levin's procedure is to calculate $\Re[Y(f)]$ from the generalized force and displacement. Here, the admittance is now defined with respect to the generalized variables. For the admittance defined in Eq. 3.3, it is easily seen that that the average dissipated power (by which

we mean the total energy lost in one cycle divided by the cycle time) is²

$$W_{\text{diss}} = \frac{1}{2} \Re\{F_0 \times [F_0 Y(f)]^*\} = \frac{1}{2} F_0^2 \Re[Y(f)]. \quad (3.13)$$

Thus, we can quite simply solve for the generalized $\Re[Y(f)]$ such that [151]

$$\Re[Y(f)] = \frac{2W_{\text{diss}}}{|F_0|^2} = \frac{4\pi f U_{\text{max}} \phi}{|F_0|^2}. \quad (3.14)$$

Here, the last equality simply relates the dissipated energy to the maximum elastic energy stored, U_{max} , via the loss angle. This follows directly from the modified Hooke's law of Eq. 3.4. Finally, by applying Eq. 3.2 to the case of generalized displacement we obtain Levin's result [151]

$$G_x(f) = \frac{k_B T |\Re[Y(f)]|}{\pi^2 f^2} = \frac{2k_B T \phi}{\pi f} \left(\frac{2U_{\text{max}}}{|F_0|^2} \right), \quad (3.15)$$

which is analogous to the simple spring case of Eq. 3.6, where $U_{\text{max}} = |F_0|^2 / (2k)$.

The final step of the procedure requires a “simple” calculation of W_{diss} for the generalized force given by Eq. 3.11 via a calculation of U_{max} for a static generalized force. The use of a static force is allowed as long as the frequency is well below any resonant frequencies of the system. In principle this can be done numerically very straightforwardly [155]. However, analytic solutions for the case of a Gaussian beam profile on a cylindrical mirror have been obtained [151, 156]. Finally, we note that the calculation method is easily extended to include the surface contribution due to a thin dielectric coating film [156]. As it turns out, this aspect of the mirror is absolutely crucial to consider, as the loss angle can be from one to four orders of magnitude larger than the bulk mirror substrate, depending on the substrate material.

Before proceeding further, we can make some qualitative statements. As in Eq. 3.6, we see that the noise of the generalized coordinate x will scale linearly with the temperature and loss angle, while it will scale inversely with the material stiffness, which is parameterized by an effective spring constant $\tilde{k} = |F_0|^2 / (2U_{\text{max}})$. In the case of the bulk substrate, which can be thought of as an infinite half-plane, dimensional analysis indicates that $\tilde{k} \propto w_0 E$, where E is the bulk Young's modulus and w_0 is the beam $1/e^2$ intensity radius.

² This computation is similar to time averages performed in electrodynamics. See, e.g., Jackson [154] for a derivation of the time average formula for oscillatory fields.

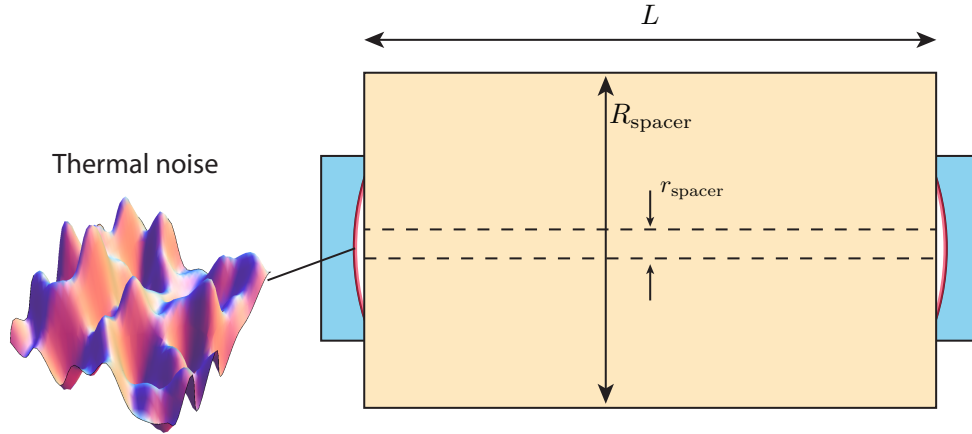


Figure 3.2: Schematic of the relevant optical components for calculating the thermal noise of an optical cavity. The mirrors substrates (blue), optical coatings (thin red line), and spacer (tan) all contribute to thermally-driven displacement noise at the mirror surface.

3.2.2 Brownian motion in optical cavities

As seen in the previous section, a powerful formalism exists for evaluating Brownian thermal noise in optical components. In the case of a cavity, the components of concern are the spacer, mirror substrate, and mirror coatings, as depicted in Fig. 3.2. In each case, the thermally driven fluctuations of the effective displacement are calculated as outlined in the previous section. While we do not go into the details of the calculation, we note that in the specific case of a Gaussian beam, it entails calculating the stored energy in an infinite half-plane (which approximates the mirror) when subject to a Gaussian pressure profile. It has been found that the one-sided power spectral density of position fluctuations (in units of m^2/Hz) arising from each of the cavity components at

Fourier frequency f are³ [156, 157, 155]

$$G_x^{\text{substrate}}(f) = \frac{2k_B T}{\pi^{3/2} f} \frac{1 - \sigma^2}{w_0 E_s} \phi_s, \quad (3.16)$$

$$G_x^{\text{coating}}(f) = \frac{2k_B T}{\pi^{3/2} f} \frac{1 - \sigma^2}{w_0^2 E_s} \left\{ \frac{1}{\sqrt{\pi}} \frac{d}{E_s E_c (1 - \sigma_c^2) (1 - \sigma_s^2)} \right. \\ \times \left[E_c^2 (1 + \sigma_s)^2 (1 - 2\sigma_s)^2 \phi_{\parallel} + E_s E_c \sigma_c (1 + \sigma_s) (1 + \sigma_c) (\phi_{\parallel} - \phi_{\perp}) \right. \\ \left. \left. + E_s^2 (1 + \sigma_c)^2 (1 - 2\sigma_c) \phi_{\perp} \right] \right\}, \quad (3.17)$$

$$G_x^{\text{spacer}} = \frac{2k_B T}{f} \frac{L}{\pi^2 R_{\text{spacer}}^2 - r_{\text{spacer}}^2} \left(\frac{\phi_{\text{spacer}}}{E_{\text{spacer}}} \right). \quad (3.18)$$

Some of the parameters used in these equations are defined in Table 3.1. We note that for the purposes of calculations in this Thesis, we assume that the coating parallel loss angle (ϕ_{\parallel}) and the coating perpendicular loss angle (ϕ_{\perp}) are equivalent.

Two qualitative remarks can be made at this point, the first of which is that both the substrate and coating displacement noise power spectral densities, given by Equations 3.16 and 3.17, respectively, do not depend on the length of the cavity. This is due to the fact that the fluctuations are localized to the mirror surface and this property can be exploited in order to reduce frequency noise. By increasing the cavity length, the fractional length fluctuations decrease, resulting in a substrate and coating thermal noise-induced optical frequency noise spectral density that is proportional to $1/L^2$. Secondly, while the spacer thermal noise contribution scales with length, and inversely with R_{spacer}^2 . Thus, for a spacer with constant aspect ratio, the spacer contribution to the total thermal noise in fact decreases with length. This is due to the fact that to convert the power spectral densities to fractional frequency fluctuations, they must be divided by L^2 . Additionally, longer optical cavities typically have larger radii in order to maintain favorable mounting geometry, meaning that as L increases, so too does R_{spacer} .

One clear avenue to decrease this noise limit is to decrease the material losses, lower the temperature, or do both. However, the situation is not so simple. For example, the loss angle of fused silica—a commonly-utilized mirror substrate material—begins to increase sharply at temperatures below ~ 250 K, ultimately suffering an almost four orders of magnitude increase before

³ There has recently been an important correction to the spacer contribution [155].

Definition of parameters	
w_0	Beam $1/e^2$ intensity radius
d	Coating thickness
ϕ_s	Substrate loss angle
$\phi_{\perp(\parallel)}$	Coating loss angle perpendicular (parallel) to substrate
$E_{s(c)}$	Substrate (coating) Young's modulus
$\sigma_{s(c)}$	Substrate (coating) Poisson ratio
$\alpha_{s(c)}$	Substrate (coating) coefficient of thermal expansion
$\kappa_{s(c)}$	Substrate (coating) thermal conductivity
$C_{s(c)}$	Substrate (coating) heat capacity
$\omega_c^{\text{sub}(\text{coat})}$	Substrate (coating) cutoff frequency
$R_{\text{spacer}}(r_{\text{spacer}})$	Spacer (spacer central bore) effective radius

Table 3.1: Summary of the parameters used in the text.

Substrate and spacer materials			
Material	ϕ	E (GPa)	σ
Fused silica (SiO_2)	10^{-6} – 10^{-8}	72	0.17
ULE glass	1.7×10^{-5}	68	0.18
Silicon	10^{-8}	130–190*	0.05–0.35*
Sapphire	3×10^{-9}	400*	0.29*
Dielectric multilayers			
Material	ϕ	E (GPa)	σ
$\text{SiO}_2/\text{Ta}_2\text{O}_5$ Bragg stack	4×10^{-4}	110	0.2
$\text{GaAs}/\text{Al}_{92}\text{Ga}_8\text{As}$ Bragg stack	2.5×10^{-5}	85*	0.32*

Table 3.2: Mechanical properties of typical optical materials. Values are obtained from [163, 164, 156, 165, 157, 166, 167]. *Orientation-dependent

it levels off at 50 K, completely eliminating the benefit of operating at these temperatures [158]. However, crystalline materials such as sapphire [159], calcium fluoride [160], and silicon [158] offer the benefits of low thermal expansion and low loss angle at cryogenic temperatures. Unfortunately, typical coating loss angles exhibit an approximate factor of 3 increase at cryogenic temperatures [161], which offsets some of the gains of operating at low temperatures. We note in passing that there is an active search for low-loss coating materials or dopants to reduce the mechanical loss of the existing coating technology [162]. It should also be noted that it becomes increasingly difficult to shield cryostat vibrations at very low temperatures, due to the large cooling powers required.

A powerful and ground-breaking approach to the coating noise problem—which currently

sets the ultimate noise floor of ultrastable optical cavities [155, 168, 43]—is to use a fundamentally different coating material for the high-reflectivity dielectric coating. The standard material is an alternating structure of $\lambda/4$ layers of SiO_2 and Ta_2O_5 . However, as seen in Table 3.2, the loss angle of a SiO_2 and Ta_2O_5 is large [169] compared to fused silica, a commonly-utilized substrate material. Indeed, for a typical optical cavity employing fused silica mirror substrates, a ULE glass spacer, and $\text{SiO}_2/\text{Ta}_2\text{O}_5$ coatings, $\gtrsim 80\%$ of the Brownian thermal noise power spectral density results from the excess mechanical loss of the conventional coating. The benefit of $\text{SiO}_2/\text{Ta}_2\text{O}_5$ coatings is their extremely low optical loss, which is at the few ppm level [170]. However, recent breakthroughs in engineering both high-reflectivity and low-mechanical-loss structures for use in optomechanics have lead to simultaneously high optical- and high mechanical-quality microresonators employing AlGaAs heterostructures[171]. As seen from the mechanical quality factor listed in Table 3.2, the loss angle of AlGaAs structures is at least an order of magnitude lower than $\text{SiO}_2/\text{Ta}_2\text{O}_5$ coatings.⁴ With a recent demonstration of optical losses of order ~ 15 ppm [172], these coatings promise an order of magnitude reduction of coating thermal noise. Experimental developments along this front will be discussed further in Chapter 4.

Finally, it is worth mentioning that a final alternative approach to reduce Brownian coating and substrate thermal noise relies not on reducing the temperature or utilizing novel materials, but instead on using specially shaped beams, such as mesa, conical, or higher order Laguerre-Gauss beams [153]. This has the effect of better averaging the position fluctuations of the mirror surface due to thermal noise. While one could simply envision working near the stability edge of an optical cavity with typical spherical mirrors to create larger mode-areas on the mirrors, the input pointing stability requirements become more stringent in these regimes. Specially shaped beams also have their own challenges as well; controlling the manufacturing process to create satisfactory mirror profiles and alignment (including linear displacement) in small-scale optics used in optical cavities is difficult, limiting the optical quality [173].

⁴ These measurements of the loss angles of AlGaAs were performed on free-standing micro-scale structures. We present evidence in Chapter 4 that verifies that the loss angle is still valid when applied to a macroscopic coating bonded to a substrate.

3.3 Thermodynamic noise

Brownian motion is not the only thermally-driven source of effective length fluctuations in optical interferometers. For any thermodynamical system comprising a bulk material, there are temperature fluctuations whose magnitude is given by [174]

$$\langle \delta T^2 \rangle = \frac{k_B T^2}{\rho C V}. \quad (3.19)$$

Here ρ is the material density, C is the heat capacity, and V is the volume over which the temperature fluctuations are considered. In materials for which the coefficient of thermal expansion (CTE) and the thermo-refractive coefficient are non-zero, these statistical temperature fluctuations can couple to the reflected phase of the optical field by two mechanisms. The first involves both the thermo-refractive and thermal expansion response of the coating itself and is known as thermo-optic noise. Thermo-optic noise is usually restricted to describing only the coating. The second mechanism involves the thermal expansion of the substrate alone and is known as substrate thermo-elastic noise.

In the theoretical treatment of both thermo-optic and thermo-elastic noise, the general approach is to calculate the effect of the bulk fluctuations as described by Eq. 3.19 on the effective degree of freedom, x , as introduced in Section 3.2.1. The general approach is to solve the heat equation in the mirror with a Langevin driving term that reproduces equation 3.19 for an arbitrary volume [174]. The solution for the heat equation then acts as a driving term for elastic expansion, and in the case of thermo-optic noise, the thermo-refractive effect. The final solution for the spectral density of fluctuations is the net result of this process. In the case of thermo-optic noise, the thermo-refractive effect and the elastic displacement must be added coherently, because they share the same driving temperature fluctuations [175].

Substrate thermoelastic and coating thermo-optic noise have been studied as a noise source for gravitational wave detectors [176, 177, 175]. There are two Fourier frequency regimes in the analysis of thermo-optic noise. The first is where the thermal diffusion length scale is smaller than the laser spot size, allowing an averaging effect to take place. This regime is known as the adiabatic

limit and only applies to time-domain Fourier frequencies f that satisfy $2\pi f \gg \omega_c$ where the cutoff frequency, ω_c , is given by

$$\omega_c = \frac{2\kappa}{w_0^2 \rho C}. \quad (3.20)$$

Here, κ is the thermal conductivity and w_0 is the intensity $1/e^2$ radius of the laser beam. Due to the small beam sizes ($\sim 100 \mu\text{m}$) and interest in the frequency noise spectrum all the way to DC in cavity-stabilized laser systems, one must be aware that ω_c is typically in the 1 Hz range. Thus, consideration of thermo-optic noise in the semi isothermal regime, at Fourier frequencies $2\pi f < \omega_c$, is necessary for a complete picture of the various contributions to the frequency noise of cavity stabilized lasers. Typically the coating cutoff frequency and the substrate cutoff frequency are different.

3.3.1 Substrate thermoelastic noise

To date, many optical cavities have employed mirrors made from ULE substrates [40, 178]. As a result, consideration of substrate thermoelastic noise is not necessary for these systems, as the material coefficient of thermal expansion (CTE) is close to zero. This approximation has also been made in the case of fused silica substrates [179]. In fact, while alarming predictions for substrate thermoelastic noise can be obtained by extrapolating the high-frequency behavior of fused silica thermoelastic to 1 Hz-level frequencies, using the appropriate expression for the low-frequency behavior verifies that the substrate thermoelastic noise is at least an order of magnitude below the Brownian noise of the substrates and coatings in the case of fused silica. For other materials such as sapphire at room temperature, this will not be the case.

It has been shown that the one-sided power spectral density of mirror length fluctuations due to the substrate is [174, 176]

$$G_x^{\text{TE,sub}}(f) = \frac{4}{\sqrt{\pi}} \alpha_s^2 (1 + \sigma_s)^2 \frac{K_B T^2 w_0}{\kappa_s} J[\Omega(f)]. \quad (3.21)$$

Here, $\Omega(f) = 2\pi f/\omega_c^{\text{sub}}$, and $J[\Omega]$ is given by

$$J[\Omega] = \sqrt{\frac{2}{\pi^3}} \int_0^\infty du \int_{-\infty}^\infty dv \frac{u^3 e^{-u^2/2}}{(u^2 + v^2) [(u^2 + v^2)^2 + \Omega^3]}. \quad (3.22)$$

While the integral can be evaluated numerically, it is more instructive to calculate thermal noise in the low and high frequency limits. Specifically,

$$G_x^{\text{TE,sub}} \rightarrow \frac{8\sqrt{2}}{3\pi} \alpha_s^2 (1 + \sigma_s)^2 \frac{K_B T^2}{\sqrt{2\pi f \kappa_s \rho_s C_s}}, \quad \Omega \ll 1 \quad (3.23)$$

$$G_x^{\text{TE,sub}} \rightarrow \frac{16}{\sqrt{\pi}} \alpha_s^2 (1 + \sigma_s)^2 \frac{K_B T^2 \kappa_s}{(2\pi f \rho_s C_s w_0)^2}, \quad \Omega \gg 1. \quad (3.24)$$

These equations indicate that at low frequencies, thermoelastic noise rises less rapidly than extrapolated from the high-frequency behavior. Qualitatively, this effect can be explained as a crossover from the regime where the thermal diffusion length is smaller than the spot size to one where it is larger. Thus, this change in behavior can be thought of as an averaging effect that is no longer valid at low frequencies [176, 177].

3.3.2 Coating thermo-optic noise

A second way that optical cavities are sensitive to thermodynamic temperature fluctuations are through a pair of correlated mechanisms present in the mirror coatings: thermorefractive and thermoelastic effects, collectively called thermo-optic noise. Typical dielectric mirrors are made of a stack (also known as a Bragg stack) of alternating high- and low-index materials whose thicknesses are chosen such that the optical path length in each layer is $\lambda/4$, where λ is the vacuum wavelength of the optical frequency of interest. For ultra-low loss coatings comprised of alternating quarter-wave layers of SiO_2 , and Ta_2O_5 , 20 pairs of such layers will give a transmission loss of 1 ppm (see, e.g., [180]). For such a mirror, it has been shown that the typically opposite signs of these coherent mechanisms reduces their impact and the total effect can be written as [175]

$$G_x^{\text{TO}}(f) = G_{\Delta T}(f) \left(\bar{\alpha}_c d - \bar{\beta}_c \lambda - \bar{\alpha}_s d \frac{C_c}{C_s} \right)^2. \quad (3.25)$$

The term in parentheses is the coherent sum of thermoelastic and thermorefractive effects; the thermo-optic noise. The parameter $\bar{\alpha}_c$ ($\bar{\alpha}_s$) is the effective coating (substrate) coefficient of ther-

mal expansion, and $\bar{\beta}_c$ is the effective coating thermo-refractive coefficients, as defined in [175]. Modifications to the mirror Bragg stack, such as depositing an extra $1/2 \lambda$ cap on the surface (a “half wave cap”), can be used to modify $\bar{\beta}_c$ and thus in principle the thermo-refractive noise can be coherently cancelled or reduced via Bragg stack engineering [181, 182]. Table 3.3 lists thermal and thermo-optic parameters for relevant materials.

As shown in Ref. [183], the averaged thermodynamic fluctuations that contribute to coating thermo-optic fluctuations coupled through the CTE are

$$G_{\Delta T}^{\text{TO}}(\omega) = \frac{8K_B T^2 \kappa}{(\rho_c C_c)} \int_0^\infty \frac{2\pi k_\perp dk_\perp}{(2\pi)^2} \int_{-\infty}^\infty \frac{dk_z}{2\pi} \frac{k_z^2 + k_\perp^2}{a^4 (k_z^2 + k_\perp^2)^2 + \omega^2} e^{-k_\perp^2 r_0^2/2} \left(\frac{1}{1 + k_z^2 l^2} \right) \quad (3.26)$$

Here, $r_0 = w_0/\sqrt{2}$, $a = \sqrt{\kappa/(\rho_c C_c)}$ and l is the optical penetration depth in the coating and is typically $< 1 \mu\text{m}$. The rightmost term in parentheses is only present in the treatment of thermorefractive noise [183, 165], and is not present for thermoelastic coating fluctuations. However, since the penetration depth, l is much smaller than w_0 . Ignoring this term only introduces an error of order l/w_0 . This expression can therefore be written

$$G_{\Delta T}^{\text{TO}}(\omega) = \frac{2\sqrt{2}K_B T^2}{\pi\kappa\omega_0} [K(\Omega) + \mathcal{O}(l/w_0)], \quad (3.27)$$

with

$$K(\Omega) = \Re \left[\int_0^\infty du u e^{-u^2/2} \frac{\sqrt{u^2 + i\Omega}}{\sqrt{u^4 + \Omega^2}} \right]. \quad (3.28)$$

Here, $\Omega = \omega/\omega_c^{\text{coat}}$, where ω_c is the cutoff frequency defined in Eq. 3.20 applied to the coating material properties. Two important limits for $K(\Omega)$ are

$$K(\Omega) \rightarrow \sqrt{\frac{\pi}{2}}, \quad \Omega \ll 1 \quad (3.29)$$

$$K(\Omega) \rightarrow \frac{1}{\sqrt{2\Omega}}, \quad \Omega \gg 1 \quad (3.30)$$

Thus, the two corresponding limits for the temperature fluctuations are

$$G_{\Delta T}^{\text{TO}} \rightarrow \frac{2K_B T^2}{\sqrt{\pi} w_0 \kappa_c}, \quad \Omega \ll 1 \quad (3.31)$$

$$G_{\Delta T}^{\text{TO}} \rightarrow \frac{2\sqrt{2}K_B T^2}{\pi w_0^2 \sqrt{\kappa_c \rho_c C_{c\omega}}}, \quad \Omega \gg 1 \quad (3.32)$$

Material	α [ppb/K]	β [1/K]	κ [W/m-K]	$\rho \times C$ [J/m ³ -K]	n
Fused silica (SiO ₂)	2.6×10^3	8×10^{-6}	1.4	1.6×10^6	1.45
ULE glass	~ 0	NA	1.31	1.7×10^6	1.48
Ta ₂ O ₅	3.6×10^3	1.4×10^{-5}	33	2.1×10^6	2.06
Silicon (124 K)	~ 0	NA	6	8×10^5	3.96
Sapphire	6×10^3	NA	46	3.1×10^6	1.77
GaAs	5.7×10^3	3.66×10^{-4}	55	1.8×10^6	3.48
Al ₉₂ Ga ₀₈ As	5.2×10^3	1.79×10^{-4}	70	1.8×10^6	2.98

Table 3.3: Thermal and thermo-optic/optical properties of common optical materials at room temperature and at 1064 nm. The symbols are α , the thermal expansion; β , the thermo-refractive coefficient; κ , the thermal conductivity; $\rho \times C$, the per-volume heat capacity; and n , the index of refraction. Values are obtained from [165, 175, 184]. For GaAs the material properties were found from [185, 186, 187, 188, 189]. Full temperature dependent material values for many of the materials listed above can be found in [184]. The thermo-refractive coefficients of ULE, Sapphire, and silicon are not applicable to the discussion because they are not used as coating materials.

A final correction comes about due to the finite thickness of the coating. We do not go into detail here, but for large coating thicknesses, the coherence between the thermo-optic and thermo-refractive effects is reduced at higher Fourier frequencies. The effect is parameterized by a function $\Gamma(f)$ as described in Ref. [175], such that $G_x^{\text{TO}}(f) \rightarrow \Gamma(f) G_x^{\text{TO}}(f)$.

3.4 Total thermal noise contribution to cavity frequency stability

The total thermally-driven (effective) displacement noise is given by

$$G_x^{\text{tot}} = \sum_{\text{L,R}} G_x^{\text{TO}} + \sum_{\text{L,R}} G_x^{\text{TE}} + \sum_{\text{L,R}} G_x^{\text{substrate}} + \sum_{\text{L,R}} G_x^{\text{coating}} + G_x^{\text{spacer}}, \quad (3.33)$$

where the sum over left and right (L, R) takes into account that the beam waist is potentially different at the left and right mirrors. The noises directly sum because they are statistically independent.

Converting the total length fluctuation power spectral density, $G_x^{\text{tot}}(f)$, into optical frequency deviations can be accomplished by use of Equation 3.1, which directly relates fractional length change to frequency fluctuations. We obtain

$$G_\nu^{\text{tot}}(f) = \nu_0^2 G_x^{\text{tot}}(f) / L^2, \quad (3.34)$$

where L is the length of the cavity and ν_0 is the laser's optical frequency.

3.4.1 Examples of thermal noise floor

We consider several test cases utilizing two different types of cavity materials and two different types of coatings: $\text{SiO}_2/\text{Ta}_2\text{O}_5$ and $\text{GaAs}/\text{Al}_{92}\text{Ga}_8$. We perform calculation utilizing Eqs. 3.21, 3.25, 3.33, and 3.34. In order to calculate the Allan deviation from the power spectral densities, a transfer-function approach is used (see, e.g., [45] Eqn 5.12). Two spacer geometries are considered due to their relevance for future experiments. Plots of the calculated Allan deviations and frequency noise power spectral densities are shown on pages 84–89. The two cavities considered are

- **Cavity A:** The spacer 25 cm in length, cylindrical in shape, with a diameter of 10 cm. The spacer material is ULE glass, while the mirror substrates are fused silica glass, each with 1 m radius of curvature (mirror radii set the beam size on each mirror, as we show in Chapter 4). The operating wavelength is 1064 nm and we consider operation at 300 K.
- **Cavity B:** The spacer is 22 cm in length, shaped as a tapered cylinder 8 cm in diameter at its widest point. The spacer material and mirror substrates are both made from single-crystal silicon, and the mirror substrates each have 1 m radius of curvature. This design is identical to the one considered in [168] (aside from the slightly different mirror radii we utilize here for clarity). The operating wavelength is 1542 nm and the operating temperature is 124 K, so that the Si coefficient of thermal expansion is nulled as in [168].

As seen from Figs. 3.3–3.8, the use of crystalline materials at cryogenic temperatures can result in a gain of an order of magnitude of stability for thermal-noise limited performance of a cavity-stabilized laser. Also, the use of a coating half-wave cap is an effective strategy to reduce the thermo-optic noise in the mirror coatings. The thermo-optic noise manifests itself at higher frequencies, and thus does not affect the long term laser stability. However, frequency noise in this band is still important for reducing the noise in atomic clocks, as described in Chapter 2, and also for gravitational wave detectors [147].

3.5 Conclusion

In this Chapter, we explored the relevant thermal noise sources for optical cavities. As shown in the results plotted in Figs. 3.3–3.8, the cavity materials are an important factor in determining the magnitude and character of the noise. The summary given in this chapter should hopefully serve as a useful reference for future cavity designs. In the next Chapter, we describe high-precision laser stabilization using optical cavities. Using the insights developed in this chapter, we will describe the construction of four ultrastable laser systems, three of which operate at the level of 1×10^{-16} . A fourth system is described in which the new coating material described in this chapter—AlGaAs—is tested, verifying its very promising optical properties and paving the way for lasers with thermal noise-limited instability at 1×10^{-17} .

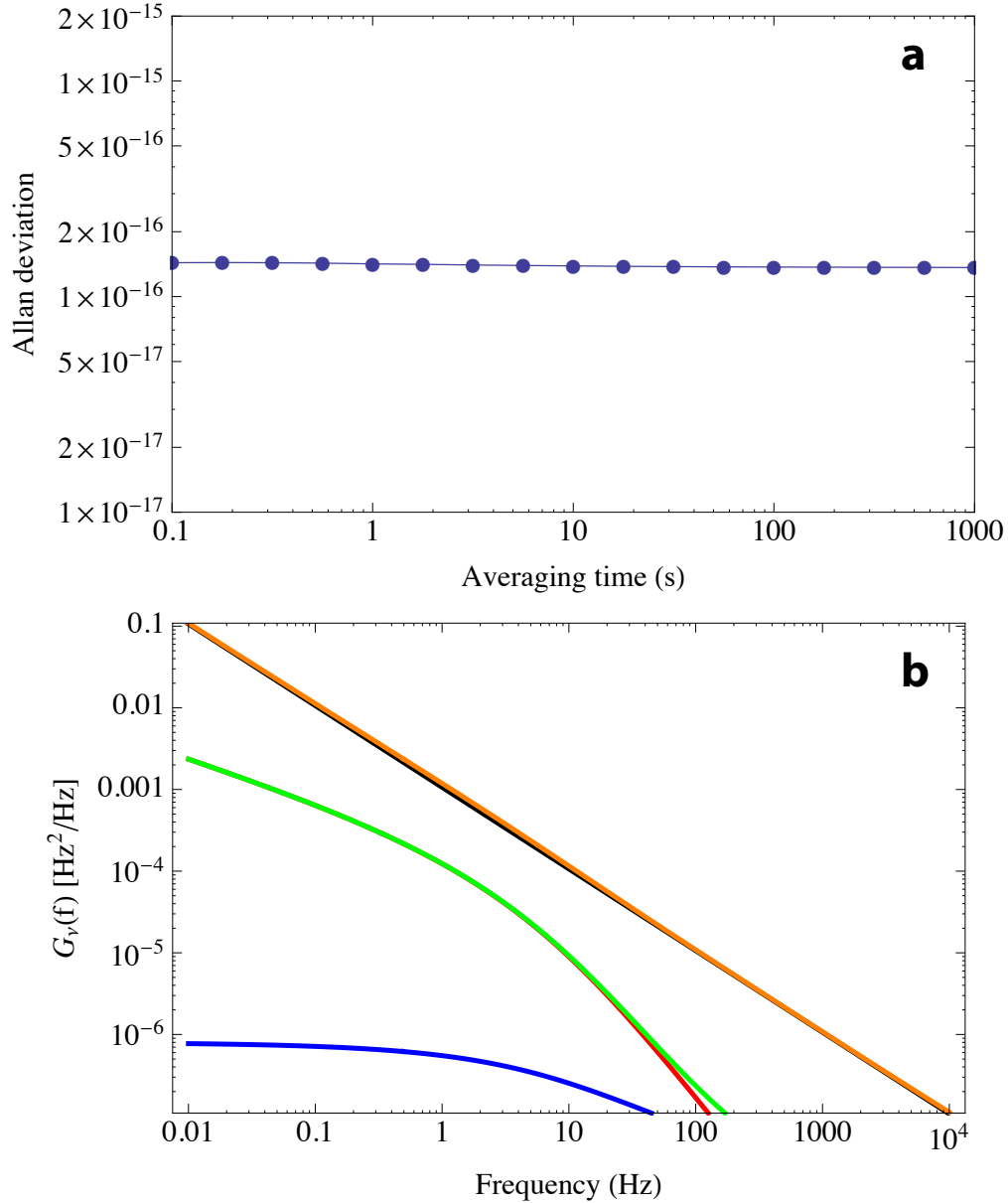


Figure 3.3: Thermal noise of cavity A with $\text{SiO}_2/\text{Ta}_2\text{O}_5$ mirrors, $T=300$ K. The Bragg stack is assumed to be 20 high/low index pairs for a coating thickness of $6 \mu\text{m}$. The beam radius at each mirror is $w_0 = 360 \mu\text{m}$. (a) Allan deviation of a laser stabilized to this cavity configuration. (b) Frequency noise power spectral density due to thermo-optic noise in the mirror coatings (blue), thermo-elastic noise in the mirror substrate (red), and Brownian noise (black). The orange curve is the sum of all these noise sources, while the green curve is the sum of only the thermo-optic and thermo-elastic noise. In this case, the coating contributes $\sim 85\%$ of the total Brownian noise. Here, the substrates contribute 13% of the Brownian noise, the coatings 84%, and the spacer 2%.

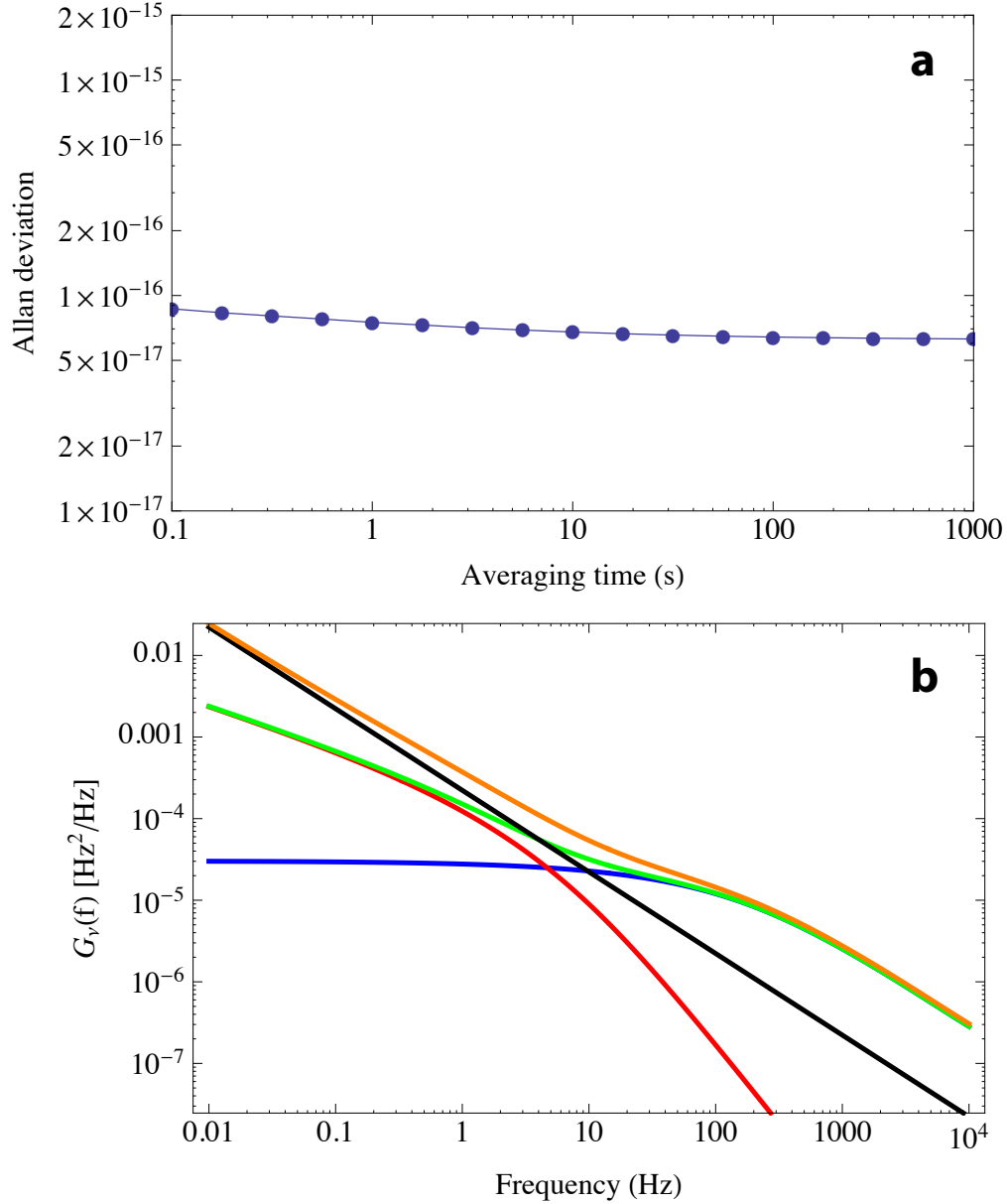


Figure 3.4: Thermal noise of cavity A with GaAs/AlGaAs mirrors, $T=300$ K. The Bragg stack is assumed to be 40 high/low index pairs for a coating thickness of $7 \mu\text{m}$. The beam radius at each mirror is $w_0 = 360 \mu\text{m}$. (a) Allan deviation of a laser stabilized to this cavity configuration. (b) Frequency noise power spectral density due to thermo-optic noise in the mirror coatings (blue), thermo-elastic noise in the mirror substrate (red), and Brownian noise (black). The orange curve is the sum of all these noise sources, while the green curve is the sum of only the thermo-optic and thermo-elastic noise. In this case, the coating only contributes $\sim 25\%$ of the total Brownian noise. Here, the substrates contribute 64% of the Brownian noise, the coatings 24%, and the spacer 12%.

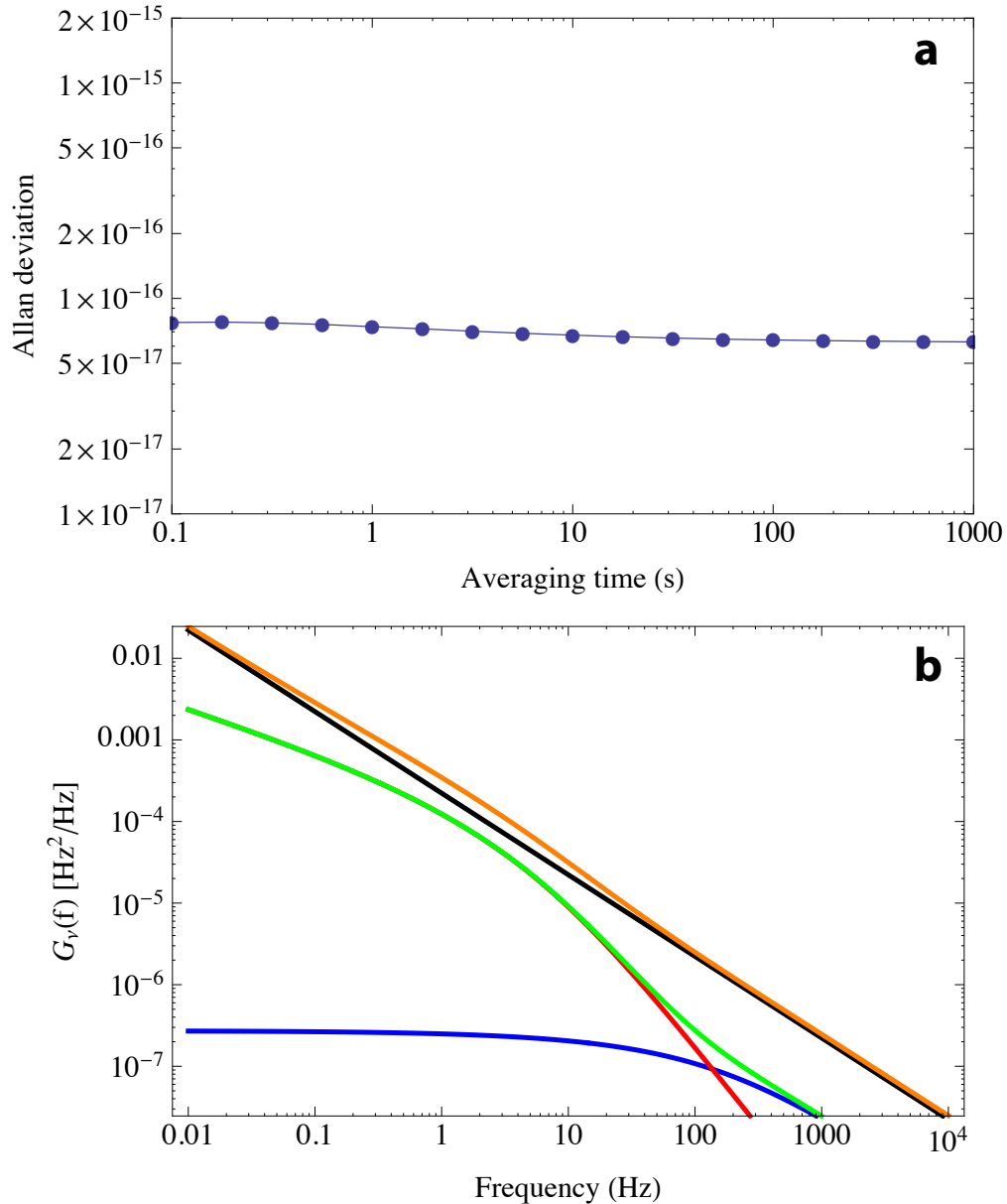


Figure 3.5: Thermal noise of cavity A with GaAs/AlGaAs mirrors and a half-wave cap, $T=300$ K. The Bragg stack is assumed to be 40 high/low index pairs for a coating thickness of $7 \mu\text{m}$. The beam radius at each mirror is $w_0 = 360 \mu\text{m}$. (a) Allan deviation of a laser stabilized to this cavity configuration. (b) Frequency noise power spectral density due to thermo-optic noise in the mirror coatings (blue), thermo-elastic noise in the mirror substrate (red), and Brownian noise (black). The orange curve is the sum of all these noise sources, while the green curve is the sum of only the thermo-optic and thermo-elastic noise. The half-wave cap dramatically reduces the thermo-optic noise contribution. Again, the substrates contribute 64% of the Brownian noise, the coatings 24%, and the spacer 12%.

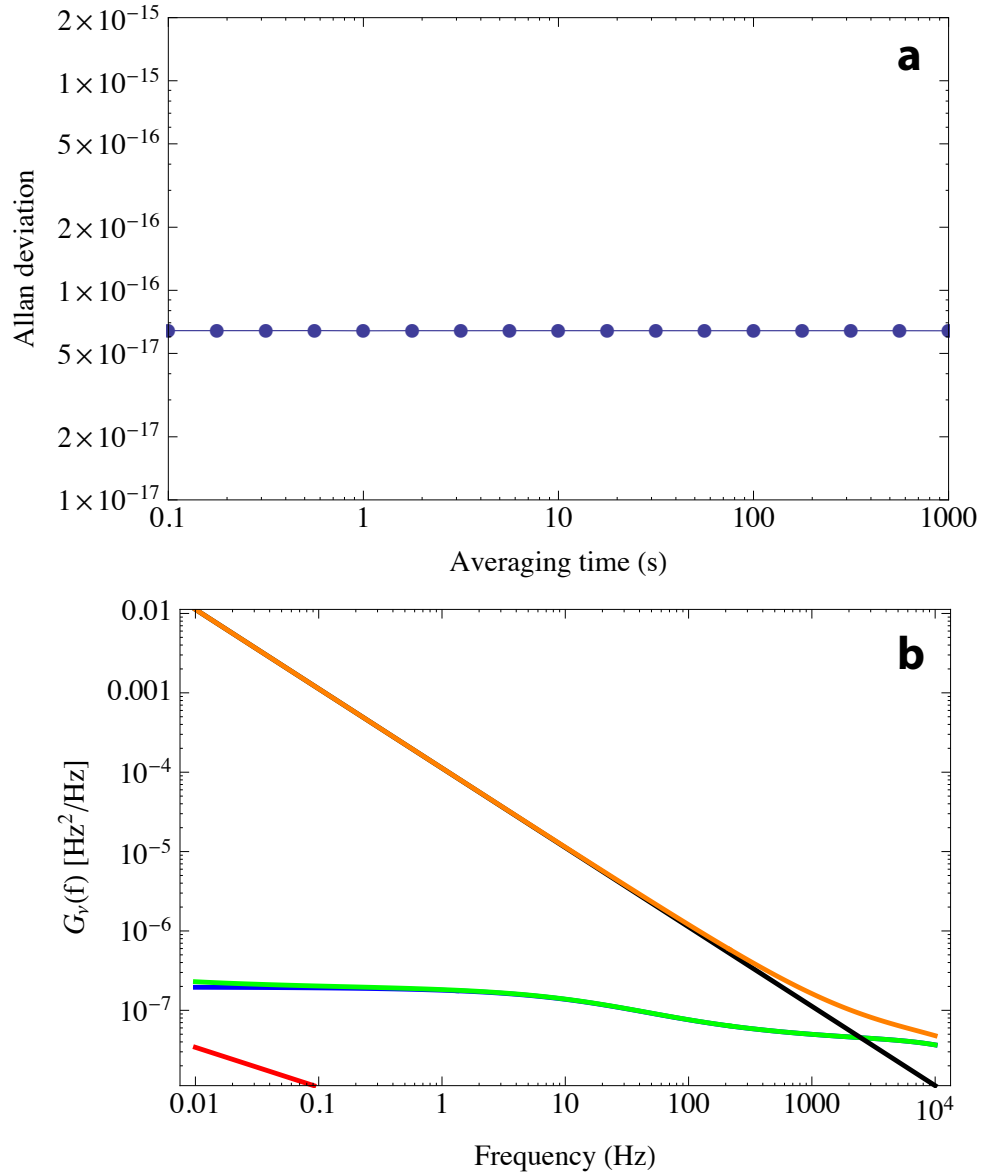


Figure 3.6: Thermal noise of cavity B with $\text{SiO}_2/\text{Ta}_2\text{O}_5$ mirrors, $T = 124$ K. The Bragg stack is assumed to be 20 high/low index pairs for a coating thickness of $9 \mu\text{m}$. $w_0 = \mu\text{m}$. The beam radius at each mirror is $w_0 = 415 \mu\text{m}$. (a) Allan deviation of a laser stabilized to this cavity configuration. (b) Frequency noise power spectral density due to thermo-optic noise in the mirror coatings (blue), thermo-elastic noise in the mirror substrate (red), and Brownian noise (black). The orange curve is the sum of all these noise sources, while the green curve is the sum of only the thermo-optic and thermo-elastic noise. Over 99% of the Brownian noise arises from the coatings.

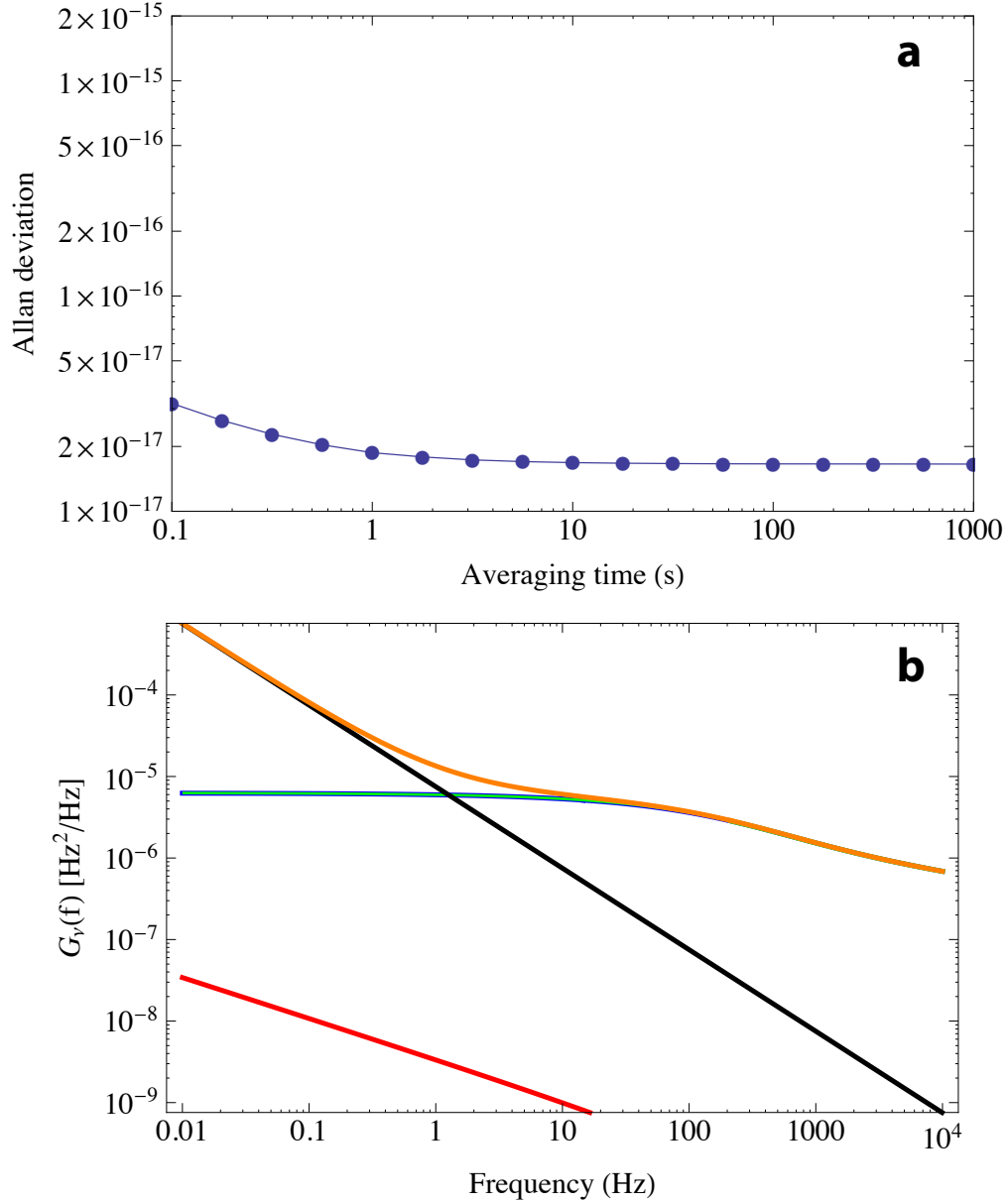


Figure 3.7: Thermal noise of cavity B with GaAs/AlGaAs mirrors, $T = 124$ K. Since the AlGaAs parameters are not well-known, extrapolated values based on the literature were used in the calculation. The Bragg stack is assumed to be 40 high/low index pairs for a coating thickness of $10 \mu\text{m}$. $w_0 = \mu\text{m}$. The beam radius at each mirror is $w_0 = 415 \mu\text{m}$. (a) Allan deviation of a laser stabilized to this cavity configuration. (b) Frequency noise power spectral density due to thermo-optic noise in the mirror coatings (blue), thermo-elastic noise in the mirror substrate (red), and Brownian noise (black). The orange curve is the sum of all these noise sources, while the green curve is the sum of only the thermo-optic and thermo-elastic noise. The thermal fluctuation noise is dominated by the thermo-optic noise, as the temperature is chosen to be near the CTE null for silicon, which also nulls the substrate thermo-elastic noise. Even with the high-Q crystalline coatings, 98% of the Brownian noise is due to the coatings.

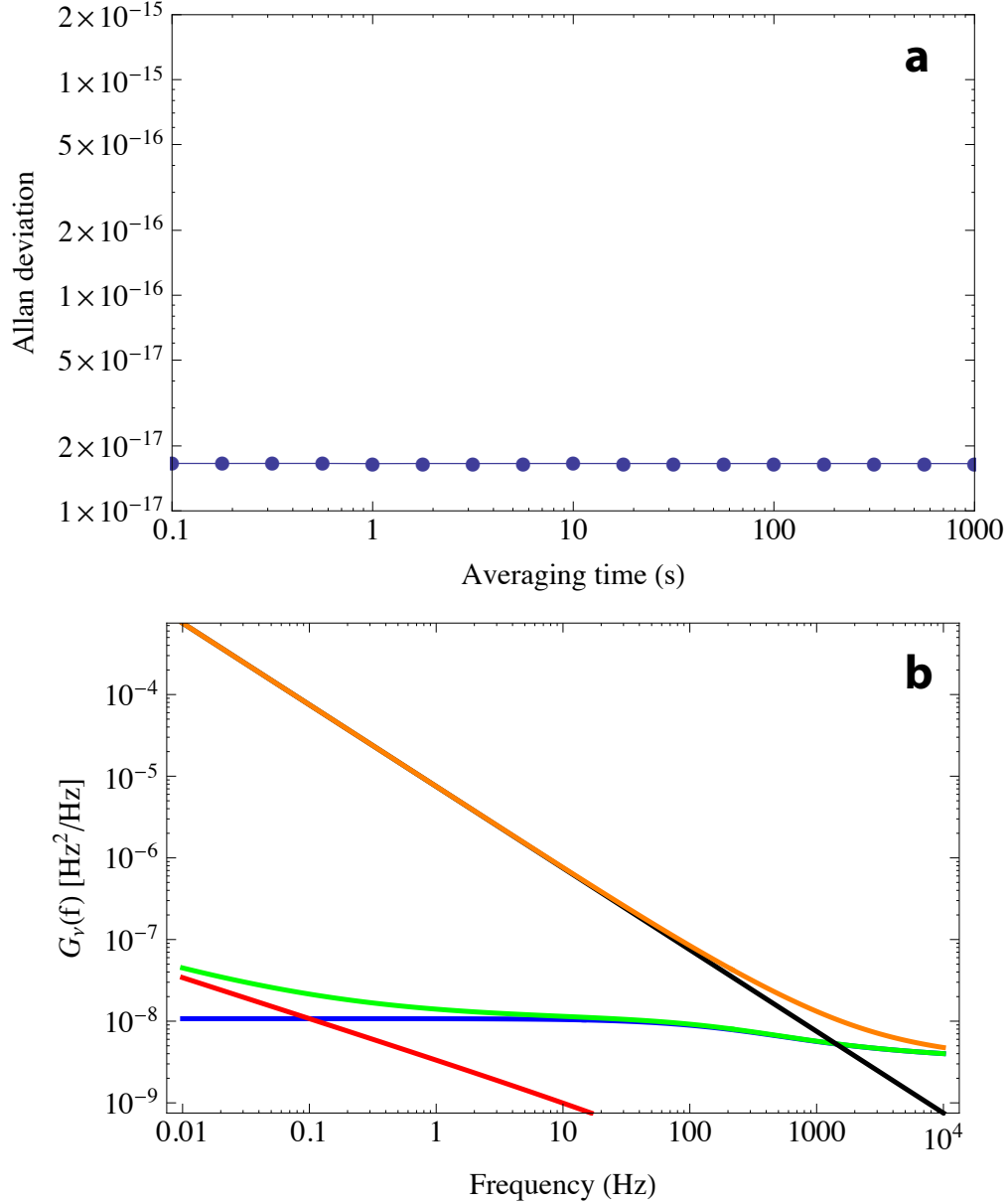


Figure 3.8: Thermal noise of cavity B with GaAs/AlGaAs mirrors and an additional half-wave cap, $T = 124$ K. Since the AlGaAs parameters are not well-known, extrapolated values based on the literature were used in the calculation. The Bragg stack is assumed to be 40 high/low index pairs for a coating thickness of $10 \mu\text{m}$. The beam radius at each mirror is $w_0 = 415 \mu\text{m}$. (a) Allan deviation of a laser stabilized to this cavity configuration. (b) Frequency noise power spectral density due to thermo-optic noise in the mirror coatings (blue), thermo-elastic noise in the mirror substrate (red), and Brownian noise (black). The orange curve is the sum of all these noise sources, while the green curve is the sum of only the thermo-optic and thermo-elastic noise. The thermal fluctuation noise is dominated by the thermo-optic noise, as the temperature is chosen to be near the CTE null for silicon, which also nulls the substrate thermo-elastic noise. Again, the addition of the half-wave cap dramatically reduces the thermo-optic contribution. Again, even with the high-Q crystalline coatings, 98% of the Brownian noise is due to the coatings.

Chapter 4

High-precision laser stabilization with optical cavities

As discussed in Chapter 2, ultrastable lasers are central to the operation of atomic clocks. Importantly, the most precise optical lattice clocks in existence today are limited by the noise of these lasers, which arises from thermally-driven fluctuations of the optical cavities to which they are stabilized. This chapter gives a detailed description of the technology required for high-precision laser stabilization and describes the development of three ultrastable laser systems that perform at the level of 1×10^{-16} . Additionally, we describe a new coating technology and present experimental results that show that the 1×10^{-17} level of laser stabilization is within reach. Finally, we briefly summarize key results with optical frequency combs, as they will play an essential role in transferring the stability of ultrastable lasers that operate in the near-IR wavelength region to the visible spectrum.

4.1 Introduction

Optical cavities are extremely useful devices in laser-based research. Within the context of precision measurement, they enable tests of the laws that govern the macroscopic structure of the universe, embodied in the search for gravitational waves [147]. At the other end of the length scale, cavity-stabilized lasers are powerful tools for precision spectroscopy that probes nature at the quantum mechanical level, through tests quantum electrodynamics [190]. Furthermore, cavities enable high-sensitivity broadband spectroscopy [191], which has practical applications in trace gas sensing; exploration of new light-matter interaction regimes in cavity QED [192]; tests of

fundamental physical principles including relativity [193, 194, 195], local position invariance [196], and the time invariance of the fundamental constants of nature [61]; and nonlinear optics, including coherent light build-up for studies of extremely nonlinear effects [51, 52]. In general, optical cavities have become indispensable tools at the heart of many modern experiments.

As discussed in Chapters 1 and 2, cavity-stabilized laser systems have enabled the development of highly precise frequency standards based on neutral atoms [197, 198, 199, 200, 31, 32] and trapped ions [201, 202, 203, 28]. In recent years, several ion-based standards [57, 27, 30, 29], and neutral atom clocks [31, 32, 33] have surpassed the fractional frequency uncertainty of the primary cesium frequency standards that define the SI second [204, 205].

Accuracy is not the only benefit of optical standards; ultrastable lasers paired with ultranarrow atomic transitions in the optical domain have allowed the realization of optical clocks that are orders of magnitude more stable than current microwave-based frequency references, with the ^{87}Sr clock now operating at $3 \times 10^{-16}/\sqrt{\tau/1 \text{ s}}$ [43], and which we discuss in this chapter. With increased stability, highly precise measurements of intricate physical effects can be made in short periods of time. For example, in Chapter 5, we will explore collisional effects between ultracold at the 10^{-17} level. This precision can now be attained within a few thousand seconds due to a 10-fold improvement of the Sr clock laser, which we describe in detail in this chapter.

As discussed in Chapter 3, thermal fluctuations set the ultimate limit to the stability of a given interferometer. The desire to further improve the stability of optical clocks will continue to drive advances in cavity-stabilized laser systems, and the next milestone will be a laser with thermal noise-limited fractional stability at 10^{-17} . In this chapter, we also discuss exciting new results that indicate that this regime should be within reach.

We begin this chapter by reviewing the basics of optical cavities and Pound-Drever-Hall (PDH) laser frequency locking. We then proceed to a detailed discussion of cavity design considerations, which are applied to several systems.

4.2 Review of optical cavities

A basic optical cavity is formed by an array of two opposite-facing mirrors (Figure 4.1). For high-precision frequency stabilization, these mirrors are typically held apart by a rigid spacer and are kept under vacuum to eliminate a varying intra-cavity index of refraction due to air. Although more complicated cavity geometries exist, including ring-type cavities (*e.g.* a cavity formed from a triangular mirror configuration) where the optical field is a running wave, we consider only this basic configuration as it is most common for precision frequency stabilization. For an incident laser of electric field amplitude E_{inc} , the steady-state electric field inside such a cavity, E_{SS} , is obtained by enforcing the condition

$$E_{\text{SS}} = E_{\text{SS}}e^{i\varphi}R + E_{\text{inc}}\sqrt{\mathcal{T}}. \quad (4.1)$$

Here, φ is the round-trip phase accumulated by the light, \mathcal{T} is the mirror intensity transmission coefficient and R is the corresponding reflectivity. In the absence of mirror absorption and scatter, it is possible to relate the magnitude of the R and \mathcal{T} coefficients by $R + \mathcal{T} = 1$. However, we choose to allow for the real-world situation, where mirror losses are influential, by leaving these distinct. The cavity phase shift, φ , can be re-written in terms of the cavity length, L , and the laser's optical frequency, $\omega = 2\pi\nu$, as¹

$$\varphi = \frac{2L\omega}{c} + \tilde{\varphi}_{m,n}. \quad (4.2)$$

The term $\tilde{\varphi}_{m,n}$ is due to an additional mode-dependent diffraction phase term and is given by

$$\tilde{\varphi}_{m,n} = -2(m+n+1)\Delta\zeta. \quad (4.3)$$

Here, the indices m and n label higher-order transverse modes (*e.g.*, TEM01, TEM11, TEM02, etc.), while for the TEM00 (Gaussian) mode, $m = n = 0$. $\Delta\zeta$ is the differential Gouy phase, which is given by

$$\Delta\zeta = \tan^{-1}(z_2/z_0) - \tan^{-1}(z_1/z_0) \quad (4.4)$$

¹ We also note that the cavity length, L , includes the effects of optical field penetration into the mirror coating, which typically requires a correction to the physical length on the order of an optical wavelength. For macroscopic cavities, this effect is negligible, but it becomes important for cavities whose size is of the order of an optical wavelength [180].

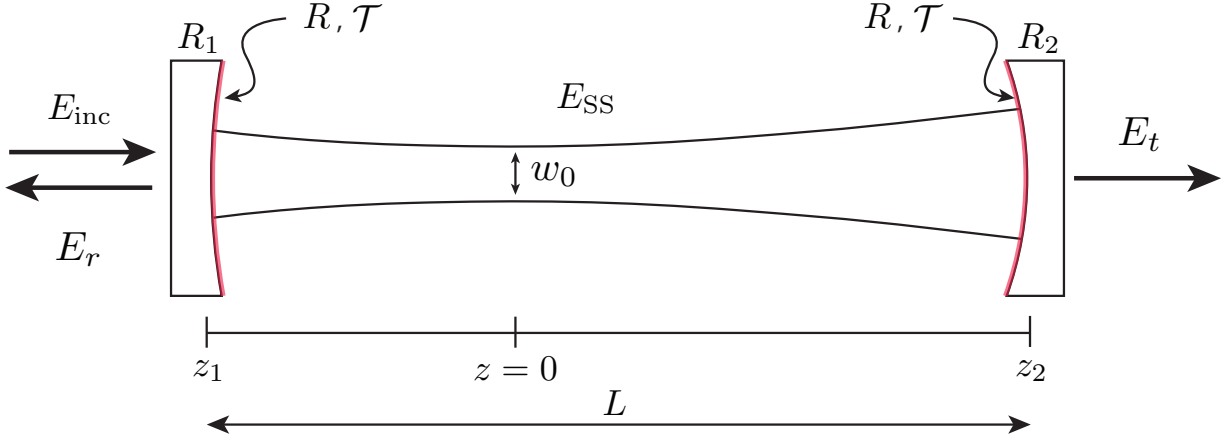


Figure 4.1: Schematic of an optical cavity in the standing wave configuration. The mirror amplitude reflectivity and transmission coefficients are given by r and t , respectively. E_{SS} is the steady-state electric field for a given incident field, E_i . Some of E_i is transmitted as E_t , while some is reflected as E_r . For simplicity, we assume the mirror properties are identical.

where $z_{2(1)}$ is the position of right (left) mirror and z_0 is the Rayleigh range of the stable mode within the optical cavity, whose waist is defined to occur at position $z = 0$. In general, for a resonator comprised of a pair of opposite-facing, concave, spherical mirrors, the Rayleigh range is given by [206],

$$z_0^2 = \frac{d(R_1 - L)(R_2 - L)(R_2 + R_1 - L)}{(R_2 + R_1 - 2L)^2}, \quad (4.5)$$

which is related to the beam waist at the center of the cavity as

$$w_0 = \sqrt{\frac{\lambda z_0}{\pi}}, \quad (4.6)$$

where, as usual, w_0 is the $1/e^2$ intensity radius. It can also be shown that [207]

$$\frac{z_1}{z_0} = -\sqrt{\frac{L(R_2 - L)}{(R_1 - L)(R_2 + R_1 - L)}} \quad (4.7)$$

and similarly

$$\frac{z_2}{z_0} = \sqrt{\frac{L(R_1 - L)}{(R_2 - L)(R_2 + R_1 - L)}}, \quad (4.8)$$

allowing us to find the beam waist at the end mirrors as

$$w(z_{1(2)}) = w_0 \sqrt{1 + \left(\frac{z_{1(2)}}{z_0}\right)^2}. \quad (4.9)$$

Commonly, $R_1 = R_2 = R_0$ and thus

$$\Delta\zeta = 2 \tan^{-1} \left(\sqrt{\frac{L}{2R_1 - L}} \right). \quad (4.10)$$

By solving Equation 4.1 for the steady-state field, we find that the transmitted field amplitude, given by $E_t = \sqrt{\mathcal{T}}E_{\text{SS}}$ is

$$\frac{E_t(\omega)}{E_{\text{inc}}(\omega)} = \frac{e^{i\varphi/2}\mathcal{T}}{1 - e^{i\varphi}R}. \quad (4.11)$$

Similarly, the reflected field, E_r , is given by

$$\frac{E_r(\omega)}{E_{\text{inc}}(\omega)} \equiv \mathcal{R}(\omega) = r \left[\frac{1 - e^{i\varphi}(\mathcal{T} + R)}{1 - e^{i\varphi}R} \right]. \quad (4.12)$$

The cavity reflection transfer function, $\mathcal{R}(\omega)$, is plotted in Fig. 4.2. As can be seen from Equations 4.11 and 4.12, the transmission (reflection) is maximized (minimized) when the round trip phase is a multiple of 2π . When this condition is met, the cavity is said to be on resonance. This results in the resonance condition

$$\nu_q = \left[q + (1 + n + m) \frac{\Delta\zeta}{\pi} \right] \frac{c}{2L}, \quad (4.13)$$

where q is the longitudinal mode index, L is the distance separating the mirrors, c is the speed of light, and $\Delta\zeta$ is given by Eq. 4.4. We note that there are geometrical configurations of the cavity such that $\Delta\zeta$ is a rational multiple of π . In these configurations, it is easy to see that there will be accidental frequency degeneracies of modes. One such example is the confocal geometry, where $R_0 = d$. Here, every even mode (i.e., $m + n$ is even) is frequency degenerate with the TEM₀₀ mode. Another example is $R_0 = 2d$, which results in degeneracy for every third higher-order mode. It should be stressed that these accidental frequency degeneracies should be avoided, as exact degeneracies are unlikely, but line-pulling due to near-degeneracies is a possibility and can be problematic.

From Eq. 4.13, it is obvious that the longitudinal modes are spaced in frequency by $c/2L$, a quantity known as the free spectral range (FSR). By analyzing the denominator of Eq. 4.12, the width of the cavity resonance in units of intensity (i.e. the width of a dip in $|\mathcal{R}|^2$), denoted as

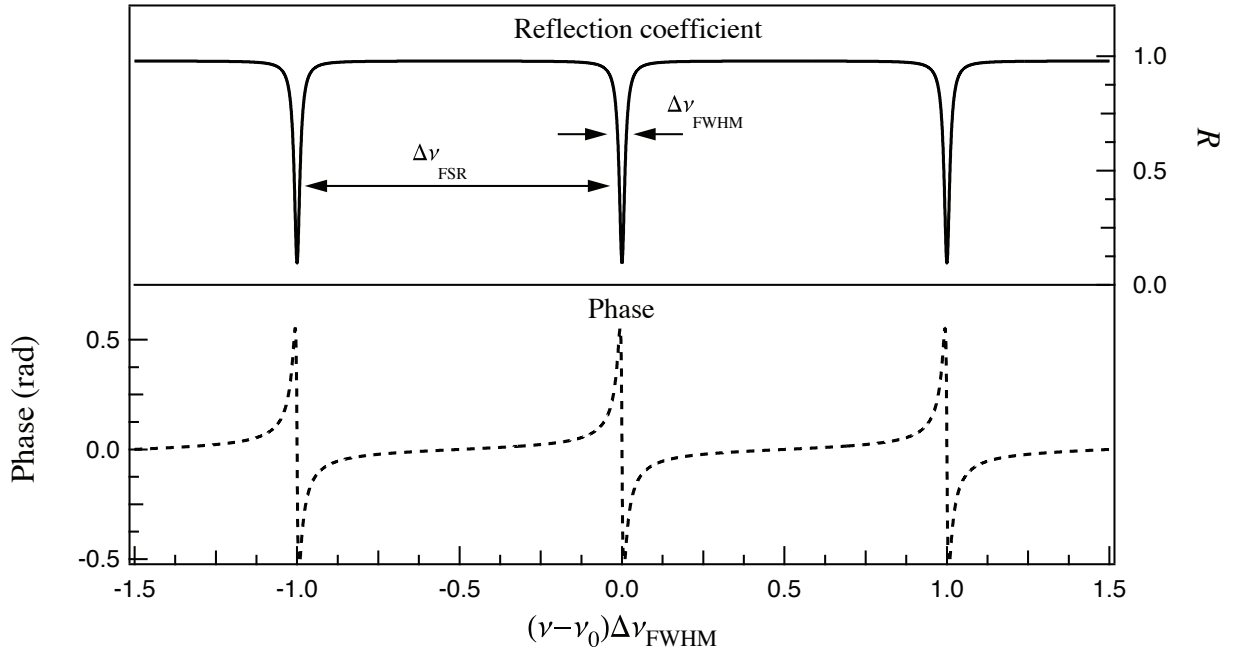


Figure 4.2: Reflection coefficient and corresponding phase shift of the reflected light incident upon an optical cavity. If there are no mirror losses, there is a discontinuity in phase as the reflected light drops to zero. Here, a small mirror loss term has been included, causing the reflection dip to not reach zero.

$\Delta\nu_{\text{FWHM}}$, is related to the FSR by

$$\mathcal{F} = \frac{\Delta\nu_{\text{FSR}}}{\Delta\nu_{\text{FWHM}}} = \frac{\pi r}{1 - r^2} = \frac{\pi\sqrt{R}}{1 - R} \simeq \frac{\pi}{1 - R}, \quad (4.14)$$

where the last equality is accurate if $\mathcal{F} > 100$. This ratio, \mathcal{F} , is known as the cavity finesse and, as Eq. 4.14 shows, depends only on the mirror reflectivity.

4.2.1 Measuring Finesse

In order to measure the finesse of an optical cavity, one approach is simply to scan a tunable laser across the cavity resonances as depicted in Fig. 4.2 and measure the width of the resonance dips. However, for very high finesse cavities, this is not a feasible approach as the resonance dip can be extremely narrow with respect to the FSR and even with respect to the laser linewidth.

The general approach used to circumvent this problem is to use a time-domain measurement. Quite generally, if an oscillatory system loses energy at a rate proportional to the amount of energy stored, then the associated time dynamics are exponentially decaying such that $U(t) = U_0 e^{-t/\tau}$, where $U(t)$ is the energy stored. Many physical systems can be described in this way. We then associate a field, $u(t)$, with the stored energy $U(t)$, such that $U(t) = |u(t)|^2$. The time dynamics of $u(t)$ are then [154]

$$u(t) = u_0 e^{i\omega_0 t - t/(2\tau)}, \quad (4.15)$$

and the transfer function of the system is given by

$$|H(\omega)|^2 \propto \frac{1}{1 + 4(\omega - \omega_0)^2 \tau^2}. \quad (4.16)$$

Thus, the FWHM of the resonance in frequency is given by

$$\Delta\nu_{\text{FWHM}} = 1/(2\pi\tau). \quad (4.17)$$

The decay constant τ is related to the quality factor, Q , as

$$Q = \nu_0/\Delta\nu_{\text{FWHM}} = \omega_0\tau. \quad (4.18)$$

The Q -factor can also be understood as the rate of stored energy loss divided by ω_0 .

In an optical cavity we can calculate τ very easily. We assume that in a time L/c , the stored energy will have been reduced by $(1 - R)$. This implies that the intensity loss rate is given by $1/\tau = (1 - R)c/L$ such that

$$\frac{dI}{dt} = -\frac{(1 - R)c}{L} I \quad (4.19)$$

We can thus calculate the finesse by noting that $\Delta\nu_{\text{FWHM}} = c/(2L\mathcal{F}) = 1/(2\pi\tau)$. We thus find that

$$\mathcal{F} = \frac{\pi c\tau}{L}. \quad (4.20)$$

Equation 4.20 implies that finding the photon decay time of the optical cavity allows a determination of the cavity finesse, assuming the length is well-characterized. One way to measure τ is to stabilize a laser to the optical cavity under test and then very quickly switch off the power.

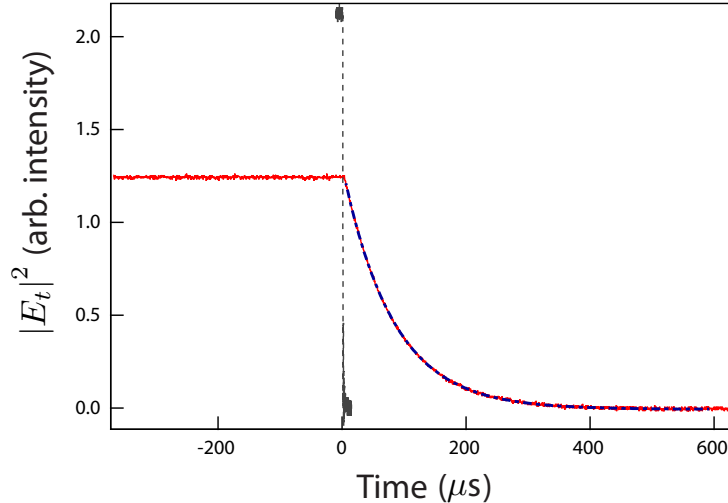


Figure 4.3: Measurement of cavity photon storage lifetime. Here, a laser was actively stabilized to the optical cavity and its power abruptly extinguished. The red solid trace is the intensity ringdown data with an exponential fit (dash-dotted line). The agreement between the measured data and the exponential fit is excellent. Also shown is the combined response time of the detector and optical power switching (dashed grey line). The photon storage time is found to be $\tau = 81.3(1) \mu\text{s}$.

This method assumes that the laser stabilization has already been achieved—making this method technologically complicated—but the results are exceedingly easy to interpret. Figure 4.3 shows an example of such a procedure. Here, a laser was locked to a high-finesse optical cavity of length $L = 39.4 \text{ cm}$ (which we will later describe in detail) and a ringdown time of $\tau = 81.3(1) \mu\text{s}$ was measured. This results in a finesse of $\mathcal{F} = 194,000$.

In many instances, it is desirable to make a finesse measurement without the added complications of locking. An alternative approach is to sweep the laser frequency across the cavity resonance and record either the transmitted or reflected time-domain signal. However, when the laser stays near the cavity resonance for a duration that is comparable to the photon storage time, interference effects can emerge which make interpreting the signal difficult. Specifically, the field inside the optical cavity given by $E(t)$ can be described by a simple differential equation for a linearly swept laser [208] as

$$\frac{dE}{dt'} = -(1 - i\tilde{\nu}t') E + i\eta. \quad (4.21)$$

Here $t' = t/\tau_s$ is the time normalized by the field ringdown time (as opposed to the intensity ringdown time) where $\tau_s = 2\tau$. The constant η is the drive rate, given by $\eta = \sqrt{\mathcal{T}}\mathcal{F}E_i/\pi$ (here \mathcal{T} is the input mirror transmission as in Fig. 4.1). The sweep rate is parameterized by $\tilde{\nu}$, where

$$\tilde{\nu} = \frac{2\mathcal{F}d\dot{\omega}\tau_s}{\pi c}, \quad (4.22)$$

with the laser frequency sweep rate denoted by $\dot{\omega}$ (in units of radians/s²). Here, $t' = 0$ when the laser is on resonance with the cavity.

While Eq. 4.21 is trivially solved numerically, it turns out that closed-form solutions exist for any initial condition. In the limit that the laser sweep starts far off resonance and we ignore all other cavity modes, the solution for the reflected and transmitted power are

$$|E_r(t)|^2 = |E_i|^2 \left| 1 - \frac{\beta}{\sqrt{\tilde{\nu}}} \left[\sqrt{\frac{\pi}{2i}} e^{-t' + i\tilde{\nu}t'^2/2 - i/(2\tilde{\nu})} + \sqrt{2i} D\left(\frac{i + t'\tilde{\nu}}{\sqrt{2i\tilde{\nu}}}\right) \right] \right|^2 \quad (4.23)$$

and

$$|E_t(t)|^2 = \frac{\beta^2 |E_i|^2}{\tilde{\nu}} \left| \sqrt{\frac{\pi}{2}} e^{-t' + i\tilde{\nu}t'^2/2 - i/(2\tilde{\nu})} + i\sqrt{2} D\left(\frac{i + t'\tilde{\nu}}{\sqrt{2i\tilde{\nu}}}\right) \right|^2. \quad (4.24)$$

Here, $D(x)$ is the Dawson integral², and β is the cavity contrast parameter, given by

$$\beta = \mathcal{T}/(1 - R). \quad (4.25)$$

On cavity resonance, the fraction of transmitted power is β^2 while the fraction of reflected power is $(1 - \beta)^2$. The closed-form solutions to Eq. 4.21 facilitate extracting τ from swept-laser ringdown measurements. As an example of a swept-laser cavity finesse measurement, Eqs. 4.24 and 4.23 were used to fit time-domain transmission and reflection signals from two different optical cavities. As seen in Fig. 4.4, the agreement with the data is excellent.

The reason \mathcal{T} and R typically differ is due to absorption or scatter in the mirror coatings, leading to extra losses beyond those due to light exiting the cavity through transmission (see e.g., [180]). Measurements of β and cavity finesse allow T and R to be extracted. In steady-state, the

² The Dawson integral is $D(x) = e^{-x^2} \int_0^x e^{\xi^2} d\xi$ and is built into Mathematica as the DawsonF function.

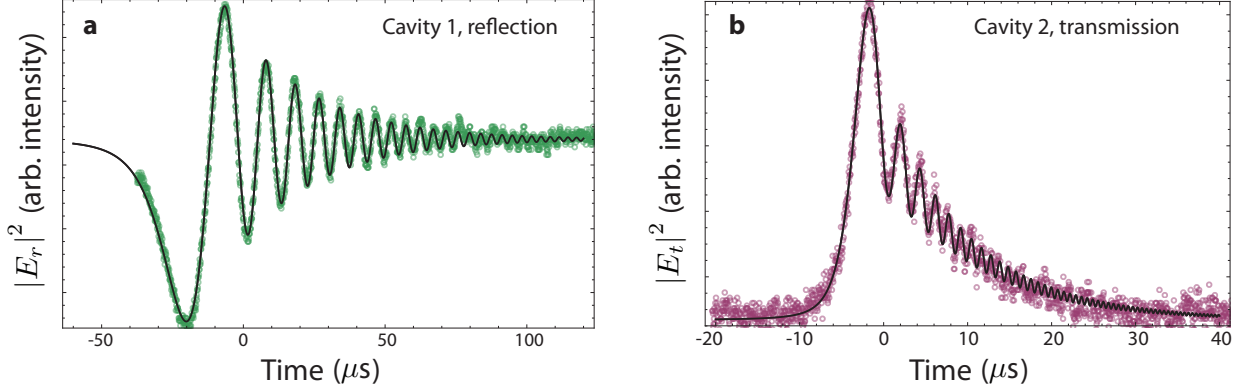


Figure 4.4: Measurement of photon storage time with a swept-frequency optical field. **(a)** Time-domain signal of the reflected optical power from a swept ringdown measurement of the cavity presented in [40]. Here the photon storage time is 14 μs , indicating a finesse of 180,000 **(b)** Swept-frequency transmission signal of the cavity presented in [56]. Here, the photon storage time is 10 μs , indicating the finesse is 280,000.

power that enters the cavity is related to the power leaving the cavity and the total input power, P_0 by

$$P_{\text{in}} = P_0 [1 - (1 - \beta)^2] \text{ and } P_{\text{out}} = P_0 \beta^2. \quad (4.26)$$

We can solve for β as

$$\beta = \frac{2}{1 + P_{\text{in}}/P_{\text{out}}}. \quad (4.27)$$

Thus, a simple measurement of P_{in} , P_{out} , and cavity photon storage lifetime is sufficient to determine the mirror properties.

4.2.2 Pound-Drever-Hall Locking

As seen in the previous section, an optical cavity defines a series of narrow resonances in the frequency domain. A common way to stabilize a laser to such a resonance is through a frequency modulation locking technique. The most commonly used and successful frequency modulation technique for laser stabilization is the Pound-Drever-Hall (PDH) stabilization scheme [209], where the frequency modulation is performed at a much higher frequency than the cavity linewidth.

There are several reasons for the widespread adoption of PDH locking. First, there are no

restrictions upon the phase modulation frequency, as long as it is larger than the cavity linewidth. A higher modulation frequency gives the lock immunity to common laser amplitude noise offsets and also permits the use of resonant electro optic modulators (EOMs). Additionally, in the PDH scheme, the lock bandwidth is not restricted by the cavity linewidth, allowing extremely narrow cavity resonance features to provide high-bandwidth stabilization.

Given the reflection spectrum of Fig. 4.2, one could imagine that a very simple locking scheme would be to slowly frequency modulate the probing beam and use this signal to determine where on the reflection dip the laser frequency lies. However, one main reason **not** to take this approach for high-finesse cavities is that laser relative intensity noise (RIN) increases at lower frequencies, in addition to electronic noise floors. These amplitude fluctuations would contaminate the locking signal, affecting the lock stability. Additionally, the lock bandwidth would be severely limited.

One way around this noise problem is to increase the laser modulation frequency well above the cavity bandwidth and beyond the spectral region with significant laser amplitude noise. In this configurations, it is best to think of the laser electric field distributed as shown in Fig. 4.5. When the modulation sidebands are well outside the cavity transmission bandwidth, the PDH locking configuration [209].

Several reviews of PDH locking and laser feedback control theory exist [210, 211, 212, 213]. Here, we briefly discuss the important results of the PDH locking technique. In order to measure the PDH error signal from an optical cavity, the laser must first be phase modulated. A phase modulated signal can be decomposed into a carrier and sidebands using the Jacobi-Anger expansion [214]:

$$E_0 e^{-i\omega_0 t - i\Delta\varphi \sin(\Omega t)} = E_0 J_0(\Delta\varphi) e^{-i\omega_0 t} + E_0 \sum_{n=1}^{\infty} J_n(\Delta\varphi) \left[e^{-i(\omega_0 + n\Omega)t} + (-1)^n e^{-i(\omega_0 - n\Omega)t} \right]. \quad (4.28)$$

Here, the term $\Delta\varphi$ is the phase modulation (PM) depth and Ω is the PM frequency. From this expansion, it is clear that the first order sidebands are 180 degrees out of phase (as are all odd order sidebands), as pictured in Figure 4.5. When the PM frequency is well outside the cavity

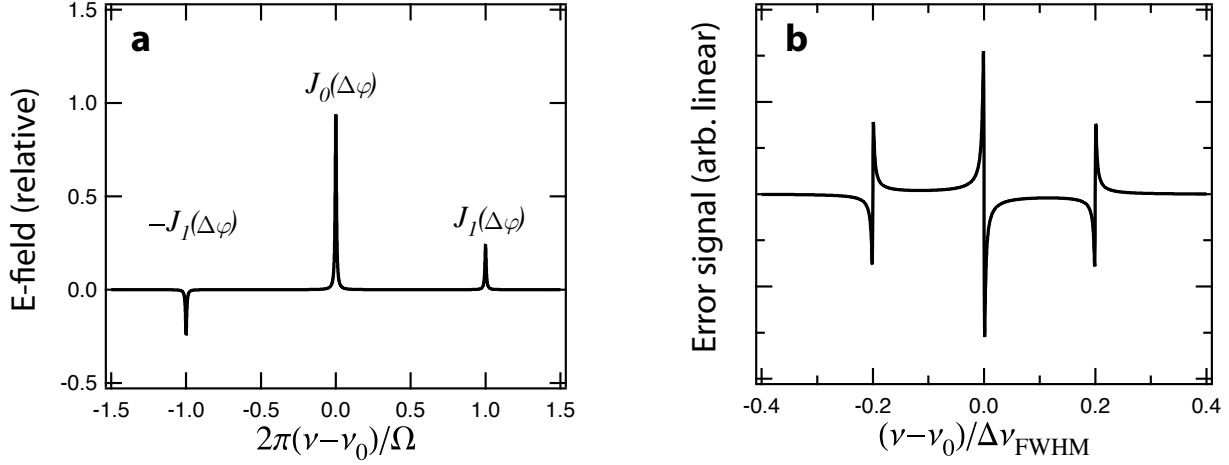


Figure 4.5: Pound-Drever-Hall sidebands and error signal. **(a)** Electric field amplitude in Fourier space in the presence of phase modulation of depth $\Delta\varphi$. **(b)** Pound-Drever-Hall error signal as a function of laser detuning from the cavity resonance.

bandwidth, these sidebands are sufficiently detuned from the cavity resonance such that they are promptly reflected from the cavity unaffected. The carrier, which is near the cavity resonance, is affected by the complex response of the cavity (as shown in Figure 4.2 and given in Equation 4.12) and interferes with the PM sidebands upon reflection.

This interference term can be explored by assuming that the PM sidebands are completely reflected and finding the time-dependent reflected optical power, $P_{\text{ref}}(t)$, when the carrier is near resonance. Making use of only the first order sidebands of Equation 4.28,

$$\begin{aligned} P_{\text{ref}}(t) &= \frac{1}{2} \left| E_{c, \text{ref}} + E_s e^{-i\Omega t} - E_s e^{i\Omega t} \right|^2 \\ &= P_{c, \text{ref}} + 2P_s - 2\text{Im} \{ E_{c, \text{ref}} E_s^* \} \sin(\Omega t) + 2\Omega \text{ terms}. \end{aligned} \quad (4.29)$$

Here, $E_{c, \text{ref}}$ ($P_{c, \text{ref}}$) is the reflected electric field amplitude (power) in the carrier and E_s (P_s) is the reflected electric field amplitude (power) in the sidebands. Keeping everything that oscillates at Ω or below, and making use of Equations 4.28 and 4.12,

$$\begin{aligned} P_{\text{ref}}(t) &= P_0 [J_0^2(\Delta\varphi) |\mathcal{R}|^2 + 2J_1^2(\Delta\varphi)] \\ &\quad + 4P_0 J_0(\Delta\varphi) J_1(\Delta\varphi) \text{Im} \{ \mathcal{R} \} \sin(\Omega t). \end{aligned} \quad (4.30)$$

When the carrier is less than a cavity linewidth from resonance,

$$\text{Im}\{\mathcal{R}\} \simeq \frac{-2\beta\mathcal{F}}{\Delta\nu_{\text{FSR}}}\delta\nu \quad (4.31)$$

Here, $\delta\nu$ is the laser detuning from cavity resonance given by $\delta\nu = \nu_{\text{laser}} - \nu_{\text{cavity}}$ and β the cavity contrast parameter defined in Eq. 4.25. The term in equation 4.30 that oscillates as $\sin(\Omega t)$, is thus given by

$$\mathcal{D}\delta\nu \sin(\Omega t), \quad (4.32)$$

where we have used the definition

$$\mathcal{D} \equiv -\frac{8\beta P_0 J_0(\Delta\varphi) J_1(\Delta\varphi)}{\Delta\nu_{\text{FWHM}}}, \quad (4.33)$$

along with the relationship $\Delta\nu_{\text{FSR}}/\mathcal{F} = \Delta\nu_{\text{FWHM}}$ to derive Equation 4.33.

Equation 4.32 gives the component of optical power that oscillates at the phase modulation frequency. For small detunings, the amplitude is linear in $\delta\nu$, and can thus be used to lock the laser to the optical cavity after the optical power has been detected on a photodiode and demodulated. The degree to which the amplitude changes for a given detuning is characterized by the parameter \mathcal{D} , which, as should be expected, varies inversely with cavity linewidth and is proportional to the product of the zero and first-order Bessel functions. In passing, we note that this can be used to define an optimal modulation depth, given by $\Delta\varphi = 1.08$. By measuring this oscillating RF signal, and demodulating by mixing in the proper quadrature at the frequency Ω , a linear control signal can be obtained with which to feedback upon the laser frequency.

While Equation 4.32 describes the behavior of the error signal near the cavity resonance, one may go a step further and include the frequency dependence of $\text{Im}\{\mathcal{R}\}$ to calculate the shape of the error signal over a broader range, as shown in Figure 4.5 [211]. When this detail is included, it can be shown that the frequency response of Eq. 4.31 needs to be multiplied by a single-pole low-pass filter function with a corner frequency equal to the cavity half-width in order to provide a better approximation of the system's frequency response. This effect can be compensated for by appropriate servo design, such that the lock bandwidth need not be limited by the cavity linewidth.

Physically, this low-passing effect represents a transition from a regime in which the cavity is sensitive to frequency fluctuations of the laser to one in which the error signal is proportional to phase fluctuations of the laser. As expected, this transition occurs at the cavity half-width.

4.2.3 Sources of lock error

There are two important considerations when frequency stabilizing the laser. The first is that the reference cavity optical length must be as stable as possible and will be discussed later. However, an equally important question is whether there are any effects that can prevent a laser from precisely tracking the reference cavity resonance, due to either technical or quantum effects.

The most fundamental but least important source of error in cavity locking systems is quantum noise (see *e.g.* [215, 210]). The optical power spectrum of shot noise on the light at the detector is given by the single-sided power spectral density

$$G_P = 2h\nu P_{\text{opt}} \quad [\text{W}^2/\text{Hz}]. \quad (4.34)$$

Thus, assuming $\beta = 1$, the expected frequency noise due to shot noise in the most ideal case (and with an ideal demodulator) is

$$G_\nu = \frac{G_P}{\eta \mathcal{D}^2} = \frac{h\nu \Delta\nu_{\text{FWHM}}^2}{16\eta P_0 J_0^2} \quad [\text{Hz}^2/\text{Hz}], \quad (4.35)$$

where η takes into account the detector quantum efficiency and $\nu = c/\lambda$ is the optical frequency. Substituting in the very modest parameters $\lambda = 1 \mu\text{m}$, $P_0 = 10 \mu\text{W}$, $\eta = 0.5$, and $\Delta\nu_{\text{FWHM}} = 10 \text{ kHz}$, the very low shot noise floor of $S_\nu = 4 \times 10^{-7} \text{ Hz}^2/\text{Hz}$ can be achieved. This can be related to the locked laser linewidth by

$$\Delta\nu_{\text{locked}} = \pi G_\nu, \quad (4.36)$$

where it is assumed that G_ν is white noise. For the parameters given above, this results in a locked linewidth of $1 \mu\text{Hz}$. Thus, for high-finesse cavities, the shot noise locking limit is far below any cavity locking result, even in experiments designed to exclude other technical and thermal effects [215]. This indicates that in practical situations, “technical” effects are most important.

Residual amplitude modulation (RAM) is a term that collectively describes a variety of effects that induce amplitude modulation at the phase modulation frequency. For example, temperature-dependent parasitic etalons within the optical system can induce RAM which is then demodulated along with the cavity error signal. This causes an offset to be introduced in the locking system. Other effects that can cause RAM are typically related to the phase modulation device, most often an electro-optic crystal-based (e.g. LiNbO₃, ADP, KDP) modulator. For instance, stress-induced birefringence in crystal devices can rotate the principle crystal axis, creating not only an electric field-dependent phase shift, but also a corresponding polarization rotation, which can be distributed across the optical wave front.

While in many cases a temperature-controlled electro-optic (EO) crystal has low enough RAM for acceptable performance, a certain degree of success has been achieved by using a DC electric field on crystal-based EO modulators to actively servo the RAM [216]. However, beam pointing deviations can cause slightly different regions of the crystal to be sampled, causing the phase of the RAM to shift, and limiting the effectiveness of the active system.

It is important to note that the effect of RAM on laser stability is reduced for cavities with narrower resonances due to the fact that a given fractional change in RAM results in a smaller change in frequency for a narrower resonance. Thus, for a given cavity length, higher cavity finesse is always desirable to help mitigate RAM-induced line pulling.

4.2.4 Choice of EOM crystal

In many cases, limiting RAM is of central importance for high-precision locking. As new materials continue to be developed to lower the fundamental thermal noise limitations to cavity locking (see Chapter 3 for a detailed description of thermal noise in interferometers), RAM-induced lock error will continue to be an important factor in high-precision laser stabilization. Here we discuss strategies for mitigating EOM-induced RAM.

Crystal symmetry plays a big role in the properties of an EOM. Lithium niobate and lithium tantalate are uniaxial crystals that both belong to the trigonal $3m$ crystal group, while ammonium

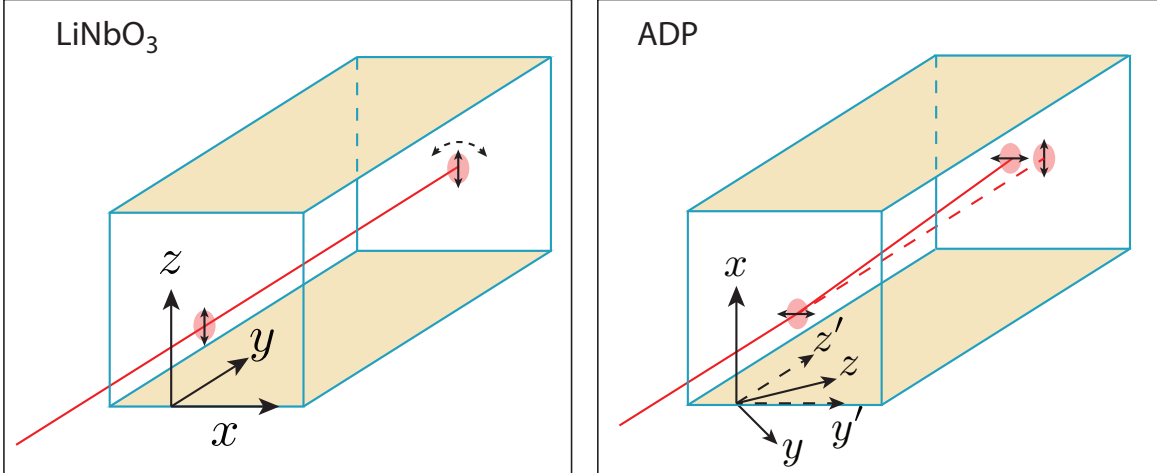


Figure 4.6: LiNbO₃ and ADP modulator configurations. In the case of ADP, the beam that receives the phase modulation (horizontally polarized in this figure), walks off from the vertically polarized component.

dihydrogen phosphate (ADP) and potassium dihydrogen phosphate (KDP), also uniaxial, belong to the tetragonal $\bar{4}2m$ crystal group. While a full discussion of the crystal symmetries and implications for electro-optic modulation of light is beyond the scope of this section, we note that in general the electro-optic coefficients—the coefficients that modify the crystal impermeability tensor in the presence of an applied field—depend directly on the type of crystal symmetry. For example, the r_{33} coefficient in trigonal $3m$ crystals—which produces an index change for light polarized along the extraordinary axis with an applied electric field along the same axis and is widely used in LiNbO₃-based EOMs—is zero for tetragonal $\bar{4}2m$ crystals, such as ADP.

We begin our discussion of the most conceptually simple of the two classes of crystals considered, the trigonal $3m$ crystal group, to which LiNbO₃ and LiTaO₃ belong. For light polarized along the z -direction and with a modulation electric field also applied along z , the change of the index of refraction can be shown to be [207]

$$n_e(E) \simeq n_e - \frac{1}{2}n_e^3 r_{33} E_z. \quad (4.37)$$

Here, $n_e \simeq 2.2$ is the index of refraction of the extraordinary axis (z -axis). This configuration is also

shown in figure 4.6. For the specific case of LiNbO₃, the r_{33} coefficient is approximately 30 pm/V and is the largest electro-optic coefficient among all of the LiNbO₃ EO coefficients [217].

One of the most important intra-EO sources of RAM is a polarization-rotation at the drive frequency that gets converted to RAM by polarization-sensitive optics in the PDH system later on [216]. Specifically, if there is any misalignment between the incoming light polarization and the LiNbO₃ extraordinary axis (z)-axis, there will be a RAM effect. Temperature fluctuations can couple to stress-induced birefringence to make the z -axis a moving target. Thus, temperature control and a very high quality, carefully aligned input polarizer are necessary for reducing the time-dependent RAM in LiNbO₃ crystals.

It turns out that ADP largely addresses the issue of polarization rotation. Due to the different crystal symmetry of tetragonal $\bar{4}2m$ crystals³ the EO coefficient of interest is r_{41} and the crystal should be cut as in Fig. 4.6. It can be shown that the index change for the ray polarized along the y' axis is [218]

$$n_{y'}(E) \simeq n_{y'} + \frac{1}{2}n_{y'}^3 r_{41} E_x, \quad (4.38)$$

where $n_{y'}$ is given by

$$n_{y'} = \sqrt{2} \left(\frac{1}{n_y^2} + \frac{1}{n_z^2} \right)^{-1/2} \simeq 1.5. \quad (4.39)$$

In the case of ADP, r_{41} is approximately 25 pm/V [218], thus it is competitive with LiNbO₃ in terms of phase modulation.

Due to the qualitatively different orientation of the axes for phase modulation, ADP can serve as its own polarizer. As shown in Fig. 4.6, the polarization component along the y' axis has a walk-off due to the fact that this axis is not a principle axis. On the other hand, the (unwanted) polarization component along x has no walk-off due to the fact that x is a principle axis. The angle between the y' polarization k -vector and the x polarization k -vector is approximately 1.8° [219]. This means that the two polarization components can be spatially separated after transmission through the crystal, as depicted in Fig. 4.6, effectively eliminating the polarization rotation effect.

³ The reader should be aware that the orientation of ADP discussed here is not common in the literature due to the fact that a different configuration is commonly utilized for amplitude modulation.

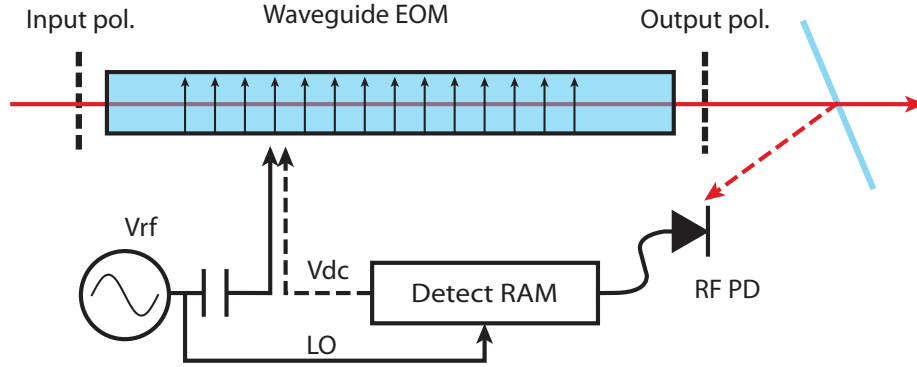


Figure 4.7: Experimental setup for active control of residual amplitude modulation (RAM) in a waveguide electro-optic modulator. The RAM is detected using the same local oscillator as is used to drive the crystal.

4.2.5 Active control of residual amplitude modulation

As discussed in the previous section, RAM can crucially depend on the polarization alignment into crystals of the trigonal $3m$ family. In general, it is possible to control the polarization alignment by careful control of the input light polarization, and to mitigate temperature-dependent stress-induced birefringence. Wong and Hall [216] devised a further step, based upon applying a DC electric field in addition to the RF drive, in order to actively cancel the polarization-rotation induced RAM. Specifically, they show that for misalignments between the crystal extraordinary axis and the input and output polarizers, given by angles θ_1 and θ_2 , respectively, there will be RAM that scales as [216]

$$\Delta P(t) = A_0 \sin(\Omega t) \sin[\Delta\phi(E_{dc})]. \quad (4.40)$$

Here

$$A_0 = -P_0 \sin(2\theta_1) \sin(2\theta_2) J_1(\Delta\varphi), \quad (4.41)$$

where P_0 is the input power, and Ω and $\Delta\varphi$ are the same quantities as utilized in Eq. 4.28; and $\Delta\phi(E_{dc})$ is the phase shift between the ordinary (o) and extraordinary (e) polarization components within the crystal. This phase shift depends on the crystal length, the crystal temperature, the difference between n_e and n_o , and importantly the applied electric field. The electric field dependence

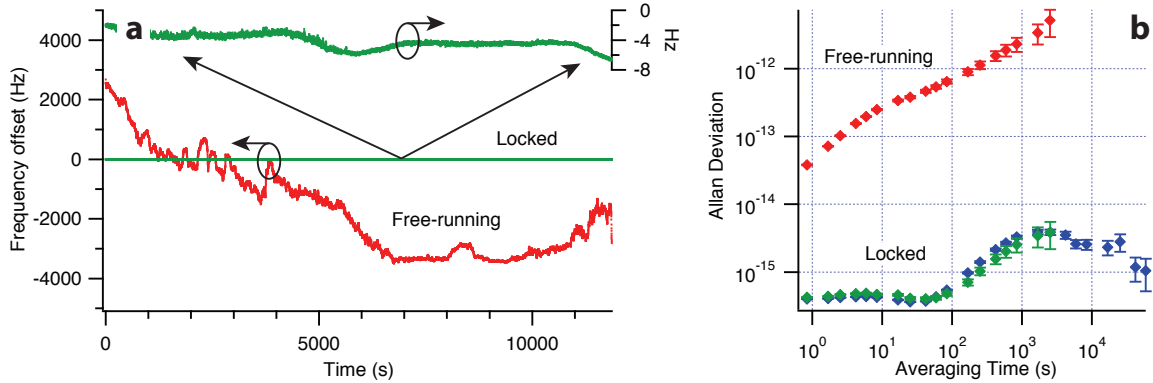


Figure 4.8: Experimental demonstration of reduced residual amplitude modulation (RAM). (a) RAM-induced frequency offsets in a lock. Here, the free running lock baseline signal was converted to frequency by the known slope of the cavity frequency discriminant. Engaging the RAM servo reduces the effect to the few-Hz level. (b) Allan deviation of the extrapolated RAM-induced frequency offset.

was exploited in Ref. [216] to actively maintain $\Delta\phi(E_{dc}) = 0$.

Equation 4.41 suggests that if $\theta_1 = \theta_2$ can be enforced, there will be no RAM. While free space modulators can come close to attaining this condition if temperature-dependent effects are carefully controlled, it rules out a fairly attractive class of modulators: waveguide-based EOMs. Waveguide EOMs can provide high modulation depth for very low applied voltage, allowing easy optimization of cavity locking systems. However, fiber based devices do not offer precise control of the input polarization due to manufacturing difficulty of aligning the polarization axes of the fiber to crystal.

Despite this difficulty, we have had great success employing the technique of Wong and Hall to null RAM-induced frequency noise. Modern fiber-based waveguide EOMs have the advantage that the waveguide defines a precise interaction region. As a result, waveguide modulators are free from beam-pointing fluctuations that can be converted to RAM. We attribute the success of this technique to this key difference and we implemented RAM servos in several optical cavity systems, most notably those described in Ref. [168]. For one cavity, the RAM servo allowed the cavity resonance to be tracked with a fractional imprecision less than a part in 10⁵. Figure 4.8 shows

an example of such a RAM servo in action, where the frequency offset of the non RAM-controlled case would be at the kHz level. Engaging the RAM servo increases the stability by two orders of magnitude. Since the RAM servo technique is insensitive to RAM beyond the RAM detection photodiode, it is quite possible that the level of stability of the data shown Fig. 4.8 was limited in part by optical etalons.

4.3 Mechanical design of optical reference cavities

Despite the considerable challenges present in building a high-quality cavity locking system that is free from residual frequency offsets, these effects are not what limit most high-finesse optical cavity frequency references. Instead, perturbations to the length of optical reference cavity are ultimately what limit the frequency stability. These perturbing effects fall into two categories: mechanical and thermal perturbations that are not fundamental, *i.e.* that are non-statistical in origin; and fundamental statistical fluctuations in the cavity spacer, substrate, and coatings that arise from their contact with a thermal reservoir at room (or cryogenic) temperature.

In this section, we discuss non-statistical perturbing effects and describe methods for their mitigation. These mechanical effects can be divided into two categories: those caused by vibrations (accelerations) that structurally deform the cavity, and those that couple through the coefficient of thermal expansion (CTE) of the cavity materials. Use of finite element analysis to optimize cavity geometries and choice of materials has drastically reduced and elucidated these effects.

4.3.1 Vibration sensitivity

Although optical cavity mirrors and spacers are typically made out of an extremely rigid substance, such as ultra low expansion glass (ULE), the length stability requirements are stringent for sub-Hz lasers. As can be seen from Equation 4.13, the fractional frequency change of a cavity resonance is directly related to the fractional length change by

$$\frac{\Delta\nu}{\nu} = -\frac{\Delta L}{L}. \quad (4.42)$$

A world record for cavity stabilization—and one that stood for over a decade—was set in 1999 with 1-second stability at 3×10^{-16} , and employed a very impressive vibration isolation scheme in order to keep the cavity length constant: the entire optical table was suspended on giant rubber bands, resulting in a highly-effective seismic isolation system [38]. Although the cavity length in Eq. 4.42 is the effective length sensed by the optical field, which is averaged over the mirror surface, it is still astounding that the length stability needed for a sub-Hz laser is sub-fm (10^{-15} m)—the length scale of the proton radius! It should thus come as no surprise that length stability at or below one part in 10^{15} takes significant engineering effort.

One approach that significantly reduces the dependence on vibration-isolating structures is to design the cavity spacer such that mirror-spacer system is insensitive to vibrations. An intuitive way to achieve this is to mount the cavity at its midplane in the vertical direction [39]. In this way, the top and bottom mirrors move equal amounts when subject to vibrations along the vertical axis. However, one can only get so far exploiting intuitive geometry for the simple reason that the support structure breaks perfect vertical symmetry. Thus to finalize any cavity design finite element analysis (FEA) must be employed [220]. This technique can be applied to a variety of cavity geometries and tailored to a specific design goal, such as insensitivity in a specific direction, and was employed to design the vertical cavity reported in [40], and which is still operating in the lab as of the time of this thesis. Further improvements of the technique have yielded even better results for a vertical design, with vibration sensitivity at the level of $10^{-11}/(\text{m/s}^2)$ [221]. These results are quite good given that the highest grade commercial isolation platforms can give isolation performance at the $50 \text{ ng}/\sqrt{\text{Hz}}$ level, resulting in a vibration-limited frequency noise performance of order $10 \text{ mHz}/\sqrt{\text{Hz}}$ for the sensitivities exhibited by modern cavities in the visible spectrum.

In principle, one is not restrained to vertical configurations. In fact, there may be good reason to choose a horizontal configuration, especially if it is expected that the majority of vibrations will be in the vertical direction. Other motivating factors include structural stability, especially for larger cavities, and the experimental ease of access for horizontal geometries. Most importantly, in the horizontal configuration, the coupling of vertical accelerations to deviations along the optical

axis is reduced by the Poisson ratio, representing roughly an 80% reduction in sensitivity. However, horizontal accelerations can still couple into mirror displacement, although the inherent symmetry in the two horizontal axes limits this effect.

4.4 Designing two ultrastable lasers for the 10^{-16} level performance

In this section, we discuss the design of two ultrastable optical cavities for laser stabilization using finite element analysis. In both cases, the ULE glass spacers were pre-existing (i.e., they were not ordered expressly for the purpose of creating a design with insensitivity to vibrations). As a result, the geometry was fixed, permitting fewer degrees of freedom to explore in the modeling. Despite this constraint, we find support configurations that yield immunity to vibrations.

4.4.1 Design of the “Big ULE” cavity

The cavity lovingly nicknamed the “Big ULE” is one of the largest ultrastable cavities to be implemented in a force-insensitive configuration [2]. This cavity first joined our lab in the early 2000s to fulfill another role. Jason Jones *et al.* employed it for direct frequency comb stabilization, and its length chosen such that the free spectral range matched the repetition rate of a Ti:Sapphire laser [222]. At 39.4 m in length, it is over six times as long as the well-known (American) “football”-shaped cavity of Ref. [199]. Its mass is over 20 kG. This author can assure the reader that every moment transporting this cavity, often with nothing more than a steady grip, was a religious experience!

In order to perform finite element modeling, we consider a symmetric half-cavity shown in Fig. 4.9. The support strategy was chosen to give the feet a uniform surface on which to sit, yet still be easy to machine. The support strategy that we decided to implement was based on milling vertical shafts with a flat support surface into the sides of the cavity (see Fig. 4.9a).

Additionally, we wanted to take a risk and use fused silica (FS) mirrors. As seen from the discussion in the previous chapter, fused silica has a much lower loss angle than ULE, and thus can lower the thermal noise floor of a cavity by about a factor of two over an equivalent design with

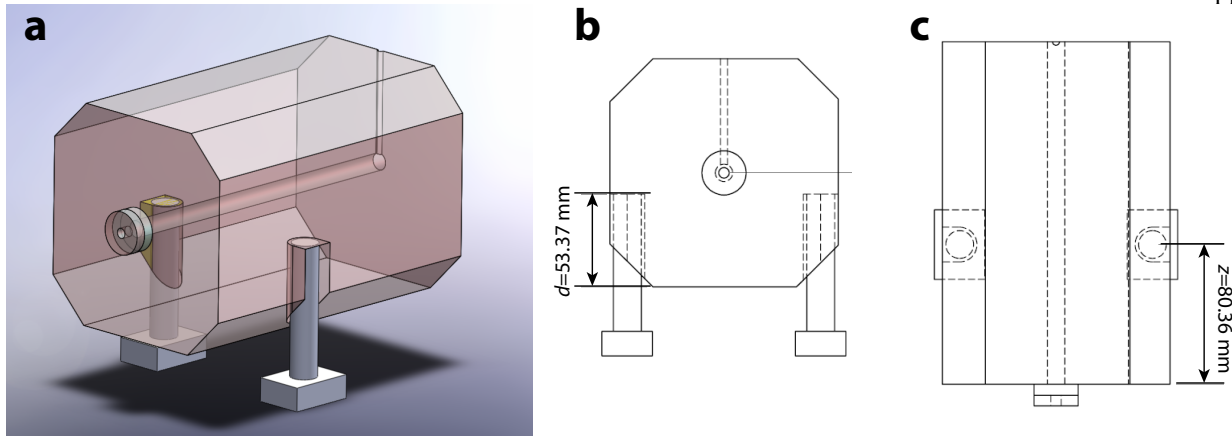


Figure 4.9: The finite element model considered for the “Big ULE” cavity. It is important to note that the teflon legs shown here are no longer in use. (a) One half of the cavity was used in the modeling due to the axis of symmetry in the midplane (b) Front view of the model used and optimal support depth, d . (c) Top view of the model, and optimum support axial displacement z .

ULE mirrors. The risk comes in the mismatch of coefficients of thermal expansion (CTEs) of the two materials. In order to mitigate the problems arising from the mismatch, we included ULE rings in the design, which were assumed to be contacted to the back surface of the FS mirrors. This had been shown to tune the the thermal expansion properties in a way that helps offset the difference in CTEs [223] (we will discuss this in more detail in Section 4.4.4.1). We note parenthetically, that, while the ULE rings were included in the mechanical modeling, their effect is not very significant, and shifts the zero crossing points by only ~ 0.1 mm.

4.4.1.1 Finding the optimal support strategy

In order to find the optimal support strategy, we modeled the cavity’s response to vertical accelerations using finite element analysis (FEA). The modeling goal was to eliminate both the mirror tilt and the mirror displacement in response to vertical accelerations. The two parameters that were tuned to find the vibrationally insensitive points are shown in Fig. 4.10. They represent the position of the support surfaces with respect to the lower surface of the spacer (d), and the distance of the support surfaces to the end of the spacer (z). In this modeling, teflon rods were assumed as the support structure. During the modeling, the distance from the optical axis to the

bottom of the foot was kept at 105 mm to fit into the vacuum assembly. We note that the teflon rods were later abandoned after the first implementation of the cavity because they led to high-Q resonances (in Chapter 6, we will see how these resonances manifested themselves in atom-based measurements).

We performed simulations for varying z and d and recorded the simulated tilt (as measured along the mirror vertically) and average mirror displacement. We assumed linear coupling between $\{z, d\}$ and, the tilt and displacement (given by θ and Δ , respectively), such that

$$\begin{pmatrix} \Delta \\ \theta \end{pmatrix} = \begin{pmatrix} a_{11} & a_{12} \\ a_{21} & a_{22} \end{pmatrix} \times \begin{pmatrix} z \\ d \end{pmatrix} + \begin{pmatrix} \Delta_0 \\ \theta_0 \end{pmatrix}. \quad (4.43)$$

More compactly, this can be written

$$\mathbf{Y} = \mathbf{A}\mathbf{X} + \mathbf{Y}_0. \quad (4.44)$$

When the displacement vector, \mathbf{Y} , satisfies $\mathbf{Y} = 0$, the optimum parameter set is given by

$$\mathbf{X} = -\mathbf{A}^{-1}\mathbf{Y}_0 \quad (4.45)$$

The planes shown in Fig. 4.10 are fits to a total of 11 different simulations, each for a different combination of z and d . The extrapolated optimal support points are found, via Eq. 4.45, to be $z = 80.36$ mm and $d = 53.37$ mm. Figure 4.11a shows the final support configuration of the Big ULE cavity, where the problematic teflon has been replaced. Since a soft material between the optical cavity and the support structure is always necessary, we used Viton hemispheres with a radius of ~ 1 cm (these can be obtained from McMaster-Carr, part 3645K7). Figure 4.11b shows the exaggerated deformation due to the acceleration of gravity in the vertical direction for the optimal support configuration.

Once the optimal support points were chosen, we checked the sensitivity to horizontal accelerations via FEA. Due to the presence of horizontal symmetry, we expected that the displacement sensitivity should be zero, and it was (to within error). However, the mirror tilt due to horizontal accelerations was quite large. We show mirror displacements due to accelerations in the vertical and horizontal directions in Fig. 4.11c. If the optical mode forms at the center of the mirror, horizontal

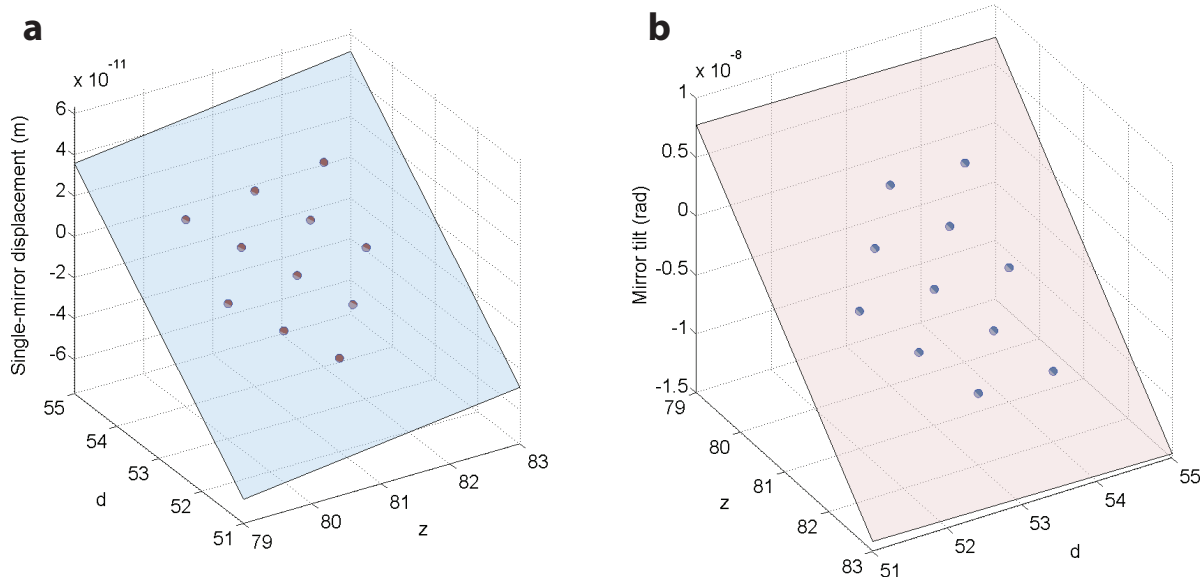


Figure 4.10: Two dimensional planar fits to offset (a) and tilt (b) as a function of z and d . The data points are obtained via finite element analysis, and a planar surface was fit to them.

accelerations would not couple to the net optical path length change. However, if the optical mode forms (or if the mirrors are optically contacted) a few mm away from the geometric center of the spacer, a residual sensitivity of $10^{-9}/g$ is possible, where g is the acceleration of gravity. In fact, this is closer to the value we estimate for the sensitivity to vibrations in the horizontal direction, and this seems to be the dominant mechanism by which vibrations perturb the optical path length.

Figure 4.12 (page 116) shows the Big ULE installed safely within its double-vacuum enclosure. The outer rough vacuum is kept below 10 Torr to provide thermal isolation from the outside world and promote temperature homogeneity over the surface of the inner vacuum chamber. The measured time constant between the inner vacuum chamber and the cavity is 1.6 days, and the actively controlled temperature of the inner chamber maintains sub-mK stability over the 1 hour timescale, and few-mK stability temperature stability over the course of a day. Figure 4.13 (page 117) shows the new support structure and heat shield of the Big ULE. This new support structure was installed after we discovered the problems with the original support structure.

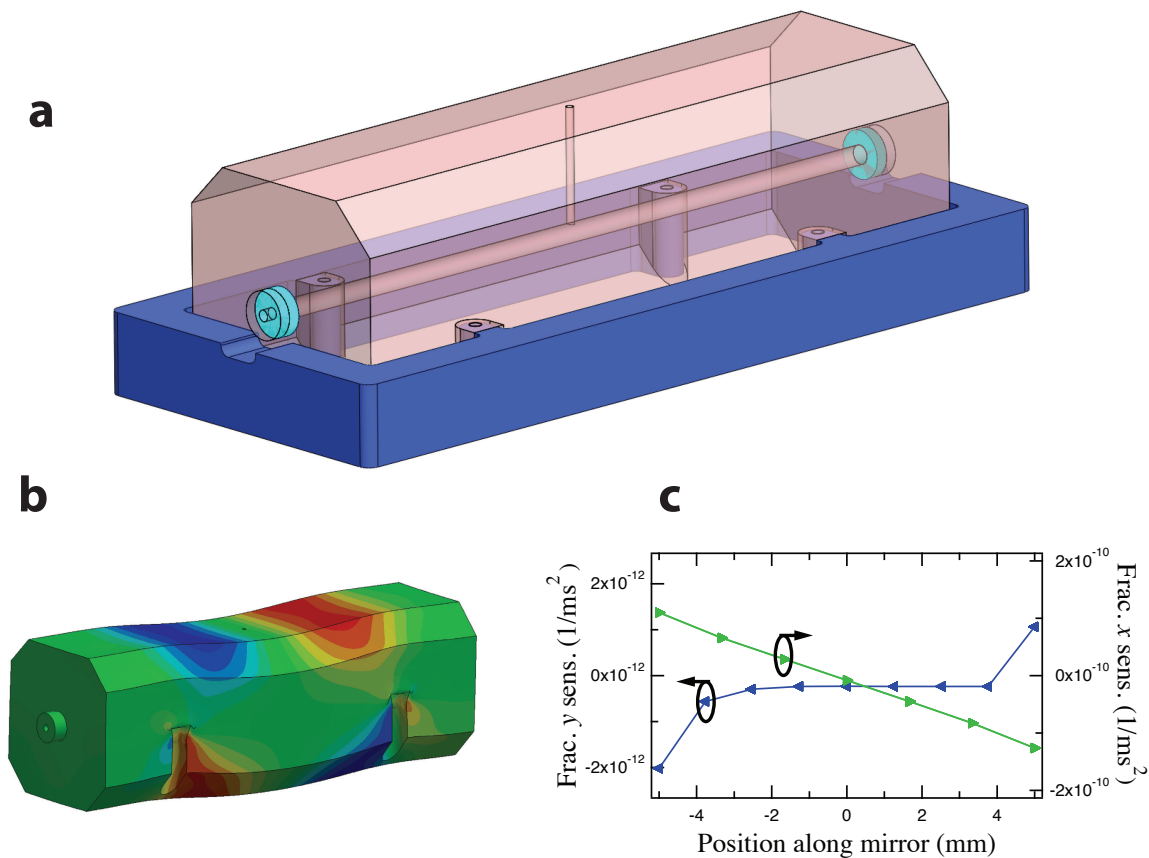


Figure 4.11: The Big ULE cavity and Zerodur support structure. (a) The final design of the Big ULE removed the teflon legs in favor of a Zerodur support shelf. The cavity rests on Viton hemispheres (not pictured). (b) Exaggerated cavity deformation in response to a vertical acceleration and when held at the optimal points via finite element analysis (FEA). (c) FEA-predicted mirror displacement per acceleration as a function of vertical (left) and horizontal (right) displacement along the mirror surface when the cavity is supported optimally.

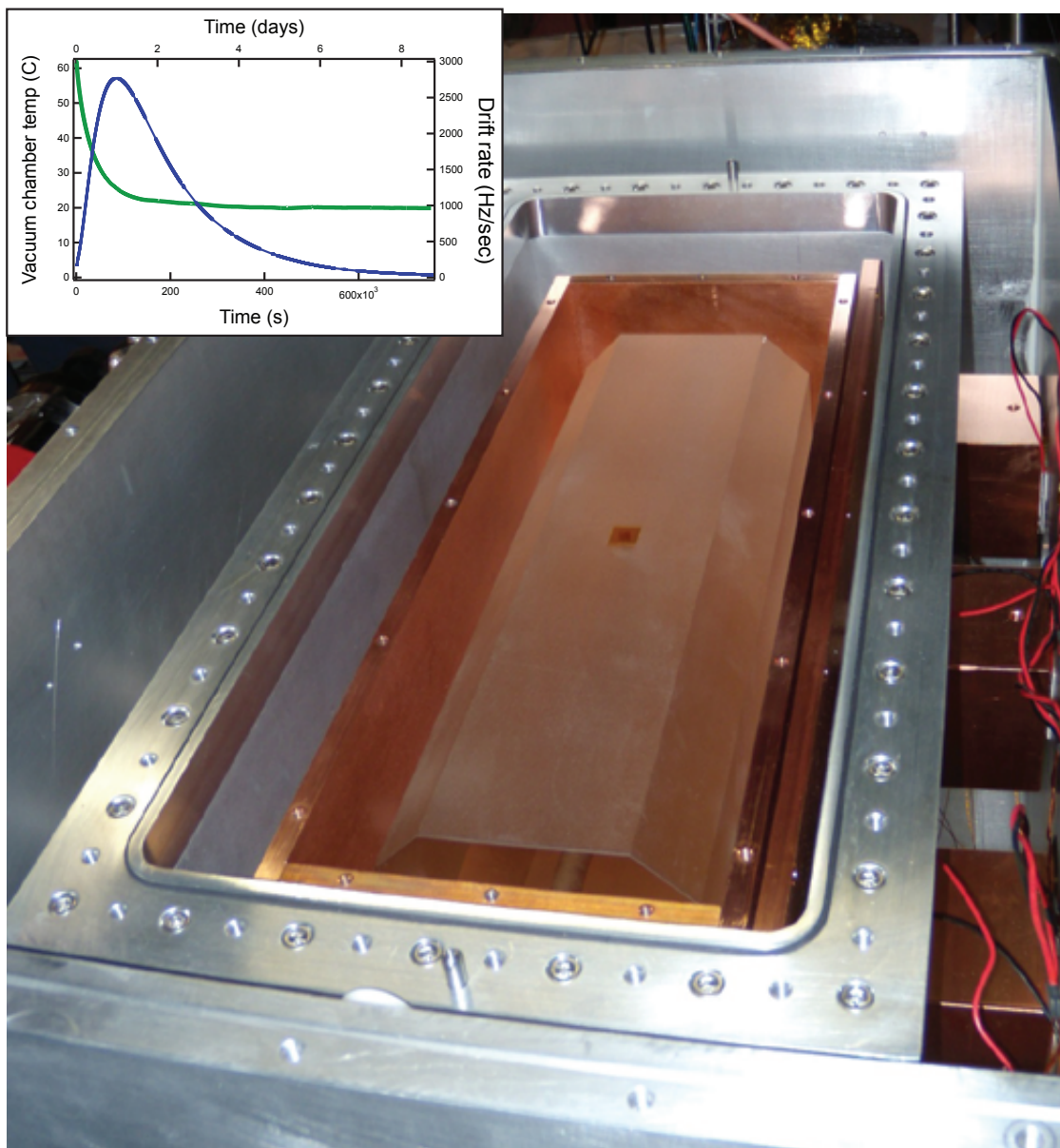


Figure 4.12: The double-layer vacuum system for the Big ULE. The inner vacuum chamber is actively temperature stabilized by Peltier elements (visible at right) to the level of several mK (sub-mK) per day (hour). The outer vacuum is kept below 10 Torr to provide thermal isolation from the outside world and promote temperature homogeneity over the surface of the inner vacuum chamber. A vacuum level of 2×10^{-8} Torr is maintained in the inner chamber with a 75 L/s ion pump. The measured time constant between the inner vacuum chamber and the cavity is 1.6 days. **Inset:** Measurement of the thermal time constant of the system. A large temperature change was applied to the system and the optical beat of the laser stabilized to the Big ULE was measured with a second stable laser system.

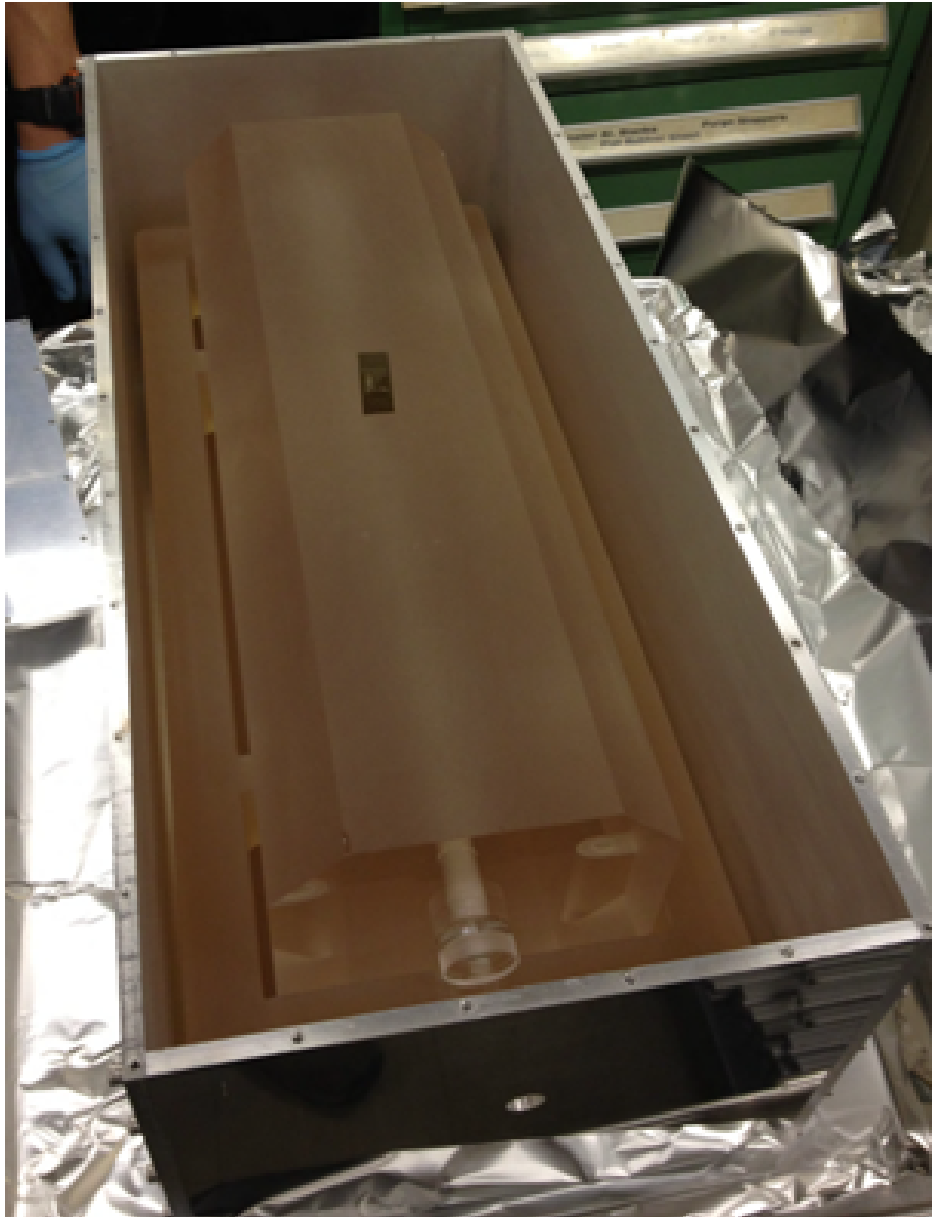


Figure 4.13: The Big ULE cavity with new Zerodur glass support structure. The cavity rests upon Viton hemispheres (not shown). Due to the change in support structure, we constructed a new heat-shield box out of polished aluminum to replace the copper one shown in Fig. 4.12.

4.4.2 Design of the “JILA cavity”

In order to support the testing of a new cavity constructed from monocrystalline silicon in collaboration with PTB,⁴ which we discuss in Section 4.6, we set out to design a second cavity that would perform at the low 10^{-16} level. The name, “JILA cavity” comes from its time at PTB, as this was an easy way to differentiate it from the other systems there. Since this system was supposed to be transportable, we attempted to make the design as compact as possible. The basic design is shown in Fig. 4.14 and uses a support scheme similar to that of [224]; the spacer is a horizontally mounted cylinder, with a diameter of 10 cm and a length of 25 cm. Support shelves, whose exact positions were chosen via FEA, extend the entire length of the spacer with four support points defined by small Teflon cylinders. In order to save space, the support scheme involving such a lip along the edge of the cavity allows the cavity to rest on a rigid rectangular support structure made of ULE glass through which the bottom half of the cavity hangs. The vacuum system is thus considerably smaller than the Big ULE, and is compact enough so that it can fit onto a single Minus-K commercial isolation platform, as shown in Fig. 4.14d. As with the Big ULE, the mirrors are fused silica and the ULE rings have been added.

4.4.2.1 Finding the zero crossing point

By tuning the depth of the cuts and z -position of support points, we extrapolated the best values from a total of 9 FEA simulations. We found that the data had a quadratic distortion due to the fact that changing the position of the support shelf removes material along the entire length of the cavity, changing the effective cross section. We therefore included couplings up to quadratic

⁴ *Physikalisch-Technische Bundesanstalt*, Germany’s standards institute. <http://www.ptb.de>.

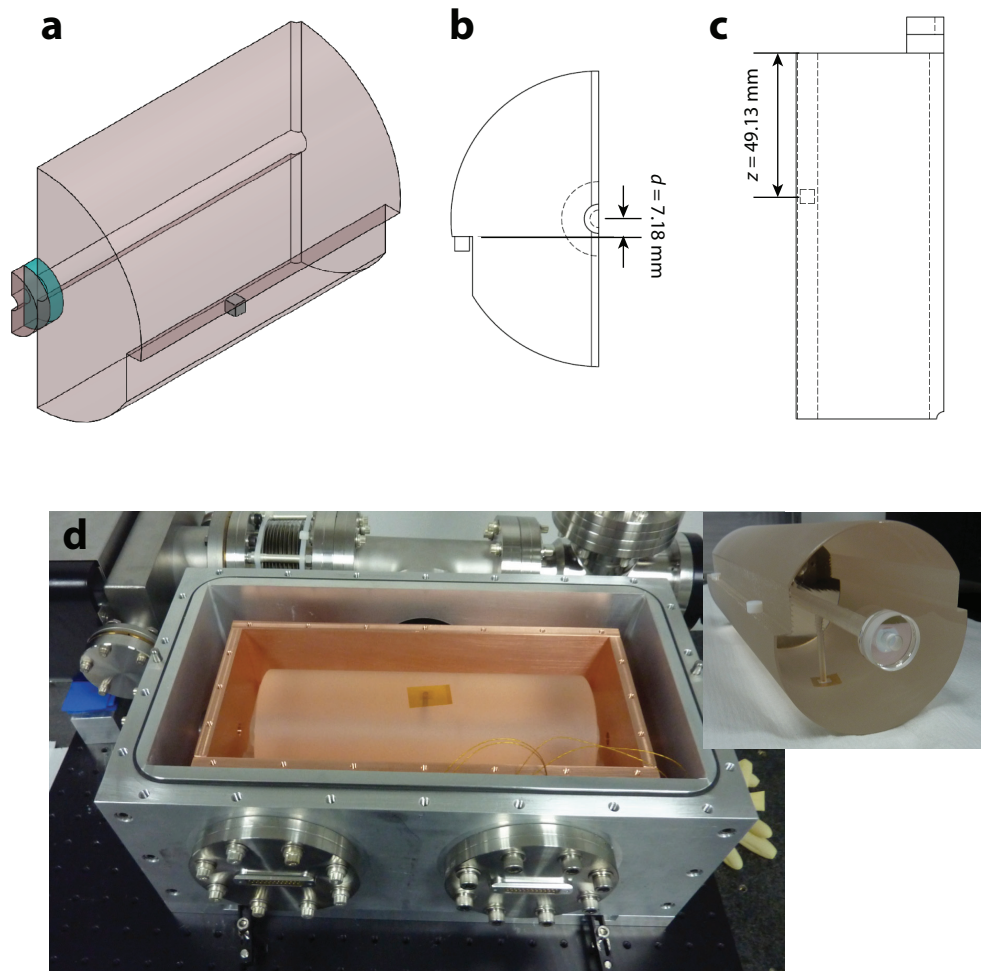


Figure 4.14: The “JILA” cavity design and vacuum system. (a) Model used for performing finite element analysis (FEA). Only 1/4 of the total cavity is shown, as there are two planes of symmetry that were exploited for the FEA modeling. The support is a small teflon cube. (b) Head-on view of the model. As depicted here, the support shelf optimal distance with respect to the optical axis was $d = 7.18 \text{ mm}$. (c) Top-down view of the cavity and optimal z displacement of 49.13 mm . (d) Cavity installed inside its vacuum chamber. The inner heat shield is made of copper and its temperature is actively controlled with four Peltier on which the heat shield directly rests. Thermal contact between the heat shield and the Peltier elements is facilitated with indium foil. The cavity is supported by four small teflon supports which rest upon a secondary ULE support structure. The support structure rests upon the heat shield with four additional teflon stand-offs. The entire system including ion pump was small enough to rest on a single commercial Minus-K platform.

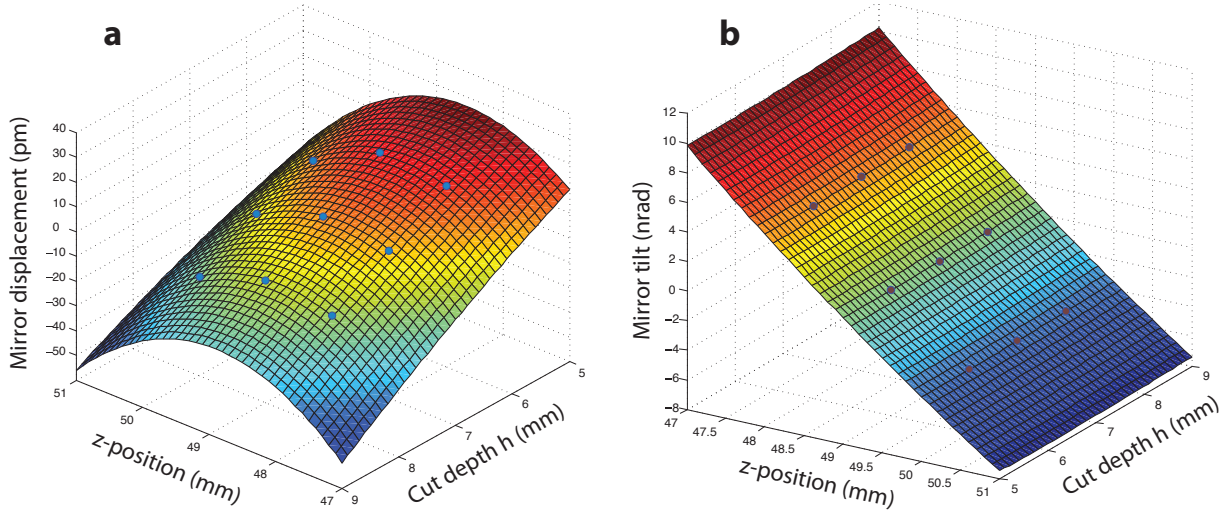


Figure 4.15: FEA simulation of the “JILA cavity.” Here, a fit up to quadratic order was used to describe the mirror (a) displacement and (b) tilt as a function of the support positions.

order in the fit to the FEA data, such that the displacement surface is described by

$$\begin{pmatrix} \Delta \\ \theta \end{pmatrix} = \begin{pmatrix} a_{11} & a_{12} & a_{13} & a_{14} & a_{15} \\ a_{21} & a_{22} & a_{23} & a_{24} & a_{25} \end{pmatrix} \times \begin{pmatrix} z \\ h \\ z^2 \\ h^2 \\ hz \end{pmatrix} + \begin{pmatrix} \Delta_0 \\ \theta_0 \end{pmatrix}. \quad (4.46)$$

The fits to the FEA data are shown in Fig. 4.15. The quadratic dependence on the support positions is clearly seen.

As before, we can write Eq. 4.46 in a more compact form: it becomes

$$\mathbf{Y} = \mathbf{A}\mathbf{X} + \mathbf{Y}_0. \quad (4.47)$$

Since \mathbf{A} is not a square matrix, we can’t invert it as before (we are still only solving for two unknown quantities), but rather find the family of solutions for

$$\mathbf{A}\mathbf{X} = -\mathbf{Y}_0. \quad (4.48)$$

Only one of the solutions is physical, and the the extrapolated values for the vibrationally insensitive mounting are $z_0 = 49.13$ mm and $h_0 = 7.18$ mm.

	Big ULE	Nezrick
Tilt	5.5 nrad/mm-g	4.3 nrad/mm-g
Displacement (fractional)	1.3×10^{-10} /mm-g	1.0×10^{-10} /mm-g

Table 4.1: Zero-crossing sensitivities obtained from the finite element modeling. Note that the z -position affects almost exclusively the mirror tilt, while the depth of the support affects almost exclusively the displacement. All values in this table are quoted against these major contributors for the parameter (tilt or displacement) of interest.

4.4.2.2 Sensitivity compared to the “Big ULE”

Having two sets of modeling results allows a comparison of how sensitive the zero-crossings are to placement errors of the support points. Using the linear models from both the JILA cavity and the Big ULE modeling (in the case of the JILA cavity, we use the linear coefficients of the model), these sensitivities can be expressed at 1 g and per mm of placement error. This is relevant for defining how accurately the support points must be defined. These quantities are listed in Table 4.1. We find that in general the Big ULE and JILA cavity have very similar sensitivity to placement errors of the support points, and even 1 mm of placement error is quite tolerable, at least in the FEA. Probably a more insidious problem is that the FEA assumes complete symmetry amongst all support points; it is easy to imagine that three of the four support positions are supporting the weight. This is why we use soft materials between the support surfaces and the rigid support structure in both the Big ULE and the JILA cavity.

4.4.3 Mesh size effect

As a final test of the modeling, we wanted to make sure that the FEA did not have a strong dependence on the discretization mesh (as in Ref. [220]). The mesh size was limited by this author’s laptop RAM, which was 2 GB (at the time of this writing already this value sounds obsolete). In the case of the Big ULE, the optimal support positions were extrapolated based upon data obtained with a 3 mm mesh. The red curve in Fig. 4.16 shows that this extrapolation is quite good, with a fractional cavity length change on the order of $1 \times 10^{-12}/g$. However, changing the mesh to smaller values perturbs this result, meaning that the optimum values of z and d in the limit of zero

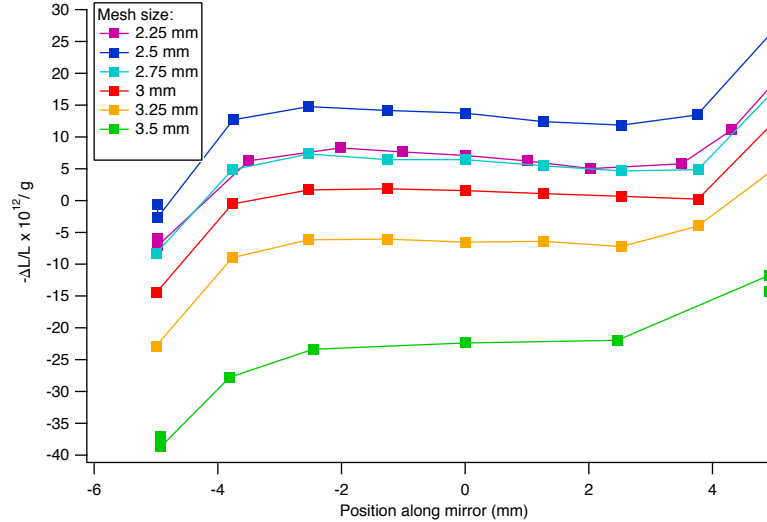


Figure 4.16: Effect of mesh size on the FEA-predicted mirror displacement. The optimal placements were calculated with a mesh size of 3 mm (red curve). The smallest mesh size of 2.25 mm is closer than 2.5 mm mesh results, indicating a turning point in the mesh size effect.

mesh size (which we hope would then be equivalent to reality) are something different. However, by reducing the mesh size to a minimum of 2.25 mm, we can see that the perturbation does not increase monotonically and that at this smallest mesh size it is even heading back in the right direction. This could indicate that our residual error based on mesh size alone could be of order $1 \times 10^{-11}/g$. This is still quite small compared to what are considered “good” sensitivities to acceleration, typically on the order of $10^{-10}/g$. From this we conclude that numerical errors due to mesh size effects will not be a dominant source of error in the modeling.

4.4.4 Thermo-mechanical perturbations

The most common cavity spacer and mirror substrate materials for ultrastable reference cavities are ULE, fused silica (FS), sapphire, and silicon. The CTEs of these materials are shown in Figure 4.17. Due to large room-temperature CTEs, the latter two materials have primarily been used at cryogenic temperatures [225, 226, 227].

In general, a cavity made of a uniform-CTE material will experience a fractional length

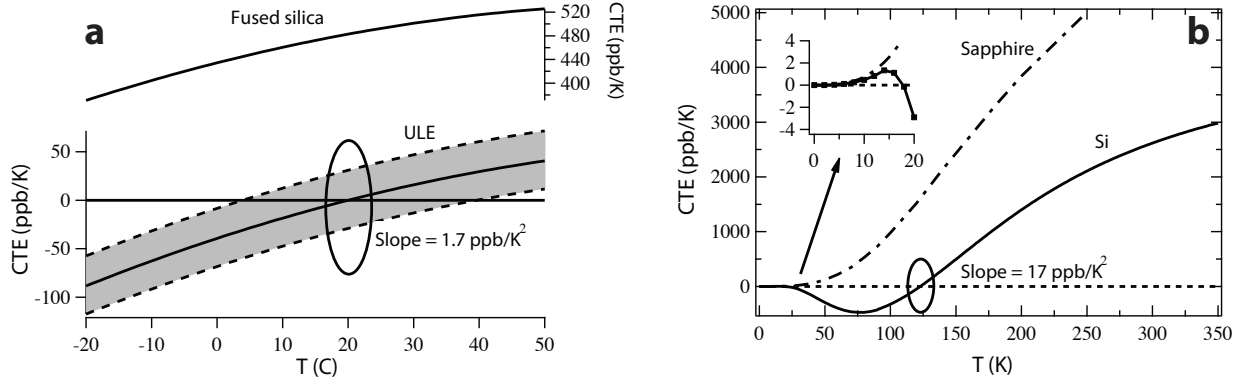


Figure 4.17: Temperature dependence of coefficients of thermal expansion (CTEs) of common cavity spacer and substrate materials. **(a)** CTEs of fused silica and ultra low expansion glass (ULE) [228] near room temperature. The gray band on the ULE curve represents the manufacturer's stated uncertainty in the zero-crossing temperature. **(b)** CTEs of sapphire [229, 230] and silicon [231]. The inset shows that silicon has a second zero-crossing 17 K in addition to the zero-crossing at 123 K.

change given by

$$\Delta L/L = \alpha(T)\delta T + \frac{1}{2}\alpha'(T)\delta T^2 + \mathcal{O}(\delta T^3), \quad (4.49)$$

where $\alpha(T)$ is the CTE at the operating temperature, T ; $\alpha'(T)$ is its first derivative; and δT are small temperature variations. Ideally, one operates a reference cavity around a zero-crossing temperature of a material's CTE, T_{ZC} , defined as

$$\alpha(T_{ZC}) = 0. \quad (4.50)$$

In the case of sapphire, which has no zero crossing, optimal operation is at cryogenic temperatures which reduce the CTE to an acceptable level. Taking Equation 4.49 in the vicinity of a zero crossing and substituting in $\alpha'(T_{ZC}) = 1.7 \text{ ppb/K}^2$ for ULE, it can be seen that the temperature needs to be stable below 1 mK for stability at the 10^{-16} level. While this is in principle quite difficult, the large thermal mass of the ULE spacer tends to limit temperature effects to longer time scales. Mechanical coupling from the vacuum chamber itself, not the CTE of the spacer material, can also induce temperature-dependent frequency shift. Thus, care should also be taken to mechanically decouple the cavity support structure from the chamber. In the case of the Big ULE and JILA

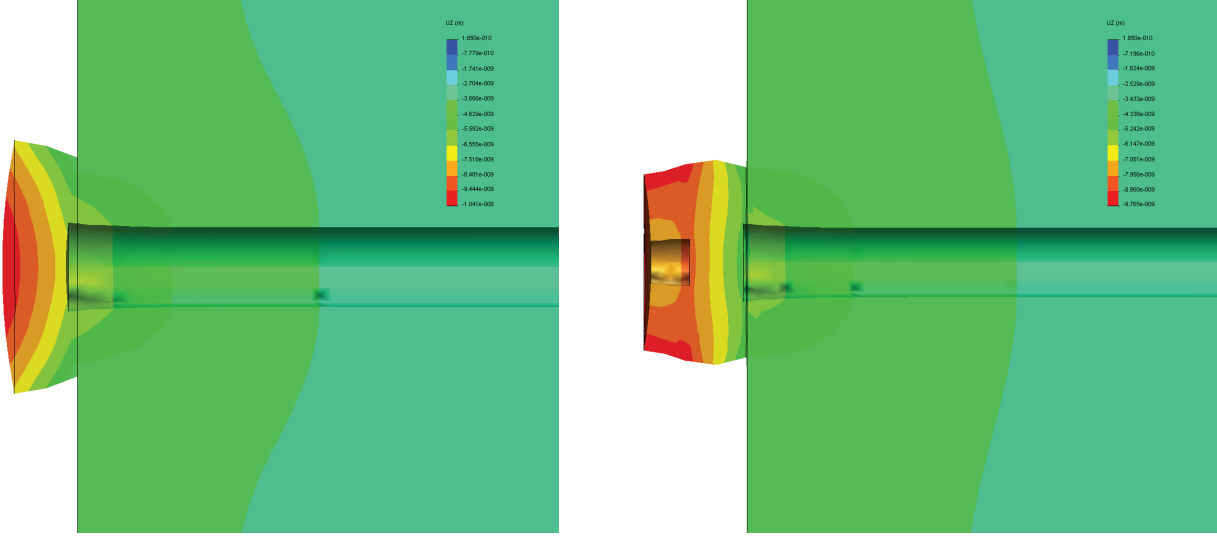


Figure 4.18: Deformation of mixed-material optical cavities. These images show the qualitative effect of the additional ULE ring as first demonstrated in [223]. At left, the effect of the CTE mismatch is seen by the bowing outward of the fused silica mirror in response to an increase in temperature. At right, this effect has been partially mitigated by the addition of a ULE ring.

cavity, this was accomplished by using Zerodur or ULE baseplate structures that were only weakly coupled to the cavity via Viton or Teflon. In this way, the baseplate support serves as a mechanical buffer between the cavity and the aluminum vacuum chamber.

4.4.4.1 Numerical thermo-mechanical modeling

In the case of a cavity with a mirror substrate made out of a different material than the spacer, extra complications arise. The two materials are typically optically contacted very firmly, such that the mismatch of CTEs causes an auxiliary mechanical effect, effectively causing the mirror substrate to bend. This modifies the effective CTE, α_{net} , such that [228]

$$\alpha_{\text{net}} = \alpha_{\text{spacer}} + 2\delta\frac{R}{L}(\alpha_{\text{mirror}} - \alpha_{\text{spacer}}) + \Gamma. \quad (4.51)$$

Here, R is the mirror radius and L is the cavity length. The term δ describes thermo-mechanical stresses coupling into length change and Γ accounts for deviations from the ideal model [228]. Thermo-mechanical finite element analysis can be used to find δ for a given cavity geometry, such

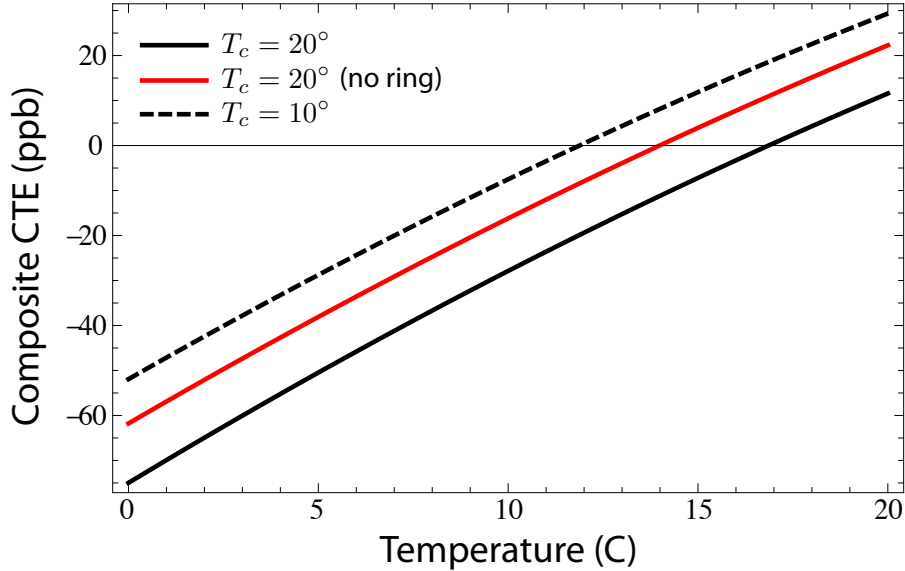


Figure 4.19: Net coefficient of thermal expansion for the Big ULE assuming a spacer T_0 of 15.4° C. The addition of a ULE ring raises the temperature of the CTE zero-crossing of the BIG ULE (solid red vs. solid black). We find a dependence of the zero-crossing temperature on the cavity assembly (i.e., the temperature at which the mirrors/rings are optically contacted to the cavity) temperature (solid black vs. dashed black). The assumed assembly temperatures, T_c are given in the legend. For the case where the contact is performed at 20° C, the ULE ring raises the zero-crossing temperature to 16.9° C.

that α_{net} can be found and minimized by operating at the new zero-crossing temperature [228, 223].

Finally, it is worth noting that there has been success tuning the zero cross point by contacting an additional piece of ring-shaped ULE glass to the back of the mirror substrate, effectively “sandwiching” the substrate between two equivalent CTE materials. By varying the parameters of the ring-shaped piece of glass, one can engineer a more favorable T_0 [223].

In order to calculate the effect of the coupling indicated by Eq. 4.51, we performed simulations of the thermo-mechanical deformation of the Big ULE. With the help of Rich Fox at NIST, we were able to measure the Big ULE spacer’s CTE zero-crossing temperature as $T_0 = 15.4$ K using a speed of sound measurement technique. We then used this information to model the net thermal expansion of the Big ULE spacer with fused silica (FS) mirrors. Figure 4.18 shows the deformation with and without the extra addition of a ring due to a temperature change. As explored in [223],

we find that the net CTE of the ULE-FS mixed-material cavity is shifted colder. When we add a ULE ring to the FS mirror, we find that T_0 shifts to higher temperatures. Additionally, we find that the temperature at which the cavity is assembled is a crucial parameter. In general, the net zero-crossing gets pulled in the direction of the temperature at which the cavity was assembled. This general effect is illustrated in Fig. 4.19. We ultimately assumed that the assembly temperature for the Big ULE was 20° C, which led to a T_0 of 16.9° C, and this is the temperature at which we maintain the Big ULE enclosure.

We note in passing that the JILA cavity spacer had a very cold $T_0 \sim 0^\circ$ C. We could not be sure if this result was reliable, since the speed of sound measurement had not been tested in that regime, but subsequent measurements with the JILA cavity at PTB indicated that its T_0 was colder than 5° C, which is inconvenient but not insurmountable.

4.5 A near quantum-limited lattice clock

In this section, we describe how the Big ULE cavity has allowed the ^{87}Sr lattice clock(s) at JILA to demonstrate the highest precision of any neutral atom clocks in the world. Crucially, the 1×10^{-16} near-thermal noise limited performance of the Big ULE has enabled the ^{87}Sr lattice clock to operate close to the quantum projection noise (QPN) limit (QPN in lattice clocks is discussed in detail in Chapter 2). Furthermore, we demonstrate that single-system systematic evaluations—typically carried out with an interleaved measurement scheme—can resolve systematic effects at 1×10^{-17} fractional uncertainty with only 1000 s of measurement time.

4.5.1 Experimental details of the Big ULE

We discussed the support strategy and mounting structure of the Big ULE cavity in Section 4.4. Here, we describe the specific details regarding the Pound-Drever-Hall stabilization, environmental isolation, and delivery of the stable light to the ^{87}Sr lattice clock.

While the finite element analysis was performed to optimize the vibration sensitivity of the Big ULE, we find that a residual sensitivity to accelerations remains at the level of $1 - 2 \times 10^{-9}/g$

in the horizontal direction. The vertical direction seems to be an order of magnitude smaller, but this is difficult to measure with precision. While this is somewhat far from the design goal of low $10^{-10}/g$, this value still reflects favorably on the technique; even though the cavity is almost seven times larger than the “football” cavity design, the vibration sensitivity is only 2–3 times as large. However, a vibration sensitivity at this level requires the best vibration isolation that is commercially available, as well as good acoustic shielding.

In order to provide the highest levels of vibration isolation, we placed the double-layer vacuum chamber that contains the Big ULE onto an actively stabilized optical table (Herzan, model 350S). The accelerations of the top surface are actively sensed and cancelled at Fourier frequencies as low as 2 Hz via piezo-actuated legs. Remarkably, the system can support very heavy loads, and in the current configuration the maximum capacity including the optical breadboard is 600 kG. We measure that the system is capable of reducing the vibrations to the level of $50 \text{ ng}/\sqrt{\text{Hz}}$ to Fourier frequencies of approximately 20 Hz, above which it appears the acoustic environment begins to affect the measurement.

The laser that we eventually stabilize to the Big ULE cavity (see Fig. 4.20 for a schematic overview of the setup) is an external cavity laser diode (ECDL) comprising an anti-reflection laser diode (Opnext/Oclaro part HL7001MG) in the Litmann-Metcalf external cavity configuration [232]. The output power is approximately 40 mW. We lock this laser first to a pre-stabilization cavity using the Pound-Drever-Hall (PDH) locking techniques as in [40], which narrows the laser spectrum to the sub kHz level. Originally we utilized a small portion of the laser output power for the lock, but recently we altered the configuration so that nearly all the laser power is now used for the pre-stabilization lock. The mirrors for the prestabilization cavity are ultra-high finesse mirrors ($\mathcal{F} > 100,000$), and they are spaced only ~ 1 cm apart so that the linewidth of the prestabilization cavity is not so narrow as to affect the ECDL lock to it. Of the 30 mW that arrives at the prestabilization cavity, $\gtrsim 10$ mW of optical power is transmitted through it when the cavity is locked. The transmitted light is used for locking to the Big ULE cavity; the linewidth of the pre-stabilization cavity (~ 100 kHz) allows extra filtration of the optical spectrum past this frequency.

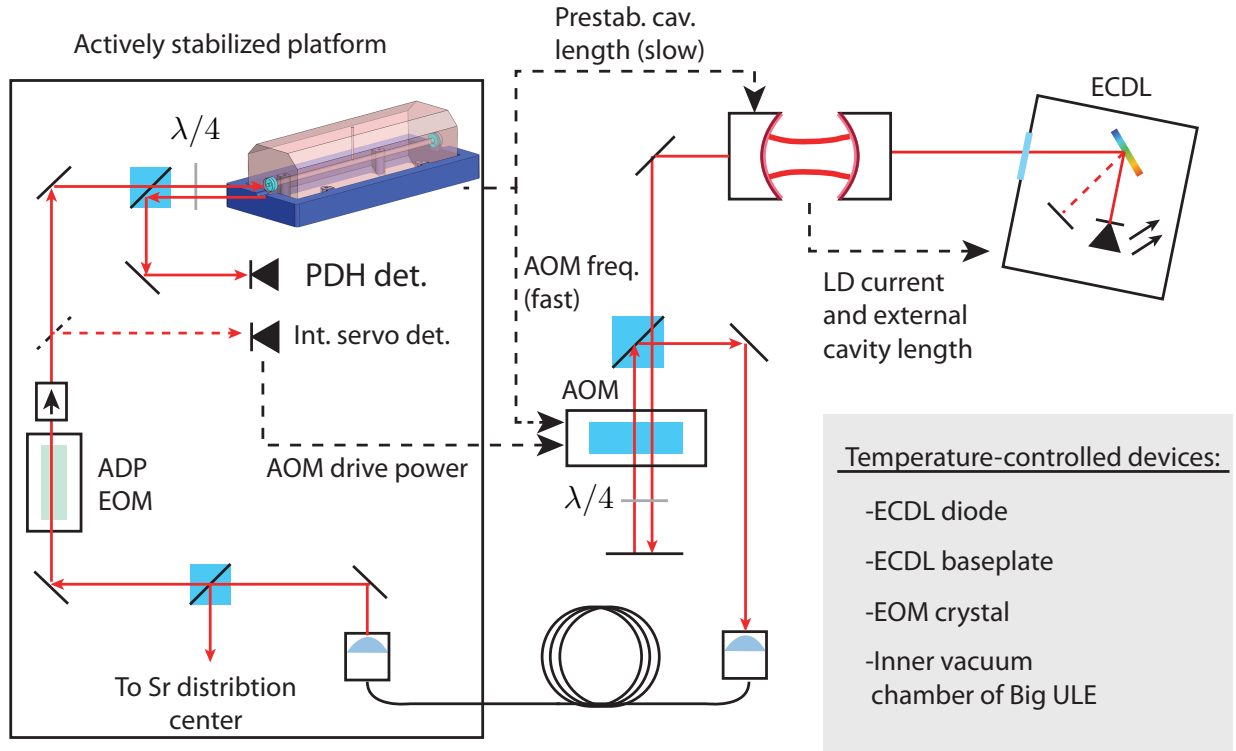


Figure 4.20: Two-stage Pound-Drever-Hall (PDH) locking for laser stabilization with the Big ULE. A fast loop locks the external cavity diode laser (ECDL) to the prestabilization cavity (lock details not pictured). The transmitted light double-passes an acousto-optic modulator (AOM) before traveling to the actively stabilized platform. The PDH lock to the Big ULE employs an ammonium dihydrogen phosphate (ADP) electro-optic modulator (EOM). Part of the $\sim 100 \mu\text{W}$ sent to the big ULE is sampled for active control of the intensity arriving at the Big ULE. A 30 m noise-cancelled fiber delivers $\sim 500 \mu\text{W}$ of power to the Sr distribution center, which is described in Chapter 2.

The laser frequency actuation for the lock to the pre-stabilization cavity is performed via feedback to the laser diode current and the external cavity length via a piezo-actuated mirror. We achieve close to a 2 MHz lock bandwidth, which allows robust tracking as the pre-stabilization cavity length is tuned by a piezo-actuated mirror.

After the prestabilization stage, the laser light goes through a double-pass acousto-optic modulator (AOM) before entering a single-mode fiber that delivers it to the actively controlled optical table and onto a secondary platform near the level of the Big ULE optical axis. We find that the double-pass configuration introduces minimal amplitude noise onto the light as the AOM

frequency is tuned over several MHz.⁵ The fiber collimator is chosen (based on the known mode field diameter within the optical fiber) such that the properly sized beam waist forms at ~ 50 cm from the fiber tip without the need of additional mode-matching optics. The Big ULE has one flat mirror, which serves as the input mirror, and one curved mirror, which serves as the output mirror. The beam waist on the input mirror is $330 \mu\text{m}$. As shown in Section 4.2.1, the finesse is measured to be 194,000, resulting in a 2 kHz cavity resonance full-width at half-maximum and thus a resonance Q -factor of 2×10^{11} . As we describe in Chapter 6, our estimate for the locked-laser linewidth is 26 mHz, indicating that we have achieved a lock precision of nearly 1 part in 10^5 .

The phase modulation sidebands are provided by an ADP-crystal electro-optic modulator. We find that the ADP modulator produces no noticeable residual amplitude modulation (RAM) for the reasons discussed in Section 4.2.4. We do find it necessary to include an optical isolator in front of the ADP modulator, as parasitic etalons can form between the crystal face and other optical elements. As a further step to reduce RAM, we stabilize the crystal temperature. We measure that the RAM and electronic drifts induce lock baseline noise below the level of the expected thermal noise floor of the Big ULE from Fourier frequencies of 10^{-2} Hz to 100 Hz.

We engage the second-stage PDH lock by feeding back to the double-pass AOM with a high bandwidth voltage-controlled oscillator (Mini-Circuits ZX95-78-S+, chosen for its large modulation bandwidth). In order to limit potential optical-power to frequency-offset conversion (i.e., the instance where a laser power change gets converted to a frequency jump), we actively control the power of the light being delivered to the Big ULE for frequency stabilization by additionally feeding back the the RF drive of the double-pass AOM. We do not find that the frequency stability has a sensitive dependence on the optical power being delivered to the Big ULE for PDH locking, but we typically keep it in the 100–200 μW range so that the PDH photodetector is near photon shot noise limited (as explained in Section 4.2.3, fully reaching the shot noise limited regime is overkill).

A portion of the light prior to the EOM is diverted towards a noise-cancelled, 30 m, polarization-

⁵ In fact, the double-pass AOM setup is so robust that the AOM alone can lock the free-running laser diode to the Big ULE cavity for tens of seconds before the ECDL drifts out of acquisition range.

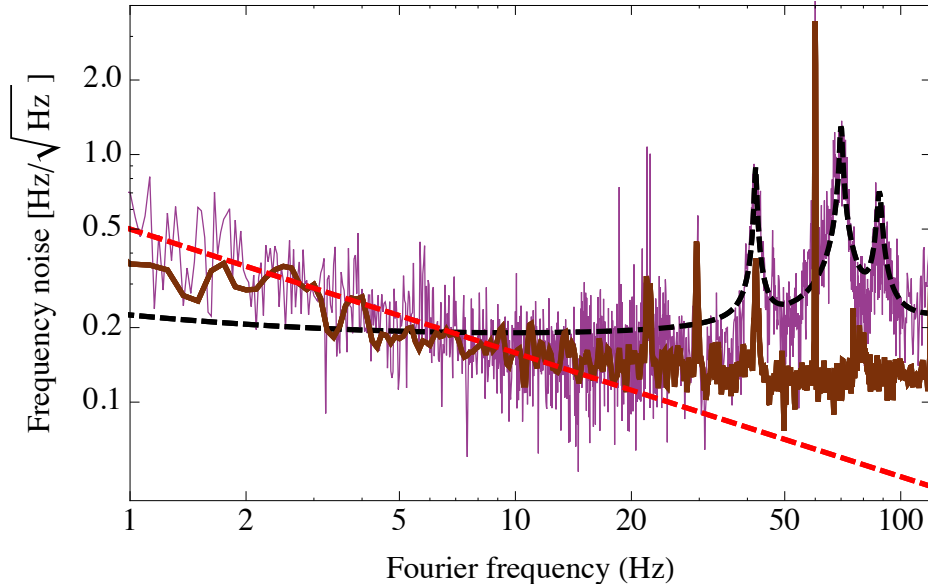


Figure 4.21: Effect of the sound-proof box on the optical frequency spectrum. The purple trace was a frequency measurement against the football cavity and is limited by that systems thermal noise floor at low frequencies (dashed red line). The dashed black trace is a model spectrum for the Big ULE system in the presence of the acoustic noise. The brown trace is the frequency noise spectrum after the installation of the sound-proof box. It is evident that the addition of this enclosure provides $\gtrsim 20$ dB of isolation at frequencies above 50 Hz. We attribute the small, sharp resonances at 22 Hz, 30 Hz, and 42 Hz to acoustic resonances within the “quiet room.”

maintaining, single-mode optical fiber. This fiber delivers light to the injection lock in the Sr “distribution center,” and this system, including the details of how light is delivered to atoms, is discussed in Chapter 2, Section 2.4.3.1.

As a final step to isolate the Big ULE from the world, we have constructed a large ($4' \times 6' \times 3'$) acoustic enclosure around the actively controlled optical breadboard. We utilized multiple layers of damping material, including a high-density polymer and large, textured sound absorbing panels. This enclosure serves to drastically reduce acoustic noise > 50 Hz by $\gtrsim 20$ dB. Figure 4.21 shows the before-and-after optical frequency noise spectra when comparing the big ULE to the old clock laser (i.e., the football cavity), indicating that the large noise peak in the vicinity of 50–100 Hz is almost completely eliminated. Small, sharp resonances remain at 22 Hz, 30 Hz, and 42 Hz. Remarkably, we attribute these to acoustic resonances inside “Jans quiet room” (this is the name for room in

which the clock laser resides), as the frequencies agree remarkably well with the expected resonant frequencies corresponding to the dimensions of the room. This leads the author to believe that small rooms are optimal for high-precision work, so that the room resonant frequencies can be more easily isolated by acoustic enclosures!

4.5.2 Verification of thermal-noise limited performance

As a test of the laser's performance, we locked the clock laser to the ^{87}Sr transition frequency as described in chapter 2. We record the frequency corrections necessary to keep the laser on resonance with the Zeeman-insensitive frequency of the average ^{87}Sr $|F = 9/2, m_F = \pm 9/2\rangle$ clock transition. These corrections are equivalent to the difference between the laser frequency and the ^{87}Sr clock frequency with a constant drift and offset removed. The in-loop error signal averages down quickly indicating that at the 10 s and beyond timescale the measured fluctuations should correspond with the laser frequency fluctuations. As seen in Fig. 4.22, the laser stability is at the level of $\sigma_y(\tau) = 1 \times 10^{-16}$, which is consistent with the theoretically predicted value of 7×10^{-17} .

In order to test the frequency resolution of the system, we scanned out ultra-narrow Rabi lineshapes. A composite scan of such lineshapes is shown in Fig. 4.23 (page 133). We observe that a line-broadening that is correlated with the atomic density, which we explore in detail in Chapter 5. At the lowest densities and using a 3 s Rabi pulse, we are able to repeatedly resolve 500 mHz lineshapes in a single scan, representing a line Q of 9×10^{14} , representing a significant milestone in optical lattice spectroscopy.

4.5.3 High stability for rapid systematic evaluation

As seen in the previous section, the Big ULE performs at the level of thermal noise. One exciting application of such a high-precision system is the possibility to quickly measure a systematic shift via interleaved measurements. The procedure is to operate two independent locks, timed such that their measurements are interleaved with one-another (e.g., lock 1, lock 2, lock 1... etc.) and such that two separate experimental conditions are utilized for each lock. For instance, lock 1

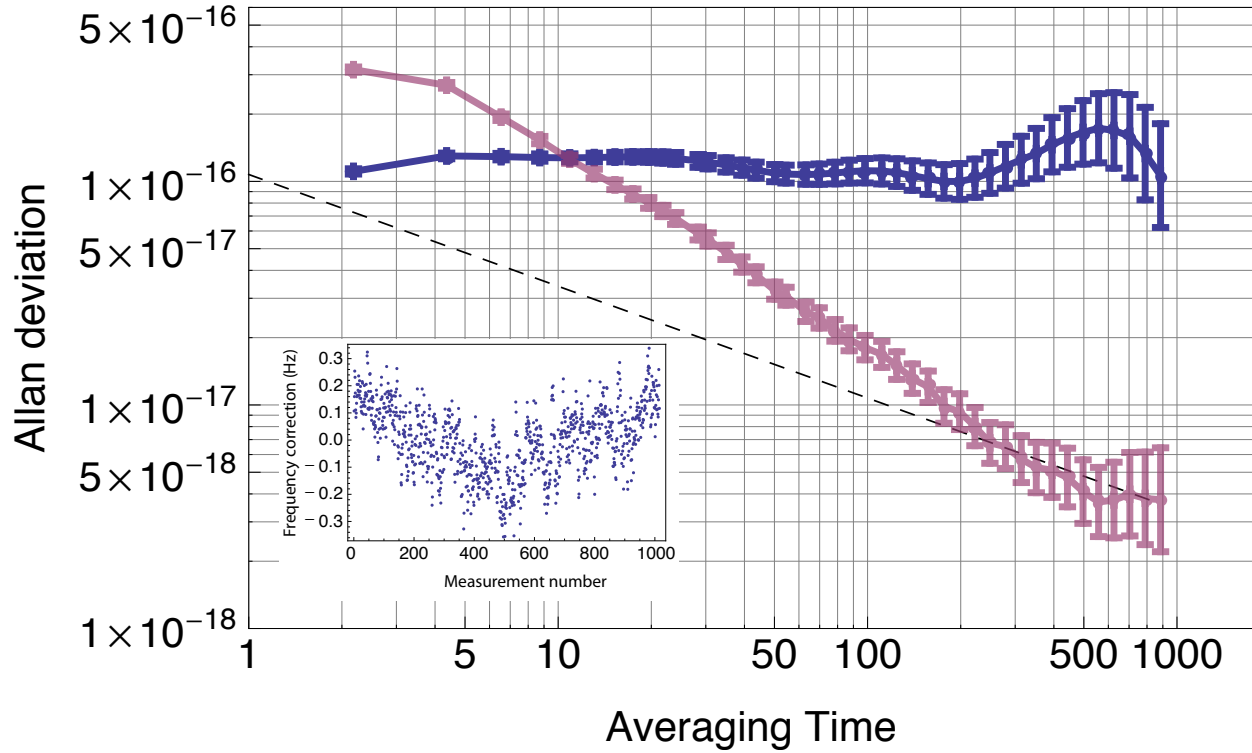


Figure 4.22: Demonstration of a thermal-noise limited laser at fractional instability of 1×10^{-16} from 1–1000 s. The laser performance is measured by analyzing the frequency corrections necessary to keep it on-resonance with the ^{87}Sr clock transition (blue). The in-loop error signal is shown in transparent red, indicating that at time scales > 10 s, the applied correction signals track the clock laser frequency, thus demonstrating that the clock laser performs with stability of 1×10^{-16} . The dashed black line is a $1/\sqrt{\tau}$ guide to the eye, indicating that the in-loop error signal averages down faster than $1/\sqrt{\tau}$. **(Inset)** Time-domain measurement of the clock laser frequency via the ^{87}Sr lattice clock. Each point represents approximately 2 s. Removing the clear quadratic drift results in sub 10^{-16} performance.

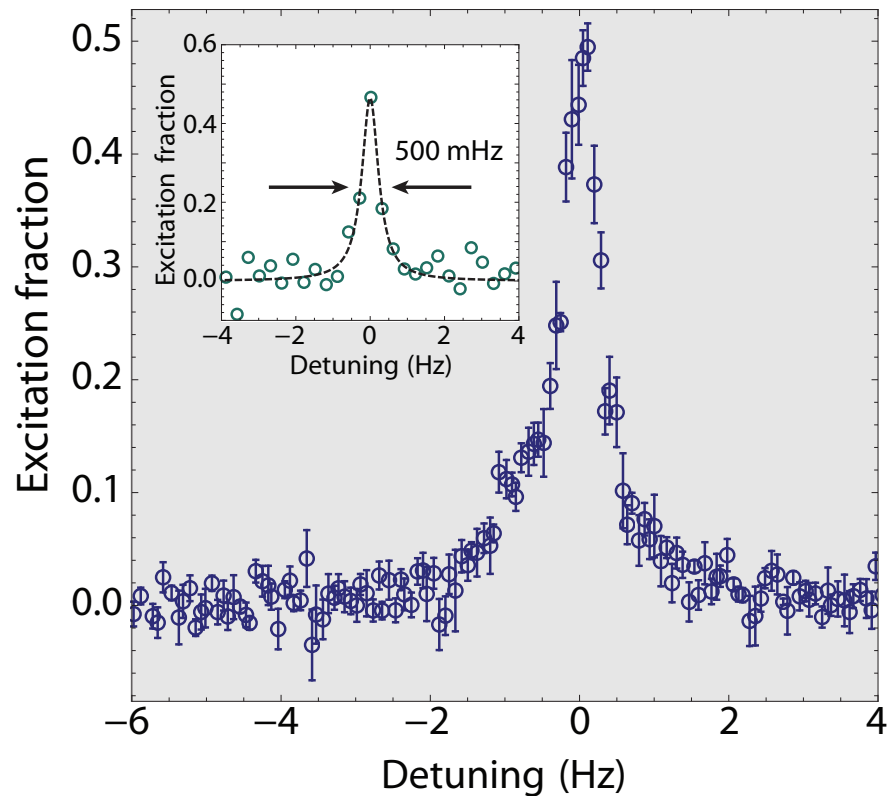


Figure 4.23: Ultra-narrow Rabi lineshapes demonstrating 3-s optical-atomic coherence. The lineshape shown in the main figure is a composite linescan comprised of a total of 20 scans. The 750 mHz linewidth is broadened from the Fourier-limited value of 400 mHz by density-dependent effects. We explore these effects in detail in Chapter 5. **Inset:** an extremely low density single scan with 3 s probe time. The linewidth is 500 mHz and was repeatable as long as the atomic density was kept extremely low. Here, the line $Q \simeq 10^{15}$, representing a milestone in optical lattice clock spectroscopy.

might be a high density condition while lock 2 corresponds to a low density condition. The rapidity with which the difference between these two locks can reach a given measurement precision sets the time scale for measuring systematics in the optical lattice clock. For instance, in the work reported in [135], many days' of averaging were required to make measurements at the level of 1×10^{-17} . However, with the stability of the Big ULE-stabilized clock laser, such measurements can be made at the 1 hour timescale. To test the ultimate performance of the techniques, we operated two independent locks to the same atomic peak (i.e., spin state) and compared the stability of their frequency difference. In order to obtain the highest precision, we used a Rabi pulse time of 500 ms. We compared the central frequency of lock 1 to lock 2 such that

$$\Delta\nu(t) = \nu_2(t + \Delta\tau) - \nu_1(t). \quad (4.52)$$

To remove biases from residual first- and second-order drift, we used a three-point string approach as in [233, 135], as this is the method used for systematic evaluations and is necessary for eliminating systematic errors due to linear and higher-order frequency drifts of the local oscillator. As shown in Fig. 4.24, the precision of a systematic evaluation measurement can reach 1×10^{-17} at 1000 s. The faster than $1/\sqrt{\tau}$ averaging in Fig. 4.24 indicates that the measurement has not yet reached the Dick effect-limited noise floor, at which point it will average down with a $1/\sqrt{\tau}$ dependence.

4.5.4 Clock comparison

At the same time that the Big ULE cavity stabilized laser system was being perfected, a second ^{87}Sr lattice clock came to life in the Ye lab. This second system, lead by Travis Nicholson and Jason Williams, is based on a similar design to the system discussed in Chapter 2 (we will henceforth refer to the system that is described in Chapter 2 and that is the subject of this thesis as “Sr1”; we will call the Nicholson/Williams system “Sr2”). The main difference between Sr1 and Sr2 is the lattice geometry; Sr2 has a cavity-enhanced horizontal lattice with a 160 μm beam waist, such that the trapping frequencies are 100 kHz in the longitudinal direction and 120 Hz in the radial direction. Due to the fact that overlapping the red MOT and the lattice with the

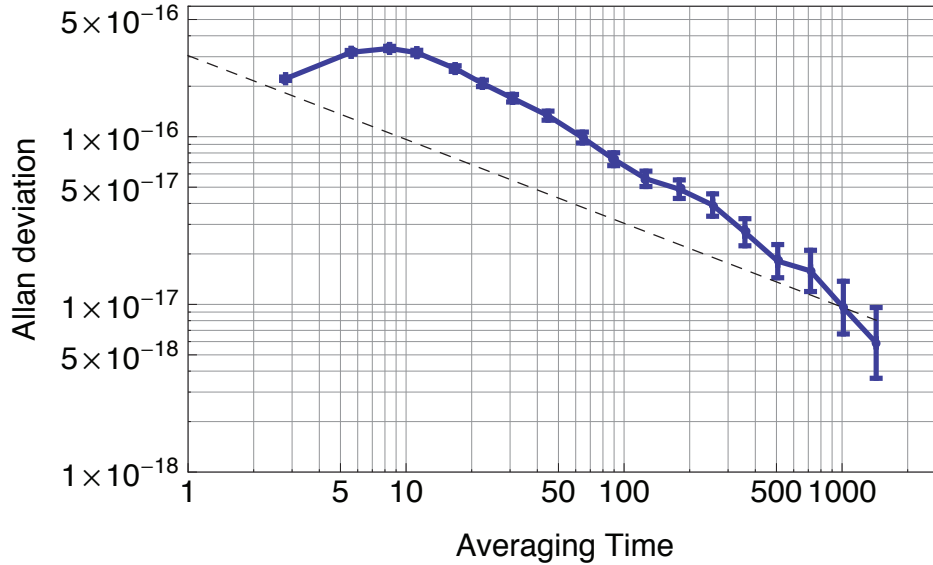


Figure 4.24: Stability of interleaved measurements for systematic evaluation with Rabi pulse duration of 500 ms. A three-point string was used to analyze the data. A new value of $\delta\nu$ is calculated with the point string analysis every experimental cycle, thus the first few points on the Allan deviation are low due to correlations between subsequent point-string filtered data points. At longer averaging times the correlations are minimal and the Allan deviation represents the true stability of lock 1 compared to lock 2.

lattice perpendicular to gravity—as opposed to along it—loads the atoms much more diffusely along the lattice, the densities of Sr2 are approximately a factor of 100 lower than those of Sr1, when combined with the reduced radial trap confinement. The better spatial overlap with the red MOT afforded by the lattice geometry, Sr2 is also capable of loading a factor of 10 more atoms into the lattice than Sr1. We note that the results discussed here can be found in [43].

In order to test the relative stability of the clocks, we used the laser stabilized to Big ULE as the clock laser for both systems. As depicted in Fig. 4.25, Sr1 and Sr2 each have an independent AOM to shift the frequency onto resonance with each clock, with frequencies f_1 and f_2 , respectively. The difference frequency between the systems is derived from the record of f_1 and f_2 . As demonstrated in Ref. [234], frequency comparisons between two clocks that sample the same frequency noise should be immune to the Dick effect. Thus, in order to test the level of instability due to the Dick effect, we performed the experiment with the clock pulses applied synchronously and a with a

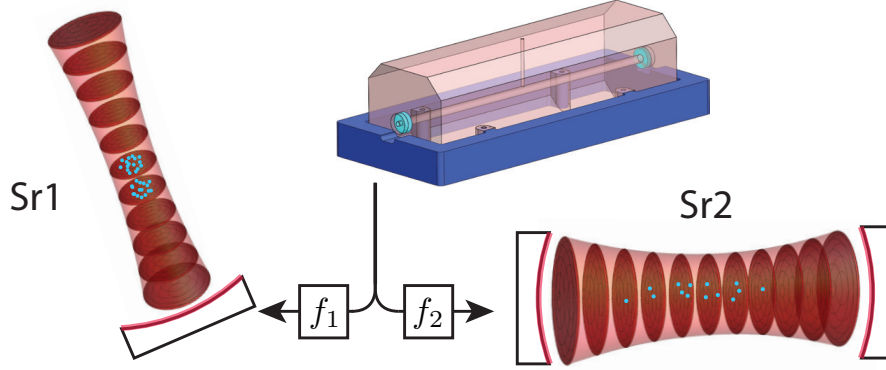


Figure 4.25: Clock comparison scheme. Two independent frequency shifts are applied to the clock laser to steer it to each clock's central frequency. As schematically depicted here, the density of Sr2 is much lower than Sr1 due to both the wider lattice waist and the longitudinal distribution of atoms.

timing offset of 10 ms longer than a single pulse duration. Additionally, in order to limit sensitivity to density-dependent shifts, Sr1 operated with 1000 atoms, while Sr2 operated with 2000 atoms. In order to eliminate first-order sensitivity to magnetic fields both clocks were operated using the two-spin-state procedure as detailed in Chapter 2. Additionally, Sr1 operated at approximately 50% the usual lattice power, such that $\nu_z = 55$ kHz. This was necessitated by the addition of a cavity in the lattice beam to act as a spectral filter, which reduced the optical power, but it also served to better control time-varying density-dependent effect, as the density was decreased with lower trap depth corresponding to $\nu_z = 55$ kHz.

We find that the Dick sensitivity function for comparing two clocks that sample the same laser frequency with a timing offset is related to that of a single clock as derived in Chapter 2 as

$$R^{(2)}(f) \rightarrow 4 \sin^2(\pi f T_0) R^{(1)}(f) \simeq 2R^{(1)}(f). \quad (4.53)$$

Here, $R^{(1)}(f)$ is the sensitivity function considered for the single clock case, and $R^{(2)}(f)$ is the clock comparison case. The most notable change is the $\sin^2(\pi f T_0)$ term, which accounts for the fact that the laser noise is coherently sampled with a time delay and can be derived using the Fourier shift theorem. If the time delay is large enough, this term is rapidly oscillating and we can

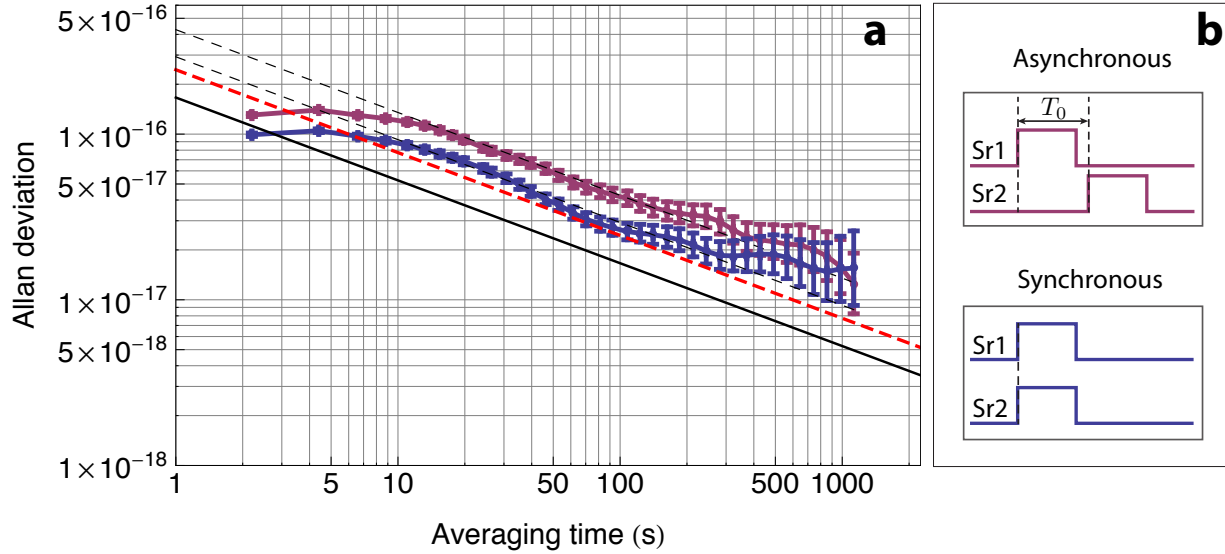


Figure 4.26: Clock comparison Allan deviations and pulse timing. **(a)** Allan deviations of the clock difference frequency with synchronous (blue data points) and asynchronous clock interrogation (red data points). The solid black line is the predicted quantum projection noise floor for the measurement, and the red dashed line is the Dick limit for a laser with thermal noise floor of 1×10^{-16} . Here, the total Rabi pulse time was 160 ms. **(b)** Timing diagrams for asynchronous (top) and synchronous (bottom) interrogation of the two clocks. For the data shown in (a), $T_0 = 170$ ms.

replace it with its average (as is done for the rightmost expression in Eq. 4.53). This represents the limit where the two clocks are operated with independent lasers. We find that the inclusion of the $\sin^2(\pi f T_0)$ term affects the predicted Dick noise limit with respect to the assumption of uncorrelated clocks, at the level of 5%. Thus, the unsynchronized comparison is a robust indicator of independent clock performance.

As shown in Fig. 4.26, the synchronous interrogation averages as $\sigma^{\text{sync.}}(\tau) \simeq 3 \times 10^{-16} / \sqrt{\tau/1 \text{ s}}$, while the asynchronous one averages down with only slightly larger instability, at $\sigma^{\text{async.}}(\tau) \simeq 4 \times 10^{-16} / \sqrt{\tau/1 \text{ s}}$. This indicates that the Dick noise plays only a small role in the clock instability. From these data, we were able to demonstrate an independent clock comparison (i.e., asynchronously operated clock comparison) to within a factor of 2 of the expected quantum projection noise limit. This represents an important milestone in the history of lattice clocks and is an order of magnitude improvement over the best comparison of ion clocks, which have attained

measurement precision of $\sigma_y(\tau) = 2.8 \times 10^{-15}/\sqrt{\tau}$ [27]. Thus, a given frequency measurement would take a factor of nearly 100 less averaging time when performed with the ^{87}Sr lattice clock vs. a single-particle clock! This turns a solid month of measurement into an afternoon.

We note that at the level of 1×10^{-16} , many other noise sources besides laser noise are also possible, including fast bias magnetic field noise (which creates its own Dick effect) and other technical sources of noise. Finally, we note that the laser is not expected to be thermal noise limited for all Fourier frequencies. In Fig. 4.22, we demonstrate that the long-term behavior of the clock laser is consistent with $1/f$ noise that produces a flicker-floor limited instability at 1×10^{-16} . However, we will see in Chapter 6 that simple spectroscopic tests indicate the presence of white noise of $G_\nu^{\text{white}}(f) = 3.3 \times 10^{-3} \text{ Hz}^2/\text{Hz}$, in addition to the flicker floor of $f \times G_\nu^{\text{flicker}}(f) = 1.3 \times 10^{-3} \text{ Hz}^2$ that corresponds to a $\sigma(\tau) = 1 \times 10^{-16}$ instability. We will show the presence of additional coherent noise features, which do not affect the Dick floor significantly for the operating conditions considered here, so we save discussion of these features for Chapter 6. The addition of the extra white noise floor, which we rigorously verify in Chapter 6, is sufficient to completely describe the measured instability in the clock comparison of Sr1 and Sr2.

4.6 PTB Si cavity and JILA cavity intercomparison

As discussed in the previous section, improvements in ultrastable lasers can have a huge impact on optical lattice clocks. This is embodied in the reduction of clock systematic measurement times from weeks to mere hours and the attainment of near QPN-limited clock performance. However, the reader may have gotten the feeling that conventional technology is approaching its limits; after all, the Big ULE is nearly 40 cm in length, so to gain another factor of 10 improvement, one would need a 4 m cavity! There are other tricks one can play, including operating in near-concentric or near Fabry-Pérot (i.e., flat-flat mirror combination) geometries, but the fact remains: gaining a factor of 10 is extremely challenging. Clearly novel technologies are needed.

One such avenue opened in 2007 in collaboration between JILA (Ye Lab) and PTB. The idea was to use single-crystal silicon as a cavity spacer and mirror substrate material. Silicon has

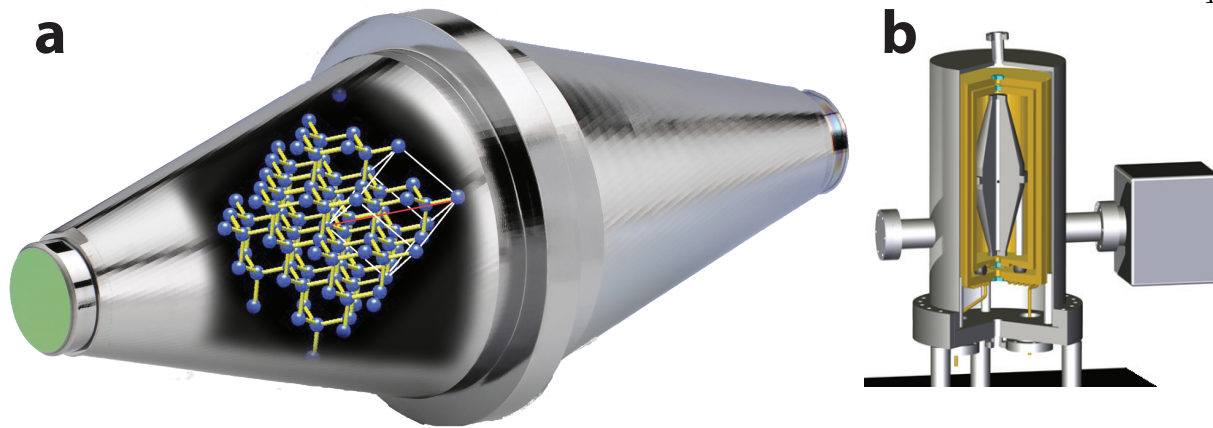


Figure 4.27: The silicon cavity. (a) Silicon cavity with inset showing the Si crystal lattice structure. The green surfaces on the mirrors are from the anti-reflection coatings applied to the Si. (b) The PTB-designed cryogenic vacuum system and support strategy. The cavity is held vertically and is supported by three symmetrically placed Teflon posts. An outer heat shield is cooled to 124 K within the vacuum envelope, while a second heat shield increases the thermal time constant between the temperature-controlled outer shield and the optical cavity to 10 days.

several advantages. Firstly, the loss angle is 1–2 orders of magnitude smaller than fused silica and doesn't suffer increase at lower temperatures as does fused silica. Secondly, the Young's modulus is also larger than that of glass by about a factor of two, which reduces thermal noise. Additionally, the stiffness of the material, or ratio of Young's modulus to density E/ρ is about a factor of 2.5 larger than ULE or fused silica, indicating that one should expect a comparable decrease in vibration sensitivity. Finally, the coefficient of thermal expansion (CTE) has two zero-crossings, of which the one at higher temperature is at 124 K. At the zero crossing, the cavity length should be extremely stable in the long-term as the crystalline nature eliminates the material creep observed in amorphous glass.

The original FEA simulations for the cavity were performed at JILA and subsequently PTB, with Lisheng Chen performing the finite element analysis on the JILA side. After several years, the design work culminated in the construction of a vibrationally insensitive high-finesse optical cavity comprised of a monocrystalline silicon spacer and optically contacted silicon mirrors with SiO₂/Ta₂O₅ coatings. The spacer geometry is shown in Fig. 4.27a. In order to exploit the crystal

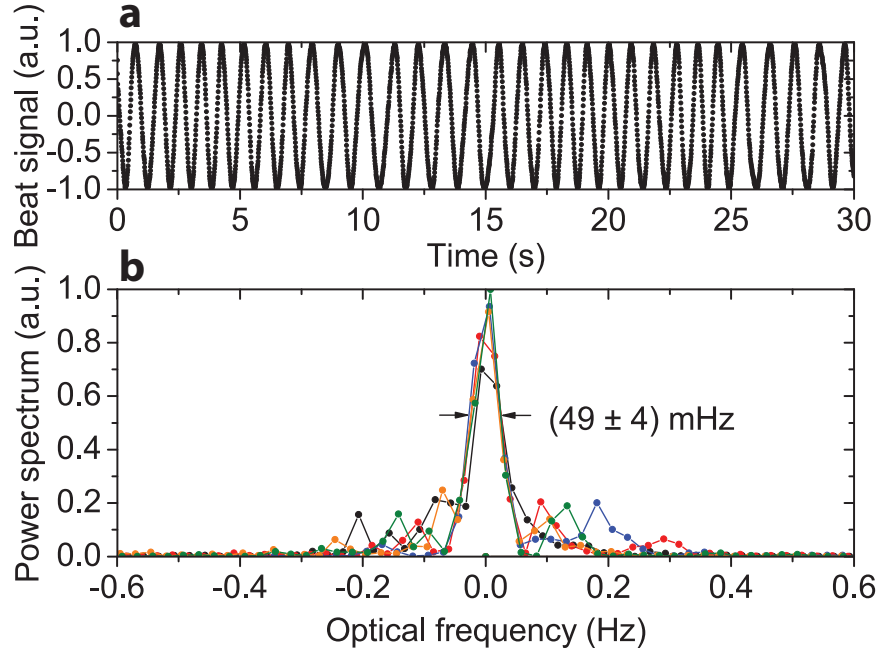


Figure 4.28: Direct optical beat between the JILA cavity and the Si cavity. (a) The time-domain signal of the optical beat mixed to near DC exhibits a ~ 10 s coherence time. (b) The power spectrum of the optical beat between the two systems displays a repeatable 50 mHz linewidth (different colors correspond to separate measurements).

symmetry, the cavity is oriented with the Si $\langle 111 \rangle$ crystal axis pointed vertically. The mirrors are contacted with the crystal axes nominally aligned, so that the entire ensemble simulates a single-crystal. The cavity is supported on Teflon legs, each along one of the three equivalent $\langle 110 \rangle$ directions [168].

To reach the CTE zero-crossing, PTB colleagues designed a novel low-vibration cryostat to house the silicon cavity and cool it to 124 K in-vacuum (the apparatus is shown in Fig. 4.27b). The cryostat uses nitrogen gas boiled off from a liquid nitrogen dewar to cool a heat shield inside the system’s vacuum chamber, achieving sub-mK stability on an outer thermal shield within the vacuum envelope. The time constant between this envelope and the cavity is 10 days, indicating that fast-temperature fluctuations will be heavily suppressed [168].

In order to test the performance of the silicon cavity, we transported the “JILA cavity,”

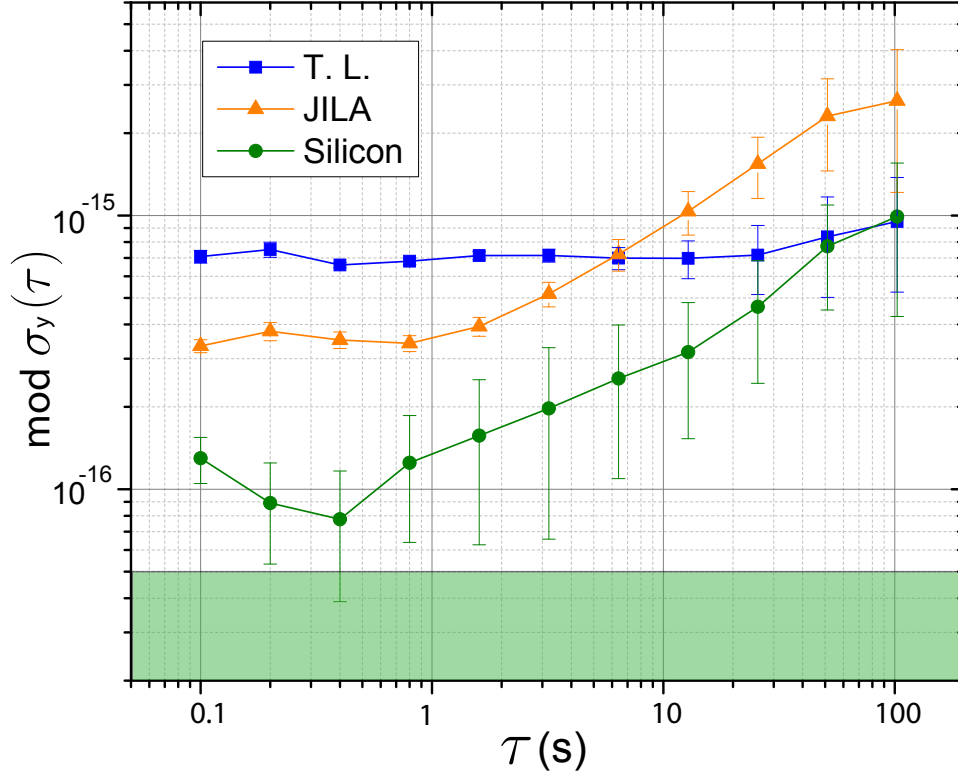


Figure 4.29: Modified Allan deviation of the stabilities extrapolated via the three-cornered-hat analysis. Here, the modified Allan variance is used to reduce sensitivity to higher frequency phase noise and better reveal the thermal noise floor.

described in Section 4.4.2 of this thesis, to Braunschweig, the charming German town on whose outskirts PTB is located. With a predicted thermal noise floor 2×10^{-16} , this cavity would be close to the predicted noise floor of the Si cavity of 7×10^{-17} . The cavity was installed in its vacuum chamber and, despite the presence of non vacuum-compatible Peltier elements and wires (we drew inspiration from Ref. [178]), we were able to pump the system to the level of 10^{-7} Torr and were able to cool the cavity to $\sim 10^\circ$ C with the in-vacuum Peltier elements. Any attempt to reach colder temperatures induced the system (which was inside a sound-proof and rather well thermally-insulated box) to go into thermal run-away.

An early setback for the JILA cavity was the discovery that the finesse of the mirrors was only 80,000. In fact, a similar problem was observed with the Si cavity for the TEM00 mode,

but fortuitously the TEM01 mode had a finesse of 240,000. Unfortunately for the JILA cavity, we had no such luck with higher order modes. This meant that any residual amplitude modulation would create a proportionally larger frequency offset, due to the small slope of the cavity frequency discriminant. However, both cavities employed waveguide modulators with the active RAM cancellation system whose development we described in Section 4.2.5. When both systems were working successfully, which took two weeks of hunting down parasitic effects, we were able to observe a 50 mHz beat between the two systems, and near 10 s optical coherence times, as shown in Fig. 4.28, and which represents a record for a measured optical linewidth between two independent lasers. This corresponds to a coherence length beyond 1×10^9 m, the length scale of the proposed Laser Interferometer Space Antenna (LISA). This result additionally demonstrates the success of the RAM servo; in order to achieve a linewidth of 50 mHz, the JILA cavity RAM cancellation servo permitted lock precision sufficient to split the cavity resonance better than 1 part in 10^5 . In the field of cavity stabilization, this level of lock precision is among the best reported (see, e.g., [215]).

We additionally note that the intercomparison between the JILA cavity verified the success of the finite element analysis. By shaking the Minus-K platform on which the JILA cavity sat and measuring both the frequency of the beat signal and magnitude of the accelerations, we found that the vibration sensitivity was $< 5 \times 10^{-10}/g$.

In order to isolate the performance of the silicon cavity, we included a third cavity-stabilized laser system in the measurement. This laser was designed and constructed by PTB colleague Thomas Legero (thus we will call this laser “T. L. cavity” system) and was designed to be transportable. It is similar to the system described in [235]. Due to its smaller size and ULE mirrors, the thermal noise floor of this cavity is 6×10^{-16} .

We performed three simultaneous beat measurements between all two-way permutations amongst the Silicon cavity-, JILA cavity-, and T. L. cavity-stabilized laser systems. The beats were performed at a common location connected by noise-cancelled fibers to all three systems. We analyzed the beat record using the “three-cornered-hat” method [236]. Assuming uncorrelated noise between three laser systems, the instability of one of the systems at a given time can be

calculated from the other two as

$$\sigma_i = \sqrt{\frac{1}{2} \left(\sigma_{ij}^2 + \sigma_{ik}^2 - \sigma_{kj}^2 \right)}, \quad (4.54)$$

where i , j , and k can represent any laser we listed above: silicon, JILA, or T. L. In order to remove the possibility of correlations amongst the lasers, we used the extended technique described in Ref. [237]. The result of this analysis is shown in Fig. 4.29. The Si cavity-stabilized laser has extrapolated performance at the level of 1×10^{-16} from 0.1 s to 10 s, showing the promise of cryogenic cavities. As mentioned previously the expected thermal noise floor of the Silicon cavity is 7×10^{-17} , and which is entirely dominated by the coating ($> 99.8\%$). The JILA cavity also performed at a near-thermal noise limited level from 0.1 s to 2 s. The $\sqrt{\tau}$ rise evident in the JILA cavity's stability in Fig. 4.29 is indicative of random walk frequency noise. We believe that this originates from material stresses in the machined ULE support structure for the JILA spacer. We have mitigated this problem in the Big ULE cavity (where it had also initially been evident) by using large, soft Viton hemispheres to only weakly couple the baseplate and cavity. Future implementations of the JILA cavity would also benefit from this support strategy. Another possible reason for the rapid increase the Allan deviation of the JILA cavity is the fact that the temperature was maintained about 10° C above the nominal zero-crossing temperature for that spacer, leading to a possible first-order temperature sensitivity of approximately 1.8×10^{-8} /K.

Finally, we note that subsequent tests of the long-term stability of the Si cavity are very promising, already demonstrating the best long-term stability of any passive optical etalon. This verifies the expectation that a crystalline material should be free of the “creep” that seems to be intrinsic to amorphous materials. For instance, the big ULE cavity is elongating at approximately 1 nm/year (or 5×10^{-17} m/s), as extrapolated by the predictable day-to-day frequency drift.⁶ In contrast, the measured long term frequency stability of the silicon cavity indicates that its long-term drift is below $200 \mu\text{Hz/s}$ [168], indicating that the mirrors are stable with respect to each other on the scale of 1 fm over the course of the day. Paired with an atomic clock, this level of stability

⁶ It is remarkable to think that one can measure these extremely slow velocities with atomic clocks. This would also seem to dispel the myth that the ripples in old windows are caused by amorphous creep!

could yield an extremely precise Kennedy-Thorndike test of relativity due to the unprecedented combination of short- and long-term stability in an optical resonator [238].

4.7 Crystalline mirrors

The results of the previous section serve to demonstrate that a cryogenic system can perform at the highest levels of stability, approaching the level of the best conventional cavities, such as the “Big ULE” cavity demonstrated in Section 4.5. However, the improvement in laser stability due to operating at 124 K alone is less than a factor of two. The real gain from silicon, which has better material properties, but **requires** operation at 124 K, is that the substrate thermal noise is almost entirely removed, leaving only the coating contribution. Indeed, for the silicon cavity described in the previous section, $> 99.8\%$ of the thermal noise is due to the coating itself. This implies that even modest improvements in coating loss angle will result in significant advances in laser stability. In this section, we report such an advance, where we extend the use of high- Q crystalline materials to the high-reflectivity mirrors themselves.

The desire to engineer cavities with components possessing the lowest possible mechanical loss shares connections with the field of quantum optomechanics, where coupling to a thermal bath via mechanical losses can impede measurement precision and quantum coherence. [171, 144]. As mentioned in Chapter 3, Section 3.2.2, heterostructures based on GaAs and $\text{Al}_x\text{Ga}_{1-x}\text{As}$ semiconductor materials (the subscripts stand for doping concentrations) have demonstrated high mechanical Q 's when used as isolated optomechanical structures, with Q -factors of up to 40,000, corresponding to a loss angle of 2.5×10^{-5} [167]. Thus, crystalline mirrors made from a multilayer GaAs/AlGaAs would be a powerful new technology for high-precision laser stability.

Luckily the group of Markus Aspelmeyer along with colleague Garrett Cole were already thinking along those lines, and provided us with the opportunity to test the feasibility of their coating technology—which works so well at the nanoscale—in macroscopic mirrors. They developed a technique to remove a film of multilayer GaAs/ $\text{Al}_{0.92}\text{Ga}_{0.08}\text{As}$ from its growth substrate and to directly bond it to a separate substrate of any other material via optical contacting. In this way,

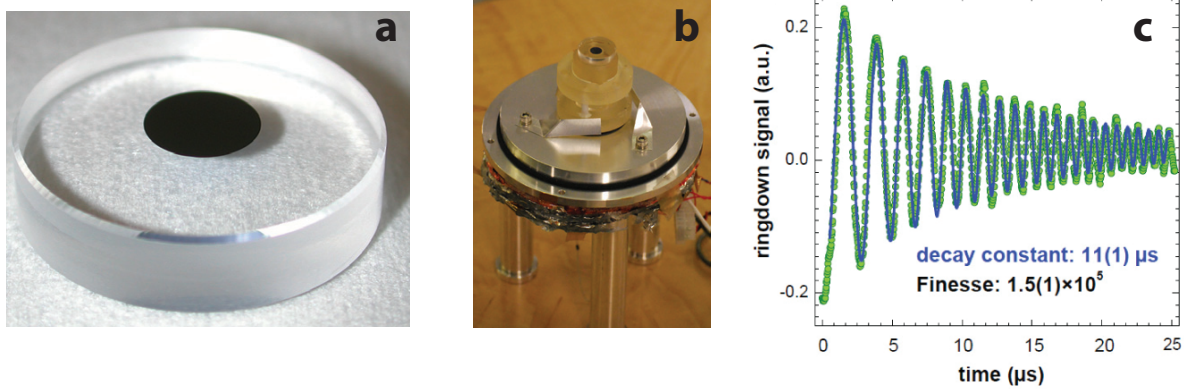


Figure 4.30: Crystalline mirror and cavity. (a) GaAs/Al_{0.92}Ga_{0.08}As crystalline mirror bonded to a fused silica mirror substrate. (b) Completed cavity 3.5 cm in length employing two optically contacted GaAs/Al_{0.92}Ga_{0.08}As mirrors for operation at 1064 nm. The cavity spacer is Zerodur (c) Optical ringdown signal with a swept input field. The extrapolated finesse is 150,000.

the film can be grown as a crystal, and the crystalline properties transferred to a host substrate, which could be crystalline silicon or sapphire, or even fused silica glass. Figure 4.30a shows a completed mirror crystalline mirror on a fused silica substrate that was constructed using this bonding method. With this technique established, all that remained was to test the optical and mechanical properties of such a composite mirror.

In order to test the optical and mechanical properties of the mirrors, a new postdoc, Wei Zhang, and this author constructed the cavity as shown in Fig. 4.30b. Here, the cavity spacer material is Zerodur glass, which was chosen due to its convenience (i.e., we already had the spacer in the lab). The length is 3.5 cm. The operating wavelength was 1064 nm, which is important given that with the semiconductor material interband optical absorption can be an issue, although in principle mirrors constructed with AlGaAs could work to 650 nm with different doping concentrations than those utilized for the 1064 nm mirrors [172]. The mirrors with the transferred crystalline coatings are optically contacted to the spacer. This particular cavity has a long history of making thermal noise measurements in the Ye lab, and was utilized in some of the first measurements to explore the effect of cavity material properties on thermal noise [239]. The first measurements that we performed with this crystalline-mirror cavity were to test the optical quality factor. The cavity

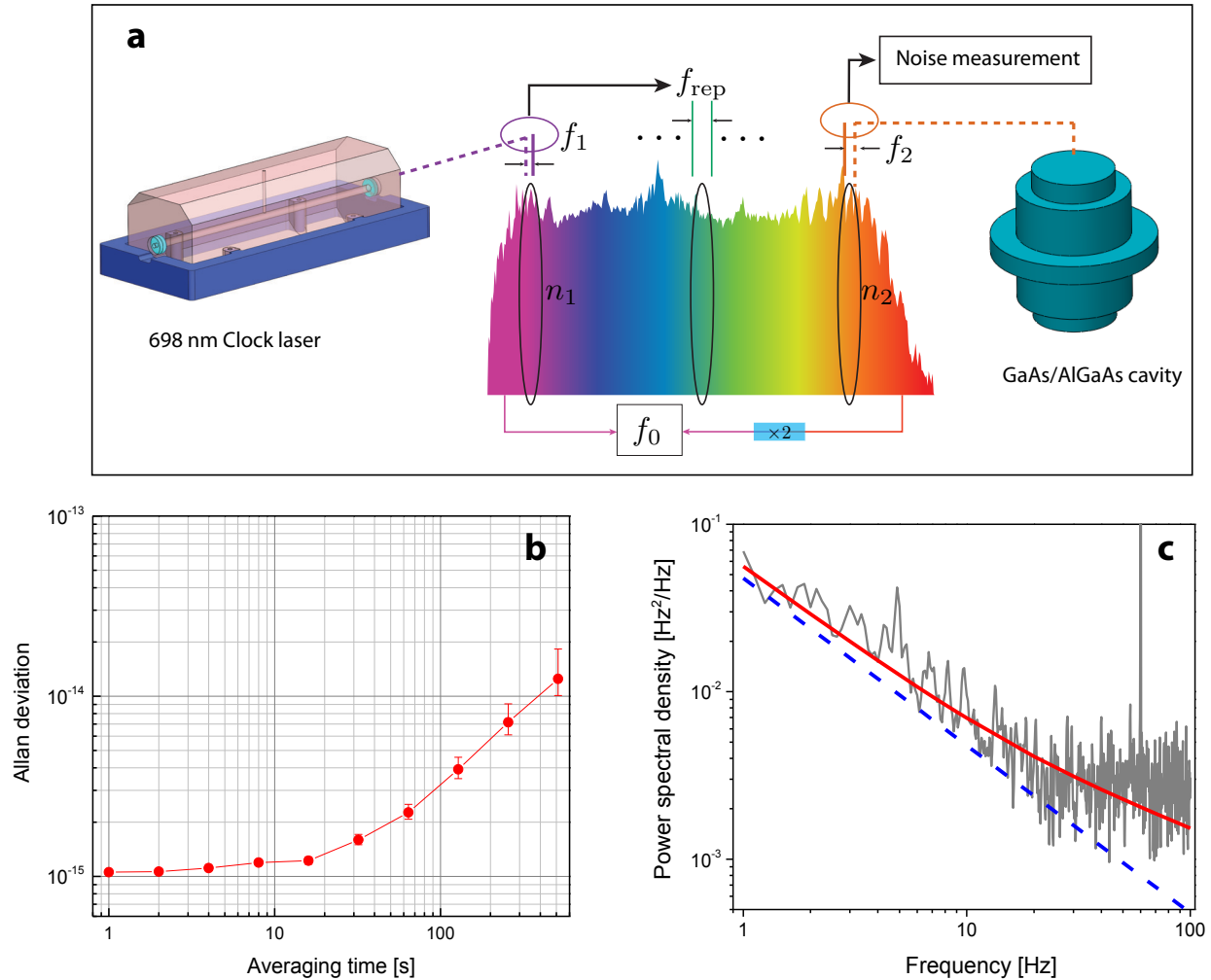


Figure 4.31: Comb frequency-transfer and stability of a laser locked to the cavity employing GaAs/AlGaAs crystalline mirrors. (a) The optical frequency comb is stabilized by locking it to the clock laser at 698 nm and locking the carrier envelope offset frequency, f_0 , to a RF reference. (b) Allan deviation of the measured beat between the crystal-mirror cavity and the comb. (c) Frequency noise power spectral density of the beat at 1064 nm (grey line). The contribution of Brownian noise is indicated by the dashed blue line. The solid red line shows the contribution of all thermal noise, including substrate thermo-elastic and coating thermo-optic.

was placed inside a temperature controlled vacuum enclosure, and we performed optical ring-down measurements. It was exciting to see measure a finesse of 150,000 (Fig. 4.30c). This, in fact, was exactly consistent with measurements of the absorption, scatter, and transmission losses, which were measured to be 13.5 ppm, 4 ppm, and 4 ppm, respectively [172].

The second test we performed on the cavity was to measure the stability of a laser locked to it. The laser source was a non-planar ring oscillator (NPRO) YAG, with excellent short-term stability, corresponding to a free-running linewidth of ~ 1 kHz. The NPRO was stabilized to the crystalline cavity. Notably, this setup also employed a waveguide modulator and RAM servo for the PDH lock, as described in Section 4.2.5. In order to measure the stability of the crystalline-mirror cavity-stabilized laser, we compared it to the Big ULE clock laser described in Section 4.9 and whose performance at the level of 1×10^{-16} was verified in Section 4.5.2. In order to span the spectral gap, we employed the Yb:fiber frequency comb described in [240]. This setup is depicted schematically in Fig. 4.31; the Yb comb is locked to the clock laser at 698 nm using fast actuation to an intra-cavity EOM, a piezo-mounted semiconductor saturable absorber mirror (SESAM), and to a fiber-stretching drum piezo. The carrier envelope offset frequency, f_0 , is also stabilized using an AOM external to the laser cavity.

Figures 4.31b and 4.31c show the measured Allan deviation at 1064 nm, and the frequency noise at 1064 nm, respectively. At 1 s, the measured Triangle deviation is $\sigma_y^\Lambda(1 \text{ s}) = 1.05(1) \times 10^{-15}$. The reason we measure Triangle deviation is because we use an Agilent 53131A counter in “time arming” mode, which corresponds to a Λ -type sensitivity function, as defined by Dawkins *et al.* [241]. By summing the thermal noise contributions of all the components as detailed in Chapter 3, we find that given the measured $\sigma_y^\Lambda(1 \text{ s})$ the loss angle of the bonded AlGaAs mirrors is $\phi_{\text{AlGaAs}} = 0(4) \times 10^{-5}$, where the error bar includes an assumed 10% error in the measured $\sigma_y^\Lambda(1 \text{ s})$, and 20% errors in the loss angles of the relevant materials, namely Zerodur and fused silica.⁷

Figure 4.31c shows the measured frequency noise power spectral density. The contribution of Brownian noise alone (dashed blue line) is compared to the total thermal noise, including thermo-optic and thermo-elastic noise, and the measured data. Importantly, we begin to see the effect of thermo-optic noise in this measurement, although it is not well resolved. This noise is at high enough Fourier frequencies that it is not a significant problem for optical clocks, but might have important

⁷ We utilized the standard loss angle for fused silica of $\phi_{FS} = 10^{-6}$. If instead we used $\phi_{FS} = 10^{-7}$, the extrapolated loss angle of the crystalline coating is $\phi_{\text{AlGaAs}} = 4(4) \times 10^{-5}$.

implications for LIGO, as the spectral region where thermo-optic noise dominates is LIGO's relevant detection band. As discussed briefly in Chapter 3, the addition of a half-wavelength cap of AlGaAs will potentially drastically reduce the contribution of thermo-optic noise. Thermo-elastic noise will be eliminated by eventually operating a cavity with Si mirrors at the CTE zero-crossing, such that the coefficient of thermal expansion of the mirror substrates is zero.

In conclusion, these measurements indicate that AlGaAs coatings are the future of high-precision laser stabilization and interferometry. AlGaAs heterostructures bonded to substrates can retain the low mechanical losses of free-standing structures. With a silicon cavity with AlGaAs mirrors, one could expect a thermal-noise limited laser stability at the level of 1×10^{-17} using the already-established cryogenic silicon system and AlGaAs crystalline coatings. Thus, instead of the daunting task of improving the thermal noise limitations of conventional cavities, the all-crystalline-cavity approach should allow rapid attainment of the next factor of 10 improvement in laser stability.

4.8 Frequency comb development: bridging spectral gaps coherently

As seen from the measurement of the crystalline-mirror cavity performance in the previous section, optical frequency combs will play a central role in the direct operation of atomic clocks. To date, frequency combs have been used primarily to connect clocks of disparate optical frequencies [31, 242] or for optical frequency measurements e.g., [1] (or even to reverse the process for ultrastable microwave generation from ultrastable optical resonators [243]). However, the recent developments in creating ultrastable lasers based on cavities constructed from crystalline mirrors have restricted the wavelengths over which ultrastable lasers can operate. A frequency comb [244] (or perhaps second harmonic generation if the appropriate wavelength is obtained) is required to connect the ultrastable laser, which may operate in the telecom spectral region, to the optical clock transition of interest. In this section, we summarize some key tests of comb stability that have been performed.

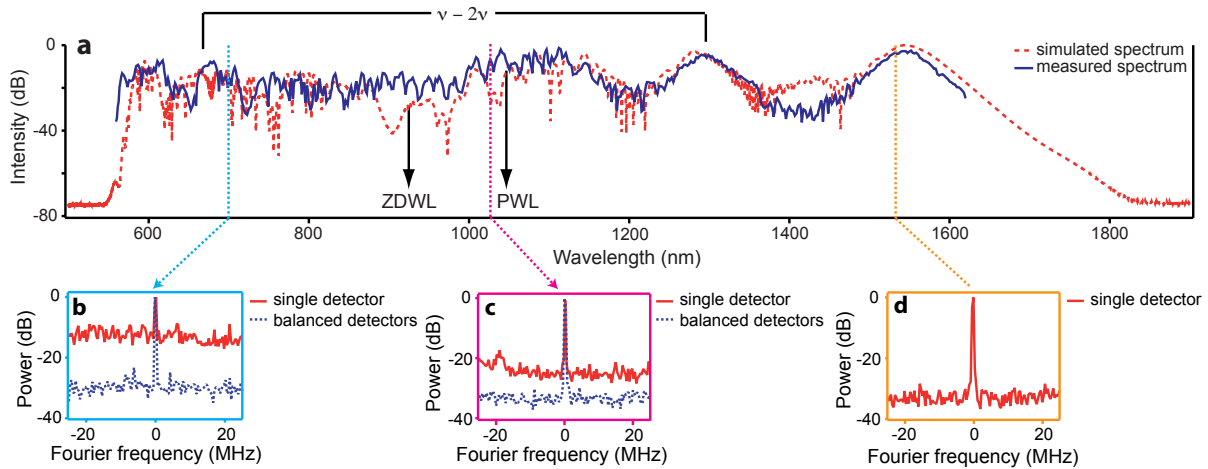


Figure 4.32: Spectrum of the ultra-broadband Yb: fiber comb and optical beats. (a) Measured optical spectrum of the comb supercontinuum (solid line) and simulated spectrum based upon the nonlinear fiber input pulse parameters (dashed). (b) Optical beat with a CW laser at 698 nm. (c) Optical beat with a CW laser at 1020 nm. (d) Optical beat with a CW laser at 1.54 μm . Plots (b–d) indicate varying levels of amplitude noise. This is evident from the beat signal-to-noise without (solid) and with (dashed) balanced detection. No excess amplitude noise was visible at 1.54 μm while at 698 nm the noise floor rose by 20 dB in the absence of balanced detection, indicating significant amplitude noise at this wavelength.

4.8.1 Ultra-broadband Yb: fiber comb

To take advantage of the relative robustness, compactness, and a gain medium that does not need to be pumped with lasers that cost $\mathcal{O}(\$100,000)$, we extended a collaboration with IMRA America Inc. to include medium power Yb: fiber laser systems. Already, a 10 W system from IMRA had shown extremely low-noise operation [245]. With the new system, we did not need 10 W optical power; instead we set out to see if we could connect the telecom and the visible wavelength regions in a single step. We briefly describe the system and results here.

The frequency comb comprised Yb: fiber similariton oscillator [246] and linear chirped pulse amplifier. Starting with 80 fs 1.4 nJ pulses at a repetition rate of 150 MHz, we broadened the spectrum to 1.5 octaves (Fig. 4.32) in a single piece of suspended-core highly nonlinear fiber [247]. As seen in Fig. 4.32a, the spectrum was highly featured. We found that these features were well

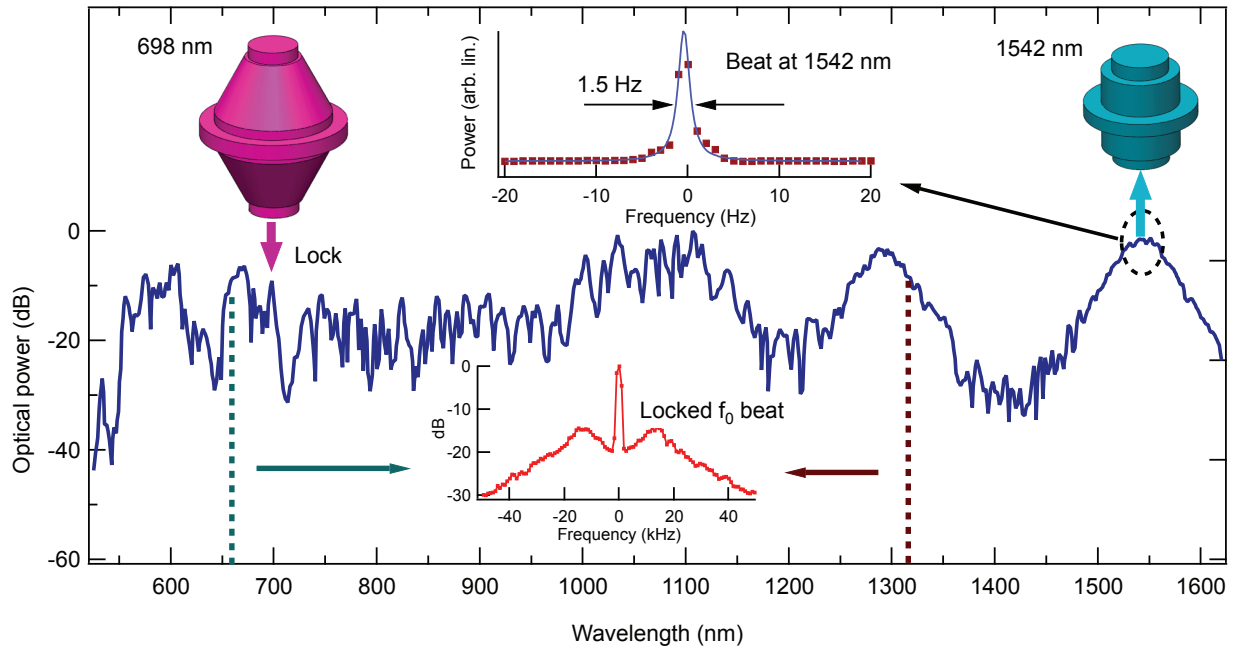


Figure 4.33: Spectrum of broadened Yb oscillator and relevant beat notes at 698 nm and 1.54 μm . The self-referenced (bottom inset) comb is locked to a 698 nm sub-Hz linewidth laser and the beat note with a second ultra-stable laser at 1.54 μm is shown (top inset).

described by the theory of supercontinuum generation in optical fibers, including the phenomena of soliton fission (responsible for the two “bumps” in the spectrum at right) and self-phase modulation. As shown in Figs. 4.32b–4.32c, balanced detection of optical heterodyne beats between the comb and CW laser sources indicated that certain spectral regions of the supercontinuum had large amounts of amplitude noise, but no phase noise. We were able to explain this phenomenon through modeling of the supercontinuum generation process, and found that quantum-seeded input noise is responsible for the presence of amplitude noise. While we do not go into detail here, these measurements also indicated that the higher fraction of Raman gain in the fiber played an important role in maintaining phase coherence [56].

In order to test the broadband comb coherence, we performed the experiment depicted in Fig. 4.33. With the carrier envelope frequency, f_0 , stabilized, we locked the broadened comb to the “football cavity”-stabilized clock laser at 698 nm [40] and analyzed the beat signal with a

second cavity-stabilized laser at 1542 nm. We found that the comb supports the coherent transfer of optical phase from 698 nm to 1542 nm at or below the level of 1.5 Hz linewidth, consistent with the expected performance of the 1.5 μm laser. This represents the largest spectral gap directly spanned between two ultra-stable lasers by a frequency comb to date. While this may not be **the best** way to connect lasers that are separated by over an octave of optical spectrum, it does serve to define a boundary of what is possible.

4.8.2 Ultimate limits of comb performance

In the previous section, we described an experiment where the test of comb coherence was limited by the ultrastable lasers used as references. Here, we describe an experiment performed with an octave spanning Ti:Sapphire frequency comb, where the octave-spanning comb locked to a reference laser and compared the same laser's second harmonic. Thus, the test was of the comb properties alone, since the reference laser's noise was common to its first and second harmonic. Viewed alternatively, this measurement represents a precision test of second harmonic generation [248].

We begin by describing the noise sources that the experiment was designed to test. A complete description of the frequency of a comb mode, including the possibility of mode-dependent noise, is given by

$$\nu_n(t) = n f_{rep}(t) + f_0(t) + \epsilon_n(t). \quad (4.55)$$

Here n is the index labeling the harmonic of the repetition rate, $f_{rep}(t)$; $f_0(t)$ is the carrier envelope offset frequency; and $\epsilon_n(t)$ accounts for mode-dependent frequency noise that is not correlated by the mode locking process. It is the terms $\epsilon_n(t)$ that we set out to test.

Perfect mode-locking occurs when $\epsilon_n(t) \rightarrow 0$ in Eq. 4.55. To test this residual comb error, we consider the case where we phase lock the heterodyne beat between comb mode n and a continuous wave (CW) laser, $f_{b,n}$, and f_0 to radio frequency (RF) references. The comb thus ideally acquires the optical phase information of the reference laser with added locking errors, $\delta f_{b,n}(t)$ and $\delta f_0(t)$, due to finite servo gain and shot noise. However it is possible to check for any residual noise

described by $\epsilon_n(t)$ by comparing the second harmonic of the CW reference laser to the comb. This yields an “out-of-loop” (OL) beat frequency

$$f_{b,2n}(t) = 2f_{b,n} - f_0 - \delta f_0(t) + 2\delta f_{b,n}(t) + \epsilon_{2n}(t) - 2\epsilon_n(t). \quad (4.56)$$

The term $\epsilon_{2n}(t) - 2\epsilon_n(t)$ accounts for relative noise introduced across the spectral gap $n \rightarrow 2n$ due to imperfect mode-locking and is indistinguishable from technical noise. In principle, the locking error due to finite servo gain given by $\delta f_{lock}(t) = -\delta f_0(t) + 2\delta f_{b,n}(t)$ can be estimated from the in-loop error signals, excluding consideration of shot noise.

The experiment was performed as schematically shown in Fig. 4.34a; we utilized the octave spanning Ti:sapphire described in [249] and which is similar to the system described in [250]. Part of the spectrum is used to lock f_0 , while the remaining optical spectrum was rebroadened to an optical octave centered near 750 nm using photonic crystal fiber (PCF) and combined with a Nd:YAG non-planar ring oscillator (NPRO) at 1064 nm. The co-propagating comb and 1064 nm CW light passed through a temperature stabilized periodically poled lithium niobate (PPLN) crystal, frequency doubling a portion of the 1064 nm CW light to produce 0.5 mW of 532 nm CW light while overlapped with the comb. The co-propagation of the light paths was important for reducing differential-path noise. A $\lambda/2$ at 1064 nm, λ at 532 nm wave plate overlaps the 532 nm CW and comb light polarization, while ensuring no 1064 nm comb light is doubled. The RF signal generated by the beat between the comb and ~ 1 mW of CW power at 1064 nm was used to stabilize the comb mode at ν_n ($n \simeq 3 \times 10^6$). The resulting beat between comb mode $2n$ and CW light at 532 nm was the out-of-loop signal.

The frequency stability beat at 532 nm was analyzed. In Fig. 4.34b we show the frequency stability, which represents the comb’s intrinsic ability to transfer optical stability. As seen from the figure, the comb performs better than any laser currently in operation, and should be sufficient for next generation ultrastable lasers that operate with fractional instability of 1×10^{-17} . We furthermore measured the optical linewidth of the beat. In order to amplify the phase noise, we employed a step-recovery diode to create the 10th harmonic of the beat signal. The power spectrum

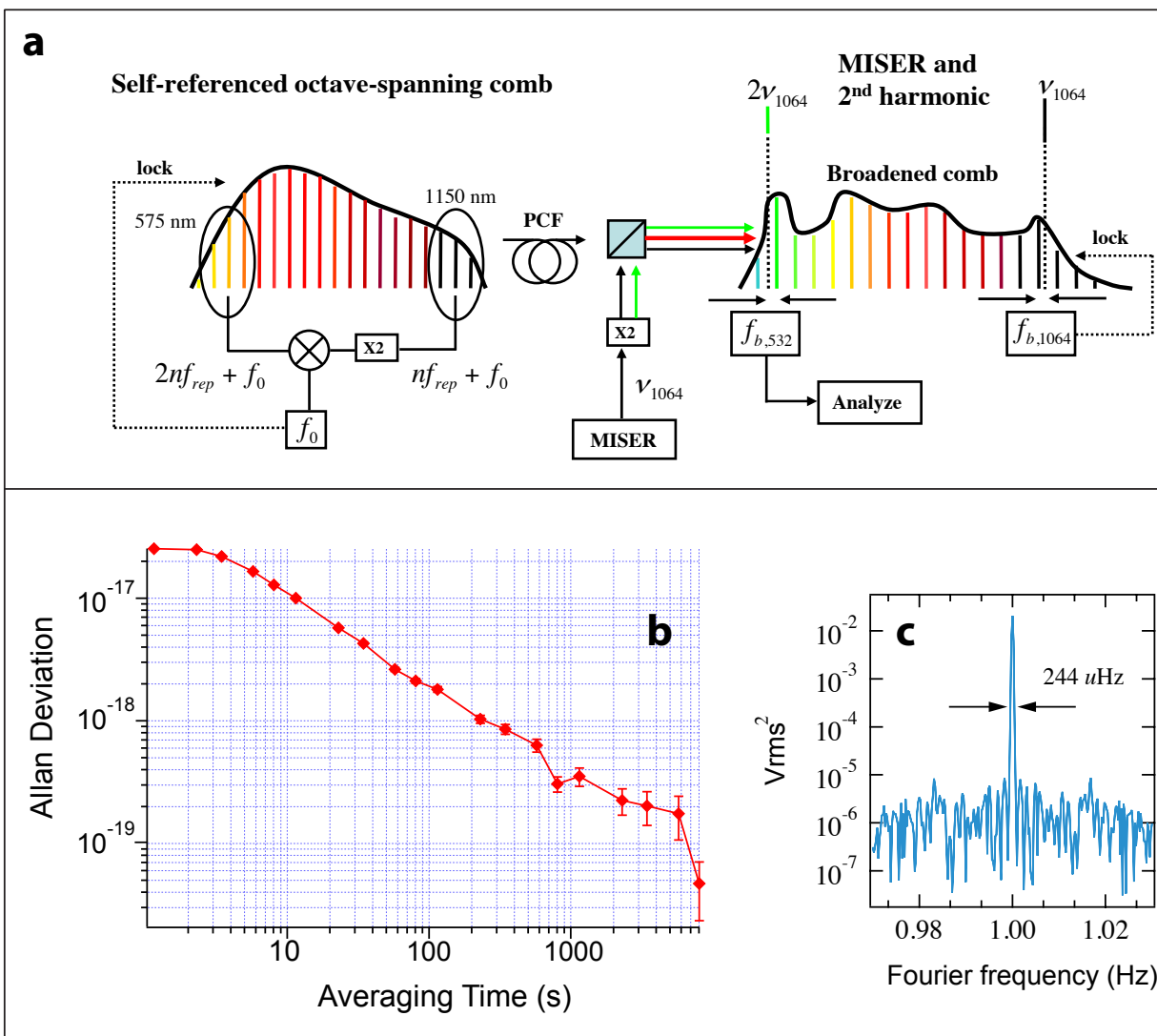


Figure 4.34: Experimental test of the intrinsic limits of the an optical frequency comb. (a) Experimental setup. An self-referenced octave-spanning frequency comb is re-broadened to an optical octave with a piece of photonic crystal fiber (PCF). It is phase locked to monolithic isolated single-mode end-pumped ring laser (MISER, also known as NPRO). The second-harmonic of the MISER co-propagates with the comb light. The heterodyne beat between the miser second harmonic and the comb, $f_{b,532}$, is the out-of-loop test signal. (b) Allan deviation of $f_{b,532}$. (c) Fourier power spectrum of the 10th harmonic of $f_{b,532}$ with a $\sim 250 \mu\text{Hz}$ measurement bandwidth.

shown in Fig. 4.34c is the 10th harmonic of the beat measured with a fast Fourier spectrum analyzer employing digitization record nearly 1 hour long, resulting in a 244 μHz measured linewidth. If we assume a white frequency noise power spectrum, then this indicates that the first harmonic could be as narrow as 2.4 μHz . Thus, as far as we can tell, the comb is a perfect device to the extent that technical sources of noise can be mitigated. These results are described detail in Ref. [132].

4.9 Outlook and conclusion

While this chapter has focused entirely on optical cavities as a means for precision laser stabilization, we mention in passing that other techniques may contribute to ultrastable optical sources for atomic clocks and precision spectroscopy. Lasers stabilized via spectral hole-burning in $\text{Eu}^{3+}:\text{Y}_2\text{SiO}_5$ represent a promising new technology for which the fundamental limits should be at the 10^{-17} level of stability [251]. Active and passive systems employing clock atoms as a continuous source for either active lasing [252] or spectroscopy [253] should be free of thermal noise contributions, as they rely solely on the atoms themselves for spectral discrimination.

As discussed in Chapter 2, the stability of current state-of-the-art neutral atom clocks is directly tied to the thermal noise present in ultrastable cavity mirror coatings and substrates. In this chapter, we demonstrated that with careful cavity design and high precision locking, we have obtained near-QPN limited clock performance with a spectroscopy time of 160 ms. While this is a significant milestone, achieving QPN-limited operation with an order of magnitude more atoms and 1 s probe times still leaves a large space for future improvements in ultrastable laser technology. While reducing the experimental dead time alone is also a promising step [254], reducing the thermal noise-induced laser frequency noise has had, and will continue to have, the largest immediate impact on neutral atom clocks. The new crystalline mirror technology we have demonstrated leaves us very confident that another factor of 10 improvement is now within reach.

In the context of systematic evaluation, the current stability of the Big ULE cavity-stabilized laser would allow a full clock evaluation at the level of 10^{-17} in one day, assuming that statistical averaging were the sole limiting factor. As we will see in the next chapter, the improvement

brought by the Big ULE cavity has already allowed rapid exploration of density-dependent effects in the ^{87}Sr lattice clock. Thus, as we will show, in addition to making better clocks, ultrastable lasers become precise tools for probing inter-atomic interactions at the sub-Hz energy scale and performing quantum state manipulation between optically separated quantum degrees of freedom, or optical qubits.

Chapter 5

The optical lattice clock as a quantum many-body system

It has long been expected that the use of identical fermions in ultracold neutral atom clocks would eliminate density-dependent frequency shifts entirely [255]. In 2008, it was found that even in a ^{87}Sr lattice clock at μK temperatures, a significant frequency shift remained, creating, at that time, a mystery as to the collision mechanism. In this chapter, we explore the fundamentally many-body collisional interactions between identical fermionic atoms in the optical lattice clock. Through precise spectroscopic tests, we elucidate the quantum many-body aspects of the clock and uncover the dominant role of the p -wave interaction channel for many-particle interactions in the optical lattice. We present the first observations of the emergence of spin correlations between the clock's optically-separated spin degrees of freedom that arise from the effective spin-spin interactions between ^{87}Sr atoms in the optical lattice.

5.1 Atomic collisions at ultracold temperatures

At ultracold temperatures, matter behaves quantum mechanically. It is the goal of this section to briefly review the basic implications of this statement. Here, we summarize the results of the partial wave theory of quantum collisions, which allows collisions to be characterized according to their angular momentum and vastly simplifies their treatment. We also discuss treatment of inter-atomic interactions using pseudopotentials.

5.1.1 Partial wave treatment of atomic interactions

Collisions at ultralow temperatures are simplified due to their quantum mechanical nature. One can represent the effect of an inter-atomic scattering event on the asymptotic wave function of a scattered particle as [88]

$$\psi(r \rightarrow \infty) \propto e^{i\mathbf{k}\cdot\mathbf{r}} + f(k, \theta, \phi) \frac{e^{ikr}}{r}. \quad (5.1)$$

The asymptotic wave function is the sum of two components. The first component is the incident plane wave, while the second term represents the outgoing wave with an angular dependence that reflects the details of the interaction potential. The differential cross section for identical particles is related to this angular dependence as [88]

$$\frac{d\sigma}{d\Omega} = |f(k, \theta, \phi) \pm f(k, \pi - \theta, \phi + \pi)|^2. \quad (5.2)$$

Here the “+” and “-” correspond to the case of identical bosons or fermions, respectively, and they are a direct consequence of the necessary (anti)symmetrization of the outgoing wave function for bosons (fermions). This distinction between the bosons and fermions will be crucial in determining by which partial waves bosons and fermions can interact.

Assuming an isotropic interaction potential (i.e., the potential has no angular dependence), we can write a general azimuthally symmetric wave function in the limit of $r \rightarrow \infty$

$$\psi(r \rightarrow \infty) = \sum_l C_l(k) P_l(\cos \theta) \frac{\sin[kr - l\pi/2 + \delta_l(k)]}{kr}, \quad (5.3)$$

for which the angular dependence of the outgoing scattered wave can be expressed as [256]

$$f(k, \theta) = \frac{1}{2ik} \sum_l (2l + 1) T_l(k) P_l(\cos \theta). \quad (5.4)$$

The quantity $T_l(k)$ relates the asymptotic phase shifts of the scattered partial waves, $\delta_l(k)$, to the cross section of Eq. 5.2 and is related directly to the asymptotic phase shift of the scattered wave by

$$T_l(k) = 1 - \exp(2i\delta_l). \quad (5.5)$$

An important consequence of the form of Eq. 5.4 is that we can write Eq. 5.2 as a sum of cross sections for a specific partial wave, and this property follows directly from the orthogonality of P_l 's. Additionally, due to the parity of the P_l 's, the cross section is identically zero for odd (even) partial waves in the case of identical interacting bosons (fermions). We can express these statements as

$$\sigma_{\text{total}}^{\text{boson}} = \sum_{l \text{ even}} \sigma_l, \quad \sigma_{\text{total}}^{\text{fermion}} = \sum_{l \text{ odd}} \sigma_l. \quad (5.6)$$

More emphatically, we can now state that identical **bosons (fermions) only interact via even (odd) partial waves**. This is a crucial difference between bosons and fermions in ultracold quantum gas experiments.

At ultralow temperatures, and for the case of a van der Waals-type interaction, the collisional phase shift is proportional to k^3 for partial waves with $l \geq 1$ [256]. In the specific case of s and p wave interactions ($l = 0$ and $l = 1$, respectively), the phase shift varies as [256]

$$\delta_l \propto k^{2l+1}, \quad \text{for } l \in \{0, 1\}. \quad (5.7)$$

For collision energies well below the centrifugal barrier, the true interaction potential can be replaced by an approximation of the atomic interaction that depends only on the relevant scattering length [257, 65]. For s - and p -wave interactions, which are the most significant contributors to ultracold collisional interactions, the scattering lengths are defined as

$$a = \lim_{k \rightarrow 0} \frac{-\tan[\delta_0(k)]}{k}, \quad b^3 = \lim_{k \rightarrow 0} \frac{-\tan[\delta_1(k)]}{k^3}, \quad (5.8)$$

where a is the s -wave scattering length and b^3 is the p -wave scattering volume.

Using definitions of Eq. 5.8, one can construct artificial potentials that encapsulate the low-energy limit of the scattering [258, 259, 260]. This technique is extremely powerful because it allows a parameterization of the low-energy interaction via a single number, and reduces the extended inter-particle interaction potential to a more tractable point-like potential. This sort of treatment is valid in the limit where the collisional energy is well below the centrifugal barrier and there are

no accidental resonances with bound states [65]. For s -wave interactions, the potential is given by

$$V_s^{\alpha\beta}(\mathbf{r}) = \frac{4\pi a_{\alpha\beta} \hbar^2}{m} \delta(\mathbf{r}). \quad (5.9)$$

Here, $\mathbf{r} = \mathbf{r}_1 - \mathbf{r}_2$, where $\mathbf{r}_{1(2)}$ is the position of atom 1(2). This is the potential employed in the prolific Gross-Pitaevski equation for the description of single-mode Bose-Einstein condensates [261]. The subscript $\alpha\beta$ indicates that the interaction can be dependent upon the internal states of the colliding particles.

Similarly, the p -wave interaction potential can be expressed as [260]

$$V_p^{\alpha\beta}(\mathbf{r}) = \frac{2\pi \hbar b_{\alpha\beta}^3}{m} \overleftarrow{\nabla}_{\mathbf{r}} \frac{\partial^3}{\partial r^3} r^3 \delta(\mathbf{r}) \overrightarrow{\nabla}_{\mathbf{r}}. \quad (5.10)$$

Here $r \equiv |\mathbf{r}_1 - \mathbf{r}_2|$ and the “ \leftarrow ” or “ \rightarrow ” symbols over the gradient operator indicate that it acts only to the left or right, respectively; the subscript on the gradient operator indicates that it acts on the center of mass coordinate, $\mathbf{r} = \mathbf{r}_2 - \mathbf{r}_1$. Higher order expressions for partial waves in a Cartesian basis become cumbersome due to the fact that the angular dependence is more naturally expressed in spherical harmonics. Luckily, our consideration of partial-wave interactions in the ^{87}Sr clock will stop with p -wave—but surprisingly will still include s -waves, even for identical fermions.

5.1.2 Considerations for clock shifts

A direct consequence of Eq. 5.8 is that in the ultracold regime, collisional phase shifts based upon s -waves can dominate over p -wave phase shifts as the collisional momentum goes to zero (*i.e.* $k \rightarrow 0$). Specifically, the ratio of the phase shifts is

$$\lim_{k \rightarrow 0} |\delta_1(k) / \delta_0(k)| = (kb)^2 b/a. \quad (5.11)$$

This implies that the ratio of p -wave collisions to s wave collisions becomes small assuming kb is also small. A similar statement can be reached by considering the action of the pseudopotentials of Eqs. 5.9 and 5.10 in Fourier space; in the case of the p -wave interaction, the two gradient operators will result in a k^2 scaling.

This relative scaling of both the scattering lengths and interaction strengths is a well-known phenomenon which, for example, limits the efficacy of evaporative cooling for gases of ultracold identical fermions [262]. For thermal gases, $k^2 \propto k_B T$ via the equipartition theorem. Thus for μK temperatures

$$|\delta_1(k)/\delta_0(k)| \propto T. \quad (5.12)$$

This property of p wave energy shifts led to the conclusion that fermionic species of atoms make more ideal frequency references than their bosonic counterparts due to their insensitivity to collisional shifts at ultralow temperatures [255].

5.2 First observations of cold-collisions in an optical lattice clock

Five years ago, as part of the effort to develop the world's first neutral-atom clock with fractional uncertainty at 1×10^{-16} , we engaged in a measurement campaign in collaboration with the NIST Time and Frequency division, where the short-term stability of a Ca neutral atom clock [197] was used to evaluate frequency shifts in the JILA Sr lattice clock [31, 114]. In this work, we used a two-state spin mixture, comprised of the $|F = 9/2, m_F = \pm 9/2\rangle$ spin states. A modest fractional frequency shift of $-8.9(8) \times 10^{-16}$ (-480 mHz frequency shift) was measured at an operating density of $\rho_0 \sim 10^{11} \text{ cm}^{-3}$. In the case of a density shift measurement in the presence of a “spectator” atom, we can write the shift due to s -wave interactions [263, 264, 265]

$$\Delta\nu = \frac{2\hbar}{m} (\tilde{a}_{eg} - a_{gg}) \rho. \quad (5.13)$$

Here, \tilde{a}_{eg} represents the effective scattering length for collisions in an incoherent mixture of e and g atoms in different nuclear spin states. In the case considered here, there is an equal population in $|F = 9/2, m_F = +9/2\rangle$ and $|F = 9/2, m_F = -9/2\rangle$, such that, $\rho = \rho_0/2$. Using the measured frequency shift, we find that $\tilde{a}_{eg} - a_{gg} \simeq -99a_0$, where $a_0 = 5.29 \times 10^{-11} \text{ m}$. Combining this result with the known ^{87}Sr g - g internuclear spin-state scattering length of $97a_0$ [266], we can deduce that a rough estimate for $\tilde{a}_{eg} \simeq -2a_0$. Here, the error in this determination of the scattering length is

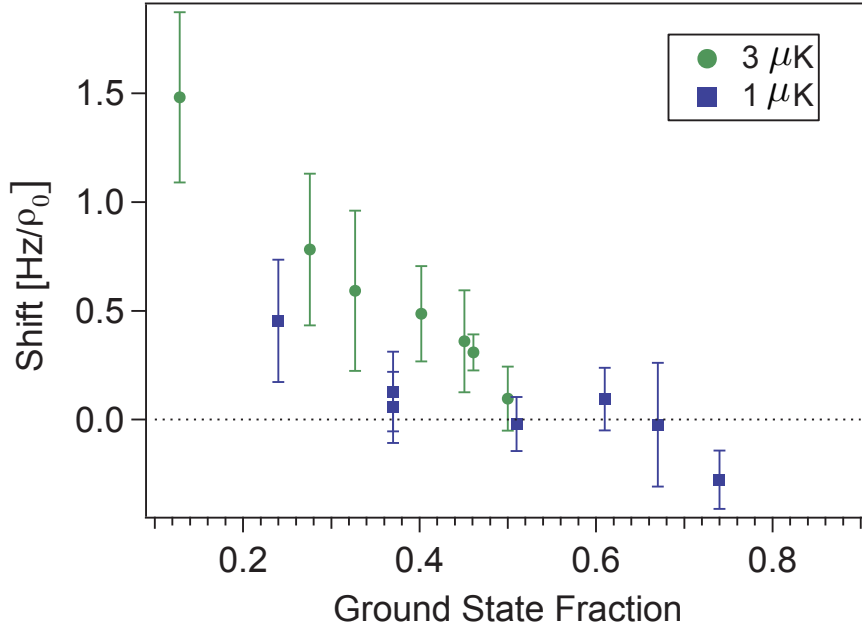


Figure 5.1: First observation of a density shift with a spin-polarized ^{87}Sr lattice clock. Here $\rho_0 \sim 10^{11}/\text{cm}^3$.

quite large due to the uncertainty in the absolute density calibration, and also because it neglects other relevant interactions on which we will further elaborate.

Although the uncertainty due to operating with a two-state mixture was small, the seemingly favorable ratio of s -wave to p wave interaction strengths in an ultracold regime implied by Eq. 5.11 indicated that spin-polarized ^{87}Sr should eliminate s -wave collisions, which should dominate over the p -wave interactions, thus eliminating the shift entirely [198]. However, our first experiments to measure the density-dependent frequency shift with spin-polarized ^{87}Sr found that the shift did not disappear as expected [31, 265].

The measurement of the density shift for the identical particles was performed by optically pumping to the $|F = 9/2, M_F = 9/2\rangle$ spin state. A fast clock pulse with a large Fourier width was employed for driving the $g \rightarrow e$ transition for the atoms in the $|F = 9/2, M_F = 9/2\rangle$ spin state only. Subsequently, all remaining ground state atoms were removed with a clean-up pulse resonant with the $^1\text{S}_0 \rightarrow ^1\text{P}_1$ transition. This ensures that the atomic polarization into the stretched spin

state is highly pure. The clock was then operated with an 80-ms π -pulse from $e \rightarrow g$. Despite operating in this highly spin-purified configuration, a shift was still observed. As can be seen in Fig. 5.3, the magnitude was similar to the spin-mixture case and has a nontrivial dependence on the final excitation fraction p (as defined in Chapter 2), which was varied by changing the width of the lock points on the de-excitation lineshape.

The measurement of these frequency shifts generated a fair amount of puzzlement. If s -wave interactions were forbidden and p -waves should have been frozen out, how can there be frequency shifts in the clock? The consideration of this question led to the discovery of an interesting mechanism that permits s -wave interactions to occur in spin polarized ultracold ^{87}Sr , although it will end up being only part of the story.

5.2.1 An s -wave collisional mechanism in a spin-polarized ^{87}Sr lattice clock

The basic idea behind the presence of s -wave shifts relies on the fact that the clock excitation is slightly inhomogeneous, as discussed in Chapter 2. This means that two fermions initially prepared in the same quantum state have the potential to evolve differentially as they are (de)excited from $g \rightarrow e$ ($e \rightarrow g$). To illustrate this, we consider two hypothetical colliding atoms in quantum states $|\psi_1\rangle$ and $|\psi_2\rangle$ given by

$$|\psi_1\rangle = \alpha|g\rangle + \beta|e\rangle \quad (5.14)$$

$$|\psi_2\rangle = \gamma|g\rangle + \delta|e\rangle \quad (5.15)$$

and such that the factors α , β , γ , and δ are time-dependent. The total wavefunction is initialized with both atoms in the ground state, which we denote as $|gg\rangle$. However, in order for the total wavefunction to be anti-symmetric under exchange, as is required for fermions, we need to include the lattice motional states labeled by $|n_1\rangle$ and $|n_2\rangle$. When the clock laser excites the atoms, $|\psi\rangle$

dynamically evolves from $|\psi_0\rangle = |gg\rangle \otimes (|n_1n_2\rangle - |n_2n_1\rangle)/\sqrt{2}$ as

$$|\psi_0\rangle \rightarrow (|\psi_1\psi_2\rangle|n_1n_2\rangle - |\psi_2\psi_1\rangle|n_2n_1\rangle)/\sqrt{2} \quad (5.16)$$

$$= |\psi^-\rangle \otimes \underbrace{(|n_1n_2\rangle + |n_2n_1\rangle)}_{\text{even}}/\sqrt{2} + |\psi^+\rangle \otimes \underbrace{(|n_1n_2\rangle - |n_2n_1\rangle)}_{\text{odd}}/\sqrt{2} \quad (5.17)$$

Only the part with the even dependence on the spatial functions n_1 and n_2 can collide via s -wave interactions. Since the wavefunction for fermions must be antisymmetrized, the electronic part of the wave function also carries a symmetry under particle exchange labeled by the “+” or “-”. It is straightforward to show that

$$\langle\psi^-|\psi^-\rangle = |\alpha\delta - \gamma\beta|^2 = 1 - |\alpha\gamma^* + \beta\delta^*|^2, \quad (5.18)$$

which is in general nonzero only when $\alpha \neq \gamma$ and $\beta \neq \delta$. Furthermore, we can identify this quantity as the zero-range second order correlation function often encountered in the mean-field theory of quantum gas interactions, $G^{(2)}(0)$. In a final step, we can then apply this $G^{(2)}(0)$ to the mean field density shift formula and get a time-dependent frequency detuning [265, 126],

$$\Delta\nu(t) = \frac{2\hbar a_{eg}^-}{m} G^{(2)}(t) (\rho_g - \rho_e). \quad (5.19)$$

Here, the minus sign in a_{eg}^- indicates that this collision is occurring between the antisymmetric electronic total wavefunction [73] and $\rho_{g(e)}$ is the atomic density of atoms in the ground (excited) state.

While Eq. 5.19 gets a lot right, there are aspects of the interaction that it misses entirely. The main problem with the mean-field energy of Eq. 5.19 is that it is, for lack of a better expression, the mean of the interaction energy. Specifically, it is only the part of the wavefunction with $|\psi^-\rangle$ that feels the s -wave interaction, yet we proceeded as if $|\psi^+\rangle$ also feels the mean energy shift. While this is a good approximation if $|\psi^-\rangle$ and $|\psi^+\rangle$ are not well-resolved (*i.e.*, the mean field shift is much smaller than the Rabi frequency), this condition is not necessarily satisfied in the clock. If we really want to treat the problem right, we must keep track of the evolution of the entire wave function; in this better approach $|\psi^-\rangle$ would feel the full interaction, while $|\psi^+\rangle$ would feel no interaction—and

we will not take the mean. Also, in this example, we used a two-particle wave function, so this means keeping track of only a few states. The problem with generalizing this approach to the ensemble is the exponential growth of complexity as we wish to treat the many-atom system. This is the subject of the next section.

5.3 Treatment of the clock shift in a many-body framework

Strongly correlated quantum many-body systems have become a major focus of modern science. Researchers are using quantum-degenerate atomic gases [64, 65, 66, 67, 68, 69], ultracold polar molecules [70, 71, 72], and ensembles of trapped ions [267, 268] to realize novel quantum phases of matter and simulate complex condensed matter systems. In particular, the $SU(N)$ symmetry in the nuclear spin degrees of freedom of fermionic alkaline earth atoms may allow implementation of unconventional frustrated quantum magnetic models including spin-orbital interactions [73, 74, 75, 76]. Degenerate gases of alkaline earth(-like) atoms have been also achieved [269, 270, 271, 272], but have not yet reached the levels of entropy required to observe these novel magnetic phases is currently not feasible in ultracold atom experiments.

In this section, it is our goal to unite these novel quantum systems with the collisional physics within the ^{87}Sr lattice clock. Atomic interactions in optical lattice clocks were first studied in the context of density-dependent frequency shifts that contribute to the clocks' systematic uncertainty [265, 273, 135]. In the previous section we presented a potential mechanism by which s -wave shifts can enter into the clock, and that even at this basic level the mean-field shift treatment might have shortcomings. Here we explore a powerful formalism to address clock shifts arising from partial wave interactions in the clock. Following the experimental discovery of the ^{87}Sr clock shift for identical fermions, the first work to pioneer this many-particle approach to treat s -wave shifts was from A. M. Rey and co-workers [274]. The two-body physics of the interacting particles was elucidated by K. Gibble [275]. A description similar to that of [274] was subsequently explored by Z. Yu and C. Pethick [276].

5.3.1 Second quantization

In order to develop the formalism for a many-body system of interacting fermionic atoms, we appeal to the substantial machinery already developed to treat interacting electrons in condensed matter systems, although the techniques we employ can be used for interacting bosons as well. We start by replacing the wavefunction with an operator, $\psi_s(\mathbf{x}) \rightarrow \hat{\psi}_s(\mathbf{x})$, such that [277]

$$\langle \mathbf{x}' s' | \hat{\psi}_s^\dagger(\mathbf{x}) | 0 \rangle = \delta_{ss'} \delta(\mathbf{x} - \mathbf{x}'). \quad (5.20)$$

Here, $\hat{\psi}_s^\dagger(\mathbf{x})$ creates an atom at position \mathbf{x} from the vacuum *ket*0 and the label s signifies its internal quantum state. In our case, these “spin” states will actually signify e (\uparrow) or g (\downarrow), where we have restricted our consideration to a single nuclear spin state, leaving only the electronic and motional degrees of freedom.

We can decompose $\hat{\psi}_s^\dagger(\mathbf{x})$ and its Hermitian conjugate $\hat{\psi}_s(\mathbf{x})$ in any orthonormal basis set as

$$\hat{\psi}_s^\dagger(\mathbf{x}) = \sum_i \phi_i^*(\mathbf{x}) \hat{c}_{i,s}^\dagger. \quad (5.21)$$

Its conjugate, $\hat{\psi}_s(\mathbf{x})$ can be written by conjugating Eq. 5.21. Here, the spatial functions $\phi_i(\mathbf{x})$ are the basis functions and $\hat{c}_{i,s}^\dagger$ and $\hat{c}_{i,s}$ are the creation and annihilation operators for mode i , respectively, with the spin denoted by s . Correspondingly, the number operator is given by

$$\hat{n}_{i,s} = \hat{c}_{i,s}^\dagger \hat{c}_{i,s}. \quad (5.22)$$

An important property of $\hat{\psi}_s(\mathbf{x})$ is that it obeys (anti)commutation relations that depend on bosonic (fermionic) nature of the particles described by the field. Since we wish to describe fermionic atoms in the clock, we therefore have

$$\{\hat{\psi}_s^\dagger(\mathbf{x}), \hat{\psi}_{s'}^\dagger(\mathbf{x}')\} = \delta(\mathbf{x} - \mathbf{x}') \delta_{ss'}. \quad (5.23)$$

Here, $\{\dots\}$ represents the anticommutation operation, defined as $\{\hat{\alpha}, \hat{\beta}\} \equiv \hat{\alpha}\hat{\beta} + \hat{\beta}\hat{\alpha}$. It is important to note that these relations are responsible for enforcing the necessary symmetries of the wavefunction and, as a direct consequence, they will play a direct role in determining by which partial waves the atoms are permitted to interact.

5.3.2 Many-body Hamiltonian

We are now prepared to write the two-atom interaction potential. The standard expression for decomposing an interaction potential into the second-quantized basis is [277, 278]

$$\hat{\mathcal{V}} = \frac{1}{2} \int d^3x d^3y \sum_{ss'} \hat{\psi}_s^\dagger(\mathbf{x}) \hat{\psi}_{s'}^\dagger(\mathbf{y}) v_{ss'}(\mathbf{x}, \mathbf{y}) \hat{\psi}_{s'}(\mathbf{y}) \hat{\psi}_s(\mathbf{x}), \quad (5.24)$$

where $\hat{\mathcal{V}}$ is the inter-atomic interaction component of the total Hamiltonian and $v_{ss'}(\mathbf{x}, \mathbf{y})$ is the two-body spin-dependent inter-particle interaction. We can therefore write the Hamiltonian of the entire interacting system as

$$\hat{H} = \hat{H}_0 + \hat{\mathcal{V}}, \quad (5.25)$$

where \hat{H}_0 is the single-particle Hamiltonian given by

$$\hat{H}_0 = \underbrace{\sum_s \int d^3x \hat{\psi}_s^\dagger(\mathbf{x}) \left[-\frac{\hbar^2}{2m} \nabla^2 + V(\mathbf{x}) \right] \hat{\psi}_s(\mathbf{x})}_{\text{motional}} + \underbrace{\frac{\hbar\omega_a}{2} \int d^3x \left[\hat{\psi}_\uparrow^\dagger(\mathbf{x}) \hat{\psi}_\uparrow(\mathbf{x}) - \hat{\psi}_\downarrow^\dagger(\mathbf{x}) \hat{\psi}_\downarrow(\mathbf{x}) \right]}_{\text{electronic}}, \quad (5.26)$$

where $\omega_a/(2\pi)$ is the clock frequency. At this point it is beneficial to select a basis for $\hat{\psi}(\mathbf{x})$ that diagonalizes \hat{H}_0 (see Eq. 5.21). For the case of atoms confined in a harmonic potential

$$V(\mathbf{x}) = \frac{1}{2}m\omega_x^2x^2 + \frac{1}{2}m\omega_y^2y^2 + \frac{1}{2}m\omega_z^2z^2. \quad (5.27)$$

The eigenstates are therefore eigenstates of the three-dimensional harmonic oscillator parameterized by $\mathbf{n}_i \equiv \{n_{x,i}, n_{y,i}, n_{z,i}\}$, such that

$$\phi_i(\mathbf{x}) = \phi_{n_{i,x}}(x) \phi_{n_{i,y}}(y) \phi_{n_{i,z}}(z), \quad (5.28)$$

where $\phi_{n_{\xi,i}}(\xi)$, with $\xi \in \{x, y, z\}$, is an eigenfunction of the one-dimensional harmonic oscillator. With this choice of basis, the “motional” part of \hat{H}_0 in Eq. 5.26 is a constant of motion, and we will therefore neglect it. This is justified because the energy scale of \hat{H}_0 is comparable to the trap frequencies, which are much larger than the interaction energy scale. The remaining part of \hat{H}_0 is the electronic energy between \uparrow and \downarrow , with the clock transition frequency of $\omega_a/(2\pi) = 429$ THz.

Thus, \hat{H}_0 becomes

$$\hat{H}_0 \rightarrow \frac{\hbar\omega_a}{2} \sum_i (\hat{n}_{\uparrow,i} - \hat{n}_{\downarrow,i}). \quad (5.29)$$

We now turn our attention to the inter-atomic interaction characterized by $\hat{\mathcal{V}}$. For an arbitrary interaction potential $v_{ss'}(\mathbf{x}, \mathbf{y})$, we can write

$$\hat{\mathcal{V}} = \sum_{ss'} \sum_{ijkl} U_{ijkl}^{ss'} \hat{c}_{i,s}^\dagger \hat{c}_{j,s'}^\dagger \hat{c}_{k,s'} \hat{c}_{l,s}. \quad (5.30)$$

Here [277],

$$U_{ijkl}^{ss'} = \frac{1}{2} \int d^3x d^3y \phi_i^*(\mathbf{x}) \phi_j^*(\mathbf{y}) v_{ss'}(\mathbf{x}, \mathbf{y}) \phi_k(\mathbf{y}) \phi_l(\mathbf{x}) \quad (5.31)$$

It is clear from the form of Eq. 5.30 that we won't get very far without some simplifications. Luckily, the trap frequencies ω_x , ω_y , and ω_z ($2\pi \times 450$ Hz, $2\pi \times 450$ Hz, and $2\pi \times 80$ kHz, respectively) are larger than any other scale in the problem, so we will first consider processes only which conserve total motional quanta. We also assume that ω_z is so large that it is frozen out (i.e., $n_z = 0$), so we only consider modes labeled as $\mathbf{n} = \{n_x, n_y\}$, where n_x and n_y are the harmonic oscillator quantum numbers in x and y . Conservation of total motional quanta still leaves a large number of possible combinations of the creation and annihilation operators. As an example we consider two colliding particles with initial motional states $\mathbf{n}_1 = \{n_{1,x}, n_{1,y}\}$ and $\mathbf{n}_2 = \{n_{2,x}, n_{2,y}\}$. In a perfectly harmonic trap, a range of final motional states are permitted, with motional quantum numbers given by $\mathbf{n}'_1 = \{n_{1,x} + l, n_{1,y} + m\}$ and $\mathbf{n}'_2 = \{n_{2,x} - l, n_{2,y} - m\}$. In the case that the potential is perfectly isotropic (i.e., $\omega_x = \omega_y$), the final states $\mathbf{n}'_1 = \{n_{1,x} + l, n_{1,y} + m\}$ and $\mathbf{n}'_2 = \{n_{2,x} - m, n_{2,y} - l\}$ are also permitted. As a first step, we assume a small but finite difference between ω_x and ω_y so as to preclude the latter process. However, even with $\omega_x \neq \omega_y$, there are still a great many final states allowed for a given initial state due to the range over which l and m can vary. Given that the thermally averaged values for n_x and $n_y \sim 100$, this means that l and m could span > 100 final states each, meaning that for the average collision between two particles, there are $> 10,000$ final states into which to scatter!

Luckily, there is a solution to this problem, and it arises from the two sources. The first is that the values of the mode-dependent coupling constants given by the overlap integral of Eq. 5.31

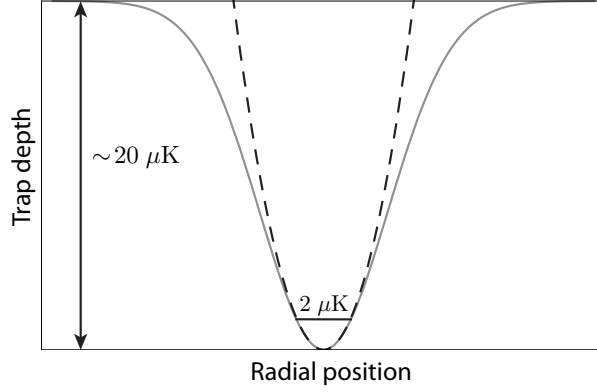


Figure 5.2: Harmonic approximation compared to the true radial profile of the trap.

tend to be much larger for the cases where motional quantum numbers are preserved or swapped [274]. The second is that for the pseudo-harmonic trap formed by the Gaussian laser profile, we can solve for the perturbed energies for radial eigenmodes labeled by n_x and n_y including quartic distortion as

$$E(n_x, n_y) = \hbar\omega_x n_x + \hbar\omega_y n_y + \frac{\hbar^2}{4mw_0^2} [3(n_x^2 + n_y^2) + 4n_x n_y + 5(n_x + n_y)] \quad (5.32)$$

Here, the first two terms are the usual harmonic oscillator eigen-energy for modes with quantum numbers n_x and n_y . The second term comes from the quartic distortion due to the gaussian beam profile, with $1/e^2$ intensity radius w_0 . Figure 5.2 shows the range of validity of the harmonic trap approximation in the radial direction. For 2 μK temperatures, the approximation is fairly good, but the quartic corrections are still significant. With one exception (the case where $\mathbf{n}'_1 = \mathbf{n}_2$ and $\mathbf{n}'_2 = \mathbf{n}_1$), the quartic distortion of the trap breaks the symmetry and enforces $l = m = 0$. Thus, we are left with only two possible energy-conserving final states:

- (1) $\mathbf{n}'_1 = \{n_{1,x}, n_{1,y}\}$ and $\mathbf{n}'_2 = \{n_{2,x}, n_{2,y}\}$: The trivial case. No modes are changed.
- (2) $\mathbf{n}'_1 = \{n_{2,x}, n_{2,y}\}$ and $\mathbf{n}'_2 = \{n_{1,x}, n_{1,y}\}$: Exchange of both motional eigenstates.

Thus, in general, for atoms i and j with initial motional states \mathbf{n}_i and \mathbf{n}_j we have two processes: $\{\mathbf{n}_i, \mathbf{n}_j\} \rightarrow \{\mathbf{n}_i, \mathbf{n}_j\}$ (direct) and $\{\mathbf{n}_i, \mathbf{n}_j\} \rightarrow \{\mathbf{n}_j, \mathbf{n}_i\}$ (exchange). This allows us to **vastly** simplify

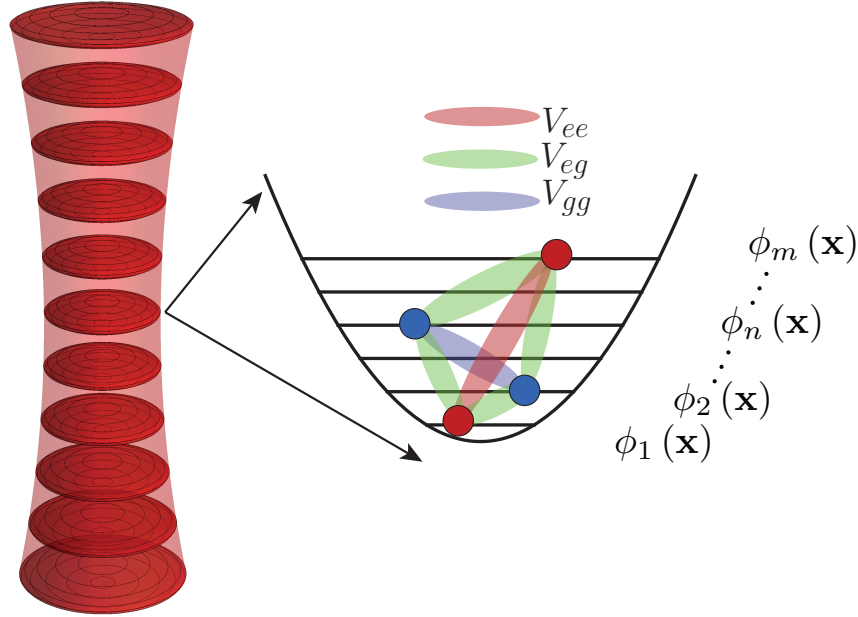


Figure 5.3: Interaction motional eigenstates within a single trap site. The functions $\phi(x)$ are harmonic oscillator motional eigenstates. The interaction strengths, depicted schematically as V_{gg} , V_{eg} , and V_{ee} are mode- and spin-dependent.

Eq. 5.30 as

$$\hat{V} \rightarrow \underbrace{\sum_{ss'} \sum_{ij} U_{ijji}^{ss'} \hat{c}_{i,s}^\dagger \hat{c}_{j,s'}^\dagger \hat{c}_{j,s'} \hat{c}_{i,s}}_{\text{direct}} + \underbrace{\sum_{ss'} \sum_{ij} U_{ijij}^{ss'} \hat{c}_{i,s}^\dagger \hat{c}_{j,s'}^\dagger \hat{c}_{i,s'} \hat{c}_{j,s}}_{\text{exchange}}. \quad (5.33)$$

Equation 5.33 represents a key result for the treatment of the many body shift. We will find that permutation symmetries of $U_{ijji}^{ss'}$ will further allow simplification of the problem. Additionally, connections with SU(2) angular momentum algebra will allow significant conceptual simplification of the problem, and allow us to make connections with the quantum theory of angular momentum. This is the subject of the next section.

5.3.3 Writing the many-body Hamiltonian with spin operators

A particularly straightforward way to form combinations of the creation and annihilation operators for spin $e(\uparrow)$ and $g(\downarrow)$ particles that obey the SU(2) spin algebra commutation relations

are [277]

$$\hat{\mathbf{S}} = \frac{1}{2} \sum_{ss'} \hat{c}_s^\dagger \vec{\sigma}_{ss'} \hat{c}_{s'} \quad (5.34)$$

Here, $\hat{\mathbf{S}} \equiv (\hat{S}^x, \hat{S}^y, \hat{S}^z)$ and $\vec{\sigma} = (\sigma^x, \sigma^y, \sigma^z)$, where σ^x , σ^y , and σ^z are the Pauli matrices. A general property of operators constructed as in Eq. 5.34 is that they obey the commutations relation

$$[\hat{S}^i, \hat{S}^j] = \frac{1}{2} \sum_{ss'} \hat{c}_s^\dagger [\sigma^i, \sigma^j]_{ss'} \hat{c}_{s'}. \quad (5.35)$$

In the specific case of \mathbf{S} , we have

$$[\hat{S}^i, \hat{S}^j] = i\epsilon^{ijk} S^k. \quad (5.36)$$

As seen from Eq. 5.36, the operators \hat{S}^x , \hat{S}^y , and \hat{S}^z map directly onto the spin operators for spin-1/2 systems. If we write them out fully, they are

$$\hat{S}^x = \sum_{n=1}^N (\hat{c}_\uparrow^\dagger \hat{c}_\downarrow + \hat{c}_\downarrow^\dagger \hat{c}_\uparrow) / 2, \quad (5.37)$$

$$\hat{S}^y = \sum_{n=1}^N (\hat{c}_\uparrow^\dagger \hat{c}_\downarrow - \hat{c}_\downarrow^\dagger \hat{c}_\uparrow) / 2i, \quad (5.38)$$

$$\hat{S}^z = \sum_{n=1}^N (\hat{c}_\uparrow^\dagger \hat{c}_\uparrow - \hat{c}_\downarrow^\dagger \hat{c}_\downarrow) / 2, \quad (5.39)$$

We will now attempt to use these operators to simplify Eq. 5.33. We begin by writing Eq. 5.33 in a slightly different way

$$\hat{\mathcal{V}} = \sum_{ss'} \sum_{i \neq j} U_{ijji}^{ss'} (\hat{c}_{i,s}^\dagger \hat{c}_{i,s}) (\hat{c}_{j,s'}^\dagger \hat{c}_{j,s'}) - \sum_{ss'} \sum_{i \neq j} U_{ijij}^{ss'} (\hat{c}_{i,s}^\dagger \hat{c}_{i,s'}) (\hat{c}_{j,s'}^\dagger \hat{c}_{j,s}). \quad (5.40)$$

Here, we've made use of the anticommutation relations for the fermionic operators to rearrange the operators into pairs enclosed by parentheses. Finally, we will relate the interaction energy terms $U_{ijji}^{ss'}$ and $U_{ijij}^{ss'}$ to one another. Specifically, for the s - and p -wave interactions considered in Eqs. 5.9 and 5.10, respectively, $U_{ijji}^{ss'}$ will have opposite parity under exchange of a given pair of $ij \rightarrow ji$.

Thus, we can write

$$U_{ijji}^{ss'} = \frac{1}{2} U_{ij}^{eg} (1 - \delta_{ss'}) + \frac{1}{2} V_{ij}^{ss'}, \quad (5.41)$$

$$U_{ijij}^{ss'} = \frac{1}{2} U_{ij}^{eg} (1 - \delta_{ss'}) - \frac{1}{2} V_{ij}^{ss'}. \quad (5.42)$$

Equations 5.41 and 5.42 define U and V . The interaction term U (V) are even (odd) under motional state exchange (i.e. $i \rightarrow j$ and $j \rightarrow i$). As a direct consequence, the corresponding spin states must have the opposite parity under exchange of s and s' . Therefore, we drop the superscript on U and simply call it U_{ij}^- because it only applies to colliding atoms in an antisymmetric electronic superposition, of which there is only one possibility for two colliding atoms. Here, the $(1 - \delta_{ss'})$ term serves to emphasize that the even-parity terms for which $s = s'$ cancel in Eq. 5.40. This is similar to the simple s -wave case considered before, where s -wave interactions between the identical fermions were only able to occur in the eg channel.

Inserting the potentials Eqs. 5.9 and 5.10 into Eq. 5.31, we find

$$U_{ij}^{eg} = \frac{4\pi a_{eg}^- \hbar^2}{m} \int d^3x |\phi_i(\mathbf{x})|^2 |\phi_j(\mathbf{x})|^2 \quad (5.43)$$

$$V_{ij}^{ss'} = \frac{12\pi b_{ss'}^3 \hbar^2}{m} \int d^3x \left| \phi_i(\mathbf{x}) \vec{\nabla} \phi_j(\mathbf{x}) - \phi_j(\mathbf{x}) \vec{\nabla} \phi_i(\mathbf{x}) \right|^2 \quad (5.44)$$

A discussion of the mode-dependence of these is given in Appendix D.

We can rearrange Eq. 5.40 by making use of the spin operators of Eqs. 5.37–5.39, to arrive at the result

$$\hat{\mathcal{V}} = \sum_{i \neq j} J_{ij}^\perp \hat{\mathbf{S}}_i \cdot \hat{\mathbf{S}}_j + \chi_{ij} \hat{S}_i^z \hat{S}_j^z + \frac{C_{ij}}{2} (\hat{S}_i^z + \hat{S}_j^z) + \frac{K_{ij}}{4}, \quad (5.45)$$

where

$$J_{ij}^\perp = V_{ij}^{eg} - U_{ij}^{eg}, \quad (5.46)$$

$$\chi_{ij} = V_{ij}^{gg} + V_{ij}^{ee} - 2V_{ij}^{eg}, \quad (5.47)$$

$$C_{ij} = V_{ij}^{ee} - V_{ij}^{gg}, \quad (5.48)$$

$$K_{ij} = V_{ij}^{gg} + V_{ij}^{ee} + V_{ij}^{eg} + U_{ij}^{eg}. \quad (5.49)$$

Interestingly, this Hamiltonian links the spin dynamics of interacting thermal fermions at μK temperatures to those of two-mode Bose-Einstein condensates (BEC) and it has been shown both theoretically [279, 280, 281, 282] and experimentally [283, 284, 285] to give rise to non-trivial many-body correlations and quantum noise-squeezed states. It is also relevant in trapped-ion quantum simulation experiments [286, 267, 268].

5.3.4 Adding the atom-laser interaction

At this point, we have a general Hamiltonian that describes two-level fermions that are subject to both s - and p -waves shifts. Writing out the full Hamiltonian, we have so far developed yields

$$\hat{H} = \hbar\omega_a \sum_i \hat{S}_i^z + \sum_{i \neq j} J_{ij}^\perp \hat{\mathbf{S}}_i \cdot \hat{\mathbf{S}}_j + \chi_{ij} \hat{S}_i^z \hat{S}_j^z + \frac{C_{ij}}{2} (\hat{S}_i^z + \hat{S}_j^z) + \frac{K_{ij}}{4}. \quad (5.50)$$

The first term is from the electronic energy separation between g and e given in Eq. 5.29. Here, we have simply expressed it in our new spin language.

In order to account for the laser excitation, we add the atom-laser interaction to this Hamiltonian. We treat the laser field classically, and the atom-laser Hamiltonian is given by [274]

$$\hat{H}_I = -\frac{\Omega_0}{2} \int d^3x \hat{\psi}_\uparrow^\dagger(\mathbf{x}) e^{i(\mathbf{k}\cdot\mathbf{x}-\omega t)} \hat{\psi}_\downarrow(\mathbf{x}) + \text{H.C.} \quad (5.51)$$

Here, \mathbf{k} is the laser propagation vector, ω is the laser angular frequency and ‘‘H.C.’’ indicates the hermitian conjugate of the previous expression. We note that the minus sign in front simply represents a specific phase convention for the probe laser electric field, and we keep it in order to be consistent with the literature. The mode-dependent Rabi frequency Ω_i is given by

$$\Omega_i = \Omega_0 \int d^3x \phi_i^*(\mathbf{x}) e^{i\mathbf{k}\cdot\mathbf{x}} \phi_i(\mathbf{x}). \quad (5.52)$$

By moving to a frame co-rotating with the laser, we finally obtain [125]

$$\hat{H} = -\delta \sum_i \hat{S}_i^z + \sum_i \Omega_i \hat{S}_i^x + \sum_{i \neq j} J_{ij}^\perp \hat{\mathbf{S}}_i \cdot \hat{\mathbf{S}}_j + \chi_{ij} \hat{S}_i^z \hat{S}_j^z + \frac{C_{ij}}{2} (\hat{S}_i^z + \hat{S}_j^z) + \frac{K_{ij}}{4}. \quad (5.53)$$

Here, $\delta \equiv \omega - \omega_a$. Equation 5.53 is the key result of this section. It expresses the relevant elastic many-body dynamics in a spin language that makes broad connections to quantum magnetic systems.

5.4 S-wave model

In the previous section, we derived a powerful machinery to treat collisional shifts in an optical lattice clock. It is the goal of this section to develop an intuitive understanding of the

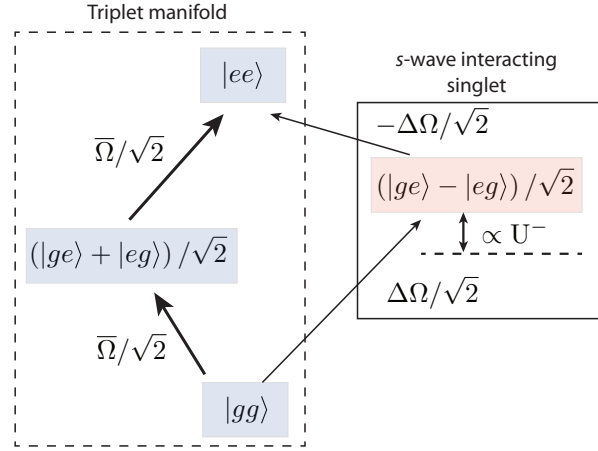


Figure 5.4: Two-particle illustration of the s -wave shift mechanism.

s -wave shift mechanism only. Eventually, we will present evidence that shows that, despite the beautiful mechanism that allows s -wave shifts in a fermion clock, s -waves are **not** a dominant collisional channel in the one-dimensional optical lattice clock if the excitation is performed in a very homogeneous manner. This has coincided with significant experimental progress in the last several years, resulting in the extremely small inhomogeneities reported in Chapter 2, and allowing peak atomic excitation fractions of nearly 100%. However, we will find that the s -wave interactions will still play an important auxiliary role in the many-body dynamics.

To begin, we consider Eq. 5.45 with only s -wave interactions so that $V_{ij}^{eg} = V_{ij}^{gg} = V_{ij}^{ee} = 0$. This was the original context in which many-body shifts were considered in the lattice clock [274]. In this limit, Eq. 5.45 reads [274]

$$\hat{\nu} = \sum_{i \neq j} -U_{ij}^{eg} (\hat{\mathbf{S}}_i \cdot \hat{\mathbf{S}}_j - 1/4). \quad (5.54)$$

This result is particularly easy to understand if we appeal to the simple picture we developed earlier employing the even and odd spatial and electronic wavefunctions of Eq. 5.17. There, the electronic wavefunction evolved via inhomogeneous excitation into a symmetric and antisymmetric part, corresponding to antisymmetric and symmetric spatial wavefunctions. There, we enforced that only the part of the wavefunction with a symmetric spatial component was allowed to “feel” the s -

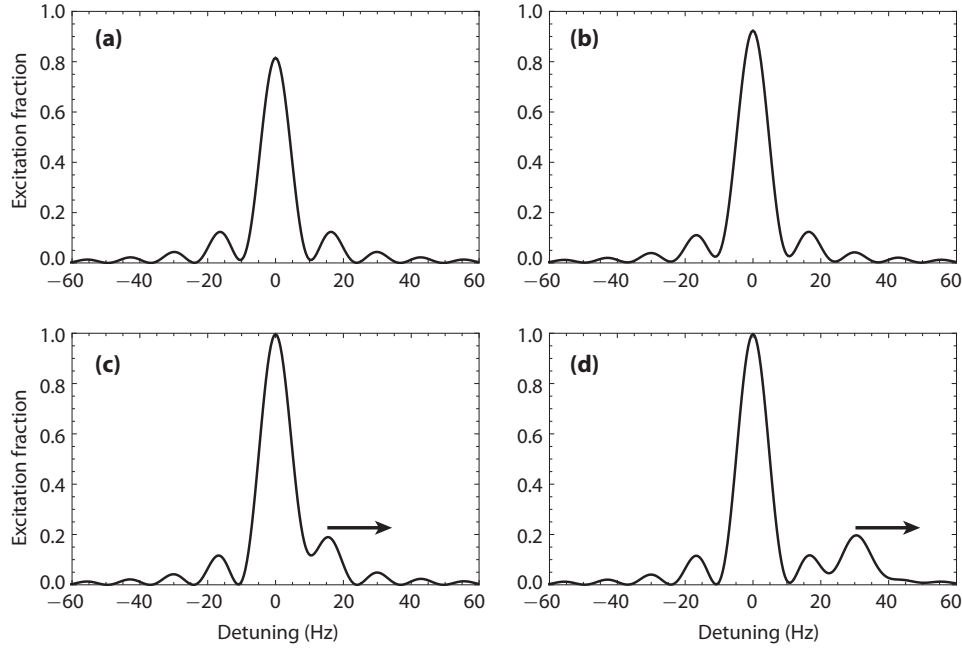


Figure 5.5: Two-particle lineshapes with s -wave interaction energy. (a) $U_{12}^- = 0$ (b) $U_{12}^- = 1\Omega$ (c) $U_{12}^- = 2\Omega$ (d) $U_{12}^- = 5\Omega$.

wave collision. We then applied this energy shift as a mean-field energy shift for the $g \rightarrow e$ transition. Likewise, in Eq. 5.54, we see that the interaction energy depends on the dot-product of the two spins of atom i and j . Since these spin operators directly map onto a spin-1/2 system, we can easily see that there are two possible values for $\hat{\mathbf{S}}_i \cdot \hat{\mathbf{S}}_j$, namely $1/4$ and $-3/4$, corresponding to the $S = 1$ and $S = 0$ total spin eigenstates of the total spin operator $\hat{\mathbf{S}}_i + \hat{\mathbf{S}}_j$. We see then that only the state with $S = 0$ (the spin-singlet $|S = 0, m_S = 0\rangle = (|ge\rangle - |eg\rangle)/\sqrt{2}$) interacts with energy U_{ij}^{eg} , while the three possible states of the triplet, $|S = 1, m_S = -1\rangle = |gg\rangle$, $|S = 1, m_S = 0\rangle = (|ge\rangle + |eg\rangle)/\sqrt{2}$, and $|S = 1, m_S = 1\rangle = |ee\rangle$ are non-interacting.

A relevant question to ask is what causes the excitation of the singlet state? As an example, we consider the case of the spin Hamiltonian of Eq. 5.53 with only s -wave interactions for two particles. We then have

$$\hat{H} = -\delta\hat{S}_{\text{tot}}^z + \sum_{i=1}^2 \Omega_i \hat{S}_i^x + -U_{12}^{eg} (\hat{\mathbf{S}}_{\text{tot}}^2 - 2). \quad (5.55)$$

The Hamiltonian can be written in a slightly different way

$$\hat{H} \rightarrow -\delta \hat{S}_{\text{tot}}^z + \bar{\Omega} \hat{S}_{\text{tot}}^x + \Delta\Omega \left(\hat{S}_2^x - \hat{S}_1^x \right) - U_{12}^- \left(\hat{\mathbf{S}}_{\text{tot}}^2 - 2 \right), \quad (5.56)$$

where $\bar{\Omega} = (\Omega_1 + \Omega_2)/2$, $\Delta\Omega = (\Omega_1 - \Omega_2)/2$, $S_{\text{tot}}^z = \hat{S}_1^z + \hat{S}_2^z$ and $\hat{\mathbf{S}}_{\text{tot}} = \hat{\mathbf{S}}_1 + \hat{\mathbf{S}}_2$. If $\Omega_1 = \Omega_2$, then we see that the hamiltonian can be written in terms of total spin operators, namely

$$\hat{H} \rightarrow -\delta \hat{S}_{\text{tot}}^z + \bar{\Omega} \hat{S}_{\text{tot}}^x - U_{12}^- \left(\hat{\mathbf{S}}_{\text{tot}}^2 - 2 \right). \quad (5.57)$$

Figure 5.4 schematically depicts this simple two-particle picture. In this instance, the initially non s -wave interacting $|gg\rangle$ ($|S = 1, m_S = -1\rangle$ in the spin parlance) state satisfies $\left(\hat{\mathbf{S}}_{\text{tot}}^2 - 2 \right) |S = 1, m_S = -1\rangle = 0$. Furthermore, since $\hat{\mathbf{S}}_{\text{tot}}^2$ commutes with the other total spin operators, it is a constant of motion and $\left(\hat{\mathbf{S}}_{\text{tot}}^2 - 2 \right)$ is always equal to zero. Thus inhomogeneities in the atom-clock laser interaction (e.g., $\Omega_1 \neq \Omega_2$) are key to the s -wave shift mechanism.

We can gain further insight if we project the Hamiltonian of Eq. 5.55 into the basis formed by $|S = 1, m_S = -1, 0, +1\rangle$ and $|S = 0, m_S = 0\rangle$. In this basis, the hamiltonian becomes [287]

$$\hat{H} \rightarrow \begin{pmatrix} \delta & 0 & \bar{\Omega}/\sqrt{2} & \Delta\Omega\sqrt{2} \\ 0 & -\delta & \bar{\Omega}/\sqrt{2} & -\Delta\Omega\sqrt{2} \\ \bar{\Omega}/\sqrt{2} & \bar{\Omega}/\sqrt{2} & 0 & 0 \\ \Delta\Omega\sqrt{2} & -\Delta\Omega\sqrt{2} & 0 & 2U_{12}^- \end{pmatrix} \quad (5.58)$$

Figure 5.5 shows the solution of the two particle Hamiltonian given above in the presence of increasing U_{12}^- . For $U_{12}^- \simeq \Omega$, we have the situation that the interacting spin-singlet is not well-resolved from the central carrier. However, when $U_{12}^- \gg \Omega$, the interacting singlet emerges as a sideband, leaving the carrier nearly unperturbed. This is immediately a qualitative difference from the mean-field model of Eq. 5.19, and shows the necessity of a true many- (or in this case two-) body model for the s -wave interaction. Specifically we see that in the limit $U_{12}^- \gg \Omega$, we can treat the term $\Delta\Omega \left(\hat{S}_2^x - \hat{S}_1^x \right)$ as a perturbation and find that the $|gg\rangle$ and $|ee\rangle$ levels are shifted $\propto \Delta\Omega^2/U_{12}^-$. In the N -atom case, this effect can be generalized to the condition $U^- N \gg \bar{\Omega}$.

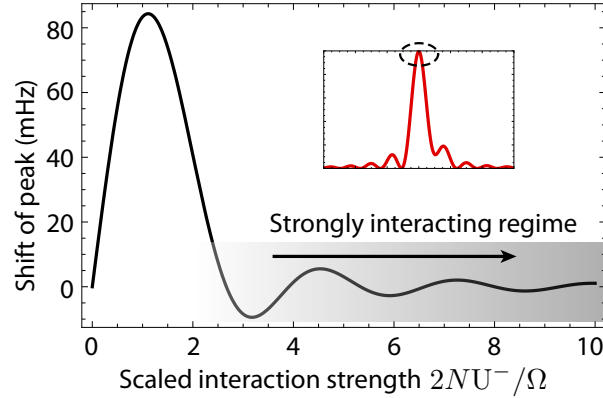


Figure 5.6: The s -wave density shift and the strongly interacting regime. The inset shows the region of the lineshape considered.

With the insights gained from the 2-atom case in mind, we re-write the Hamiltonian of Eq. 5.54 as [274]

$$\hat{H} = -\delta\hat{S}_{\text{tot}}^z + \bar{\Omega}\hat{S}_{\text{tot}}^x + \sum_i (\Omega_i - \bar{\Omega}) \hat{S}_i^x - \sum_{i \neq j} U_{ij}^{eg} (\hat{\mathbf{S}}_i \cdot \hat{\mathbf{S}}_j - 1/4). \quad (5.59)$$

Here, it is the term $\sum_i (\Omega_i - \bar{\Omega}) \hat{S}_i^x$ that perturbatively couples the maximally-symmetric non s -wave interacting manifold to the family of states with $S_{\text{tot}} = N/2 - 1$ that do interact via s -waves [274]. However, in the strongly interacting limit, defined for the N -atom case as $NU_{12}^- \gg \bar{\Omega}$, excitation of the non fully-symmetric states via inhomogeneity is suppressed via a protective energy gap. Furthermore, the coupling to the interacting manifold is governed by the degree of inhomogeneity in the system—in this specific case excitation inhomogeneity parameterized by $\Delta\Omega^2 = \sum_i (\Omega_i - \bar{\Omega})^2 / (N - 1)$.

5.4.1 Concluding remarks regarding s -wave interactions

In the preceding discussion, we explored some of the non-trivial aspects of the s -wave interaction in a lattice clock of initially identical fermions. Most importantly, a criterion for strong interactions was identified: the strongly interacting regime is reached when the $\mathbf{S}_i \cdot \mathbf{S}_j$ term in the Hamiltonian becomes large enough to block excitation of the interacting state. As an illustration

of this principle, we plot the analytical solution to the shift of the peak of Rabi lineshape as derived by Rey *et al.* [274] in Fig. 5.6. The peak of the resonance is maximally shifted when $2NU \simeq \bar{\Omega}$. In the strongly interacting regime, the line center as defined by the peak becomes less affected as U increases.

These theoretical results were sufficient to explain all phenomena that had been experimentally observed, including the 2009 density shift [31, 265], reduced density shifts in a strongly confining 2D lattice [135], and resolved interaction sidebands in the 2D lattice clock [288]. However, this is not the end of the story with interaction in the ^{87}Sr lattice clock.

5.5 New experimental evidence for p -wave interactions

The results of the previous section were well-established when the new laser came on line (see Chapter 4 for a description of the new laser, also known as the “Big ULE” cavity.). With the promise of 10-fold improved stability the prospect of a high-resolution probe of the density shift via sub-Hz spectroscopy was a reality. However, we began to see evidence that was not consistent with the predictions of the model employing solely s -wave interactions. Here we describe the initial experimental evidence for beyond s -wave collisional physics.

5.5.1 Inelastic loss

Inelastic losses between atoms in the $^3\text{P}_0$ state of ^{88}Sr were measured in 2009 by two separate groups [289, 290]. The collision rate is important for determining the feasibility of producing BEC using metastable states ($^3\text{P}_0$ or $^3\text{P}_2$), whose elastic collisional properties are potentially more favorable for evaporative cooling. In these experiments, loss coefficients of $\gamma_{ee} = 4.0 \pm 2.5 \times 10^{-12} \text{ cm}^{-3}\text{s}^{-1}$ in a quasi two-dimensional trap [290] and $1.9 \pm 1.2 \times 10^{-11} \text{ cm}^{-3}\text{s}^{-1}$ in a three-dimensional trap [289] were measured. In Ref. [290], large elastic effects on the clock transition in ^{88}Sr were also observed, including a strong collisional dephasing and a density shift an order of magnitude larger than for ^{87}Sr .

These collisions had not been observed in ^{87}Sr and it had been assumed that the large

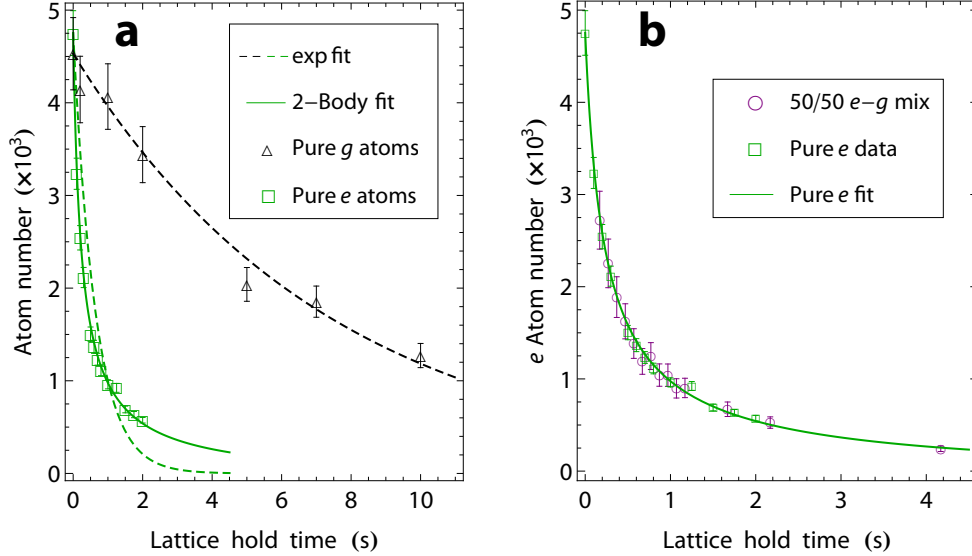


Figure 5.7: Atom loss as a function of lattice hold time. Atoms in 1S_0 have a lifetime of 8 s, and the time-dependence is exponential, indicating that the primary loss mechanism is residual gas collisions. Atoms in the 3P_0 $|F = 9/2, m_F = +9/2\rangle$ state decay an order of magnitude more quickly. The time-dependence of the decay is consistent with that of a two-body inelastic loss mechanism, and clearly does not fit an exponential decay model.

centrifugal barrier of $75 \mu\text{K}$ for 3P_0 [81] should strongly suppress such collisions. Our previous experimental tests with ^{87}Sr had not shown any loss from 3P_0 consistent with two-body decay due mainly to the dominant residual gas collisional lifetime of 2 s in the experimental chamber.

After adding an additional differential pumping stage on the oven-side of the experiment (see Fig. 2.3 Chapter 2), we were able to increase the vacuum lifetime to 8 s. This allowed us to clearly resolve the effect of 2-body collisions in the excited state. As shown in Fig. 5.7a, the inelastic decay proceeds approximately an order of magnitude more rapidly than the residual gas collision limited case. The equation for the density decay due to two-body inelastic collisions in the presence of a background one-body loss due to residual gas collisions, with a rate Γ , is

$$\frac{dn}{dt} = -\Gamma n - \gamma_{ee} n^2. \quad (5.60)$$

Here, n is the density and γ_{ee} is the two-body loss term. By integrating over the spatial density profile, the excited state population within a single trap site (labelled with the index i) as a function

of time is given by [290]

$$N_i(t) = \frac{N_i(0) \exp(-\Gamma t)}{1 + [N_i(0) \gamma_{ee} / (\pi^{3/2} \Gamma w_r^2 w_z)] [1 - \exp(-\Gamma t)]}. \quad (5.61)$$

Here, $N_i(0)$ is the initial population within a trap site i at $t = 0$, $w_{r(z)}$ is the radial $1/e^2$ density radius in the radial (axial) direction. Explicitly, the density profile is

$$n_i(\mathbf{x}) = N_i \left(\frac{2}{\pi} \right)^{3/2} \frac{\exp[-2(x^2 + y^2)/w_r^2 - 2z^2/w_z]}{w_r^2 w_z}, \quad (5.62)$$

for which the density-weighted average density is given by

$$\bar{n}_i = \frac{1}{N_i} \int d^3x [n_i(\mathbf{x})]^2 = \frac{N_i}{\pi^{3/2} w_x w_y w_z}. \quad (5.63)$$

We fit the loss for atoms initially prepared in e with the model of Eq. 5.61 averaged over the site occupancy. As seen in Fig. 5.7a, the model fits the data extremely well, while at the same time ruling out any purely single-particle decay mechanism, as might be caused by photon scattering from the lattice, which we also independently ruled out (see Chapter 2).

In order to test for the presence of an eg inelastic loss channel, as measured for the case of ^{88}Sr by Lisdat *et al.*, we created a mixture of coherently prepared e and g atoms by using a $\pi/2$ laser pulse on resonance and measured the resulting decay. Figure 5.7b shows the result of a pure e a sample and a 50/50 e/g mixture with an equivalent number of atoms in e (i.e., the sample initially started with twice the number of atoms, 50% of which were in the excited state). We were unable to resolve any inelastic loss process between e and g , which is evident from the excellent agreement between the data and theoretical curves for the mixture state as compared to the pure e mixture.

To further probe the loss dynamics we took inelastic loss data under varying atomic temperature and in the presence of a second nuclear spin state. In order to explain the observation of inelastic loss in the identical, non-spin mixture fermi sample, a p -wave model was necessary, because the atoms were unquestionably prepared in a pure quantum state. Our theory colleagues (G. Quémener *et al.*) were able to use a model with two fit parameters: the unknown phase shift of the short range potential, and the probability that an atom is lost during its penetration into the

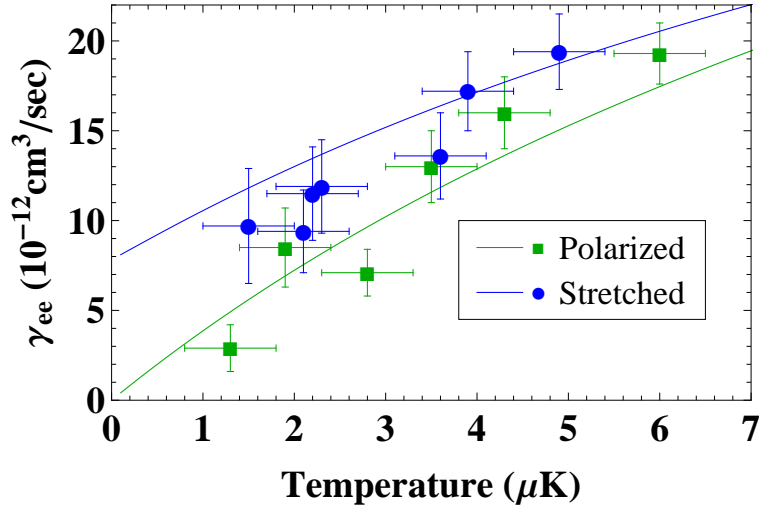


Figure 5.8: Two-body loss coefficient γ_{ee} for spin polarized ^{87}Sr in $^3\text{P}_0$ $|F = 9/2, m_F = +9/2\rangle$ and, in a separate experiment, a statistical mixture of $^3\text{P}_0$ $|F = 9/2, m_F = +9/2\rangle$ and $^3\text{P}_0$ $|F = 9/2, m_F = -9/2\rangle$

short-range regime. It was found that the loss probability, p_{ls} , was significantly below unity, with a best-fit value of $p_{\text{ls}} = 0.4$ for the short-range regime of $30 a_0$. The same parameters described the inelastic loss rate in the spin-mixture case, giving us confidence in the model, and also reproducing the s -wave losses observed in ^{88}Sr . Importantly, the relatively inefficient loss at short ranges means that the s - and p - wave inelastic loss channels are comparable in magnitude, whereas normally s -wave losses would be expected to dominate by nearly two orders of magnitude [116].

As shown in Fig. 5.8, the agreement between the theory and the temperature dependent loss rates for the pure spin-state and spin-mixture cases is quite good. The generalization for Eq. 5.61 for the case with the spin mixture is

$$\frac{dn_\alpha}{dt} = -\Gamma n_\alpha - \gamma_{ee} n_\alpha^2 - \left(K_s^{\text{dist}} + K_p^{\text{dist}} \right) n_\alpha n_\beta. \quad (5.64)$$

Here, n_α and n_β represent the densities of the two components of the gas. The additional two-body loss coefficients, K_s^{dist} and K_p^{dist} , represent s - and p - loss channels for two-body inelastic collisions between the two different spin states, which are distinguishable. This can be simplified somewhat due to the decoupling of the electronic and nuclear degrees in ^{87}Sr , and so we expect that $K_p^{\text{dist}} = \gamma_{ee}/2$ [291]. The parameters we theoretically extract for ^{87}Sr are ultimately $\gamma_{ee} =$

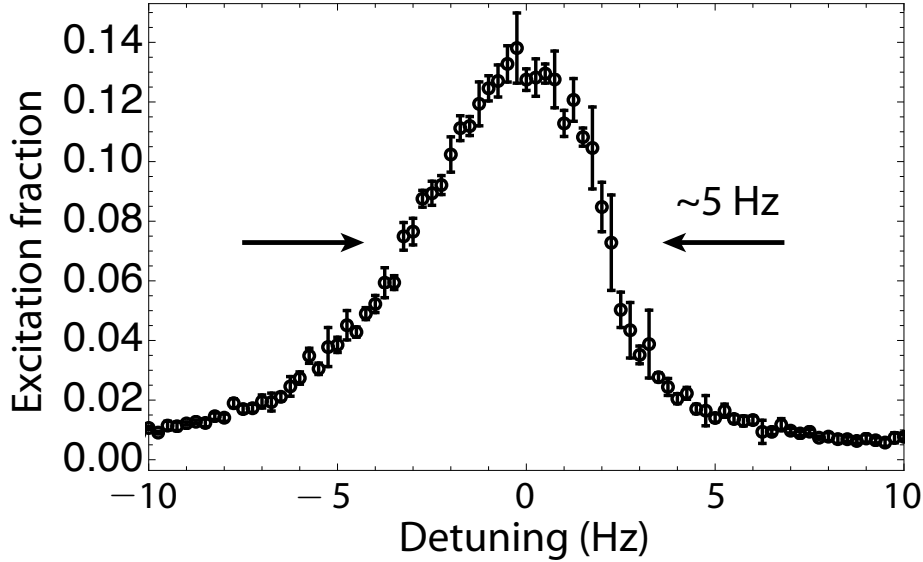


Figure 5.9: Broadened lineshape with 1 s atom-light interaction time. The observed linewidth of approximately 5 Hz is more than a factor of five broader than expected from the Fourier linewidth, and the asymmetry effectively excludes laser noise.

$T \times (4 \pm 2) 10^{-6} \text{ cm}^3/\text{s}/\text{K}$ and $K_s^{\text{dist}} = T \times (4 \pm 2) 10^{-6} \text{ cm}^3/\text{s}/\text{K}$. The agreement with the measured loss rates as a function of temperature is quite good. The simple model also reproduced the ^{88}Sr e - e inelastic loss rate reported by Lisdat *et al.* [290].

5.5.2 Lineshape distortion and loss of Ramsey fringe contrast

The observation of a p -wave inelastic loss mechanism was an important additional piece of information to add to our knowledge of the nature of the interactions between ^{87}Sr in an optical lattice. This observation was made directly possible by an increased vacuum lifetime. Similarly, with the new laser described in Chapter 4, the “Big ULE,” we were prepared to make frequency shift and spectroscopy measurements with an order of magnitude increase in precision. In these initial investigations, we found signatures of **elastic** interactions that also deviated from the s -wave picture that had previously been developed.

Upon installing the new laser, we decided to perform a demanding test of the optical-atomic coherence of the system. We also set out to beat the long-standing record of 2 Hz spectroscopic

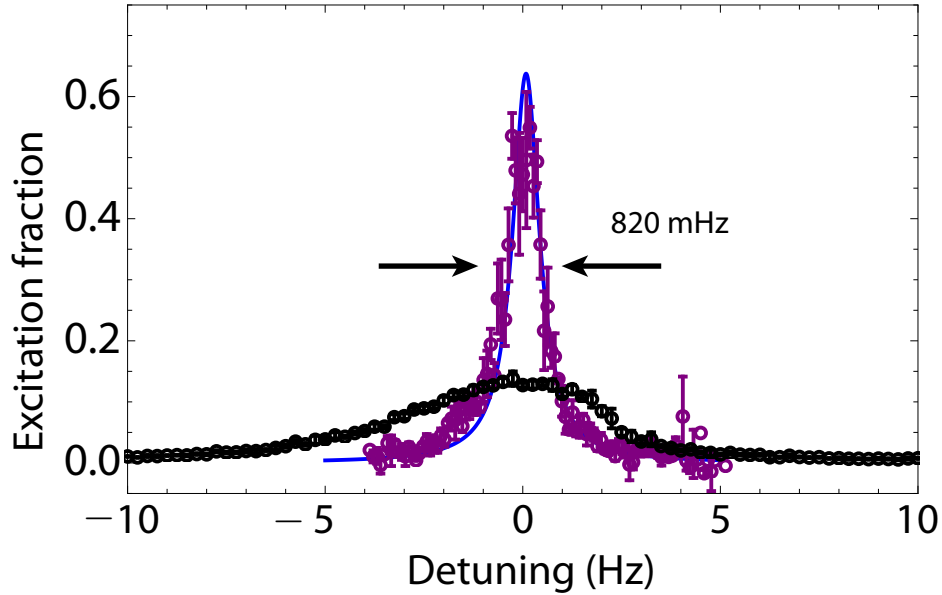


Figure 5.10: Low density lineshape vs. high density lineshape with lattice depth consistent with $\nu_z = 80$ kHz (purple circles). The blue line is a Lorentzian fit. The data from Fig. 5.9 (black circles) is shown for comparison.

features with coherent spectroscopy in ^{87}Sr , which had stood for around half a decade [40]. As a first test, we performed Rabi spectroscopy with a π -pulse duration of 1 s, which should result in a Rabi lineshape with full width at half-maximum (FWHM) of 0.8 Hz. Instead, we observed the lineshape shown in Fig. 5.9 with a FWHM of approximately 5 Hz! Here, the temperature was approximately $4 \mu\text{K}$ and the density was $\rho = 6 \times 10^{11} \text{ cm}^{-3}$. Another striking difference was that the peak excitation fraction, which should theoretically be unity, was nearly an order of magnitude lower than expected. The data in Fig. 5.9 is comprised of approximately 20 individual scans of the line which were subsequently centered upon one another and binned using a bin size of 250 mHz. This has the effect of allowing a high resolution lineshape to be formed in a way that is insensitive to slow laser excursions. Linear laser drifts were removed to the 5 mHz/s level, but to be sure there was no biasing due to scan direction, we altered the sign of the frequency stepping for the laser within a given scan.

We then reduced the atom number by an order of magnitude, such that the density was

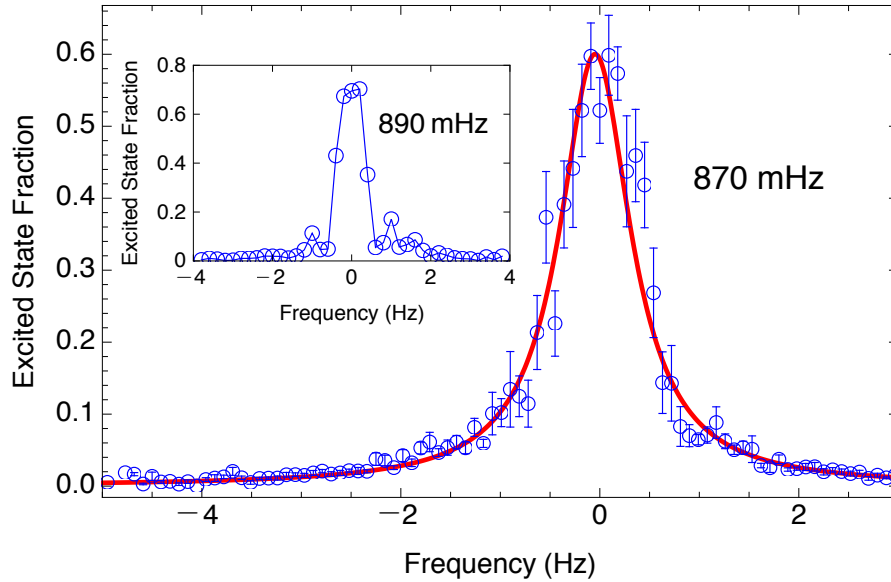


Figure 5.11: Narrow line scan (1 s probe time) with 40% the typical lattice power and a sample temperature of $1 \mu\text{K}$. Here, despite the density of $\rho = 1 \times 10^{11}/\text{cm}^3$, a narrow line is recovered. **(Inset)** Representative single-scan with no binning or averaging.

$\rho = 5 \times 10^{10} \text{ cm}^{-3}$. Under this condition, the line dramatically narrowed to nearly the expected linewidth, with a FWHM of 820 mHz. The linescan is shown in Fig. 5.10 along with the high-density data for reference. Also shown is a Lorentzian fit to the data, which indicates an asymmetry similar in shape to the high-density case, but far less pronounced.

In a final test, we pre-cooled the sample using Doppler and sideband cooling (see Chapter 2, Section 2.7) and subsequently reduced the lattice intensity to 40% of the typical operating intensity using an adiabatic ramp, which had the simultaneous effect of lowering the density, temperature, and total atom number such that the final temperature was $1 \mu\text{K}$ and the density reduced to $\rho = 2 \times 10^{11} \text{ cm}^{-3}$. Under this condition, the line was also narrowed to near the expected lineshape, as shown in Fig. 5.11. For both this condition and the low-density condition described previously, the data was processed and binned as described for the high-density and high-lattice case.

From the three experimental conditions that we explored, we were able to deduce that the dominant line-broadening mechanism was density. This is an important distinction because some calculations of the lattice photon scattering rate had estimated scattering rates as high as $\sim 3 \text{ Hz}$

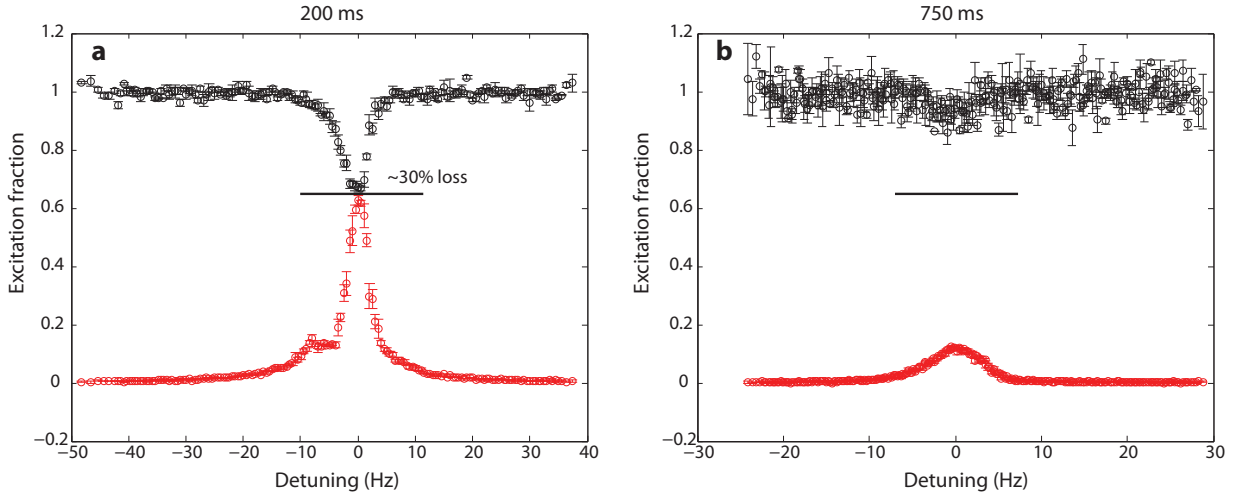


Figure 5.12: Comparison of two lineshapes taken under similar atom number conditions of $N_{\text{tot}} \simeq 5000$. The upper data (black circles) is the total population scaled by the off resonant atom number. The lower traces (red circles) are plots of excitation vs laser detuning. These lineshapes are composites formed from approximately 20 scans each that have been centered upon one another. **(a)** The probe (and resonant π -pulse) time is 200 ms. The peak excitation of the line is approximately 60% of that of the non-interacting case. **(b)** The probe (and resonant π -pulse) time is 200 ms. The peak excitation of the line is approximately 20% of that the non-interacting case. Here, almost no inelastic loss is observed, as can be seen from the discrepancy between the upper data points and the horizontal line indicating the loss from the 200 ms case. The line is also significantly broadened beyond the ~ 1 Hz linewidth expected for a 750 ms probe time.

for a lattice depth of $\sim 120 E_{\text{rec}}$ [292]. However, in addition to ruling out lattice photon scattering as a contributing mechanism to line broadening, as described above, we have rigorously—both experimentally and theoretically—ruled this mechanism out entirely for **all** lattice depths currently accessible to us (see Chapter 2, Section 2.6).

Beyond the general observations discussed above, the lineshapes gave us initial evidence that the s -wave dominated picture of interactions might not be the end of the story. One mechanism that was initially considered was the effect of two-body inelastic loss. However, the observed broadening was much larger than could be accounted for by simply inelastic collisions alone. Furthermore, the two-body loss under conditions with the most severely broadened lineshape under the longest π -pulses was minimal, while the two-body loss for shorter π -pulses was increased. The difference between a 200 ms π -pulse and a 750 ms π -pulse is shown in Fig. 5.12, where in the case of the

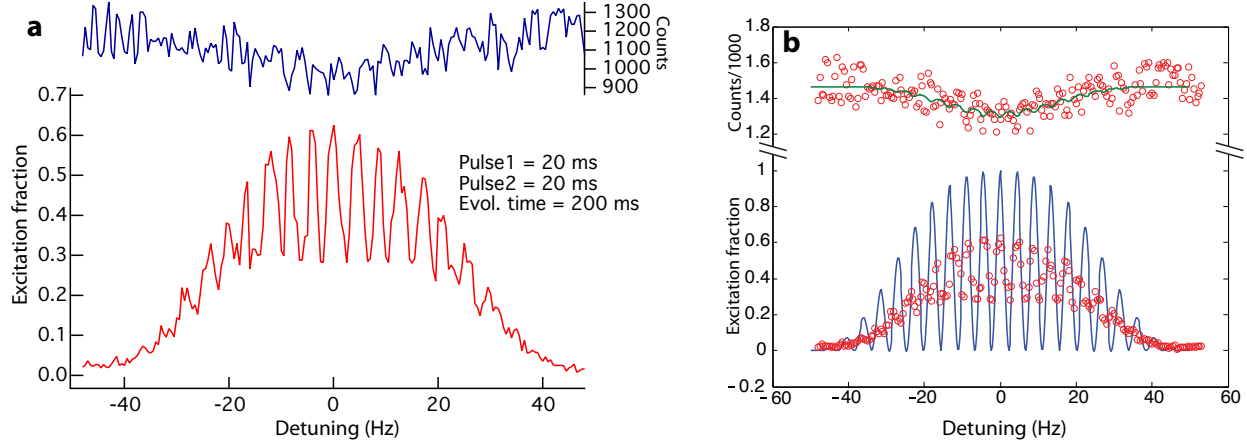


Figure 5.13: Ramsey fringes contrast and two body-loss. (a) Ramsey lineshape observed using the parameters listed in the inset of the figure. A marked decrease in the contrast was observed (bottom trace, red), along with a net atom loss when near resonance (top trace, blue curve; 1 count= 5 atoms). (b) Density matrix model fit to the Ramsey lineshape with ee inelastic losses as the only collisional mechanism. The ee loss rate was tuned to match the net observed atom decay. The effect on the Ramsey fringe contrast is minimal.

latter pulse duration, the two-body loss has been almost completely inhibited.

Finally, we observed strong decoherence of Ramsey fringes during a Ramsey experiment (see Appendix A for a description of Ramsey spectroscopy) where two-body losses were responsible for $\sim 20\%$ losses of total atom number while the fringe contrast decayed to only 30% of the theoretical value of unity. These experimental data are shown in Fig. 5.13a. Under a typical Ramsey experiment, it can be shown that for small two body losses, the fringe contrast should decay quadratically with fraction of atoms lost via excited state two-body loss if this is the only inelastic loss channel. A numerical solution to the optical Bloch equations is shown in Fig. 5.13b for the case of only inelastic two-body loss. For the appropriate two-body decay coefficient, the fringe decay is so small that it is hardly apparent.

These strong pieces of evidence ultimately led us to believe that there was a blockade mechanism of **elastic** origins at work. Since the effect on the carrier was so dramatic, we could rule out s -wave elastic collisions, which should be reduced in strength with respect to the carrier by $\Delta\Omega/\Omega$, which is $\ll 10\%$ for all experimental conditions probed, as shown in Chapter 2. The

natural way to include beyond s -wave effects is via the next partial wave: p -waves. p -wave shifts were observed in a neutral atom clock based on fermionic ^{171}Yb [273, 293], which operates at close to an order of magnitude higher temperatures than the ^{87}Sr lattice clock. However, these results were another important indicator that p -wave interactions can be important, even for collisional energies well below the centrifugal barrier.

5.6 p -wave many-body model

As discussed in the previous section, the s -wave model fails to describe the qualitative features of the spectroscopic lineshapes, even when inelastic p -wave collisions are included. Therefore, it is natural to seek answers from the next available partial wave. In this section, we will apply successive simplifying approximations to the p -wave many-body model, which allows good agreement between the observed lineshapes and density shifts in the linear response regime. We find, however, that certain experimental observables require that beyond mean-field effects within the p -wave theory are retained in order to agree with experiment. Ultimately, these measurements allow us to benchmark the effectiveness of describing the system via a many-body spin-Hamiltonian, opening the door to exploring many-body effects and entanglement between optical degrees of freedom in lattice clocks.

5.6.1 Collective model

We begin our consideration of elastic p -wave effects in the clock by considering the Hamiltonian of Eq. 5.53, given by

$$\hat{H} = -\delta \sum_i \hat{S}_i^z + \sum_i \Omega_i \hat{S}_i^x + \sum_{i \neq j} J_{ij}^\perp \hat{\mathbf{S}}_i \cdot \hat{\mathbf{S}}_j + \chi_{ij} \hat{S}_i^z \hat{S}_j^z + \frac{C_{ij}}{2} (\hat{S}_i^z + \hat{S}_j^z) + \frac{K_{ij}}{4}. \quad (5.65)$$

Here, the mode-dependent constants are given by Eqs. 5.46–5.49. The p wave component of the interactions parameters is characterized by the $V_{ij}^{\alpha\beta}$ terms. As shown in Appendix D, the mode-dependence of the s - and p -wave coefficients is smoothly varying. In the case of the p -wave interaction parameter for two-dimensional traps, the thermal average is independent of the temperature [125].

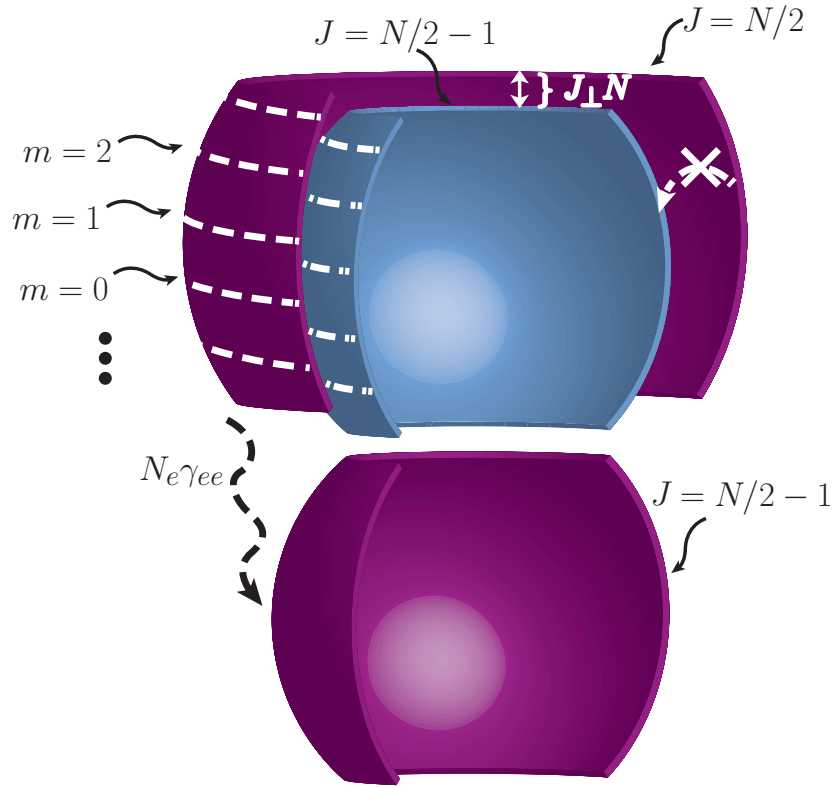


Figure 5.14: Visual depiction of the collective model. The many-body Hamiltonian has eigenstates comprised of maximally symmetric superpositions (Dicke states, for which $S = N/2$) of electronic ground and excited states, depicted as purple shells. Because of the weak inhomogeneities in the coupling strengths, the maximally symmetric manifold is coupled to the next lowest manifold with $S = N/2 - 1$, depicted as a nested blue shell. However, this coupling is prevented by an energy gap present in the many body Hamiltonian as a result of the $J^\perp \vec{S} \cdot \vec{S}$ term, which is depicted by an offset of the two manifolds in this figure. Two-body inelastic losses (dashed black arrow) connect maximally symmetric manifolds of $S \rightarrow S - 1$, and thus are not a strong decoherence mechanism.

Motivated by the weak dependence of the interaction parameters on the mode, we make a simplifying assumption that will be verified by the experimental evidence subsequently presented.

We replace all the interaction parameters by their mode-averaged quantities given by, e.g.,

$$C = \sum_{i \neq j} C_{ij} / [N(N - 1)] \quad (5.66)$$

and the averaged laser excitation term is

$$\bar{\Omega} = \frac{1}{N} \sum_i \Omega_i. \quad (5.67)$$

Here, the sums are averaged over thermally populated distributions of the harmonic oscillator states, $\{|n_i\rangle\}$. Using the averaged quantities, Eq. 5.65 becomes

$$\hat{H} = \underbrace{-\delta\hat{S}^z + \bar{\Omega}\hat{S}^x + J^\perp\hat{\mathbf{S}} \cdot \hat{\mathbf{S}} + \chi(\hat{S}^z)^2}_{\text{collective}} + CN\hat{S}^z + \sum_{ij} \hat{\epsilon}_{ij}. \quad (5.68)$$

Here, the operators without mode subscript are collective operators such that

$$\hat{S}^{\{x,y,z\}} \equiv \sum_i \hat{S}_i^{\{x,y,z\}}. \quad (5.69)$$

We have also moved all the residual mode-dependence to the last term of Eq. 5.68. This term is a perturbative parameter that is small compared to the collective part of the Hamiltonian. It is interesting to note that the collective part of the Hamiltonian in Eq. 5.68 maps onto that of a Bose-Einstein in a double-well potential [294, 295].

The collective Hamiltonian of Eq. 5.68 is nearly diagonal in the Dicke state basis, $|J, m\rangle$, $J \in \{N/2, N/2 - 1, \dots\}$ [296, 297] in the case that there is no laser excitation, *e.g.*, $\Omega_j \rightarrow 0$. Fully symmetric Dicke states are formed by the fully symmetric permutations of ground and excited state atoms subject to the constraint $S^z|N/2, m\rangle = m$. Specifically [297],

$$|N/2, m\rangle = \left[\frac{N!}{(N/2 + m)!(N/2 - m)!} \right]^{-1/2} \sum_S \prod_{n \in S} |g\rangle_n \prod_{n \notin S} |e\rangle_n. \quad (5.70)$$

Here, \mathcal{S} represents the set of all permutations for N atoms with the total number of atoms in the excited state given by $N_e = N/2 + m$.

When an ideal rotation is applied via a spectroscopy pulse, the prepared state is given by a product state of single particle states given by

$$|\theta, \phi\rangle_N = \prod_{n=1}^N [e^{i\phi/2} \sin(\theta/2) |e\rangle_n + e^{-i\phi/2} \cos(\theta/2) |g\rangle_n] \quad (5.71)$$

The Bloch states can be written as sums of the Dicke states as

$$\begin{aligned}
 |\theta, \phi\rangle_N &= \sum_{m=-N/2}^{N/2} \left[\frac{N!}{(N/2+m)!(N/2-m)!} \right]^{-1/2} \\
 &\times e^{im\phi} \sin^{N/2+m}(\theta/2) \cos^{N/2-m}(\theta/2) |N/2, m\rangle
 \end{aligned} \tag{5.72}$$

The states $|\theta, \phi\rangle_N$ can easily be prepared via fast excitation such that $\bar{\Omega} \gg N\{V_{ee}, V_{eg}, V_{gg}\}$. This is the case for Ramsey spectroscopy.

5.6.2 The collective model and density shifts in a 2D optical lattice

As mentioned in Chapter 2, Section 2.8, a two-dimensional lattice (which creates quasi-one-dimensional trap sites) was employed to enter the strongly interacting regime (*i.e.*, where atom-laser and atom-atom interactions are energetically comparable), at the expense of reducing the occupancy to one or two atoms per site [135]. Here p -wave effects were not considered and the excitation inhomogeneity was much higher [135, 288]. Within the many-particle collective model, the role of s -wave interactions in the absence of excitation inhomogeneity is limited to an enlargement of J^\perp , thus enhancing the gap protection and enforcing the validity of the collective spin Hamiltonian.

5.7 Mean-field and perturbative tests of the many-body dynamics

In this section we consider only the collective part of the Hamiltonian of Eq. 5.68. This is a significant assumption, but one we can validate through experiment. These approximations are important for the beyond mean-field treatment of the model as well. Theoretically, there are several aspects of the collective Hamiltonian that justify its use. They are

- (1) The atoms are initialized in the fully symmetric $|J, -J\rangle$ state and will remain in the fully symmetric manifold under laser excitation as long as $\Delta\Omega \ll J^\perp$.
- (2) In a quasi-2D trap, χ and C are highly insensitive to the sample temperature T for a fixed atom number, given that the linear growth of the p -wave interaction with T is compensated

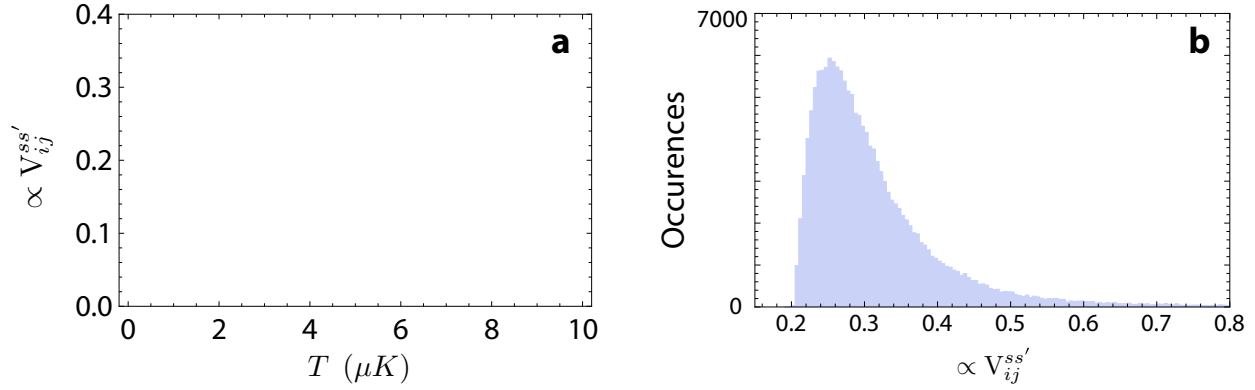


Figure 5.15: Temperature dependence of the p -wave interaction energies and their thermal distribution. (a) Temperature-dependence of the average p -wave interaction parameters. They exhibit a large insensitivity to the temperature due to the quasi-2D confinement. (b) Histogram of the distribution of p -wave interaction parameters at $5 \mu\text{K}$. In both cases a Boltzmann distribution of the populated modes was used [125].

by a corresponding $1/T$ decrease of the density. The validity of this assumption is shown in Fig. 5.15a.

- (3) The interaction parameters have a weak dependence on the thermally populated modes i and j , which is reflected on the fact that their thermal distributions are peaked about their averages (see Fig. 5.15b) [125].
- (4) There is a protective gap given by the $J^\perp \hat{\mathbf{S}} \cdot \hat{\mathbf{S}}$ term, which should be larger than the p -wave interactions due to the s -wave term in J_{ij}^\perp , where $J_{ij}^\perp = V_{ij}^{eg} - U_{ij}^{eg}$. This energetically forbids $J \rightarrow J - 1$ due to the inhomogeneous term in Eq. 5.68, $\sum_{ij} \hat{\epsilon}_{ij}$, which is $\ll J^\perp$.

5.7.1 Perturbative tests of the many-body Hamiltonian

If the system is excited such that only a small fraction of the atoms are promoted from the ground to excited states, the shift of the line center in a single trap site is

$$\Delta\nu_{\text{LRR}}^i \simeq (C - \chi)(N_i - 1), \quad (5.73)$$

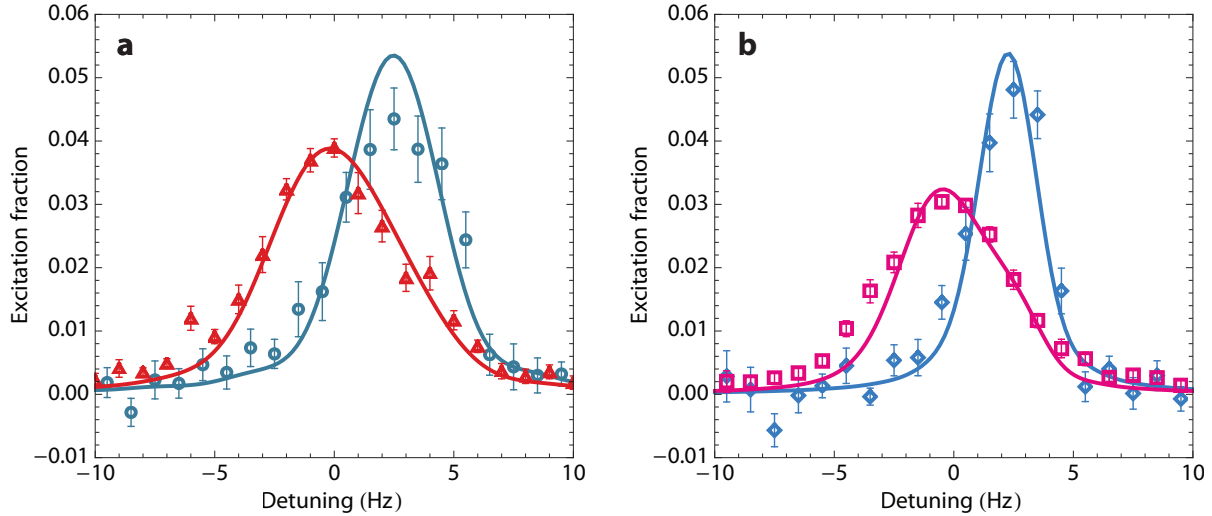


Figure 5.16: Spectroscopy of the clock transition in the linear response regime with pulse area fixed to $\theta = 0.2\pi$. **(a)** Spectroscopy in the linear response regime with $t_R = 250$ ms. The high atom number curve (red triangles) is shifted to lower detuning with respect to the high frequency curve (teal blue circles). The low atom number is $N_{\text{tot}} \simeq 2000$ and high atom number is $N_{\text{tot}} \simeq 5000$ **(b)** Spectroscopy in the linear response regime with $t_R = 500$ ms. The low atom number is $N_{\text{tot}} \simeq 1500$ and high atom number is $N_{\text{tot}} \simeq 4000$.

where the index i labels the individual site. The total shift in the linear response regime is given by an average of $\Delta\nu_{\text{LRR}}^i$ over the site occupancy distribution. The site occupancy distribution is described in Appendix E.

In order to probe the linear response regime experimentally, we reduced the clock laser probe intensity such that for a given probe time, the pulse area was $\theta \equiv \bar{\Omega}t_R = 0.2\pi$. We then took lineshape measurements under four conditions. In the first condition, we set the pulse duration to $t_R = 250$ ms and took scans with low ($N_{\text{tot}} \simeq 2000$) and high ($N_{\text{tot}} \simeq 5000$) atom number conditions. These data are depicted in Fig. 5.16a. We then increased the total probe time to $t_R = 500$ ms, but decreased the probe intensity so that, as before, $\theta = 0.2\pi$. This longer-probe time data is shown in Fig. 5.16b. Under this second condition, the low atom number was $N_{\text{tot}} \simeq 1500$ and the high atom number was $N_{\text{tot}} \simeq 4000$.

Importantly, as seen in Fig. 5.16, the data support the simple description of the shift given by Eq. 5.73. Here, the theoretical lineshapes are formed by averaging the linear-response shift over

the average site occupancy distribution as described in Appendix E. Two important features are immediately evident. The first is that the line center is clearly shifted, even with the weak excitation. This is in clear contradiction with the s -wave-dominant picture of the density shift, where sidebands create a line-pulling effect, and should be negligibly small for such weak excitation. The second is that the line centers are shifted approximately the same, even though the probe time is different by a factor of two. We note that this statement is not completely rigorous because the total atom numbers in both cases, in addition to the difference in atom number between the high and low conditions, were not exactly the same. However, the fact that there is no dramatic difference between 250 ms data and the 500 ms data reproduces the universal behavior we expect of the shift in the limit of weak, perturbative probing of the linear response. The data is fit according to a composite lineshape formed of Lorentzians shifted according to Eq. 5.73 and weighted by the atom numbers distribution. The data are consistent with a $C - \chi = -0.3(1)$ Hz.

5.7.2 Mean-field solution of the collective model

Even in its vastly simplified form, the collective Hamiltonian of Eq. 5.68 still represents a formidable calculation. In the absence of the laser driving (i.e. $\bar{\Omega} = 0$), the Hamiltonian is diagonal in the maximally symmetric Dicke state [296] basis, and exact solutions for the time dynamics have been obtained [280]. However, in the presence of a laser drive, the dynamics of the collective spin model are complicated, but numerically tractable [125]. It is our goal to analyze the dynamics in a simplified regime. Here, we will find several experimental observables that are well-described by using a so-called mean-field treatment of time evolution so-called because it considers only the evolution of field operators by making the simplifying assumption that no correlations form.

We begin by defining new operators based upon the previously-defined spin operators. The first two operators are the number of atoms “spin-up” (i.e. in the excited state) and conversly “spin-down,” given by

$$\hat{N}_{\uparrow} = \hat{S}^z + N/2, \quad \hat{N}_{\downarrow} = N/2 - \hat{S}^z. \quad (5.74)$$

The second operators we define are the canonical angular momentum raising and lowering operators formed by linear combinations of \hat{S}^x and \hat{S}^y , and which are given by

$$\hat{S}^{\pm} = \hat{S}^x \pm i\hat{S}^y. \quad (5.75)$$

We find the time evolution of these operators under the action of the collective Hamiltonian via the Heisenberg equation of motion and obtain

$$\begin{aligned} \frac{\partial}{\partial t} \hat{S}^{\pm} &= i \left[H/\hbar, \hat{S}^{\pm} \right] \\ &= \pm \bar{\Omega} S^z \pm i[-\delta + C(N-1)] \hat{S}^{\pm} \pm i\chi \left(\hat{S}^{\pm} \hat{S}^z + \hat{S}^z \hat{S}^{\pm} \right) \end{aligned} \quad (5.76)$$

and

$$\frac{\partial}{\partial t} \hat{N}_{\uparrow} = -\frac{\partial}{\partial t} \hat{N}_{\downarrow} = i\bar{\Omega} \left(\hat{S}^+ - \hat{S}^- \right) / 2. \quad (5.77)$$

We then replace operators by their expectation values, thus removing quantum fluctuations associated with operators and arising from their commutation relations. **This will be our operational definition of mean-field dynamics.** We will use the convention that $\langle \hat{\mathcal{O}} \rangle \equiv \mathcal{O}$. To the mean field limit to the dynamics of the many-body equations of motion we additionally add a inelastic two body loss term (as in Refs. [290] and [116]), Γ_{ee} , to properly account for the inelastic loss described previously. The mean-field equations of motion become

$$\frac{\partial}{\partial t} S^{\pm} \simeq \pm i \frac{\bar{\Omega}}{2} S^z \pm i \left[-\delta + 2\chi S^z + CN \pm i \frac{\Gamma_{ee}}{2} N_{\uparrow} \right] S^{\pm}, \quad (5.78)$$

$$\frac{\partial}{\partial t} N_{\downarrow} = i\bar{\Omega} (S^+ - S^-) / 2, \quad (5.79)$$

$$\frac{\partial}{\partial t} N_{\uparrow} = i\bar{\Omega} (S^- - S^+) / 2 - \Gamma_{ee} N_{\uparrow}^2. \quad (5.80)$$

Without loss (i.e., $\Gamma_{ee} \rightarrow 0$), these equations behave as if there is an effective magnetic field-like term in the hamiltonian, with magnitude given by $B(N) = NC + 2\chi S_z$.

5.7.3 Density shift in the mean field limit

We begin our consideration of Eqs. 5.78–5.80 by treating the case of Ramsey spectroscopy, which provides a clean way to decouple the time evolution. Specifically, during the dark time,

analytic expressions for $N_e(t)$ and $S^\pm(t)$ can be found and then used as driving terms for Eq. 5.78.

We start by noting that the general expression for S^\pm is given by

$$S^\pm(t) = S_0^\pm \exp \left[\pm i \int_0^\tau dt u^\pm(t) \right], \quad (5.81)$$

where

$$u^\pm(t) \simeq \left[-\delta + 2\chi S^z(t) + CN(t) \pm i \frac{\Gamma_{ee}}{2} N_e(t) \right]. \quad (5.82)$$

From this expression, the frequency shift with respect to the non-interacting case is easily inferred.

Specifically,

$$\Delta\omega = \frac{1}{\tau} \int_0^\tau dt [2\chi S^z(t) + CN(t)] = 2\chi \overline{S^z} + C\overline{N}. \quad (5.83)$$

Here, $\overline{S^z}$ and \overline{N} are the time-averaged values of S^z and N , respectively. Thus, only knowledge of $\overline{S^z}$ and \overline{N} is required in a given measurement to find χ and C , and knowledge of the specific time-dependence of these quantities is not strictly necessary. Stated another way,

$$\Delta\omega = \overline{N} [2\chi (\overline{f} - 1/2) + C]. \quad (5.84)$$

Here, \overline{f} is the average number-weighted excitation fraction and is given by $\overline{f} \equiv \overline{Nf}/\overline{N}$. This value is approximately equal to the time-averaged value of the time-dependent excitation fraction, $f(t)$ as used in Ref. [293].

5.7.4 Measuring the density shift with a Ramsey interrogation scheme

As can be seen from Eq. 5.84, the shift in Ramsey spectroscopy should be linear with \overline{f} as long as the mean-field expression is valid. This suggests a very straightforward way to extract the interaction parameters: by performing Ramsey spectroscopy using a modified sequence, one can vary \overline{f} by varying the initial Ramsey pulse area, θ_1 , while keeping the second pulse area, θ_2 fixed to be $\theta_2 = \pi/2$ and thus maximizing fringe contrast and therefore measurement precision. This was the general approach employed in Refs. [273] and [293], and was the first conclusive proof of p -wave collisions in a fermionic ^{171}Yb optical lattice clock.

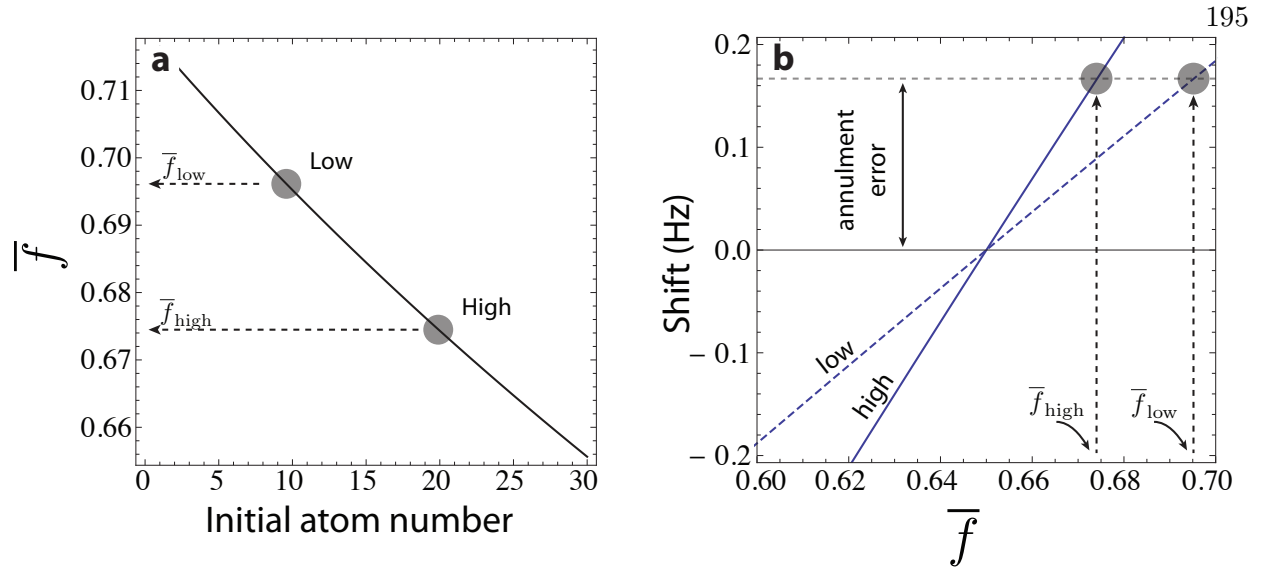


Figure 5.17: Effect of two-body losses on the density shift measurement for two test cases, with $\chi = 2\pi \times 0.2$ Hz, $C = -0.3\chi$, and $\Gamma_{ee} = 2\pi \times 0.07$ Hz. “High” corresponds to an initial single-site atom number of 20, while “low” corresponds to an initial number of 10. **(a)** Atom-number weighted average excitation fraction, \bar{f} , as a function of initial atom number with an initial excited state fraction of 72%. Due to the nonlinearity of the two-body loss, \bar{f} depends upon the initial atom number. **(b)** Annulment of the density shift between “high” and “low” atom number conditions. The annulment between the two conditions is achieved as desired, but the shift with respect to vanishing density is still finite due to the influence of the two-body on \bar{f} between the two conditions.

Due to the two-body inelastic loss, however, measuring the Ramsey shift in a self-consistent way is potentially fraught with peril. To illustrate the problems, we consider a Hypothetical measurement, with a “high” atom condition, corresponding to an initial site occupancy of 20 atoms, and a “low” atom condition, corresponding to an initial site occupancy of 10 atoms. The idea is to use the relative shift between the high and low condition to extrapolate χ and C . However, as shown in Fig. 5.17a, the two-body loss couples total atom number to \bar{f} , such that when the atom number is varied between the high and low conditions, \bar{f} is inadvertently varied.

A given density shift measurement is obtained by comparing the Ramsey fringe central frequency under the high density condition to the low density case, such that

$$\Delta\omega_{\text{meas}} = \Delta\omega_{\text{high}} - \Delta\omega_{\text{low}} = 2\chi\bar{N}_{\text{high}}(\bar{f}_{\text{high}} - p^*) - 2\chi\bar{N}_{\text{low}}(\bar{f}_{\text{low}} - p^*). \quad (5.85)$$

Here, \bar{N}_{high} and \bar{N}_{low} represent the ensemble- and time-averaged single-site occupancy for the high

and low density conditions, respectively. The explicit goal of our measurement is to extract the zero-crossing fraction, p^* , which can be written as a function of χ and C (see Eq. 5.84) and also the nonlinear parameter χ . By forming a new weighted quantity of \bar{f}_{high} and \bar{f}_{low} we can achieve this goal. We define a new average quantity of the excitation fraction, which represents a weighted average of both average excitation fraction as

$$\bar{\bar{f}} \equiv \frac{\bar{N}_{\text{high}}\bar{f}_{\text{high}} - \bar{N}_{\text{low}}\bar{f}_{\text{low}}}{\bar{N}_{\text{high}} - \bar{N}_{\text{low}}} \quad (5.86)$$

such that it is algebraically true that

$$\Delta\omega_{\text{meas}} = 2\chi(\bar{N}_{\text{high}} - \bar{N}_{\text{low}})(\bar{\bar{f}} - p^*). \quad (5.87)$$

Equations 5.86 and 5.87 are important because they are universal as long as Eq. 5.84 is valid. It also gives us an unambiguous way to plot the data. By defining $\bar{\bar{f}}$ in this manner, which is a derived quantity rather than a directly measured one, we have removed the effect of the cross-coupling between $\bar{N}_{\text{high(} \text{low)}}$ and $\bar{f}_{\text{high(} \text{low)}}$.

One important conclusion of the analysis presented above is that a measurement of a null shift between two different density conditions for a given initial excitation fraction does **not** imply that the total shift is zero at this initial excitation fraction, nor does it give an accurate value for p^* . This is true even when the fraction of total atoms lost is only at the level of several percent. To see this, we assume that $\chi = 2\pi \times 0.2$ Hz, $C = -0.3\chi$, and $\Gamma_{ee} = 2\pi \times 0.07$ Hz, resulting in $p^* = 0.65$ (these will turn out to be very nearly the measured values for ^{87}Sr). Next, the measurement is performed using an initial “high” initial site occupancy of 20 and an initial “low” site occupancy of 10. This will yield $\bar{\bar{f}} = p^* = 0.65$ for a properly nulled shift, while on the other hand $\bar{f}_{\text{high}} = 0.67$ and $\bar{f}_{\text{low}} = 0.70$. Thus, if we were to choose the “high” conditions as our operating point, the remaining shift with respect to the zero-density limit would be $\simeq 2\chi\bar{N}_{\text{high}} \times 0.02$, which represents a shift of 4×10^{-16} . This is a huge error and nearly four times larger than the entire clock uncertainty. Interestingly, if we had instead chosen to use the “low” conditions as our operating parameters (leading to a frequency error of $\simeq 2\chi\bar{N}_{\text{low}} \times 0.05$) we would still have exactly the same frequency

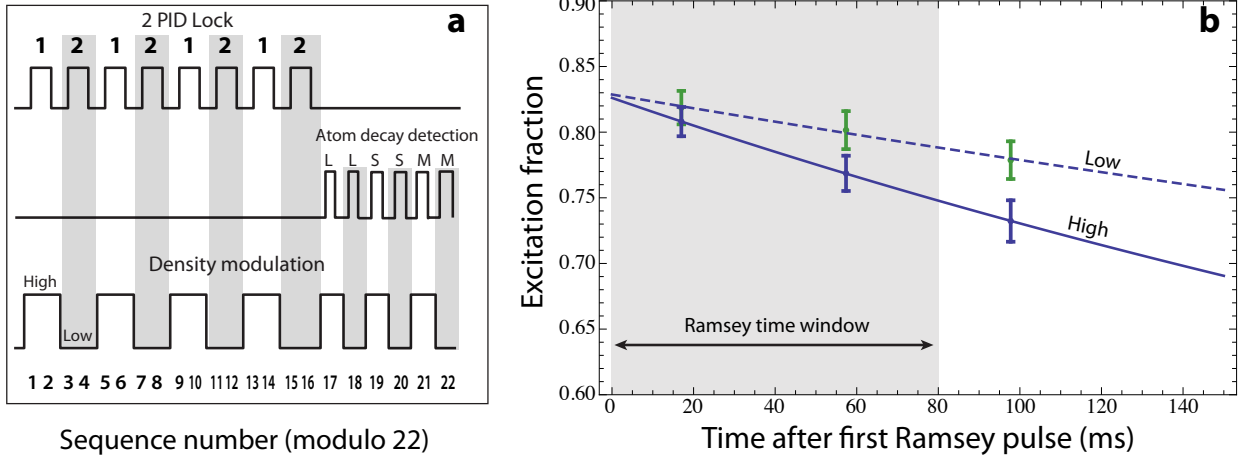


Figure 5.18: Timing sequence and example of inter-sequence excitation fraction measurement. **(a)** Timing diagram for the multiplexed Ramsey density shift measurement. Two independent PID locks are utilized to measure the differential frequency between the high and low density condition. After four locking cycles, which are alternated for each PID, an atom–decay measurement is performed. During this measurement, three delays are utilized to extrapolate the two-body loss curve: short (S), medium (M), and long (L). **(b)** Example of experimental data for the measurement of 2-body losses during the Ramsey measurement sequence. The low and high density conditions are fit with two-body loss curves. Error bars are standard deviations and therefore represent the scatter of the data, not the uncertainty of the mean.

error of 4×10^{-16} . This in fact must be true, since the shift was indeed measured as a relative null between the high and low operating conditions. Figure 5.17b illustrates this mechanism, whereby the relative shift is nulled but the total shift is not. The conclusion we must draw from this example is that we can only use density shift measurements to extrapolate the proper operating fraction of the clock, given by $\bar{f} = 0.65$. In the presence of two-body loss, one cannot directly rely on a measured null shift alone to determine either the location of the true zero-crossing lies, and care must be taken when using such a measurement as proof that the clock has achieved a target operating uncertainty.

We performed a modified density shift measurement to extract the density shift as a function of \bar{f} . The technique is based upon that used in Ref. [135]. As depicted schematically in Fig. 5.18, we operate two independent locks to the atoms and modulate the relative density between them. The frequency difference between periodically modulated conditions is recorded. After four pairs of

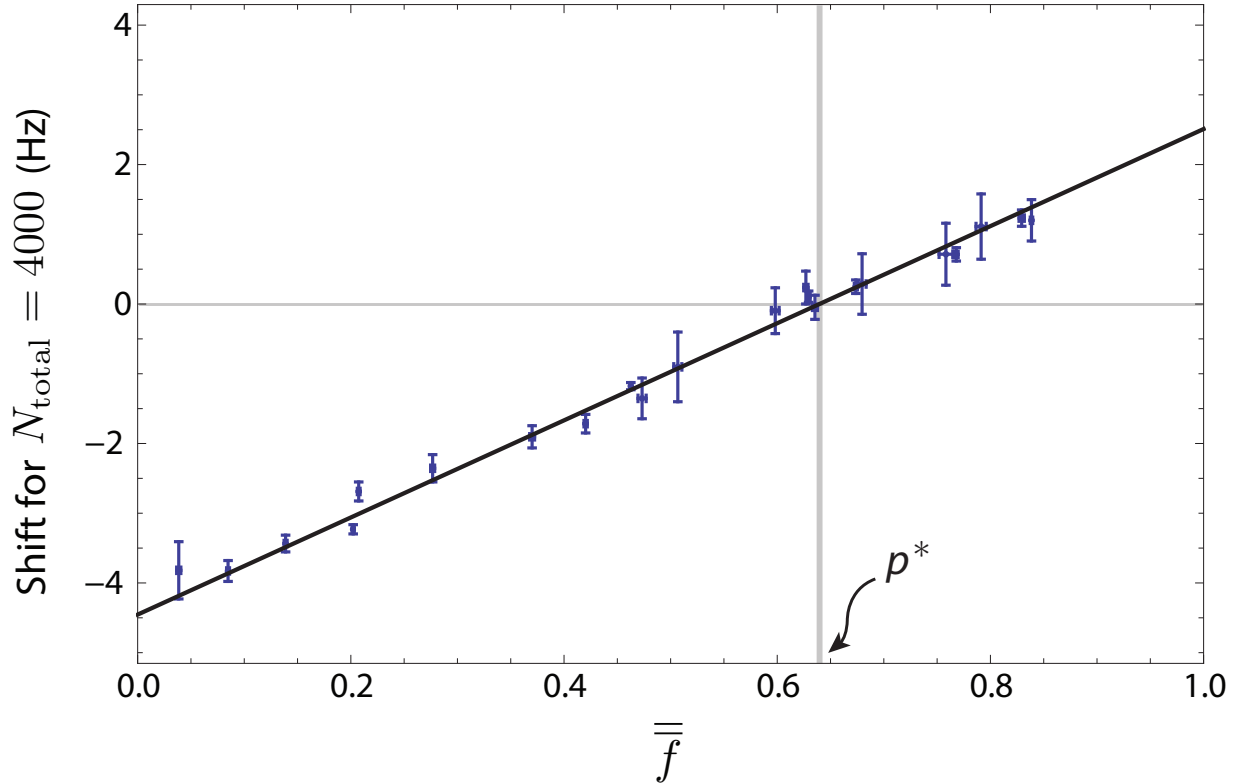


Figure 5.19: Measured Ramsey shift as a function of the scaled excitation fraction \bar{f} . The vertical error bars are standard errors calculated from the statistical scatter of the measured shift coefficient. The horizontal error bars are the standard error of \bar{f} calculated from separate measurement sequences inserted into the density shift measurement sequence. Fluctuations in \bar{f} mainly arise from fluctuations in the total atom number. The reduced χ^2 statistic for the linear fit is 1.3. As described in the text, this measurement yields $p^* = 0.640(6)$, $\chi = 2\pi \times 0.21(4)$ Hz, and thus $C = -0.280(12)\chi$.

high-low measurement cycles, we devote six experimental cycles to measuring the two-body losses during the Ramsey experiment. Briefly, this decay-measuring cycle proceeds with a single pulse of area θ_1 , which is identical to the first pulse of the Ramsey sequence. The time between this pulse and the atom number measurement phase is varied, allowing excited state atom decay as a function time to be measured. We then fit the decay curves, which consist of three points taken at each density condition, with two-body decay lineshapes. This allows us to calculate the the relevant quantities, namely \bar{f} , \bar{N}_{high} , and \bar{N}_{low} .

The results of the Ramsey density shift measurement are shown in Fig. 5.19. As seen from the data, the linear dependence of the shift predicted by Eq. 5.87 agrees extremely well with the experimental observation, over the full range of excitation fractions. From these measurements we extract $p^* = 0.640(6)$. The extracted slope is measured with comparable fractional precision, but converting the experimentally measured shift parameter to χ introduces extra uncertainty due to the uncertainty in atom number calibration and axial intra-site distribution. If we fix the atom number such that the total time-averaged atom number is $N_{\text{total}} = 4 \times 10^3$, then the slope plotted in Fig. 5.19 is 6.96(15) Hz. For the same value of N_{total} , the ensemble-averaged single-site occupancy will be $\bar{N} \simeq 16.3$ (see Appendix E). This yields $\chi = 2\pi \times 0.21(4)$ Hz. Here the uncertainty comes mainly from the atom number and site distribution uncertainty. Finally, knowledge of p^* allows us to relate C to χ , with $C = -0.280(12)\chi$.

As a final note, it is interesting to consider exploiting the measured zero-crossing to cancel density-dependent shifts as proposed in [293]. With a relatively short three-day sequence of measurements, resulting in the data shown in Fig. 5.19, we are able to locate the zero-crossing to better than 1%. If we operate with a total number of atoms $N_{\text{total}} = 1 \times 10^3$, then the resulting frequency uncertainty is 2.4×10^{-17} . However, other effects such as repump efficiency and spin polarization efficiency would need to be considered before firmly claiming a final number. It is nice to know however, that even under very high-density operating conditions there are no fundamental impediments to operating with a density shift contribution at the 10^{-17} level. In fact, a day of focused density shift measurements could push the statistical uncertainty of the zero-crossing point below 1×10^{-17} , if a shift uncertainty at this level were to become necessary.

5.7.5 Describing spectroscopic lineshapes with the mean-field model

In the presence of a laser drive, the many-body system has two relevant energy scales, which represent a boundary between a laser-drive-dominated regime, where $\bar{\Omega} > N\chi$ and an interaction-dominated regime, where $\bar{\Omega} < N\chi$. This type of transition phenomenon is observed in the dynamics of double-well BEC systems, which are described by a Hamiltonian equivalent to the collective

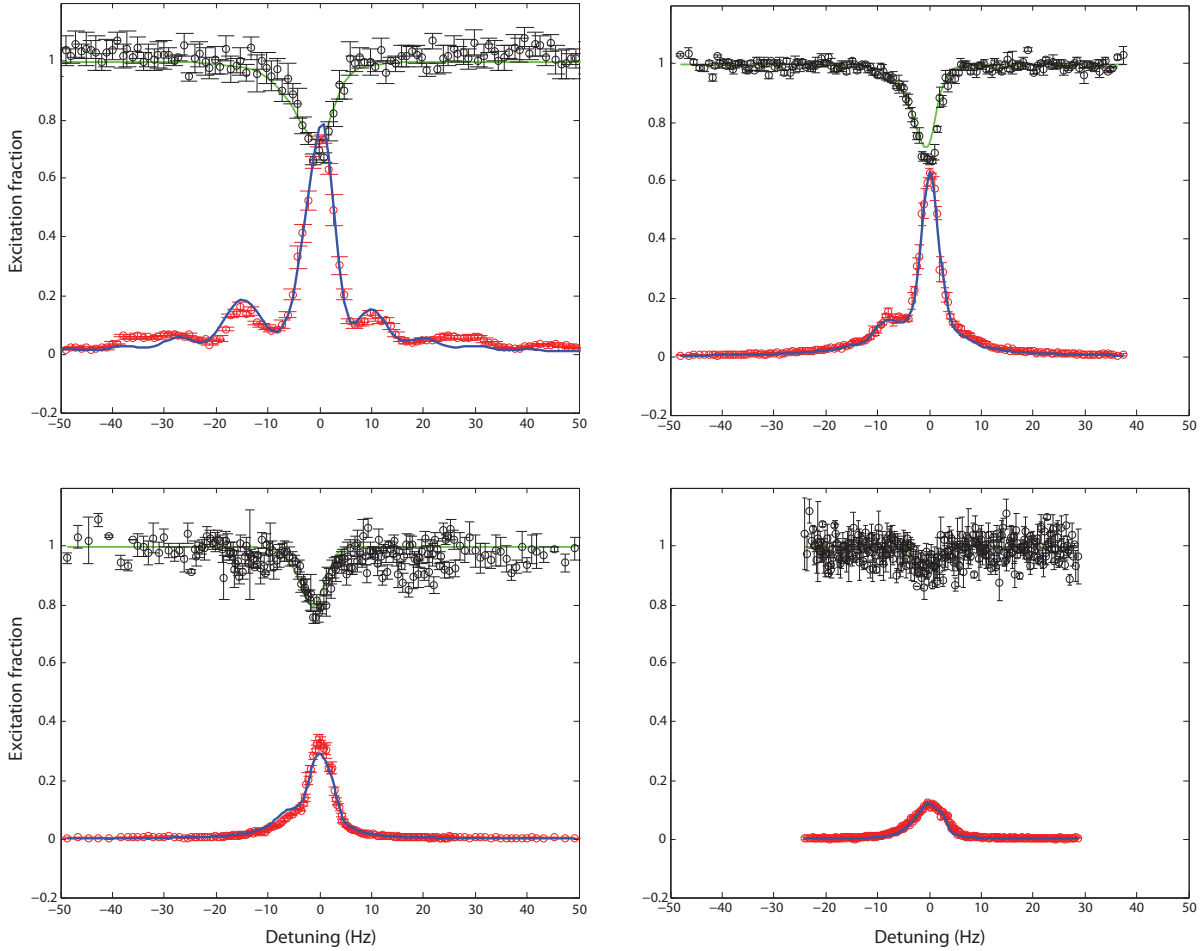


Figure 5.20: Lineshape (red circles) and normalized total atom number (black circles) as a function of detuning and for decreasing $\bar{\Omega} \simeq \pi/t_R$. In all plots, $\bar{N} \simeq 5000$. (a) $t_R = 100$ ms (b) $t_R = 200$ ms (c) $t_R = 300$ ms (d) $t_R = 750$ ms

Hamiltonian of Eq. 5.68 and can lead to phenomena such as excitation blockade or macroscopic self-trapping [294, 298, 295]. In principle, this transition could be accompanied by a non-trivial shift in the behavior from a system that is well-described by a mean field treatment to one in which the true quantum many-body nature of the eigenvalues becomes important.

In order to probe the spin model in the presence of a laser coupling term, we performed Rabi spectroscopy under a variety of atom numbers and coupling strengths, characterized by $\bar{\Omega}$. Figure 5.20 shows both the measured spectroscopic lineshape and atomic loss curves in detail for

$N_{\text{total}} \simeq 5 \times 10^3$. Here, each lineshape is a composite of 10 individual scans that have been centered atop one another. The theoretical fits are numerical solutions of the mean-field evolution given by Eqs. 5.78–5.80 and are computed for a given initial atom. The results are averaged over the site-occupancy distribution (Appendix E). In order to account for the effect of laser noise within a given scan and also between scans, a phenomenological dephasing term, L , has been added to the time evolution of S^\pm , such that [116]

$$\frac{\partial}{\partial t} S^\pm \simeq \pm i \frac{\bar{\Omega}}{2} S^z \pm i \left[-\delta + 2\chi S^z + CN \pm i \left(\frac{\Gamma_{ee}}{2} N_\uparrow + L \right) \right] S^\pm. \quad (5.88)$$

We find that values of $L = 2\pi \times 0.4$ Hz and $\Gamma_{ee} = 2\pi \times 0.075$ Hz work well for these particular data. With subsequent improvements we made to the laser, it is likely that L will be found to be reduced in future measurements of this type. Additionally, while the laser-atom interaction time is nominally fixed such that $\bar{\Omega}t_R \simeq \pi$, due to the difficulty of experimentally verifying a $\bar{\Omega}t_R = \pi$, the equality is only approximate, and in the numerical simulations the pulse area is left as a free parameter, which can vary from at the level of 10%. As seen from Fig. 5.20, the quantitative agreement between the theory and data is quite good, including the predicted total atom loss when the spectroscopy laser is on resonance.

A more thorough display of the different interaction regimes is shown in Fig. 5.21. In this figure, we show lineshapes obtained by varying the ratio of $\chi\bar{N}$ to $\bar{\Omega}$ in two ways. In the first approach, we keep $\bar{\Omega}$ fixed at $2\pi \times 2.5$ Hz while varying the total atom number. At the lowest two atom numbers, $\chi\bar{N} < \bar{\Omega}$. For the largest three atom number conditions, $\chi\bar{N} > \bar{\Omega}$. In the second approach, we instead vary $\bar{\Omega}$ while keeping the atom number fixed at 5×10^3 . In this latter case, all but the curve with $t_R = 100$ ms are in the regime where $\chi\bar{N} > \bar{\Omega}$, with the last curve satisfying $\chi\bar{N}/\bar{\Omega} \simeq 6$. Even in this extreme interacting regime, with $\chi\bar{N}/\bar{\Omega} \simeq 10$, the model does a good job describing the lineshape. In such a strongly interacting regime, effects analogous to macroscopic self-trapping [294] are playing a role in many of the trap sites as shown in Fig. 5.21.

Finally, we note that density-dependent effects are visible in the lineshape even for very low densities/atom numbers of $< 10\%$ of those typically utilized. Using a 2 s rabi pulse, we scanned

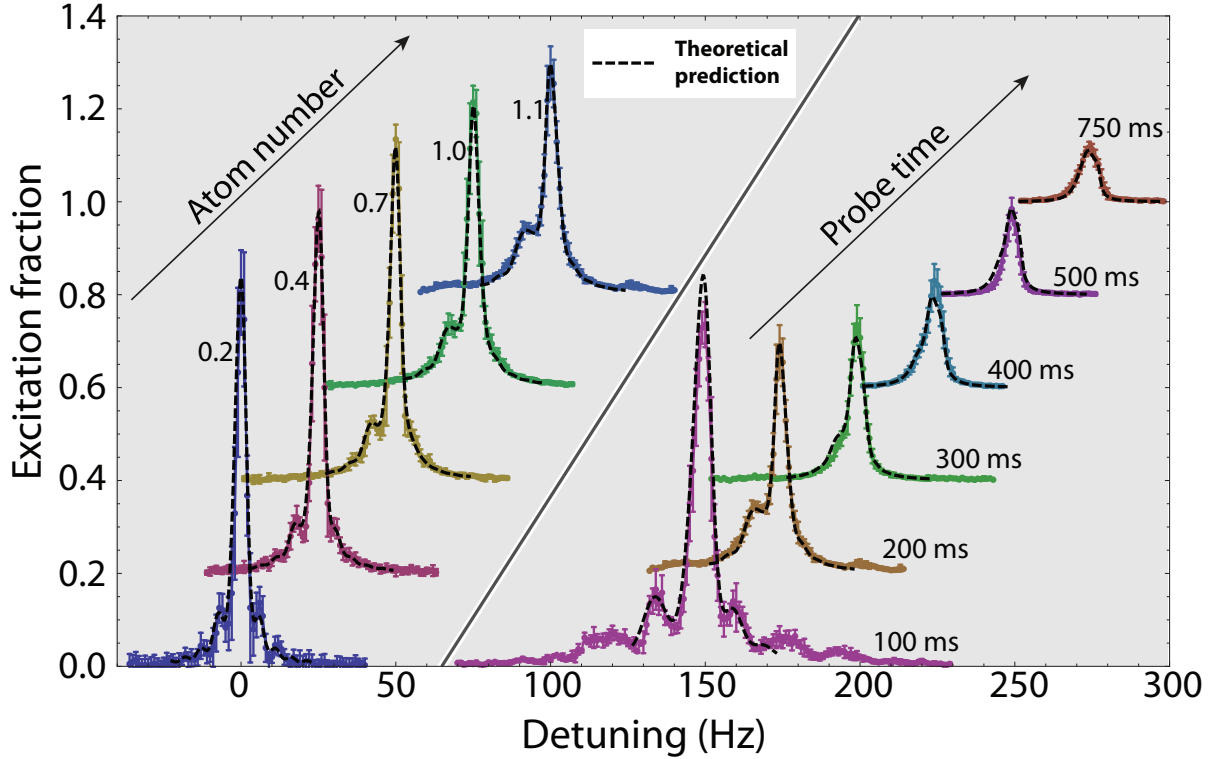


Figure 5.21: Lineshape as a function of experimental parameters. Each curve is a composite of multiple scans that have been centered atop one another and the data subsequently binned. The curves are offset in both the vertical and horizontal directions for visual clarity. **Left side:** Lineshape as a function of density (normalized by ρ_0), with a π -pulse time of 200 ms. **Right side:** Lineshape for $\rho \simeq \rho_0$ as a function of probe time. Theoretical curves, obtained with the mean-field treatment including loss, are shown as dashed black lines and agree well with the measurements.

out the lineshape shown in Fig. 5.22a. The linewidth of this composite lineshape is approximately 750 mHz. Even at the sub-Hz energy scale, the interactions manifest themselves as a clear asymmetry in the lineshape. As shown in Fig. 5.22b, we have verified that as the atom number decreases, the observed linewidth approaches the ideal Fourier-limited value for a 2 s Rabi pulse. At the very lowest densities and with a 3 s Rabi pulse, we observe repeatable linewidths of 500 mHz (Inset, Fig. 5.22a), representing a record for coherent atomic spectroscopy and a line Q of nearly 10^{15} .

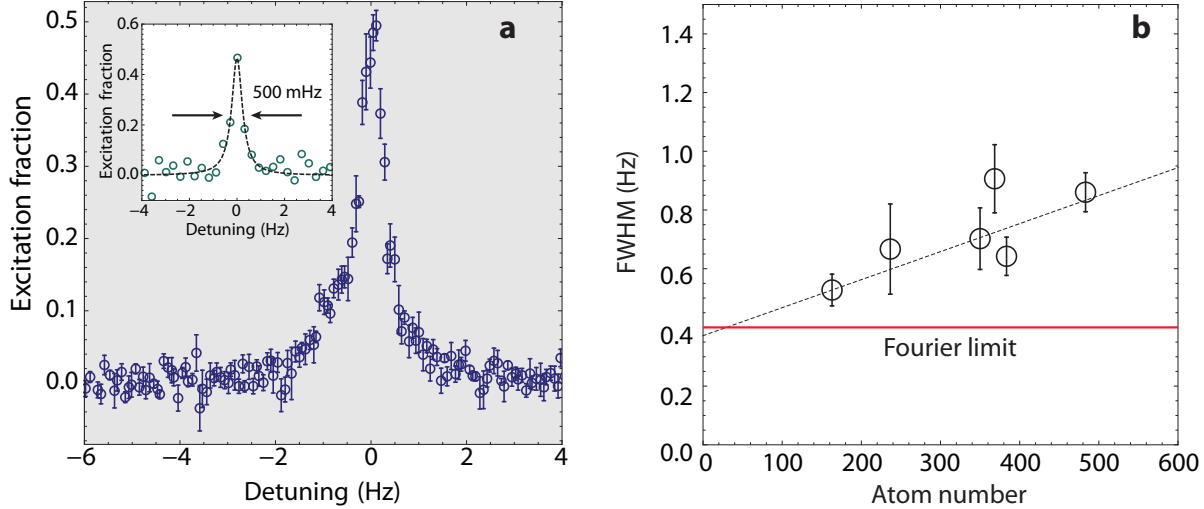


Figure 5.22: Interaction effects visible at the sub-Hz energy scale. **(a)** Composite lineshape obtained at an operating density of $0.1\rho_0$ with a 2 s clock probe, where ρ_0 is the density obtained for 5×10^3 atoms, and is given by $\rho_0 = 5(2) \times 10^{11} \text{ cm}^{-3}$. The line shape shows a clear distortion due to the density-dependent interaction at the sub-Hz energy scale. **(Inset)** Extremely low density scan ($\rho = 5 \times 10^{-2}\rho_0$) with a 3 s clock probe, demonstrating the ultimate frequency resolution of the system. This is a single scan thus no binning or averaging was applied. **(b)** measured linewidth as a function of Atom number in the low-density regime for the scans compiled to create the figure at left. As seen from the data, the density-dependence of the linewidth extrapolates to the 0.4 Hz Fourier limit for the 2 s Rabi pulse used.

5.8 Beyond mean-field effects

In the previous section, we explored two experimental observables that were well-described by the mean-field approximation of the collective spin Hamiltonian. For the Ramsey density shift and Rabi lineshapes, spin correlations that may develop during the time-dependent evolution do not manifest themselves in the measurement. Furthermore, we expect that in the case of Rabi spectroscopy, the strong elastic “blockade-like” excitation-inhibition as well as two-body losses prevent these correlations from forming. However, this was useful for us; from these measurements we were able to extract the relevant interaction parameters for the collective spin model.

In this section we consider two experimental observables that **do** have a sensitivity to quantum correlations, and thus require a treatment beyond the mean-field approximation. These two observables are the Ramsey fringe contrast, and the quadrature dependence of the spin noise. We

find that in order to accurately treat the Ramsey fringe contrast decay, we must include higher order corrections due to virtual motional excitations. We furthermore discuss a method to capture the beyond mean-field dynamics of the model using the truncated Wigner approximation. These theoretical methods are briefly discussed in the next two sections. We then describe the measurements that confirm the observation of quantum many-body effects that necessitate a beyond mean-field description.

5.8.1 Perturbative corrections to the spin model

In the derivation of the collective Hamiltonian, we disregarded mode-changing terms, where the final occupied motional states are different than the original ones (see Section 5.3.2), because they were energetically disallowed by the trap anharmonicity. We recall that the only allowed processes were $\{\mathbf{n}_i, \mathbf{n}_j\} \rightarrow \{\mathbf{n}_i, \mathbf{n}_j\}$ (direct) and $\{\mathbf{n}_i, \mathbf{n}_j\} \rightarrow \{\mathbf{n}_j, \mathbf{n}_i\}$ (exchange). However, the inclusion of virtual processes introduces higher-order corrections of order $(S^z)^3$. A similar effect has been observed in interacting bosons, where these processes manifest themselves as an effective three-body interaction [299].

The additional terms can be included using second order perturbation theory. In order to proceed, we separate the spin system into two manifolds comprised of spin wavefunctions and motional states. The first manifold is what we considered originally, namely that no mode-changing collisions have arisen and the total energy is conserved. Specifically, we write this manifold as [125, 300]

$$|\Phi_{\vec{\sigma}_i}^{\Sigma}\rangle = |\sigma_{\mathbf{n}_1}, \sigma_{\mathbf{n}_2}, \dots, \sigma_{\mathbf{n}_N}\rangle, \quad E_0^{tot} \equiv \sum_{j=1}^N E_{\mathbf{n}_j}. \quad (5.89)$$

Here, the $\sigma_{\mathbf{n}_j}$ terms label the spin in the g - e basis for the particle in the \mathbf{n}_j motional state. The second manifold, which is connected to the first via the many body Hamiltonian, is

$$|\Psi_{\vec{\sigma}_k}^{\Upsilon}\rangle = |\sigma_{\mathbf{k}_1}, \sigma_{\mathbf{k}_2}, \dots, \sigma_{\mathbf{k}_N}\rangle, \quad E_{\vec{\mathbf{k}}}^{tot} \equiv \sum_{j=1}^N E_{\mathbf{k}_j} \neq E_0^{tot}. \quad (5.90)$$

Since these two manifolds are connected by a virtual excitation process, these can be included via

second-order perturbation theory. The effective Hamiltonian, $\hat{H}^{(2)}$, is given by

$$\langle \Phi_{\vec{\sigma}_n}^\Sigma | \hat{H}^{(2)} | \Phi_{\vec{\sigma}'_n}^\Sigma \rangle = - \sum_{\sigma_{\vec{k}}} \frac{\langle \Phi_{\vec{\sigma}_n}^\Sigma | \hat{H} | \Psi_{\vec{\sigma}_k}^\Upsilon \rangle \langle \Psi_{\vec{\sigma}_k}^\Upsilon | \hat{H} | \Phi_{\vec{\sigma}'_n}^\Sigma \rangle}{E_{\vec{k}}^{tot} - E_0^{tot}}, \quad (5.91)$$

When \hat{H}^{S_2} is written in terms of spin operators and is projected into the collective Dicke manifold as above, it can be shown [125, 300] that it gives rise to terms proportional to $\hat{S}^z, (\hat{S}^z)^2$ and $(\hat{S}^z)^3$. Among those corrections, the first two can be absorbed into the spin Hamiltonian given by Eq. 1, and are included in the measured quantities χ and C . Thus, only the third correction proportional to $(\hat{S}^z)^3$ gives rise to additional corrections.

5.8.2 Truncated Wigner approximation

In order to solve for the many-body dynamics beyond the mean-field level, several approaches can be used. We note that, in general, solutions to the elastic part of the collective Hamiltonian are well-known (e.g., [280]). The difficulty comes when including the inelastic two-body loss, which requires a master equation approach. We note that under certain approximations, the master equation approach restricted to solving the collective part of the dynamics governed by Eq. 5.68, while computationally intensive, is still tractable [125, 300]. A master equation approach for solving Eq. 5.65 in the presence of inelastic losses for the experimentally relevant atom numbers is not possible due to the exponential scaling of the Hilbert space. Here, we describe a flexible and powerful approach to treating beyond mean-field effects in the spin model.

For a spin system with $N \gg 1$, we can write [301, 300]

$$\langle \hat{\mathcal{O}}(t) \rangle \simeq \int d^3 \mathbf{S}_0 W(\mathbf{S}_0) \mathcal{O}^{\text{MF}}(t), \quad (5.92)$$

where $\mathcal{O}^{\text{MF}}(t)$ is the time-dependent mean field solution for the operator expectation value, and $W(\mathbf{S}_0)$ is the Wigner function for the spin system's initial state. This forms an approximation known as the Truncated Wigner Approximation (TWA) [301]. For

$$\mathbf{S}_0 \equiv (S_0^x, S_0^y, S_0^z) = \frac{N}{2} (\sin \theta_1, 0, -\cos \theta_1) \quad (5.93)$$

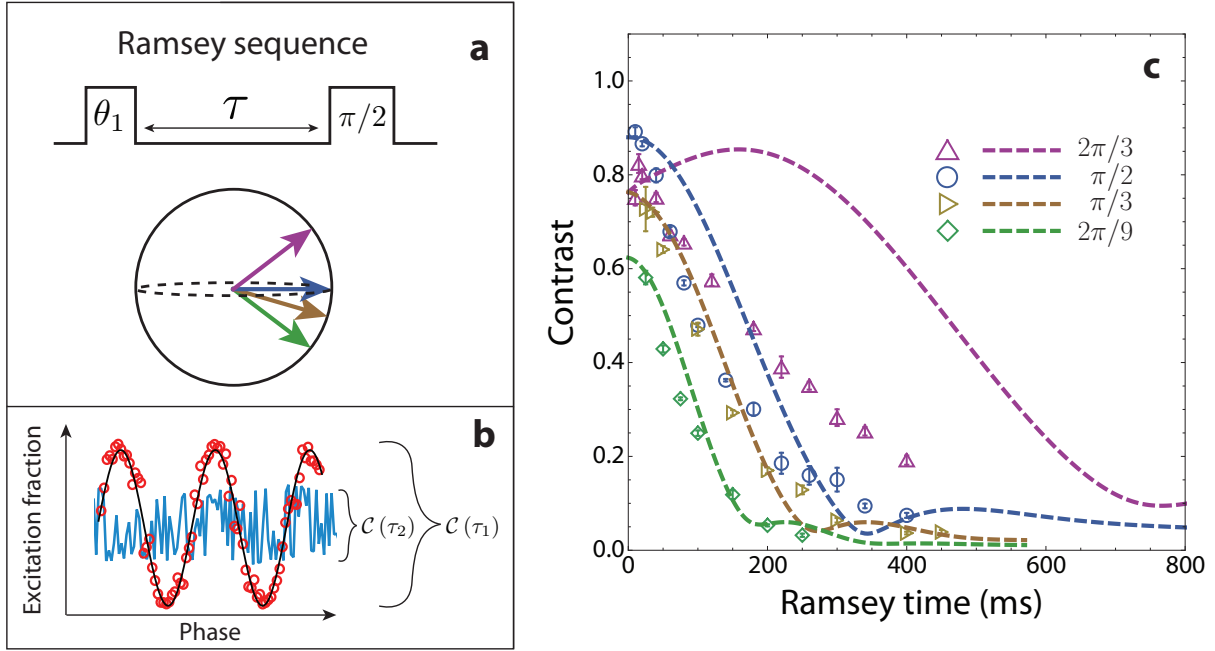


Figure 5.23: Ramsey contrast decay measurement scheme and the failure of mean-field model. (a) The sequence employed to measure the contrast decay. An initial pulse tips the Bloch vector by an angle θ (the pulse area). (b) Examples of contrast extraction from measured excitation probabilities. The red points are an example of contrast data taken with very little dark time, while the blue line is taken with longer dead time. Even though the laser phase noise washes out the sinusoidal nature of the fringe, its amplitude is still resolvable. (c) Failure of the mean field model (dashed lines) to match the experimentally observed Ramsey fringe contrast decay as a function of Ramsey time τ . The legend indicates the initial pulse area used for the measurement.

(i.e., the initial state is prepared in the x - z plane) $W(\mathbf{S}_0)$ is given by [301, 300]

$$W(\mathbf{S}_0) = \left(\frac{2}{\pi N} \right) \delta(S_0^z \cos \theta_1 - S_0^x \sin \theta_1 + N/2) e^{-2(S_0^y)^2/N} e^{-2(S_0^z \sin \theta_1 + S_0^x \cos \theta_1)^2/N}. \quad (5.94)$$

We note that if we wish to compute products of operators, such as the case where $\hat{O} = \hat{O}_1 \hat{O}_2$, that Eq. 5.92 still applies, with $\mathcal{O}^{\text{MF}}(t) = \mathcal{O}_1^{\text{MF}}(t) \mathcal{O}_2^{\text{MF}}(t)$.

This approach successfully describes the evolution of the expectation values of spin operators $\langle \hat{S}^{x,y,z} \rangle$ as well as products of spin operators such as $\langle (\hat{S}^z)^2 \rangle$, $\langle \hat{S}^x \hat{S}^z \rangle$ etc. in the limit where $\sqrt{N} \chi \tau \ll 1$ [125, 300].

5.8.3 Ramsey fringe contrast decay

Many-body effects can manifest themselves as periodic collapses and revivals of the Ramsey fringe contrast, which reflect the quantized structure of the many-body spectrum. Specifically, for a fixed N and neglecting both the losses and the $(\hat{S}^z)^3$ term, the amplitude of the Ramsey fringe evolves as Z^{N-1} with $Z^2 \equiv 1 - \sin^2(\theta_1) \sin^2(\chi\tau_{\text{dark}})$. At short times (*i.e.*, $\sqrt{N}\chi\tau_{\text{dark}} \ll 1$), the contrast is approximately $1 - (N-1)\chi^2 \sin^2(\theta_1)\tau_{\text{dark}}^2/2$ [125]. On the contrary, the mean-field model at the single-site level (with fixed N) predicts no decay of the Ramsey fringe contrast, as a magnetic field $B(N)$ can only lead to a pure precession of the collective Bloch vector. By summing over the atom distribution among lattice sites and properly treating two-body loss during the Ramsey dark time, the mean-field model does show a decay of the contrast, as shown in Fig. 5.23c. However, this decay is associated mainly with dephasing arising from different precession rates exhibited by sites with different N and, as seen in Fig. 5.23c, fails badly for $\theta_1 > \pi/2$. This dephasing effect is most relevant for low excitation fractions where $B(N)$ is large and the inelastic loss is suppressed.

In order to observe beyond mean-field effects, we performed measurements of the Ramsey fringe contrast for different experimental conditions, as illustrated in Fig. 5.23. The initial pulse area $\theta_1 = \Omega T_R$, was chosen such that $0 < \theta_1 < \pi$, controlled the initial value of $\langle \hat{S}_{\text{tot}}^z \rangle$. Here, \hat{S}_{tot}^z is the sum of \hat{S}^z over the ~ 100 relevant sites, such that $-N_{\text{tot}}/2 \leq \langle \hat{S}_{\text{tot}}^z \rangle \leq N_{\text{tot}}/2$, where N_{tot} is the total number of atoms loaded into the lattice. After applying a pulse of area θ_1 , we allowed the system to evolve for time τ . We then applied a final pulse of area $\pi/2$ and measured the resulting excitation fraction as a function of the optical phase of the second pulse relative to the first pulse. The Ramsey pulse durations were < 6 ms, satisfying $\Omega \gg N\chi$, to suppress interaction effects during the pulses. We applied the final $\pi/2$ readout pulse with a variable relative optical phase of $0^\circ - 360^\circ$. We recorded the fraction of excited atoms as a function of the readout phase, which constituted the Ramsey fringe.

For $\tau \gtrsim 100$ ms, there is a significant additional random phase added due to the frequency fluctuations of the ultrastable clock laser. A given excitation fraction measurement p_i will yield $p_i =$

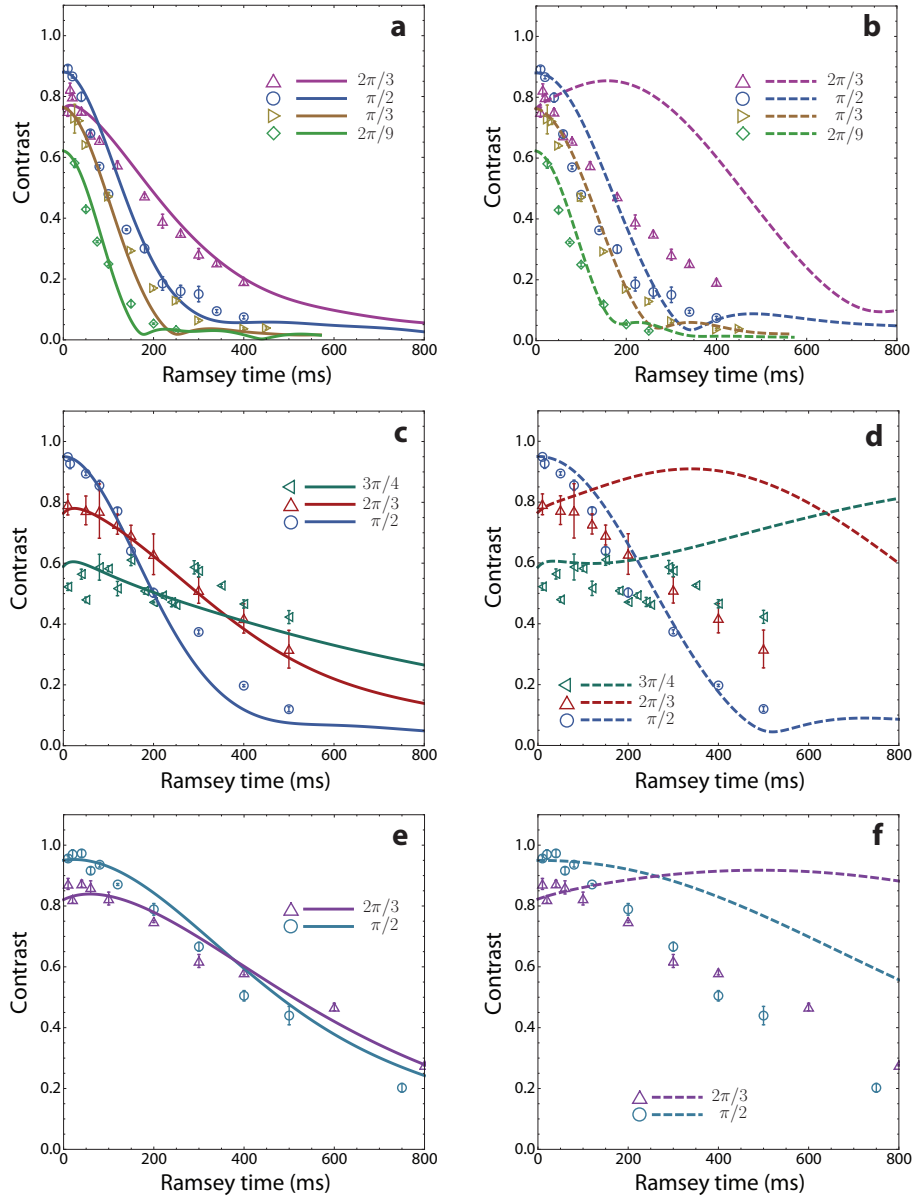


Figure 5.24: Ramsey fringe contrast decay vs. initial pulse area. The pulse area values for the data and corresponding theory are given in the legends of the plots. Error bars represent the statistical error of each contrast measurement, and thus do not account for systematic drifts that occur over the course of the experiment. The solid lines (top panels) are the many-body calculations, while the dashed lines (bottom panels) are using the mean-field approximation of the theory. The many-body model and the mean-field approximation agree in the limit of small initial pulse area (*i.e.*, Bloch vector polar angle), but disagree for pulse areas $\gtrsim \pi/2$. This is an important confirmation of the dominance of many-body effects in this parameter regime. **(a, b)** $\nu_Z = 80$ kHz, $\nu_R = 450$ Hz, and $N_{\text{tot}} = 4000$; **(c, d)** $\nu_Z = 65$ kHz, $\nu_R = 370$ Hz, and $N_{\text{tot}} = 4000$; and **(e, f)** $\nu_Z = 80$ kHz, $\nu_R = 450$ Hz, and $N_{\text{tot}} = 1000$.

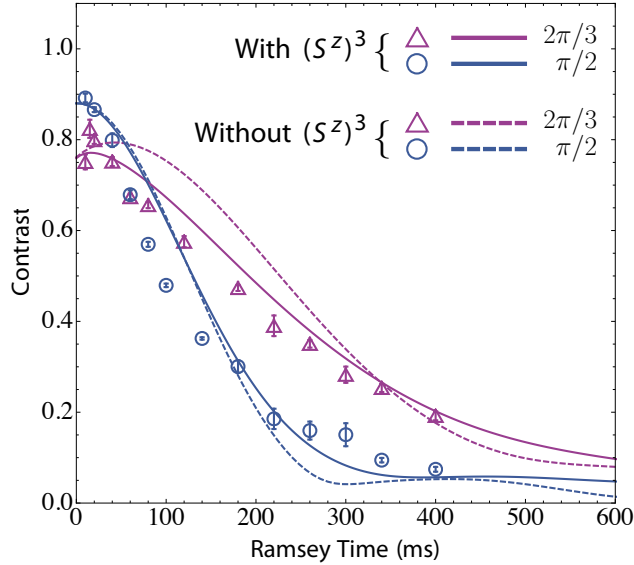


Figure 5.25: Effect of the $(S^z)^3$ term on the Ramsey fringe contrast. Its inclusion improves agreement between the measured fringe contrast and the theory.

$\mathcal{C} \sin^2(\Delta\phi_i)$, where \mathcal{C} is the contrast and $\Delta\phi_i$ is the i th realization of the both deterministically and randomly varied laser phase. Here we have assumed that the contribution of quantum projection noise is small in comparison, which is true for all experimental conditions we explore. By analyzing $\text{Var}[p] = \mathcal{C}^2/8$, and assuming a uniform distribution of $\Delta\phi_i$, we obtain the contrast in a way that is insensitive to the laser noise, yielding a powerful technique for exploring many-body effects.

We explored three distinct experimental conditions to rule out single-particle decoherence mechanisms and thoroughly test the model. The first condition represents the typical operating parameters of the lattice clock, with $N_{\text{tot}} = 4 \times 10^3$ and $\nu_Z = 80$ kHz. In the second case, we reduced the lattice intensity such that $\nu_Z = 65$ kHz, which results in a reduction of the density by a factor of ~ 1.8 . Finally, we maintained $\nu_Z = 80$ kHz but reduced the atom number to $N_{\text{tot}} = 1 \times 10^3$. Under all conditions, the predictions of the collective many-body model, calculated using the TWA as described in Section 5.8.2, are supported by the experimental observations (Figs. 5.24a, 5.24c, and 5.24e). The inclusion of the $(\hat{S}^z)^3$ correction improves the theory-experiment agreement, especially for pulse areas $\theta_1 > \pi/2$ and for the high-density conditions, as shown in Fig. 5.25. While the need

for the $\langle \hat{S}^z \rangle^3$ was rigorously derived (see Section 5.8.1), its magnitude was left as a fit parameter. We also observe a striking breakdown of the mean-field model for $\theta_1 \gtrsim \pi/2$ where many-body corrections are expected to be dominant.

5.8.4 Quadrature-dependent noise measurement

The frequency shift, lineshape, and Ramsey fringe contrast are quantities that all depend on the first-order expectation values of the spin operators $\langle \hat{S}^{x,y,z} \rangle$. We now turn our attention to the distribution of quantum noise, which depends on the second-order moments of the spin operators, *e.g.*, $\langle (\hat{S}^x)^2 \rangle - \langle \hat{S}^x \rangle^2$, $\langle \hat{S}^x \hat{S}^z + \hat{S}^z \hat{S}^x \rangle - 2\langle \hat{S}^x \rangle \langle \hat{S}^z \rangle$, etc. Given that the form of the Hamiltonian in Eq. 5.68 is known to produce squeezed and entangled states [280], the distribution of the quantum noise becomes a compelling measurement to probe physics beyond the mean field. However, until now, optical clocks have lacked the requisite laser precision to probe the quantum noise distribution. The recent advance in the Sr clock laser has allowed access to this regime.

To minimize single particle decoherence effects and dephasing due to the distribution of site occupancies, we added a spin-echo pulse to the Ramsey sequence. As a result, the sensitivity to low-frequency laser noise was reduced at the expense of increased sensitivity to high-frequency laser noise. With atoms initialized in $|g\rangle$, we followed the pulse sequence shown in Fig. 5.26 to manipulate and measure the spin noise of the many-body state. The theoretical evolution of the spin distribution using the TWA is shown in more detail for evolution times of 0 ms–60 ms is shown in Fig. 5.27. For each value of the final rotation angle, representing a specific quadrature in which we measure the spin noise, we repeatedly recorded $\langle \hat{S}_{\text{tot}}^z \rangle / N_{\text{tot}}$ via measurements of the final atomic excitation fraction after the Ramsey sequence. From the data, we determine $\sigma^2 \equiv \langle (\hat{S}_{\text{tot}}^z)^2 \rangle / N_{\text{tot}}^2 - \langle \hat{S}_{\text{tot}}^z \rangle^2 / N_{\text{tot}}^2$ by analyzing the pair variance for successive measurement of $\langle \hat{S}_{\text{tot}}^z \rangle / N_{\text{tot}}$. We note that the quantum limit of σ^2 is important for defining the ultimate stability of lattice clocks [43]. For an ideal coherent spin state of the entire ensemble, the standard quantum limit of σ^2 is given by $\sigma_{\text{sql}}^2 = p(1-p)/N_{\text{tot}}$, where p is the probability of finding an atom in the excited state, and can be estimated as $p = \langle \hat{S}^z \rangle / N_{\text{tot}} + 1/2$.

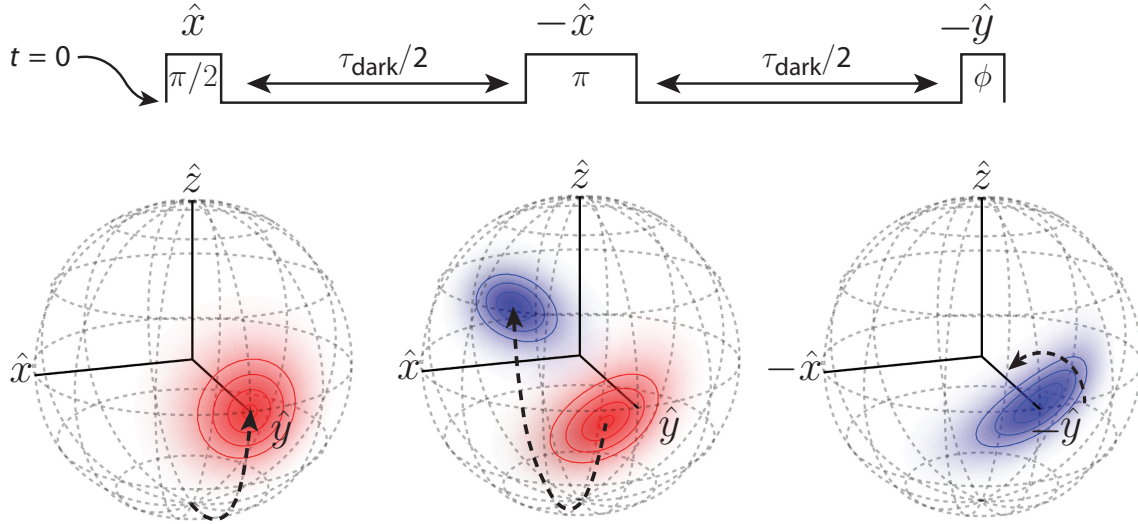


Figure 5.26: Spin noise measurement sequence. An initial pulse prepares a coherent state along \hat{y} , which then evolves for $\tau_{\text{dark}}/2$. An echo pulse then rotates the many-body state 180° about $-\hat{x}$. After an additional evolution time of $\tau_{\text{dark}}/2$, a final pulse rotates the state about $-\hat{y}$ and the spin noise is measured. The many-body state depicted here represents the spin evolution of a 20 atom ensemble in a single trap site with $\tau_{\text{dark}} = 40$ ms.

We performed quadrature-dependent spin noise measurements, as described above, at a given target atom number $N_{\text{tot}} = 1 \times 10^3$ or $N_{\text{tot}} = 4 \times 10^3$. During the course of these measurements, we typically observed slow fluctuations of the atom number on the order of $\pm 10\%$ as we operated the experiment and measure spin noise over the course of ~ 10 hours. In most instances, these fluctuations were negligible due to the normalization techniques we employ as part of clock spectroscopy. However, the atomic spin noise depends directly on the atom number, and a slowly varying atom number could result in unintended systematic biases. Specifically, spin noise for the coherent spin state typically considered in optical clocks scales as $1/\sqrt{N_{\text{tot}}}$. Thus, the deviations in atom number can cause variations on the order of $\pm 5\%$ in the measured spin noise. Ideally, these fluctuations are randomly distributed and should not result in interpretation as a false-positive for non-trivial spin-noise correlations. In the unlikely possibility that these fluctuations were correlated with a specific measurement quadrature, they could cause a spurious phase shift in the spin noise minimum. We

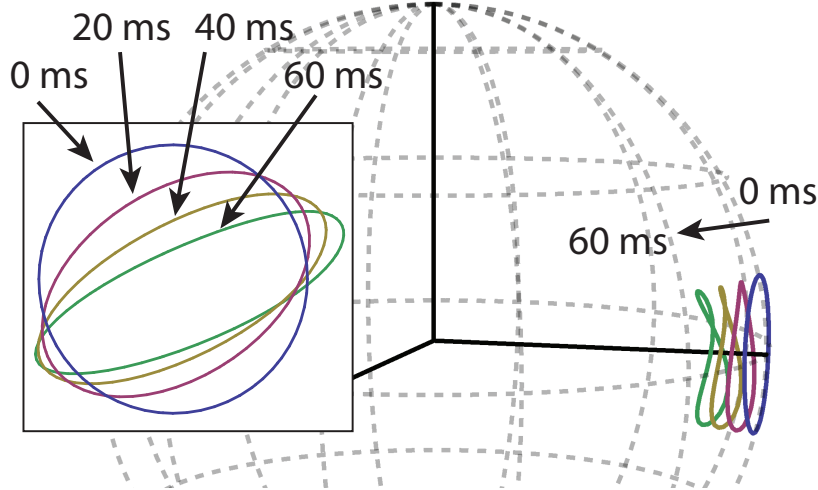


Figure 5.27: Bloch sphere evolution as a function of dark time for $N_{\text{tot}} = 20$. Due to the two-body inelastic loss, the Bloch vector shrinks in length as a function of hold time. The lines represent the mapping of a contour of the spin probability distribution within the truncated Wigner approximation.

thus take care to analyze the data in a way that is immune to this potential bias. In the following section, we describe our process for removing the variability in the spin noise data due to a slowly fluctuating total atom number.

5.8.4.1 Data analysis methodology for measuring quadrature-dependent noise

A given measurement of $\langle \hat{S}_{\text{tot}}^z \rangle / N_{\text{tot}}$ is accomplished by independently measuring $N_{e(g)}$, the number of atoms in the excited (ground) state after a single Ramsey experimental sequence (see Chapter 2, Section 2.5). We determine its i th value, $\langle \hat{S}_{\text{tot}}^z \rangle_i / N_{\text{tot}}^i$, by measuring the i th value of $N_{e(g)}$ (which we denote as $N_{e(g)}^i$) and obtain

$$\langle \hat{S}_{\text{tot}}^z \rangle_i / N_{\text{tot}}^i = \frac{N_e^i}{N_e^i + N_g^i} - 1/2. \quad (5.95)$$

From the j th set of measurements of $\langle \hat{S}_{\text{tot}}^z \rangle$, denoted $\{\langle \hat{S}_{\text{tot}}^z \rangle_1, \dots, \langle \hat{S}_{\text{tot}}^z \rangle_i, \dots, \langle \hat{S}_{\text{tot}}^z \rangle_{n_j}\}_j$, we estimate $\sigma_j^2 \equiv \langle (S_{\text{tot}}^z)^2 \rangle / N_{\text{tot}}^2 - \langle \hat{S}_{\text{tot}}^z \rangle^2 / N_{\text{tot}}^2$ using a pair variance, such that

$$\sigma_j^2 = \frac{1}{2(n_j - 1)} \sum_{i=1}^{i=n_j} \left(\langle \hat{S}_{\text{tot}}^z \rangle_{i+1} - \langle \hat{S}_{\text{tot}}^z \rangle_i \right)^2. \quad (5.96)$$

For white noise, the pair variance is a good estimator for the standard deviation [45], while remaining insensitive to noise processes that only manifest themselves on long time scales. The number of measurements in a set, n_j , was typically $n_j \simeq 80$. For a given measurement quadrature, we average the results of many such measurement sets to produce one experimental data point.

In order to maintain insensitivity to slow fluctuations in atom number between sets j and j' , we consider the standard expression for quantum noise for the case of a coherent spin state, σ_{sql} , which is expected in the absence of many-body interactions. The explicit goal is to remove any mechanism by which the trivial case—where the spin noise is described by σ_{sql} —can mimic the many-body effect we predict from the theory. We calculate the j th value of σ_{sql} as

$$\left(\sigma_{\text{sql}}^j\right)^2 = p_j(1 - p_j)/N_{\text{tot}}^j, \quad (5.97)$$

where $p_j = \text{Mean}[\{N_e^1/(N_e^1 + N_g^1), \dots, N_e^i/(N_e^i + N_g^i), \dots, N_e^{n_j}/(N_e^{n_j} + N_g^{n_j})\}_j]$. We additionally consider a technical noise term, which represents the effect of intrinsic technical detection noise, given by Δs_j . This noise is characterized by a separate measurement. The detection noise accounts for 10% of the observed noise at typical low atom numbers, while at high atom number it is only $\sim 1\%$ of the observed noise, and is therefore negligible. It is quadrature-independent in all cases. From the σ_j^2 , we subtract the atom-number-dependent $\left(\sigma_{\text{sql}}^j\right)^2$ such that

$$\tilde{\sigma}_j^2 = \sigma_j^2 - \left(\sigma_{\text{sql}}^j\right)^2 - \Delta s_j^2. \quad (5.98)$$

Here, $\tilde{\sigma}_j^2$ represents only the effects of non-trivial spin noise and laser noise.

The many-body theory for a given measurement condition is calculated at fixed atom number. To facilitate comparison with the many body theory, we add a noise term back to $\tilde{\sigma}_j^2$ that corresponds to σ_{sql}^2 for the mean atom number over the entire data set, $\overline{\sigma_{\text{sql}}^2}$. We emphasize that $\overline{\sigma_{\text{sql}}^2}$ is a constant number, with no quadrature dependence. The many-body theoretical prediction is calculated based upon the same mean atom number used to calculate $\overline{\sigma_{\text{sql}}^2}$. Ultimately, the net effect of this process is to remove the variability due to slow fluctuations in atom number, but to retain the part of the noise that departs from σ_{sql} due to both laser noise and many-body effects.

5.8.4.2 Observation of spin-correlations

We performed measurements under three conditions in order to probe the time evolution of the quantum noise distribution: $\tau_{\text{dark}} = \{20 \text{ ms}, 40 \text{ ms}, 60 \text{ ms}\}$. For these dark times, we used π -pulse times of $T_R = \{10 \text{ ms}, 20 \text{ ms}, 20 \text{ ms}\}$, respectively. We found that utilizing long π pulses reduces the sensitivity to spurious high-frequency components of laser noise. As shown in Fig. 5.28, for $N_{\text{tot}} = 1 \times 10^3$, the quantum noise contribution to the spin noise is comparable to that of the laser noise. However, with $N_{\text{tot}} = 4 \times 10^3$, the laser noise is responsible for a larger fraction of the noise in repeated measurements of $\langle \hat{S}^z \rangle$. There are qualitative differences between the low and high atom number cases; for example, for $N_{\text{tot}} = 4 \times 10^3$ with $\tau_{\text{dark}} = 20 \text{ ms}$ and 40 ms , we observed a phase shift for the minimum of the spin noise. We have verified that in the limit of small τ_{dark} , the phase shift is no longer prevalent. To compare the predictions of the full many-body master equation with the experiment, we add the effect of laser noise in quadrature with the calculated spin quantum noise. We additionally find it necessary to fully treat the effects of interactions during the laser pulses, which can still be accomplished within the TWA formalism. As shown in Figs. 5.28 and 5.29, the theory predicts a direction and magnitude of the phase shift of the noise minimum that agree with the experimental observations. The theory also predicts significant spin noise for rotations near $\pm 90^\circ$ due to an effect analogous to anti-squeezing. Despite the high sensitivity to laser noise at this rotation quadrature, the measurements of the total noise are consistent with theory.

5.9 Conclusion

In this Chapter, we have explored the many-body nature of interactions between atoms in the ^{87}Sr lattice clock as revealed in the density shifts, lineshape distortion, and Ramsey fringe contrast decay. We have shown evidence that spin-correlations develop during the Ramsey spectroscopy via measurement of a quadrature-dependence of the spin noise. Interestingly, these spin correlations still manifest themselves in the presence of the excited state loss mechanism. In a sense, the lattice

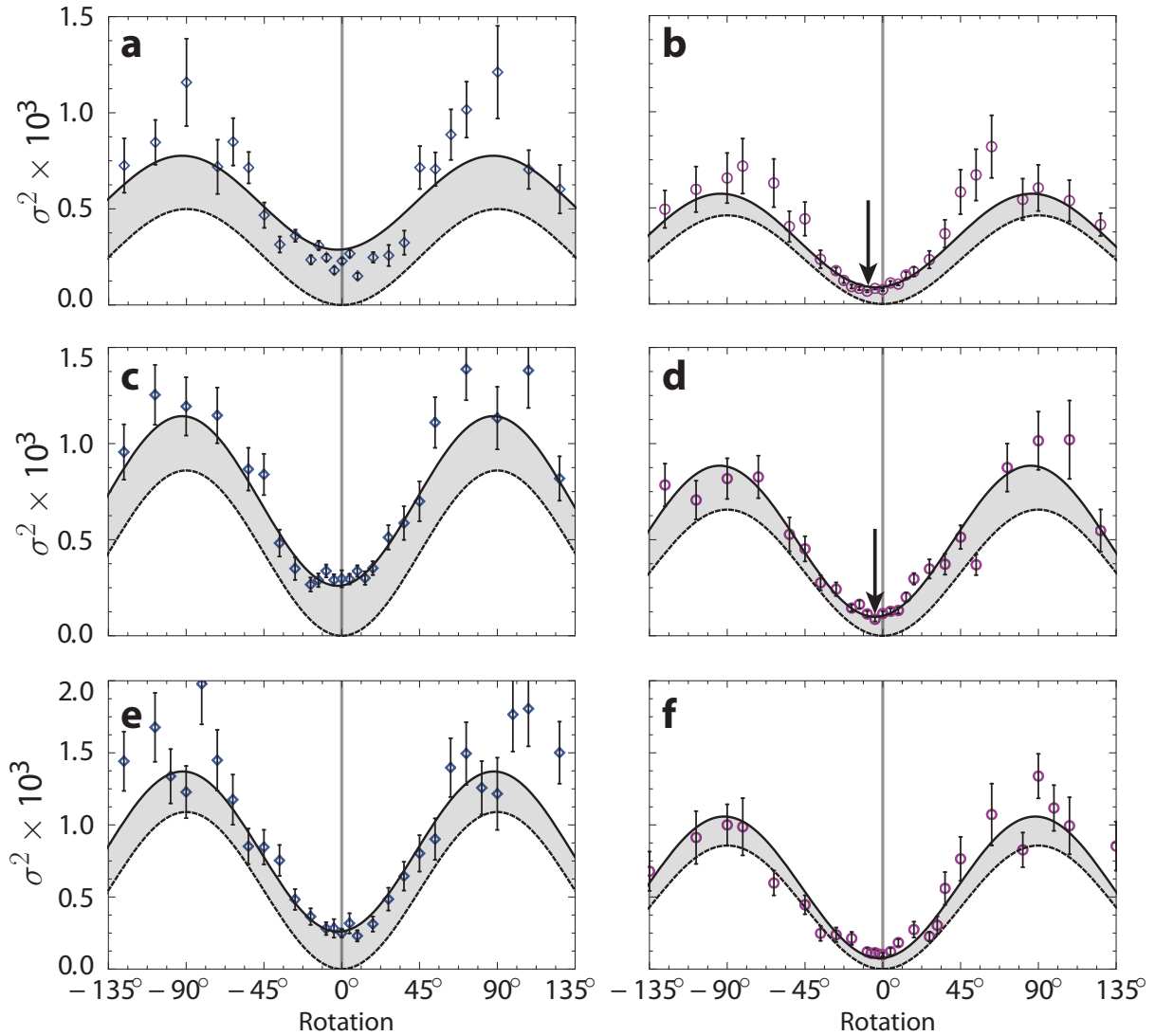


Figure 5.28: Spin noise vs. rotation quadrature. In all plots, the dashed line is the pure laser noise extracted from a fit to the data. The solid line is the laser noise plus the full many-body prediction of the spin noise. This full theory is simultaneously fit to both the low and high atom number curves to extract the common laser noise for a given dark time. Vertical arrows indicate significantly phase-shifted minima in the experimentally measured spin noise, consistent with the predictions of the many-body theory. Plots (a, b): Spin noise for $N_{\text{tot}} = 1 \times 10^3$ and $N_{\text{tot}} = 4 \times 10^3$, respectively, with an interaction time of $\tau_{\text{dark}} = 20$ ms and a π -pulse time of 10 ms. A clear phase shift is observed near the origin for plot (b), the high atom number case. (c, d): Spin noise for $N_{\text{tot}} = 1 \times 10^3$ and $N_{\text{tot}} = 4 \times 10^3$, respectively, with $\tau_{\text{dark}} = 40$ ms and a π -pulse time of 20 ms. In plot (d), a clear phase shift is also observed near the origin. (e, f): Spin noise for $N_{\text{tot}} = 1 \times 10^3$ and $N_{\text{tot}} = 4 \times 10^3$, respectively, with $\tau_{\text{dark}} = 60$ ms and a π -pulse time of 20 ms.

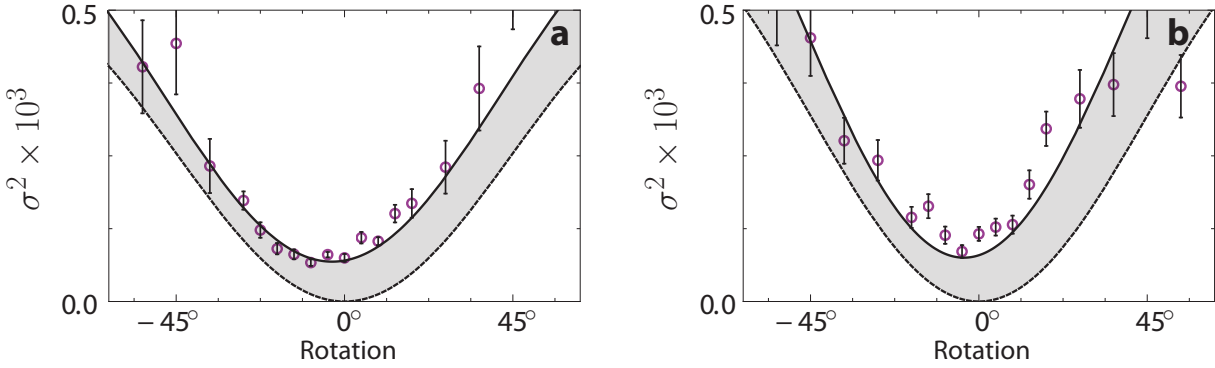


Figure 5.29: Magnified in spin noise vs. rotation quadrature. These plots show the regions marked with arrows in Figs. 5.28b (a) and 5.28d (b)

clock can be considered an “open” quantum system and can thus open up experimental exploration of the intricate competition between coherent interactions and dissipation as a means to enhance and engineer many-body correlations—an emerging theme in modern quantum science [302, 303, 304]. The capabilities demonstrated here, such as near-quantum limited spin resolution, will develop into important tools to explore the rich interplay between many-body effects and dissipation in alkaline-earth atoms confined in optical lattices, and possibly other systems such as polar molecules [70, 71, 72, 305, 306]. Furthermore, as a matter of practical importance, these techniques could be used to generate interaction-induced spin squeezing in an optical lattice clock [77]. Although the investigation described here is restricted to nuclear-spin-polarized gases, exploration of similar many-body effects in a clock making use of additional nuclear spin degrees of freedom is a promising first step towards the investigation of $SU(N)$ orbital magnetic models in ultracold atoms and future experiments are already being prepared to explore $SU(N)$ physics using the precision of the ^{87}Sr optical lattice clock.

Chapter 6

Measuring laser noise via quantum state manipulation

It is the goal of this chapter to present a general theoretical treatment of laser noise in multi-pulse spin echo sequences. This analysis yields information concerning the laser frequency noise power spectral density. The consideration of the effect of noise during these operations can be important for quantum state manipulation, as well as for pulse sequences utilized to study many-body effects as in the previous chapter.

6.1 Introduction to the general formalism

In Section 5.8.4 of the previous chapter, we utilized the spin echo technique, which allows a sample of inhomogeneously broadened quantum systems to “rephase” after an appropriate period of time evolution. This technique was first demonstrated in the context of nuclear magnetic resonance spectroscopy [307]. In the case of the lattice-trapped ^{87}Sr atoms, the different density shifts between each lattice site introduced an effective inhomogeneous broadening that the spin echo was able to remove, thus leaving only the nonlinear part of the Hamiltonian. The spin echo technique represents a simple example of the powerful technique of dynamic decoupling, where such echo pulses can be used to decouple a qubit from a noisy bath [308, 309, 310, 311, 312, 313]. If the bath itself is a quantity to be measured, such as in the case of magnetometry, where the “bath” might be a time-varying magnetic field, such dynamical decoupling pulse sequences can be used to measure field amplitudes at specific Fourier components [314, 315] and even phase quadratures [316].

In this chapter, our goal is not to measure the background fluctuations, but rather to measure the frequency spectrum of the local oscillator laser; we expect that in comparison, any background fluctuations (e.g., magnetic field noise) will be small compared to the frequency noise of the clock laser. The techniques we will use draw direct analogy to dynamical decoupling and spin manipulation because the Hamiltonian for a two-level atom in the presence of a detuned laser field can be written (see Appendix A)

$$\hat{H} = \frac{1}{2}\hbar\Omega(\mathbf{r})\hat{\sigma}_\phi - \frac{1}{2}\hbar\Delta(t)\hat{\sigma}_z. \quad (6.1)$$

In this Chapter, we treat the atoms as **non-interacting** two-level systems governed by the above Hamiltonian, which maps directly onto the case of a spin-1/2 qubit in a magnetic field. This is the case considered in, e.g., [311]. Here, the laser detuning $\Delta(t) = \omega_L(t) - \omega_a$ takes the place of the magnetic field term (often called an “effective” magnetic field). The Rabi frequency is the magnitude of the interaction between the atoms and the laser field, and ϕ is the relative phase of the laser field. We can change this phase by applying deterministic phase shifts to the light, and thus we choose to keep it separate from $\Delta(t)$ (instantaneous phase changes of the laser can be inserted as Dirac Delta functions in $\Delta(t)$, if desired [36]). Throughout this Chapter and treatment, we assume that the atoms are spin-polarized, and we will only consider a single spin state ($m_F = +9/2$).

Our theoretical approach will be as follows: for a given pulse sequence, the spectroscopy laser may be on for a small segment of times (e.g., to produce the Ramsey pulses). As a result, we can split up the evolution into two different stages in the limit of where the Rabi frequency is much larger than $\Delta(t)$, which is almost always the case for multi-pulse sequences where the Rabi frequency $\gg 2\pi \times 10$ Hz. The two phases of evolution are

- (1) $\Omega(t) = 0$. Here the evolution is determined solely by the $-\Delta(t)\hat{\sigma}_z$ term of the Hamiltonian.
- (2) $\Omega(t) = \Omega_0 \gg \Delta(t)$. In this case, we can treat $\Delta(t)$ using the theory of time-dependent perturbations.

In the end, we will effectively stitch the solutions together to determine the evolution of the wavefunction.

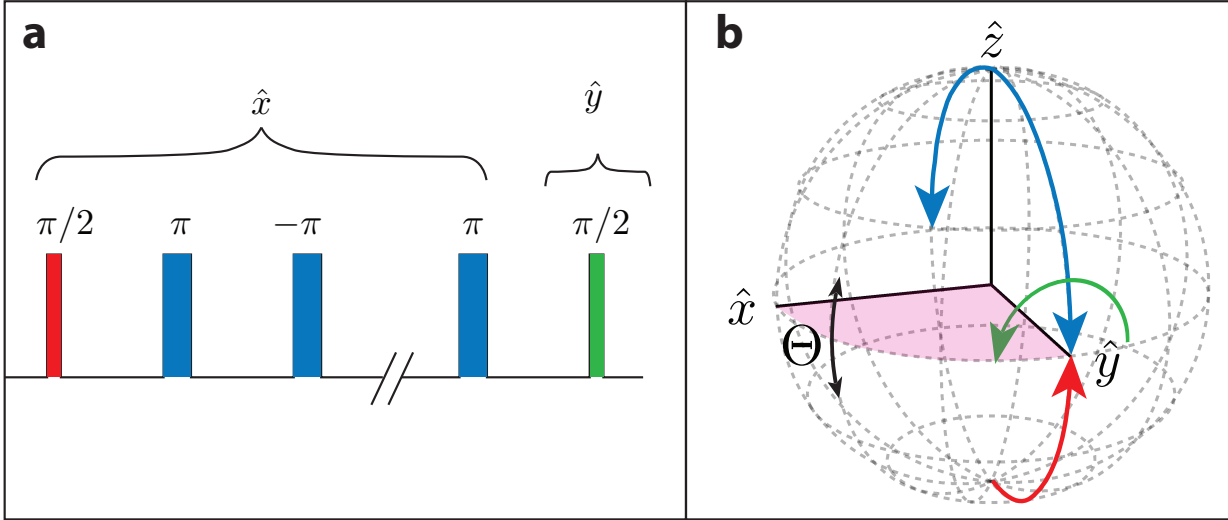


Figure 6.1: The spin echo sequence being considered. (a) The spin echo pulse sequence we consider here. First, a $\pi/2$ pulse rotates the quantum state to point along $|y\rangle$ [red arrow in (b)]. Then, a series of echo pulses, which alternate between π rotations about \hat{x} and $-\hat{x}$, constitute the echo sequence [blue arrow in (b)]. Finally, a final $\pi/2$ pulse is applied about \hat{y} (green). This final pulse serves to rotate variations in the azimuthal angle that are due to local oscillator noise onto the polar angle. (b) Bloch sphere depiction of the rotation operations. The colors in (a) correspond to the operation depicted by the same color in (b). Measurements of total excited state population, f_{exc} reveal fluctuations in polar angle Θ with respect to the x - y plane.

Finally, we mention that although our treatment is completely general, and can be applied to arbitrary pulse sequences, in this chapter we consider only periodic pulse sequences. This is because periodic sequences are the most experimentally relevant types for measuring noise at a specific Fourier frequency. They also have clean closed-form analytic solutions. Specifically, we consider a $\pi/2$ preparation pulse, followed by a series of even spaced π -pulses. This sequence is depicted in Fig. 6.1a, and the corresponding rotations on the Bloch sphere in Fig. 6.1b. We note that the sequence with evenly spaced pulses is different from the typical multi-pulse spin-echo sequence, where the spacing between the first and last π pulses and the preparation and readout $\pi/2$ pulses are half the spacing between π -pulses¹.

¹ The timings for the normal echo sequence are so chosen so that there is no residual sensitivity to dc magnetic fields/laser noise.

6.2 Limit of infinitely short pulses

In this section we consider the limit where the spin manipulation pulses are infinitely short, such that we do not need to consider dynamic noise processes occurring during the pulse. During the time when $\Omega(t) = 0$, the formal solution to the Hamiltonian of Eq. 6.1 is given by

$$\psi(t) = \hat{R}_z \left[- \int_{t_0}^t dt' \Delta(t') \right] \psi(t_0), \quad (6.2)$$

where $\hat{R}_z(\Phi)$ is simply the SU(2) rotation operation about the z -axis, given by

$$\hat{R}_z(\Phi) = \exp \left[-\frac{i}{2} \hat{\sigma}_z \Phi \right]. \quad (6.3)$$

Therefore, a general solution to a spin echo sequence as depicted in Fig. 6.1a is given by

$$\begin{aligned} \psi(t) &= R_y[\pi/2] \hat{R}_z[\Phi_n] \hat{R}_x[\pi] \hat{R}_z[\Phi_{n-1}] \dots \\ &\quad \hat{R}_z[\Phi_2] \hat{R}_x[\pi] \hat{R}_z[\Phi_1] \hat{R}_x[\pi/2] \psi(t_0) \end{aligned} \quad (6.4)$$

In this particular case we do a final rotation about y as the last pulse. The quantity Φ_i is given by

$$\Phi_i = - \int_{t_i}^{t_{i+1}} dt' \Delta(t') \quad (6.5)$$

Equation 6.4 can be simplified in the limit of perfect echo pulses to

$$\psi(t) = \hat{R}_y[\pi/2] \hat{R}_z[\Theta] \hat{R}_x[\pi/2] \psi(t_0) \quad (6.6)$$

$$= \hat{R}_x[\Theta] \hat{R}_x[\pi/2] \psi(t_0). \quad (6.7)$$

In the last equality, the accumulated rotations about z have been converted to a rotation about x by the final $\pi/2$ -pulse about y . Thus, the atomic population becomes a readout of laser noise.

Specifically, in Eq. 6.7, Θ is given by

$$\Theta = \Phi_1 + \sum_{j=1}^{n-1} (-1)^j \Phi_j + (-1)^n \Phi_n, \quad (6.8)$$

where n is the total number of echo pulses. Equation 6.8 can be simplified to

$$\Theta = - \int_{t_0}^t dt' r(t') \Delta(t'). \quad (6.9)$$

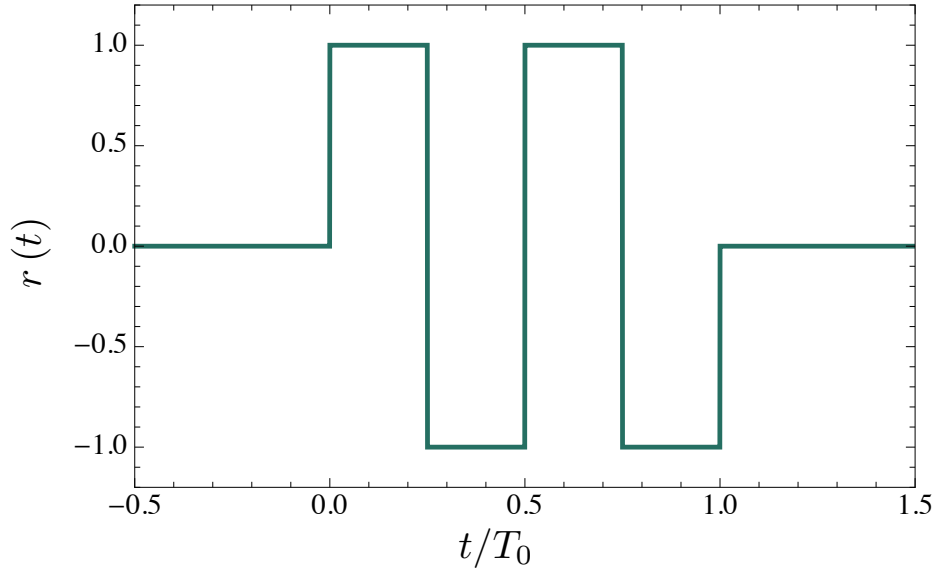


Figure 6.2: The sensitivity function, $r(t)$ of a four-pulse echo sequence in the limit of infinitely short π -pulses. The x-axis has been normalized to T_0 , the total duration of the echo sequence.

Here, $r(t')$ is a sensitivity function that in the limit of infinitely short pulses looks like a square wave train. An example of a three-pulse echo sequence is shown in Fig. 6.2.

Ultimately then, in the limit of perfect pulses, our echo sequence under consideration has the effect of integrating frequency fluctuations of the laser with the weighting function $r(t)$ and then converting these azimuthal fluctuations into polar angle fluctuations that are characterized by the angle Θ . We have only considered a single experimental cycle in this section, it will be our goal in the next section to treat the noise over many experimental runs and predict $\langle \Theta_i^2 \rangle$ and $\langle (\Theta_{i+1} - \Theta_i)^2 \rangle / 2$ (Allan variance), where i represents the i th measurement of Θ via a direct measurement of S_z (via measurements of atomic excitation fraction).

6.2.1 Computing variances from the sensitivity function

A large class of time-domain filtration operations can be described via a transfer function approach [45], where, in contrast to performing operations on the time-domain data, a power spectral density is weighted by the appropriate transfer function in order to calculate statistical

quantities such as the variance. We consider as our experimental observable the accumulated phase difference between a Ramsey atomic coherence and the probe laser that has been rotated into polar angle by the final $\pi/2$ pulse. At the end of a given sequence, the polar angle on the Bloch sphere for the i th measurement is (see Eq. 6.9)

$$\Theta_m = - \int_{-\infty}^{\infty} \Delta(t) r_m(t) dt. \quad (6.10)$$

Here, $r_m(t)$ is related to $r_0(t)$, the sensitivity function for the first measurement and which is assumed to occur at $t = 0$ (e.g., the sensitivity function shown in Fig. 6.2) by

$$r_m(t) = r_0(t - mT_c). \quad (6.11)$$

Here, T_c is the clock measurement cycle time, which includes the time necessary to prepare a new atomic sample.

6.2.2 Computing the variance

As a first step, we might want to compute the quantity

$$\text{Var}[\phi] = \langle \Theta_i^2 \rangle - \langle \Theta_i \rangle^2 = \langle \Theta_i^2 \rangle. \quad (6.12)$$

For the last equality, we assume that the noise has no mean value. We can rewrite $\langle \Theta_i^2 \rangle$, by making use of Eq. 6.10, as

$$\langle \Theta_i^2 \rangle = \left\langle \int_{-\infty}^{\infty} \int_{-\infty}^{\infty} dt_1 dt_2 \Delta(t_1) r_i(t_1) \Delta(t_2) r_i(t_2) \right\rangle. \quad (6.13)$$

Equation 6.13 can be simplified in terms of autocorellation functions as

$$\langle \Theta_i^2 \rangle = \int_{-\infty}^{\infty} \int_{-\infty}^{\infty} dt_1 dt_2 R_{\Delta}(t_1 - t_2) r_0(t_1) r_0(t_2) \quad (6.14)$$

$$= \int_{-\infty}^{\infty} dt (R_{\Delta} \star r_0) r_0(t) \quad (6.15)$$

where we have used the relation

$$\langle \xi(t_1) \xi^*(t_2) \rangle = \mathcal{R}_{\xi}(t_1 - t_2), \quad (6.16)$$

where \mathcal{R}_ξ is the autocorrelation function. The star represents the convolution operation. We will drop the “0” subscript on $r_0(t)$ for the remainder of this section, although it is implied. In practice, it will not matter which $r_m(t)$ we use, since $r_m(t)$ is just a time-shifted version of $r_0(t)$.

Parseval’s theorem states that

$$\int_{-\infty}^{\infty} dt x(t) y^*(t) = \int_{-\infty}^{\infty} df X(f) Y^*(f), \quad (6.17)$$

where $x(t)$ [$y(t)$] and $X(f)$ [$Y(f)$] are related by a Fourier transform. Thus Eq. 6.15 becomes,

$$\int_{-\infty}^{\infty} dt (\mathcal{R}_\Delta \star r) r(t) = \int_{-\infty}^{\infty} df \mathcal{F}[\mathcal{R}_\Delta \star r] R^*(f), \quad (6.18)$$

where $R(f) \equiv \mathcal{F}[r(t)]$, and \mathcal{F} represents the Fourier transform operation which we define, for completeness, as

$$\mathcal{F}[\xi(t)] = \int_{-\infty}^{\infty} dt e^{-i2\pi ft} \xi(t). \quad (6.19)$$

Finally, we apply both the convolution theorem and the Wiener-Khinchin theorem to Eq. 6.18 to obtain

$$\langle \Theta_i^2 \rangle = \int_{-\infty}^{\infty} df S_\Delta(f) |R(f)|^2. \quad (6.20)$$

Here, $S_\Delta(f)$ is the (two-sided) laser frequency noise power spectral density in units of angular frequency. We can relate this to the more commonly reported laser frequency noise power spectral density in units of Hz as $S_\Delta(f) = (2\pi)^2 S_\nu(f)$, leading to the final result

$$\langle \Theta_i^2 \rangle = (2\pi)^2 \int_{-\infty}^{\infty} df S_\nu(f) |R(f)|^2 = (2\pi)^2 \int_0^{\infty} df G_\nu(f) |R(f)|^2, \quad (6.21)$$

Where $G_\nu(f)$ is the single-sided power spectral density, as usual. At this point, the function $r(t)$ is completely general, and this treatment applies to any valid r_0 . We note that since the expression depends only on the magnitude of $R(f)$, the expression is time-shift invariant.

In general, however, the variance is a bad way to characterize the noise. This is because it will become infinite for noises that diverge as $f \rightarrow 0$ for any function $r(t)$ such that

$$\int_{-\infty}^{\infty} dt r(t) \neq 0, \quad (6.22)$$

or in other words if $R(0) > 0$. This is in fact one of the main reasons that the Allan variance and similar methods have superseded the variance as a way to characterize time-domain stability. So while it is helpful to go through the procedure to calculate the variance, for many sensitivity functions $r(t)$ we will get something that diverges due to the $1/f$ character of the laser frequency noise. In the next section, we consider the connection between Allan Variance and the sensitivity function.

6.2.3 Computing the Allan variance

As introduced in Chapter 1, the Allan Variance [44] is a useful tool for characterizing frequency noise. One of the reasons that it is so useful is that it does not diverge for many noise processes that diverge as $f \rightarrow 0$. We begin our calculation of the Allan variance by first considering the two-sample case, and then generalize to the n sample case. The quantity we wish to compute for the two-sample Allan variance is

$$\sigma_{\Theta}^2(T_c) = \frac{\langle (\Theta_{i+1} - \Theta_i)^2 \rangle}{2}. \quad (6.23)$$

Here, Θ_i is defined as in Eq. 6.10. It is straightforward to see that we can perform the operation $\Theta_{i+1} - \Theta_i$ by an extension of Eq. 6.10 if we make the replacement [317]

$$r_i(t) \rightarrow \tilde{r}_i(t) = \frac{r_{i+1}(t) - r_i(t)}{\sqrt{2}}. \quad (6.24)$$

We may thus write

$$\frac{\Theta_{i+1} - \Theta_i}{\sqrt{2}} = \int_{-\infty}^{\infty} \Delta(t) \tilde{r}_i(t) dt. \quad (6.25)$$

From this point, the same analysis of Eqs. 6.13–6.21 applies with $r \rightarrow \tilde{r}$. The result for the two-point Allan variance is

$$\sigma^2(T_c) = \frac{1}{2} \langle (\Theta_{i+1} - \Theta_i)^2 \rangle \quad (6.26)$$

$$= (2\pi)^2 \int_{-\infty}^{\infty} df S_{\nu}(f) |\tilde{R}(f)|^2. \quad (6.27)$$

Here, in analogy to Eq. 6.21, $\tilde{R} \equiv \mathcal{F}[\tilde{r}(t)]$. For the two-point case, we can relate $|\tilde{R}(f)|^2$ to $|R(f)|^2$ by an application of the Fourier shift theorem, such that

$$|\tilde{R}(f)|^2 = \frac{|1 - e^{i2\pi f T_c}|^2}{2} |R(f)|^2 = 2 \sin^2(\pi f T_c) |R(f)|^2. \quad (6.28)$$

Here, T_c is the time between consecutive measurements of Θ_i .

If we wish to calculate the Allan deviation for longer averaging times, we make use of the definition of the Allan deviation

$$\sigma_{\Theta}^2(nT_c) = \frac{1}{2} \left\langle (\bar{\Theta}_{(i+1)n} - \bar{\Theta}_{in})^2 \right\rangle \quad (6.29)$$

$$= \frac{1}{2} \left\langle \left(\frac{1}{n} \sum_{k=0}^{n-1} \Theta_{(i+1)n+k} - \frac{1}{n} \sum_{k=0}^{n-1} \Theta_{in+k} \right)^2 \right\rangle. \quad (6.30)$$

It is then straightforward to see that

$$\tilde{r}^{(n)}(t) = \frac{1}{n} \sum_{k=0}^{n-1} r_{n+k}(t) - \frac{1}{n} \sum_{k=0}^{n-1} r_k(t). \quad (6.31)$$

Again, applying the Fourier shift theorem, we find that

$$|\tilde{R}^{(n)}(f)|^2 = 2 \frac{\sin^4(\pi n f T_c)}{n \sin^2(\pi f T_c)} |R(f)|^2, \quad (6.32)$$

which reduces to Eq. 6.28 for $n = 1$. An interesting limit for Eq. 6.32 is where $n \rightarrow \infty$. We obtain

$$\lim_{n \rightarrow \infty} |\tilde{R}^{(n)}(f)|^2 = \frac{\text{comb}(f T_c)}{n T_c} |R(f)|^2, \quad (6.33)$$

In this case we obtain

$$\sigma_{\Theta}^2(nT_c) \rightarrow \frac{1}{nT_c} \sum_{m=0}^{\infty} |R(m/T_c)|^2 G_{\nu}(m/T_c). \quad (6.34)$$

Equation 6.34 has direct connections to the Dick effect, as seen in Chapter 2, specifically Eq. 2.62.

6.2.4 The sensitivity function $R(f)$ and experimental results

In the previous two sections, we showed that essentially any measurement of the variance or Allan deviation of Θ_i is directly related to the Fourier transform of the time-domain sensitivity function, $r(t)$. Since the sensitivity function for the instantaneous pulse approximation is always a

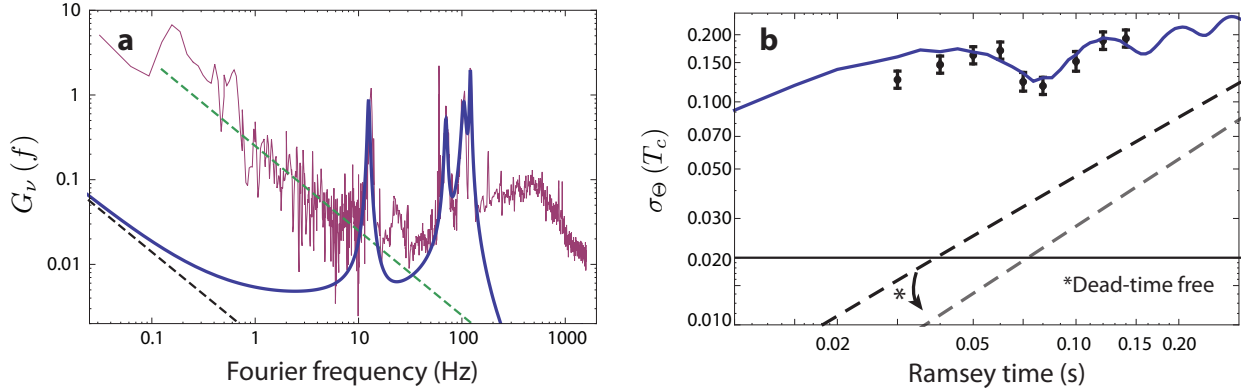


Figure 6.3: Diagnosing the laser spectrum with spectroscopy. **(a)** Laser noise spectrum assumed for the Big ULE-stabilized laser (solid blue) compared to the measured frequency noise spectrum (red trace). The theoretical prediction of thermal noise-limited laser frequency noise for the football cavity agrees with the measurement at low frequencies (dashed green), while the Big ULE thermal noise floor is two orders of magnitude below (dashed black). **(b)** Prediction of Eq. 6.27 (solid blue) versus two-point Allan deviation of the optical clock polar angle Θ , which serves as a readout for laser phase (black points). The horizontal solid black line is the measured/predicted quantum projection noise for 2500 atoms. The dashed lines represent the purely thermal noise-limited case with dead time (dashed black) and in the limit where the cycle time and the spectroscopy time are the same (dashed grey).

periodic function of square waves as shown in Fig. 6.2, it is easy to find the Fourier transform for the whole “train” by utilizing the Fourier shift Theorem. Then, all we need to know is the Fourier power spectrum of a single square pulse, which is a sinc^2 function. We find that the power spectrum of the time-domain sensitivity function for arbitrary numbers of infinitely short echo pulses is

$$|R(f; n)|^2 = \frac{1}{f^2 \pi^2} \sin^2 \left[\frac{\pi}{2} (1 + n + 2fT_0) \right] \tan^2 \left(\frac{\pi f T_0}{1 + n} \right). \quad (6.35)$$

One important limiting case is where $n = 0$, which is the case of Ramsey spectroscopy. Here, we obtain the Ramsey sensitivity function plotted given in Chapter 2 (and for $r(t)$ corresponding to Eq. 2.66)

$$|R(f; 0)|^2 = \frac{\sin^2(\pi f T_0)}{(\pi f)^2} \quad (6.36)$$

In late 2011, we utilized this sensitivity function to diagnose the laser noise spectrum. At this time, the laser cavity was supported by long Teflon posts. We performed Ramsey spectroscopy on the clock transition with spin polarized ^{87}Sr using the sequence depicted in Fig. 6.1, but with

no echo pulses. A given measurement of Θ_i was obtained by measuring the population fluctuations after the i th spectroscopic sequence. For $\Theta_i \simeq \pi/2$,

$$\Theta_i \simeq 2p_i. \quad (6.37)$$

Thus, by measuring a set of $\{p_i\}$ at a given T_0 , we were able to measure $\sigma_\Theta(T_c)$ for a variety of spectroscopy times T_0 . At the same time, we performed an optical beat with the “football cavity” [40]. While the low-frequency noise of the beat was dominated by the thermal noise of the football cavity, we could see Fourier components at discrete frequencies as seen in Fig. 6.3a. We suspected that the first peak at 12 Hz was on the Big ULE cavity-stabilized laser and that it was caused by a high- Q resonance in the support structure. By measuring $\sigma_\Theta(T_c)$ as a function of Ramsey spectroscopy time, T_0 , we were able to confirm the existence of the 12 Hz peak from the character of the oscillations in the noise as a function of spectroscopy time as seen in Fig. 6.3b. While the measured data were completely consistent with the noise spectrum of the 12 Hz peak, we could not specifically verify the presence of the other noise components at higher Fourier frequencies (we later verified these were due to acoustic noise and removed them by constructing the sound-proof box). However, Fig. 6.3 was such strong confirmation of the problematic mechanical resonance that we changed the laser suspension to the configuration described in Chapter 4.

6.3 Adding the effects of frequency noise during the pulses

As we saw in the previous section, the simple treatment of Ramsey pulse sequences yielded insights into the laser noise spectrum, and confirmed the presence of an unwanted Fourier noise component. In order to improve upon the technique, a natural extension is to include more echo pulses in the sequence. However, experimentally we are limited in how much optical power we have, making π -pulse times less than 1 ms difficult. As the number of echo pulses increases, their finite duration becomes an important modification to the transfer function derived in the previous section. Also, it turns out that extending the time of the echo pulses effectively low-passes the frequency sensitivity given by Eq. 6.35 to several or even tens of milliseconds, which can be useful.

Thus, we will now treat the case where the preparation and echo pulses are long enough that we must treat laser noise during the pulse.

We again consider the Hamiltonian of Eq. 6.1. During the periods where $\Omega(t) = 0$, the evolution corresponds to the rotation about the z -axis as before. Here, however, we consider the case where $\Omega(t) \gg \Delta$, but not so much so that we ignore $\Delta(t)$ during the laser pulse, as we did before. In order to proceed, we split the Hamiltonian into two parts,

$$H = H_0 + H_I \quad (6.38)$$

$$H_0/\hbar = \frac{\Omega_0}{2} \hat{\sigma}_x, \quad H_I/\hbar = \frac{\Delta}{2} \hat{\sigma}_z \quad (6.39)$$

From the theory of time-dependent perturbations we can write

$$\psi = e^{-iH_0 t/\hbar} \psi_I \quad (6.40)$$

where

$$\frac{d\psi_I}{dt} = e^{iH_0 t/\hbar} H_I e^{-iH_0 t/\hbar} \psi_I. \quad (6.41)$$

This becomes

$$\begin{aligned} i \frac{d\psi_I}{dt} &= -\frac{\Delta(t)}{2} [\hat{\sigma}_z \cos(\Omega_0 t) + \hat{\sigma}_y \sin(\Omega_0 t)] \psi_I \\ &= \frac{\hat{H}_{\text{eff}}(t)}{\hbar} \psi_I(t). \end{aligned} \quad (6.42)$$

We can write the formal solution to Eq. 6.42 by using a Dyson series [131]. However, since the pulses are short and in general $\Delta(t) \times T_{\text{pulse}} \ll 1$, it is sufficient to keep only the first order term in the Dyson series, such that the time evolution operator for ψ_I , where $\psi_I(t) = \hat{U}(t) \psi_I(t_0)$ becomes

$$\hat{U}(t) \simeq 1 + i \frac{\hat{\sigma}_y}{2} \int_{t_0}^t dt' \sin[\Omega_0 \times (t' - t_0)] \Delta(t') \quad (6.43)$$

$$+ i \frac{\hat{\sigma}_z}{2} \int_{t_0}^t dt' \cos[\Omega_0 \times (t' - t_0)] \Delta(t') \quad (6.44)$$

$$\simeq \hat{R}_y(\theta_Q) \hat{R}_z(\theta_I) \quad (6.45)$$

Just to be explicit

$$\theta_I = - \int_{t_0}^t dt' \cos [\Omega_0 \times (t' - t_0)] \Delta (t') \quad (6.46)$$

$$\theta_Q = - \int_{t_0}^t dt' \sin [\Omega_0 \times (t' - t_0)] \Delta (t') \quad (6.47)$$

$$(6.48)$$

Thus, the total effect of the pulse plus noise is

$$\psi (t_f) = e^{-iH_0 t_f / \hbar} \psi_I = \hat{R}_x (A) \hat{R}_y (\theta_Q) \hat{R}_z (\theta_I) \psi (t_0). \quad (6.49)$$

Here $A = \Omega \times (t - t_0)$. We note that this is in agreement with the result obtained by Kotler *et al.* [316]. Similarly, for the final rotation about y , we can write an expression for the error introduced in the rotation as

$$\psi (t_f) = \hat{R}_y (A) \hat{R}_x (-\theta_Q) \hat{R}_z (\theta_I) \psi (t_0). \quad (6.50)$$

This expression shows the importance of considering the laser noise during quantum state manipulations, as the laser noise couples to spurious rotations around both x and z axes when the rotation is applied about y . This particular operation is important and relevant for the final rotation in the spin echo sequence shown in Fig. 6.1. It has also been used to measure both quadratures of the effective magnetic field term, as parameterized by θ_I and θ_Q [316] (in this reference the “effective magnetic field” was in fact a real magnetic field).

To illustrate the full model, we consider the echo sequence with only a single echo pulse. We have taken a considerable amount of data using this sequence, as seen in Chapter 5. The time evolution is

$$\begin{aligned} \psi (t) = & \left[R_y (A) R_x (-\theta_Q) \hat{R}_z (\theta_I) \right] \hat{R}_z (\Phi_2) \times \\ & \left[\hat{R}_x (\pi) \hat{R}_y (\theta_Q) \hat{R}_z (\theta_I) \right] \hat{R}_z (\Phi_1) \times \\ & \left[\hat{R}_x (\pi/2) \hat{R}_y (\theta_Q) \hat{R}_z (\theta_I) \right] \psi (t_0). \end{aligned} \quad (6.51)$$

Here, the composite operators in square brackets represent the first $\pi/2$ pulse, the middle π pulse, and the final arbitrary rotation of angle A about y with noise included. The intermediate z -rotation

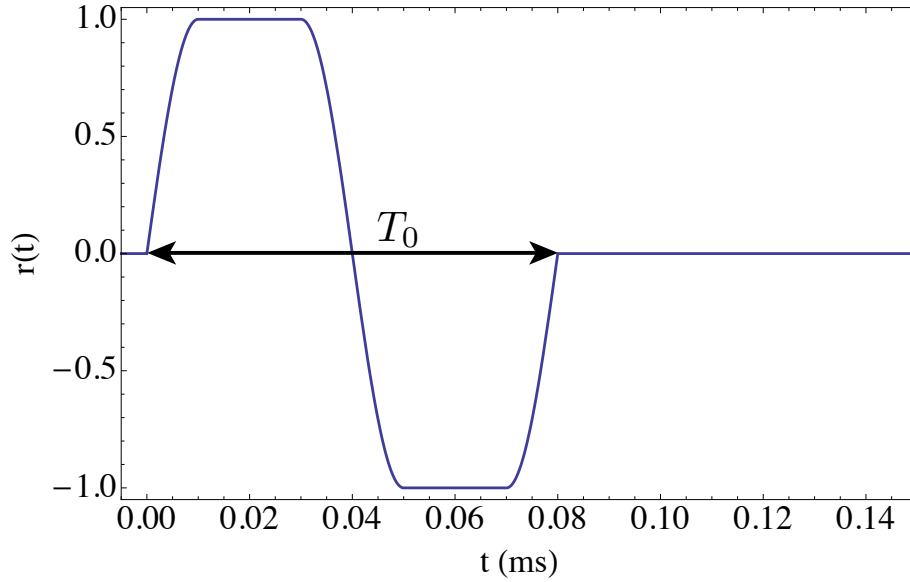


Figure 6.4: The time-domain sensitivity function $r(t)$ for the echo sequence with 80 ms duration and 20 ms π -pulses.

operators are as before, where the dark-time evolution is described as a simple rotation about z as in Eq. 6.3.

If we assume that $\psi(t_0) = |g\rangle$, we can ignore $\hat{R}_z\psi(t_0)$. Similarly, if we ignore the \hat{R}_y operation of the second square bracketed term, which is justified if the state it is acting on is approximately equal to an eigenstate of $\hat{\sigma}_y$ (this approximation is valid when keeping only rotations to first order), then Eq. 6.51 reduces to

$$\psi(t) = [R_y(A) R_x(-\theta_Q)] \hat{R}_z(\tilde{\Phi}) \times \underbrace{|-y\rangle}_{|\psi(t_0)\rangle}. \quad (6.52)$$

Here, $\tilde{\Phi}$ is given by

$$\tilde{\Phi} = \int_{t_0}^t dt' \sin[\theta(t')] \Delta(t') = \int_{t_0}^t dt' r(t') \Delta(t') \quad (6.53)$$

where

$$\theta(t') = \int_{t_0}^{t'} dt'' \Omega(t''). \quad (6.54)$$

This is exactly the result of [316] except that since we initialize our system in $|-z\rangle$ and they in $|x\rangle$; this difference is resolved by replacing $\sin \rightarrow \cos$ in Eq. 6.53. For a typical echo sequence, $A = \pi/2$

and thus the time-dependent Rabi frequency is given by

$$\Omega(t) = \begin{cases} \Omega_0 & \text{if } 0 \leq t < T_{\text{Rabi}}/2 \\ 0 & \text{if } T_{\text{Rabi}}/2 \leq t < (\tau - T_{\text{Rabi}})/2 \\ \Omega_0 & \text{if } (\tau - T_{\text{Rabi}})/2 \leq t < (\tau + T_{\text{Rabi}})/2 \\ 0 & \text{if } (\tau + T_{\text{Rabi}})/2 \leq t < \tau - T_{\text{Rabi}}/2 \\ \Omega_0 & \text{if } \tau - T_{\text{Rabi}}/2 \leq t < \tau \\ 0 & \text{elsewhere} \end{cases} \quad (6.55)$$

This procedure is generalized to any number of echo pulses, where the Rabi frequency is a piecewise function corresponding to the periods where the laser is turned off or on, and $r(t)$ is given by

$$r(t) = \sin[\theta(t)]. \quad (6.56)$$

Figure 6.4 shows the sensitivity function for a specific case of a single echo with a sequence duration of 80 ms and a π -pulse time of 20 ms. Qualitatively, this has the effect of rounding out the edges of the sensitivity function, which introduces a low-pass effect that “turns on” at the Rabi frequency. Due to the periodic nature of the sensitivity function, we can apply the same trick that we did for the case infinitely-short pulses: we use the Fourier shift theorem to derive the sensitivity function for an arbitrary number of echo pulses as

$$|R(f; n)|^2 = \frac{\Omega_0^2}{[\pi f \Omega_0^2 - 4(\pi f)^3]^2} \left\{ 2\pi f \cos(\pi f \tau) + \Omega_0 \sin \left[\pi f \left(\tau - \frac{\pi}{\Omega_0} \right) \right] \right\}^2 \times \frac{\sin^2 \left[\frac{\pi}{2} (1+n)(1+2f\tau) \right]}{\cos^2(\pi f \tau)}. \quad (6.57)$$

Here, τ is the duration of one of the periodically repeated features of $r(t)$ and is given by $\tau = T_0/(n+1)$, where T_0 is the total spectroscopy time and n is the number of echo pulses as before. Figure 6.6 on page 233 shows a large array of sensitivity functions $|R(f; n)|^2$ for a sequence with T_0 85 ms, and a π -pulse time of 5 ms.

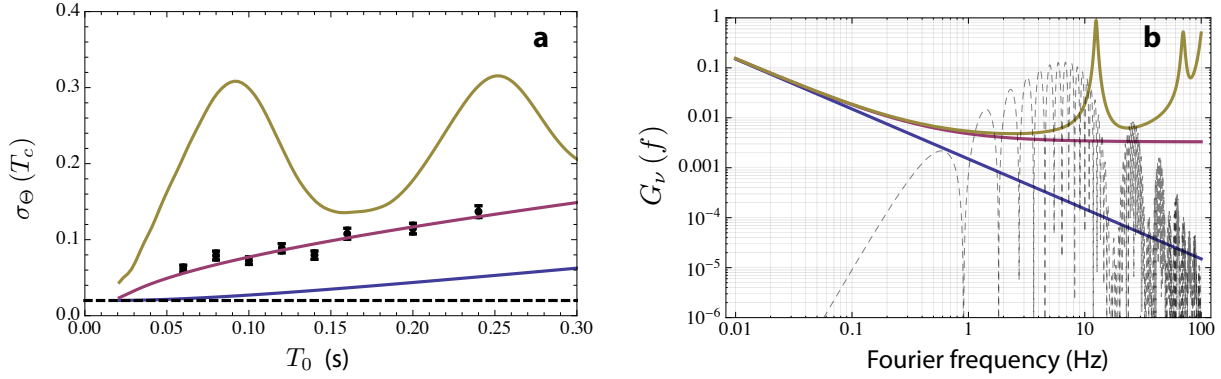


Figure 6.5: Verification of improved laser noise spectrum with a spin echo sequence. (a) Measured Allan deviation of polar angle Θ as a function of measurement time for a π -pulse time of 20 ms (markers). The three different solid lines correspond via color to the three noise spectra in (b). The dashed black line is the quantum projection noise floor of the measurement. (b) The solid lines are the three test laser noise spectra used to produce σ_{Θ} at left. The dashed line is Allan deviation transfer function $|\tilde{R}(f)|^2$ (See Eq. 6.28. Arbitrary units are used.) calculated for the case of finite pulse time and for the measurement sequence with $T_0 = 120$ ms.

We applied the calculated sensitivity function to test the new laser suspension and acoustic isolation. Using a sequence with a 20 ms π -pulse and one echo, we measured $\sigma_{\Theta}(T_c)$ as a function of total echo sequence time T_0 . In order to carefully account for fringe contrast decay, we were careful to scale each noise measurement by the measured contrast for that given condition to make a proper estimate of set $\{\Theta_i\}$ for a given T_0 . As also suggested by comparing the laser to the football cavity stabilized system, we found that the large spike at 12 Hz was gone. Also gone were the large acoustic spikes at 50–100 Hz thanks to the sound-proof box (see Chapter 2, Fig. 4.21). Figure 6.5 shows the measured noise and several test spectra. The old, noisy spectrum did not even qualitatively fit the data. However, the laser was still above the noise floor predicted for a flicker-floor stability of 1×10^{-16} . One way to account for this is to add a white noise floor. We find that good agreement with the data is obtained for a laser frequency noise of

$$G_{\nu}(f) = \frac{h_{-1}}{f} + h_0 \quad (6.58)$$

where $h_{-1} = 1.5 \times 10^{-3} \text{ Hz}^2$ and $h_0 = 3.3 \times 10^{-3} \text{ Hz}^2/\text{Hz}$. This implies that the laser reaches a thermal-noise dominated stability regime at Fourier frequencies below 450 mHz.

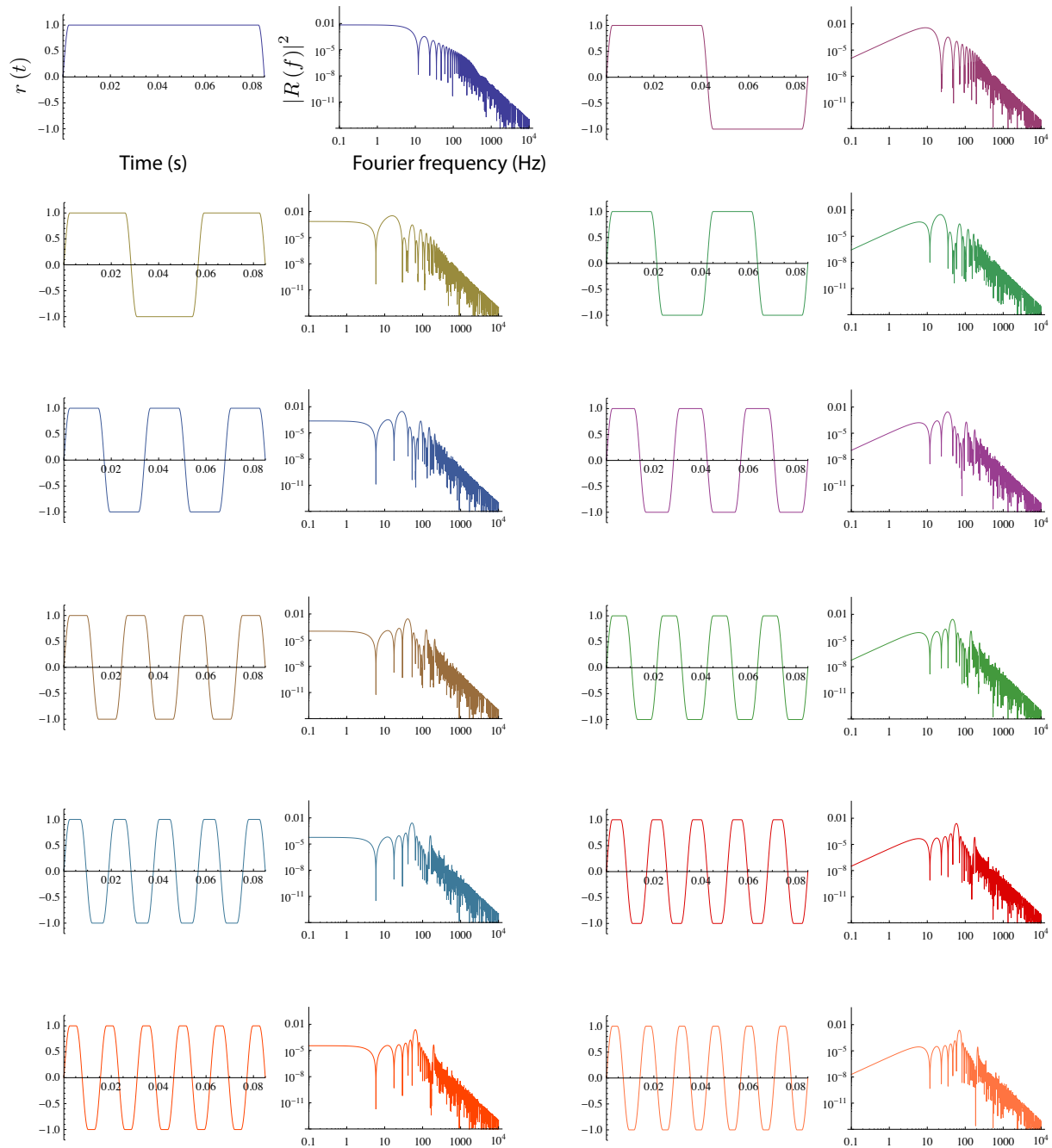


Figure 6.6: Overview of the sensitivity functions $|R(f)|^2$ for increasing echo pulse number (increasing left to right, top to bottom). The upper left corner is the zero echo pulse condition (i.e., Ramsey spectroscopy). The bottom right-hand plot is the 11-echo pulse sequence. The horizontal and vertical axes are all as labelled for the pair of plots in the upper left corner: the horizontal axes of the plots are time in seconds and Fourier Frequency in Hz. The vertical plot axes are the time-domain sensitivity function and its Fourier-space magnitude. Here, $T_0 = 85$ ms and the π -pulse time is 5 ms.

6.3.1 Sensitivity function for Rabi spectroscopy

Finally, we briefly derive the Fourier-domain sensitivity function for Rabi spectroscopy. Rabi spectroscopy is qualitatively different than Ramsey spectroscopy in that typically it is performed with a static detuning $\Delta_0 \simeq \Omega_0$ such that

$$\Delta(t) = \Delta_0 + \delta\omega(t). \quad (6.59)$$

Thus, the perturbative approach used in the previous section is much more difficult to apply because Eq. 6.1 becomes

$$\hat{H} = \frac{1}{2}\hbar\Omega(\mathbf{r})\hat{\sigma}_\phi - \frac{1}{2}\hbar\Delta_0\hat{\sigma}_z - \frac{1}{2}\delta\omega(t)\hat{\sigma}_z. \quad (6.60)$$

Thus, the rotations are applied about non-orthogonal axes. While it is difficult to derive the general rotation errors on the Bloch sphere, as we were able to do in the previous section, it is straightforward to derive the population fluctuations caused by $\delta\omega(t)$ for a given Δ_0 . This is exactly the Rabi sensitivity function discussed in Chapter 2 and derived in Appendix A; it is defined by

$$\delta f_{\text{exc}} = \frac{1}{2} \int_0^{T_0} dt \delta\omega(t) r^{\text{Rabi}}(t; \Delta_0). \quad (6.61)$$

Additionally, if the spectroscopy is performed such that the expected final population is 50%, then measured population fluctuations correspond to polar angle fluctuations via Eq. 6.37.

The time-domain Rabi sensitivity function is (see Appendix A for a derivation)

$$r^{\text{Rabi}}(t; \Delta_0) = - \left(\frac{\Delta_0 \Omega_0^2}{\Omega^3} \right) \left\{ \sin(\Omega t) - \sin\left(\pi \frac{\Omega}{\Omega_0}\right) + \sin\left[\frac{\Omega}{\Omega_0}(\pi - t\Omega_0)\right] \right\}, \quad (6.62)$$

where the generalized Rabi frequency, Ω , is given by $\Omega = \sqrt{\Omega_0^2 + \Delta_0^2}$. The magnitude of the Fourier transform of $r^{\text{Rabi}}(t)$ is given by

$$\begin{aligned} \left| R^{\text{Rabi}}(f; \Delta_0) \right|^2 = \\ \frac{\Delta^2 \Omega_0^4}{\Omega^4 (\pi f \Omega^2 - 4\pi^3 f^3)^2} \left[\Omega \sin\left(\frac{\pi^2 f}{\Omega_0}\right) \sin\left(\frac{\pi \Omega}{\Omega_0}\right) - 4\pi f \cos\left(\frac{\pi^2 f}{\Omega_0}\right) \sin^2\left(\frac{\pi \Omega}{2\Omega_0}\right) \right]^2 \end{aligned} \quad (6.63)$$

When $\Delta_0 \simeq \pm 0.80\Omega_0$, the final Bloch vector points in the x - y plane. In this limit, as already mentioned, we can calculate polar angle fluctuations on the Bloch sphere via measurement of population fluctuations.

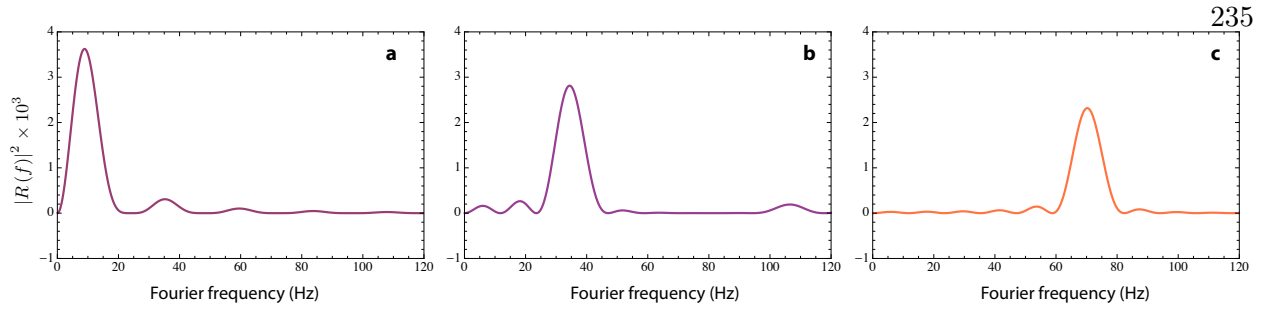


Figure 6.7: Linear scale plots of the Fourier-space sensitivity functions. As in Fig. 6.6, $T_0 = 85$ ms and the π -pulse time is 5 ms. The number of echoes are one (a), five (b), and eleven (c). As seen in this figure, the sensitivity function is sinc²-like and is sharply peaked. The width of the peak varies inversely with the total sequence time.

6.4 Mapping the laser spectrum: multi-echo sequences

In this final section we describe continuing work to utilize the sensitivity functions developed in this chapter, and apply them to multi-pulse echo sequences. As this thesis was being written, Sr1 teammates Mike Bishof and Xibo Zhang utilized a combination of Rabi, Ramsey, and echo pulse sequences to map out the laser noise systematically [318]. As before, the spectrum was constrained with the help of the measured spectrum between the Big ULE system and the football cavity. Several discrete resonances were added to the model of Eq. 6.58 to better match noise spikes observed in the laser comparison frequency noise spectrum. As shown in Fig. 6.7, the Fourier-space sensitivity functions are rather sharply peaked when viewed on a linear scale, and it is this feature, along with different regions of frequency sensitivity determined by the number of echoes, that makes the transfer function a powerful diagnostic tool.

The final extrapolated spectrum is shown in Fig. 6.8a, and the corresponding noise plots shown in Fig. 6.8b. For the single- and seven-pulse echo sequences, the computed deviation is the standard deviation of the data sets and the theory corresponds to the same quantity. For the Ramsey and Rabi measurements, the deviation used is the Allan deviation. The reason Allan deviation was used for the Rabi and Ramsey cases is that the sensitivity function for the variance diverges with $1/f$ noise, but the sensitivity function for Allan deviation does not.

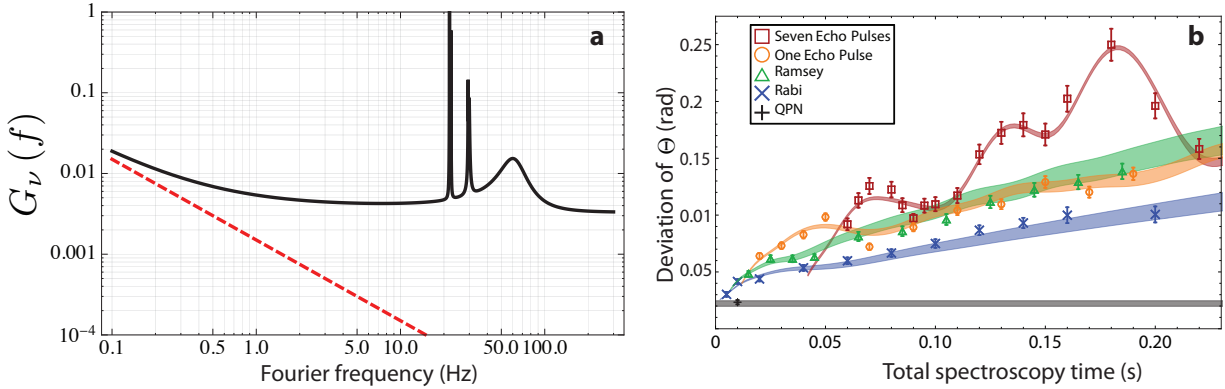


Figure 6.8: Multi-pulse extrapolation of laser noise spectrum. **(a)** Extrapolated laser spectrum for the Big ULE-stabilized laser (solid black line). The $1/f$ flicker noise floor corresponding to a stability of 1×10^{-16} is also shown (dashed red line). **(b)** Measured excitation noise (expressed as noise in Θ) as a function of total spectroscopy time (T_0). The pulse sequences are as indicated in the legend. The bands indicate the range of uncertainty for the flicker and white noise floors as indicated in the text. For the Rabi and Ramsey cases, the Allan deviation was computed. For the echo sequences, the standard deviation of the measured $\{\Theta_i\}$ is reported. A measurement of quantum-projection noise (QPN) is shown for reference.

Day-to-day fluctuations as well as discrepancies between different pulse sequences required small changes in the fit parameters. Ultimately, the best fit parameters are $h_{-1} = 1.5(5) \times 10^3 \text{ Hz}^2$ and $h_0 = 3.3(3) \times 10^{-3} \text{ Hz}^2/\text{Hz}$. The $1/f$ term agrees very well with the thermal noise floor measured using the atomic clock correction signal as a frequency discriminator. This is gratifying because those clock measurements were sensitive to the $1/f$ noise only at long time scales (see Chapter 4, Fig. 4.22), whereas these measurements are taken over a shorter timescale. As shown in Fig. 4.22, the flicker noise reaches $1.1(1) \times 10^{-16}$, which indicates $h_{-1} = 1.6(2) \times 10^{-3} \text{ Hz}^2$, in good agreement with these measurements. We also note that this combination of flicker and white noise indicates that the laser linewidth can be as narrow as 26 mHz [318].

The complete laser noise spectrum is directly relevant for the intercomparison reported in Chapter 4. In Fig. 6.9 (page 238) we plot the Dick effect-limited clock stability using the new spectrum plotted in Fig. 6.8. As seen from Fig. 6.9, the Dick effect is dominated by the $1/f$ and white noise portions of the new spectrum. When we apply this spectrum to the conditions of the clock intercomparison, we obtain that the Dick-effect-limited instability should be $5 \times 10^{-16} / \sqrt{\tau/1 \text{ s}}$,

which is close to the observed $4 \times 10^{-16}/\sqrt{\tau/1 \text{ s}}$, and approximately within the stated uncertainty in the noise amplitudes. Thus, by characterizing the laser noise in such a detailed manner, future clock experiments will have the benefit of precisely predicting the Dick effect or other spurious Bloch sphere rotations.

6.5 Conclusion

In this chapter, we derived a general technique to treat errors arising from the local oscillator frequency noise. We applied this formalism to a model laser spectrum and then used the measured atomic population noise to adjust the model parameters. This was useful for demonstrating that the cavity support resonance was eliminated by changing the support strategy. We were additionally able to demonstrate that the laser $1/f$ noise spectrum crosses a white noise floor at approximately 450 mHz and to verify and calibrate the presence of additional resonant features in the Fourier spectrum.

These measurements show the promise of using spin echo techniques paired with optical standards to fully characterize the noise spectrum of ultrastable lasers. A natural next step will be to develop a **model-independent** extension so that the noise can be mapped tomographically, without need for a pre-existing model of the laser spectrum as obtained here by direct comparison with a second system.

Finally, we note that these measurements give us confidence in something we have assumed all along: that the atoms are “perfect” frequency references. While we know that there are perturbing systematics, this is the first time that the clock atoms themselves have been put to such a stringent test on short time scales. Since we only used a single spin state in these measurements, it is possible that some of the noise that was measured is due to the small $\sim 500 \text{ Hz/G}$ magnetic sensitivity of the $m_F = +9/2$. However, we note good agreement with the $1/f$ floor obtained from operating the clock with both $m_F = \pm$ spin states, as we did for the clock comparison measurements. Thus, we do **not** foresee that technical perturbation to the atoms themselves will be an impediment to reaching QPN-limited instabilities of $1 \times 10^{-16}/\sqrt{\tau/1 \text{ s}}$.

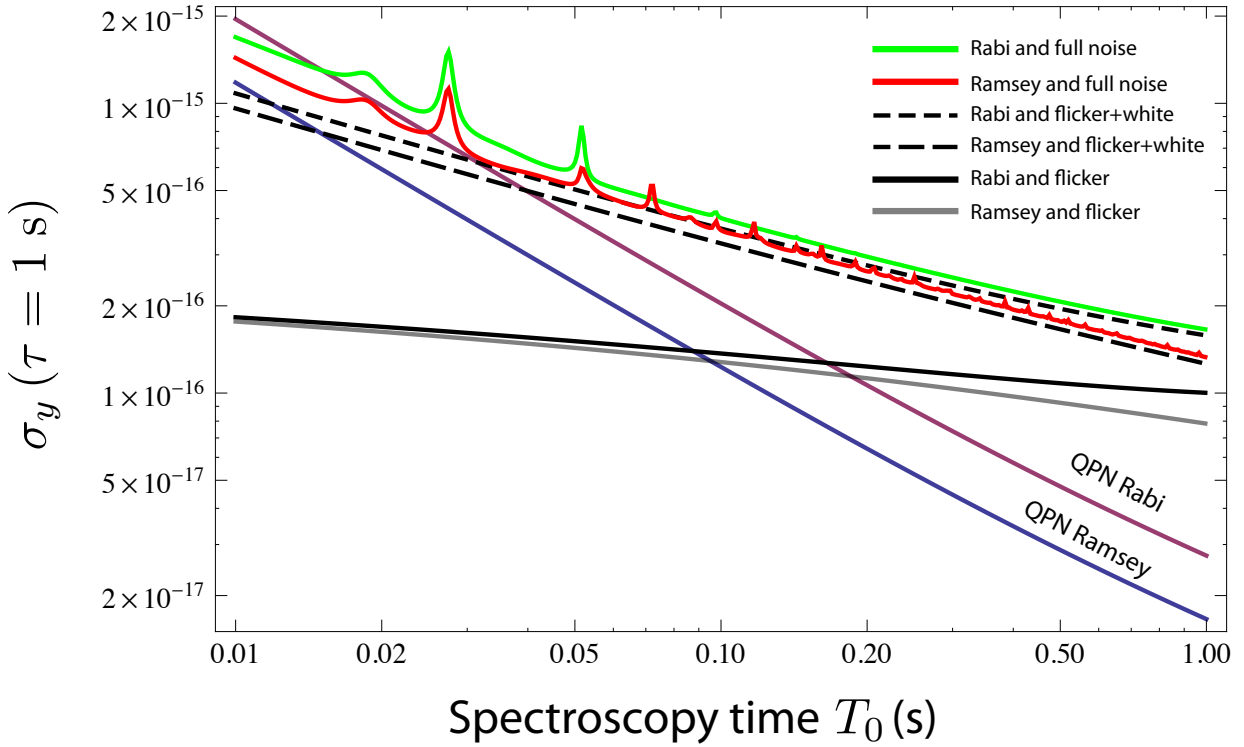


Figure 6.9: Dick effect-limited laser performance with the newly evaluated laser spectrum. Here, the loading time is 1 s, such that the cycle time $T_c = 1 + T_0$. We plot the quantum projection noise (QPN) instability for Rabi and Ramsey spectroscopy (red and blue, respectively) and the Dick-limited instability for a laser with flicker floor $\sigma_y(\tau) = 10^{-16}$ for Rabi (solid black) and Ramsey (grey) spectroscopy. As discussed in this chapter, the real laser spectrum has a white noise component and discrete resonances in addition to the $1/f$ component. These specific cases are listed in the legend. In all cases the instability has been extrapolated to 1 s, so that $\sigma(\tau) = \sigma(1) / \sqrt{\tau/1 \text{ s}}$.

Chapter 7

Conclusion

This final chapter summarizes the key results presented in this thesis, and we additionally discuss the outlook for the ^{87}Sr lattice clock in the context of both metrology and quantum many-body physics.

7.1 Summary of key results

Optical lattice clocks are powerful platforms for quantum measurement. As described in Chapter 2, the parallel interrogation of many atoms permits a \sqrt{N} enhancement of measurement precision, where N is the total number of particles in the clock, allowing fractional instabilities of order $10^{-16}/\sqrt{\tau}$ to be within reach for even modest parameters. Yet until recently, only synchronous interrogation of clocks had demonstrated the benefit of utilizing many atoms [234]. In this thesis we described the development of an ultrastable laser system with fractional frequency instability of $1.1(1) \times 10^{-16}$. This system allowed the realization of independent clocks operating near this limit set by quantum fluctuations. This represents an important milestone in the development of lattice clocks, and represents an order of magnitude improvement in measurement precision over that of ion clocks [27].

In addition to improving the local oscillator clock laser for the Sr experiments at JILA, we reported the construction of a second laser in support of a joint PTB-JILA collaboration to construct a laser cavity of monocrystalline silicon. The JILA support laser compared with the silicon cavity demonstrated a record-low beat linewidth of 50 mHz [168]. While the silicon system operated

at 1×10^{-16} stability, showing the promise of cavities constructed from crystalline materials, it was still limited by the amorphous mirror coating. We additionally reported the success of a new mirror technology whereby the optical coatings are replaced by GaAs/AlGaAs heterostructures. With these new mirrors, thermal noise limitations should be as low as 1×10^{-17} for cryogenic, all-crystalline optical cavities.

An important systematic facing clocks with many particles is the potential for collisions to perturb the clock frequency. This is part of the motivation for the extensive study of collisional effects that has taken place over the last several years [265, 135, 273, 293, 43]. However, the well-characterized environment and exquisite measurement precision of lattice clocks paired interacting many-body systems represents a new opportunity for quantum science beyond timekeeping. In Chapter 5, we described the discovery that p -wave effects dominate the density-dependent effects within the ^{87}Sr lattice clock. In the many-particle trap sites, the p -wave interaction leads to strong, collective interactions. We uncovered and elucidated the quantum many-body nature of these interactions, and demonstrated the power and validity of a spin-model description of the many-body interactions. Furthermore, we reported the observation of spin-noise correlations as revealed by noise tomography. Thus, the optical lattice clock becomes a platform for studying many-body physics.

Finally, in Chapter 6, we described how atomic measurements employing periodic spin echo sequences can act as a spectrum analyzer for the clock laser frequency fluctuations. Via this method, we demonstrated a characterization of the laser noise spectrum. This knowledge will benefit future clock comparisons as well as further experiments exploring the many-body nature of the ^{87}Sr lattice clock, and this general technique will support the development of the next generation of ultrastable lasers.

7.2 Outlook

The proposal for the lattice clock is barely over a decade old [82], yet in that time, remarkable progress has been achieved. Only a few years after the first demonstration of magic wavelength

confinement and Lamb-Dicke spectroscopy [319], the ^{87}Sr lattice clock achieved uncertainty lower than that of the Cs primary frequency standard [31]. In subsequent years, different groups have tackled different different systematic effects: at JILA we focused on understanding and controlling the collisional effects [274, 125] culminating in an evaluation of the Sr2 density shift at 1×10^{-18} [43]. Meanwhile, colleagues at SYRTE carried out a complete study of the vector and tensor polarizabilities, in addition to the hyperpolarizability and M1/E2 effects, verifying that there are no problems on the horizon above 1×10^{-17} due to the optical lattice [110]. Recently, colleagues at PTB reported the first measurement of the DC polarizability and extrapolated the dynamic polarizability, as is necessary for an accurate correction of the blackbody radiation (BBR) shift [115]. Finally, as we report in this thesis and in Ref. [43], the ^{87}Sr lattice clock has reached near-quantum-limited performance due to advances in ultrastable laser technology.

As should therefore be evident, this progress owes its rapidity and breadth to the large international effort aimed at developing the Sr lattice clock. As of this writing three groups worldwide have evaluated ^{87}Sr lattice clock systematics at the 1×10^{-16} level and the international agreement on the ^{87}Sr frequency is superb [31, 33, 34]. Thus, as even more groups around the world continue to develop ^{87}Sr optical lattice clocks, we can expect further recognition of the ^{87}Sr lattice clock's potential role in redefining the SI second via an optical frequency standard [320]. At the very least, it can continue to serve as a powerful secondary representation of the second along with other highly-successful optical clocks.

In terms of developing a working frequency standard that is competitive in systematic uncertainty with the best ion clocks, the next biggest hurdle for ^{87}Sr is obviously the BBR shift. Unfortunately, Sr has the largest BBR shift coefficient of the alkine earth(-like) species being pursued as lattice clocks. However, there are several avenues forward. If one could maintain a known and well-controlled blackbody environment at room temperature and 100 mK temperature uncertainty, then the BBR shift uncertainty would be below 1×10^{-17} . An (albeit complex) two-species optical lattice clock (e.g., two separate but nearby lattices of ^{87}Sr and ^{171}Yb) could in principle form a weighted clock transition, as proposed in [321], that is insensitive to temperature as long

as the DC polarizabilities are known. Fortuitously, the DC polarizability for both Sr [115] and Yb [139] have been measured to high accuracy.

One final comment with respect to clock uncertainty is that the Sr lattice clock now finds itself in an interesting situation: the 1 s stability of the ^{87}Sr lattice clock is very nearly equivalent to its **total** systematic uncertainty, and the flicker noise of the clock laser presented in this thesis is actually slightly below it. As we have mentioned in this thesis, this level of stability makes measurement and control of many relevant systematic shifts a trivial undertaking; formerly month-long measurement campaigns can be completed in one day. While this does not directly help to solve the BBR problem, the improvement in precision will undoubtedly enable rapid progress in reducing uncertainty through systematic measurement.

Sr and other alkaline earth atoms show great promise for quantum science beyond frequency standards—with room for fruitful overlap at the boundaries. For example, many-particle lattice clock systems are highly decoherence-free testbeds for quantum measurement science, and the demonstration of an entangled lattice clock would have profound implications for the ultimate limit of clock stability [322]. Additionally, the confluence of quantum degeneracy and many-particle clocks will yield rich scientific opportunity. In the case of ^{88}Sr , where the measured inelastic loss rate is similar to that of ^{87}Sr while the elastic interaction strength is at least an order magnitude larger [290], degeneracy could yield an interaction-induced entanglement analogous to that obtained in the microwave domain [284], allowing sub-standard-quantum-limit measurement precision. In the context of atomic interactions, dipolar couplings between clock atoms in three-dimensional lattices have been studied as a potential systematic, and could also yield rich excitation dynamics [323].

Due to their $\text{SU}(N)$ symmetry, where N is the number of nuclear spin states, alkaline earth(-like) atoms show promise for simulating complex condensed matter systems and realizing novel, highly-frustrated quantum states [73, 74, 75, 76]. The presence of the metastable clock state furthermore allows quantum simulation in the presence of an artificial gauge field [324]. The clock transition can also serve as a readout and probe of the many-body spectrum [325]. However, we note that while degenerate gases of alkaline earth(-like) atoms have been demonstrated [326,

269, 270, 271, 272], including a recent demonstration obtaining quantum degeneracy by direct laser cooling [94], they have not yet reached the levels of entropy required to observe these novel magnetic phases, although the large numbers of spin-degrees of freedom in fermionic alkaline earth atoms permits an effect similar to Pomeranchuk cooling to potentially reduce the entropy to the required levels [327]. We additionally note that the large, electronically decoupled nuclear spin manifolds of alkaline earth atoms represent a promising register for quantum information science [328, 329, 330]. Here, the electronic level structure of, e.g., ^{87}Sr could permit manipulation and readout of nuclear spin-encoded qubits, and the ability to spectroscopically distinguish nuclear spin sublevels via clock spectroscopy enables the implementation of phase gates between spatially separated qubits [329].

In the specific case of many-body physics with ^{87}Sr in a one-dimensional optical lattice, Fermi degeneracy should more strictly enforce the approximations of the spin model, while at the same time allowing the study of $\text{SU}(N)$ physics via clock spectroscopy and clean readout of many-body states. The operation of a Fermi-degenerate optical clock would be in itself an important milestone. In the case of the one-dimensional lattice, the attainment of single-site resolution would yield enormous gains for the study of many-body effects, since each measurement cycle would yield many parallel measurements of the many-body dynamics and would not suffer from averaging. Single-site resolution would be extremely challenging, but might be possible using a large magnetic field or light-shift gradient to spectroscopically isolate the different spatial locations of each lattice site. Additionally, a non-retroreflected lattice laser could be employed, which would enhance the spacing between lattice sites.

Finally, we mention that alkaline earth atoms represent a novel regime for cavity QED where both the critical photon and atom number can be far less than unity, leading to highly collective quantum effects including steady-state superradiance [331]. It has been proposed that such a superradiant system of ^{87}Sr could operate at the heart of the **ultimate** laser, with linewidth of 1 mHz [252]. In that case, we could finally remove all reliance on length standards (optical cavities) for probing the ^{87}Sr optical lattice clock for quantum metrology and explorations of many-body physics.

Bibliography

- [1] G. K. Campbell *et al.*, “The absolute frequency of the ^{87}Sr optical clock transition,” *Metrologia* **45**(5), 539–548 (2008).
- [2] M. D. Swallows *et al.*, “Operating a ^{87}Sr optical lattice clock with high precision and at high density,” *IEEE Transactions on Ultrasonics, Ferroelectrics and Frequency Control* **59**(3), 416–425 (2012).
- [3] I. Rabi, S. Millman, P. Kusch, and J. Zacharias, “The Molecular Beam Resonance Method for Measuring Nuclear Magnetic Moments. The Magnetic Moments of $\text{Li}63$, $\text{Li}73$ and $\text{F}199$,” *Physical Review* **55**(6), 526–535 (1939).
- [4] J. Kellogg, I. Rabi, N. Ramsey, and J. Zacharias, “The Magnetic Moments of the Proton and the Deuteron. The Radiofrequency Spectrum of H_2 in Various Magnetic Fields,” *Physical Review* **56**(8), 728–743 (1939).
- [5] W. E. Lamb and R. C. Retherford, “Fine structure of the hydrogen atom by a microwave method,” *Physical Review* **72**(3), 241–243 (1947).
- [6] P. Kusch and H. Foley, “The Magnetic Moment of the Electron,” *Physical Review* **74**(3), 250–263 (1948).
- [7] N. Ramsey, “A New Molecular Beam Resonance Method,” *Physical Review* **76**(7), 996–996 (1949).
- [8] T. H. Maiman, “Stimulated Optical Radiation in Ruby,” *Nature* **187**(4736), 493–494 (1960).
- [9] T. W. Hänsch, I. S. Shahin, and A. L. Schawlow, “Optical resolution of the Lamb shift in atomic hydrogen by laser saturation spectroscopy,” *Nature Physical Science* **235**, 63–65 (1972).
- [10] D. Berkeland, E. Hinds, and M. Boshier, “Precise Optical Measurement of Lamb Shifts in Atomic Hydrogen,” *Physical Review Letters* **75**(13), 2470–2473 (1995).
- [11] Y. V. Baklanov, B. Y. Dubetsky, and V. P. Chebotayev, “Non-linear ramsey resonance in the optical region,” *Applied Physics* **9**(2), 171–173 (1976).
- [12] J. Bergquist, S. Lee, and J. Hall, “Saturated Absorption with Spatially Separated Laser Fields: Observation of Optical “Ramsey” Fringes,” *Physical Review Letters* **38**(4), 159–162 (1977).

- [13] D. Wineland and H. Dehmelt, “Proposed 10^{-14} $\delta\nu/\nu$ laser fluorescence spectroscopy on Tl+ mono-ion oscillator,” *Bulletin of the American Physical Society* **20**, 637 (1975).
- [14] T. W. Hänsch and A. L. Schawlow, “Cooling of gases by laser radiation,” *Optics Communications* **13**(1), 68–69 (1975).
- [15] D. J. Wineland and W. M. Itano, “Laser cooling of atoms,” *Physical Review A* **20**(4), 1521–1540 (1979).
- [16] W. D. Phillips, J. V. Prodan, and H. J. Metcalf, “Laser cooling and electromagnetic trapping of neutral atoms,” *Journal of the Optical Society of America B* **2**(11), 1751–1767 (1985).
- [17] S. Chu, L. Hollberg, J. Bjorkholm, A. Cable, and A. Ashkin, “Three-dimensional viscous confinement and cooling of atoms by resonance radiation pressure,” *Physical Review Letters* **55**(1), 48–51 (1985).
- [18] D. Pritchard, E. Raab, V. Bagnato, C. Wieman, and R. Watts, “Light Traps Using Spontaneous Forces,” *Physical Review Letters* **57**(3), 310–313 (1986).
- [19] E. Raab, M. Prentiss, A. Cable, S. Chu, and D. Pritchard, “Trapping of Neutral Sodium Atoms with Radiation Pressure,” *Physical Review Letters* **59**(23), 2631–2634 (1987).
- [20] F. Ruschewitz *et al.*, “Sub-Kilohertz Optical Spectroscopy with a Time Domain Atom Interferometer,” *Physical Review Letters* **80**(15), 3173–3176 (1998).
- [21] C. W. Oates, E. A. Curtis, and L. Hollberg, “Improved short-term stability of optical frequency standards: approaching 1 Hz in 1 s with the Ca standard at 657 nm,” *Optics letters* **25**(21), 1603 (2000).
- [22] R. Rafac *et al.*, “Sub-dekahertz Ultraviolet Spectroscopy of 199Hg^+ ,” *Physical Review Letters* **85**(12), 2462–2465 (2000).
- [23] M. Kasevich, E. Riis, S. Chu, and R. DeVoe, “rf spectroscopy in an atomic fountain,” *Physical Review Letters* **63**(6), 612–615 (1989).
- [24] S. R. Jefferts, C. Monroe, E. W. Bell, and D. J. Wineland, “Coaxial-resonator-driven rf (Paul) trap for strong confinement,” *Physical Review A* **51**(4), 3112–3116 (1995).
- [25] H. Katori, M. Takamoto, V. Pal’chikov, and V. Ovsiannikov, “Ultrastable Optical Clock with Neutral Atoms in an Engineered Light Shift Trap,” *Physical Review Letters* **91**(17), 173,005 (2003).
- [26] J. Ye, H. J. Kimble, and H. Katori, “Quantum State Engineering and Precision Metrology Using State-Insensitive Light Traps,” *Science* **320**(5884), 1734–1738 (2008).
- [27] C. W. Chou, D. B. Hume, J. C. J. Koelemeij, D. J. Wineland, and T. Rosenband, “Frequency Comparison of Two High-Accuracy Al^+ Optical Clocks,” *Physical Review Letters* **104**(7), 070,802 (2010).
- [28] T. Rosenband *et al.*, “Frequency ratio of Al^+ and Hg^+ single-ion optical clocks; metrology at the 17th decimal place,” *Science* **319**(5871), 1808 (2008).

- [29] A. A. Madej, P. Dube, Z. Zhou, J. E. Bernard, and M. Gertsvolf, “ $^{88}\text{Sr}^+$ 445-THz Single-Ion Reference at the 10^{-17} Level via Control and Cancellation of Systematic Uncertainties and Its Measurement against the SI Second,” *Physical Review Letters* **109**(20), 203,002 (2012).
- [30] N. Huntemann *et al.*, “High-Accuracy Optical Clock Based on the Octupole Transition in $^{171}\text{Yb}^+$,” *Physical Review Letters* **108**(9), 090,801 (2012).
- [31] A. D. Ludlow *et al.*, “Sr Lattice Clock at 1×10^{-16} Fractional Uncertainty by Remote Optical Evaluation with a Ca Clock,” *Science* **319**(5871), 1805–1808 (2008).
- [32] N. Lemke *et al.*, “Spin-1/2 optical lattice clock,” *Physical Review Letters* **103**(6), 063,001 (2009).
- [33] S. Falke *et al.*, “The ^{87}Sr optical frequency standard at PTB,” *Metrologia* **48**(5), 399–407 (2011).
- [34] R. L. Targat *et al.*, “Experimenting an optical second with strontium lattice clocks,” arXiv.org (2013).
- [35] S. Blatt *et al.*, “New Limits on Coupling of Fundamental Constants to Gravity Using ^{87}Sr Optical Lattice Clocks,” *Physical Review Letters* **100**(14), 140,801 (2008).
- [36] G. Santarelli *et al.*, “Frequency stability degradation of an oscillator slaved to a periodically interrogated atomic resonator,” *IEEE Transactions on Ultrasonics, Ferroelectrics and Frequency Control* **45**, 887–894 (2008).
- [37] C. Audoin, G. Santarelli, A. Makdissi, and A. Clairon, “Properties of an oscillator slaved to a periodically interrogated atomic resonator,” *IEEE Transactions on Ultrasonics, Ferroelectrics and Frequency Control* **45**(4), 877–886 (1998).
- [38] B. Young, F. Cruz, W. Itano, and J. Bergquist, “Visible Lasers with Subhertz Linewidths,” *Physical Review Letters* **82**(19), 3799–3802 (1999).
- [39] M. Notcutt, L.-S. Ma, J. Ye, and J. L. Hall, “Simple and compact 1-Hz laser system via an improved mounting configuration of a reference cavity,” *Optics letters* **30**(1), 1815–1817 (2005).
- [40] A. D. Ludlow *et al.*, “Compact, thermal-noise-limited optical cavity for diode laser stabilization at 1×10^{-15} ,” *Optics letters* **32**(6), 641–643 (2007).
- [41] Y. Y. Jiang *et al.*, “Making optical atomic clocks more stable with 10^{-16} -level laser stabilization,” *Nature Photonics* **5**(3), 158–161 (2011).
- [42] S. Webster and P. Gill, “Force-insensitive optical cavity,” *Optics letters* **36**(18), 3572 (2011).
- [43] T. L. Nicholson *et al.*, “Comparison of Two Independent Sr Optical Clocks with 1×10^{-17} Stability at 10^3 s,” *Physical Review Letters* **109**, 230,810 (2012).
- [44] D. W. Allan, “Statistics of atomic frequency standards,” *Proceedings of the IEEE* **54**(2), 221–230 (1966).
- [45] J. Rutman, “Characterization of phase and frequency instabilities in precision frequency sources: Fifteen years of progress,” in *Proceedings of the IEEE*, pp. 1048–1075 (1978).

- [46] W. Itano *et al.*, “Quantum projection noise: Population fluctuations in two-level systems,” *Physical Review A* **47**(5), 3554–3570 (1993).
- [47] P. Lemonde *et al.*, “Cold-Atom Clocks on Earth and in Space,” in *Frequency Measurement and Control*, A. Luiten, ed., vol. 79 of *Topics in Applied Physics*, pp. 131–153 (Springer Berlin / Heidelberg, 2001).
- [48] U. Sterr *et al.*, “Ultrastable lasers: new developments and applications,” in *Time and Frequency Metrology II*, T. Ido and D. T. Reid, eds., vol. 7431, p. 74310A (SPIE, 2009).
- [49] T. Udem, R. Holzwarth, and T. Hänsch, “Optical frequency metrology,” *Nature* **416**(6877), 233–237 (2002).
- [50] S. Cundiff and J. Ye, “Colloquium: Femtosecond optical frequency combs,” *Reviews of Modern Physics* **75**(1), 325–342 (2003).
- [51] C. Gohle *et al.*, “A frequency comb in the extreme ultraviolet,” *Nature* **436**, 234–237 (2005).
- [52] D. C. Yost *et al.*, “Vacuum-ultraviolet frequency combs from below-threshold harmonics,” *Nature Physics* **5**, 815–820 (2009).
- [53] F. Adler *et al.*, “Mid-infrared Fourier transform spectroscopy with a broadband frequency comb,” *Optics Express* **18**(21), 21,861–21,872 (2010).
- [54] D. J. Jones *et al.*, “Carrier-Envelope Phase Control of Femtosecond Mode-Locked Lasers and Direct Optical Frequency Synthesis,” *Science* **288**(5466), 635–639 (2000).
- [55] S. M. Foreman *et al.*, “Coherent Optical Phase Transfer over a 32-km Fiber with 1 s Instability at 10^{-17} ,” *Physical Review Letters* **99**(15), 153,601 (2007).
- [56] A. Ruehl *et al.*, “Ultrabroadband coherent supercontinuum frequency comb,” *Physical Review A* **84**(1), 11,806 (2011).
- [57] W. H. Oskay *et al.*, “Single-atom optical clock with high accuracy,” *Physical Review Letters* **97**(2), 020,801 (2006).
- [58] S. M. Foreman *et al.*, “Remote transfer of ultrastable frequency references via fiber networks,” *Review of Scientific Instruments* **78**(2), 021,101 (2007).
- [59] G. Grosche *et al.*, “Optical frequency transfer via 146 km fiber link with 10^{-19} relative accuracy,” *Optics letters* **34**(15), 2270–2272 (2009).
- [60] K. Predehl *et al.*, “A 920-Kilometer Optical Fiber Link for Frequency Metrology at the 19th Decimal Place,” *Science* **336**(6080), 441–444 (2012).
- [61] T. M. Fortier *et al.*, “Precision Atomic Spectroscopy for Improved Limits on Variation of the Fine Structure Constant and Local Position Invariance,” *Physical Review Letters* **98**(7), 070,801 (2007).
- [62] C. W. Chou, D. B. Hume, T. Rosenband, and D. J. Wineland, “Optical Clocks and Relativity,” *Science* **329**(5999), 1630–1633 (2010).

- [63] J. Bollinger, W. Itano, D. Wineland, and D. Heinzen, “Optimal frequency measurements with maximally correlated states.” *Physical Review A* **54**(6), R4649–R4652 (1996).
- [64] M. Greiner, O. Mandel, T. Esslinger, T. W. Hänsch, and I. Bloch, “Quantum phase transition from a superfluid to a Mott insulator in a gas of ultracold atoms.” *Nature* **415**(6867), 39–44 (2002).
- [65] I. Bloch and W. Zwerger, “Many-body physics with ultracold gases,” *Reviews of Modern Physics* **80**(3), 885–964 (2008).
- [66] Y.-J. Lin, R. L. Compton, K. Jiménez-García, J. V. Porto, and I. B. Spielman, “Synthetic magnetic fields for ultracold neutral atoms,” *Nature* **462**(7273), 628–632 (2009).
- [67] G. B. Jo *et al.*, “Itinerant ferromagnetism in a Fermi gas of ultracold atoms,” *Science* **325**(5947), 1521–1524 (2009).
- [68] S. Will *et al.*, “Time-resolved observation of coherent multi-body interactions in quantum phase revivals,” *Nature* **465**(7295), 197–201 (2010).
- [69] J. Simon *et al.*, “Quantum simulation of antiferromagnetic spin chains in an optical lattice.” *Nature* **472**(7343), 307–312 (2011).
- [70] K. K. Ni *et al.*, “A high phase-space-density gas of polar molecules,” *Science* **322**(5899), 231–235 (2008).
- [71] M. H. G. de Miranda *et al.*, “Controlling the quantum stereodynamics of ultracold bimolecular reactions,” *Nat. Phys.* **7**(6), 502–507 (2011).
- [72] A. Chotia *et al.*, “Long-lived dipolar molecules and Feshbach molecules in a 3D optical lattice,” *Physical Review Letters* **108**, 080,405 (2012).
- [73] A. V. Gorshkov *et al.*, “Two-orbital SU(N) magnetism with ultracold alkaline-earth atoms,” *Nature Physics* **6**(4), 289–295 (2010).
- [74] C. Wu, J.-p. Hu, and S.-c. Zhang, “Exact SO(5) symmetry in the spin-3/2 fermionic system.” *Physical Review Letters* **91**(18), 186,402 (2003).
- [75] M. A. Cazalilla, A. F. Ho, and M. Ueda, “Ultracold gases of ytterbium: ferromagnetism and Mott states in an SU(6) Fermi system,” *New Journal of Physics* **11**, 103,033 (2009).
- [76] M. Hermele, V. Gurarie, and A. M. Rey, “Mott Insulators of ultracold fermionic alkaline earth atoms: underconstrained magnetism and chiral spin liquid,” *Physical Review Letters* **103**(13), 135,301 (2009).
- [77] M. Foss-Feig, A. J. Daley, J. K. Thompson, and A. M. Rey, “Steady-state many-body entanglement of hot reactive fermions,” arXiv:1207.4741v1 (2012).
- [78] T. Kurosu and F. Shimizu, “Laser Cooling and Trapping of Calcium and Strontium,” *Japanese Journal of Applied Physics* **29**(Part 2, No. 11), L2127–L2129 (1990).
- [79] K. R. Vogel, T. P. Dinneen, A. C. Gallagher, and J. L. Hall, “Experiments with strontium in a vapor cell magneto-optic trap,” in *Optoelectronics and High-Power Lasers & Applications*, B. L. Fearey, ed., pp. 77–84 (SPIE, 1998).

- [80] T. Loftus, T. Ido, M. Boyd, A. Ludlow, and J. Ye, “Narrow line cooling and momentum-space crystals,” *Physical Review A* **70**(6), 063,413 (2004).
- [81] R. Santra, K. Christ, and C. Greene, “Properties of metastable alkaline-earth-metal atoms calculated using an accurate effective core potential,” *Physical Review A* **69**(4), 042,510 (2004).
- [82] H. Katori, “Spectroscopy of strontium atoms in the Lamb-Dicke confinement,” in *Proceedings of the 6th Symposium on Frequency Standards and Metrology*, P. Gill, ed., pp. 323–330 (World Scientific, Singapore, 2002).
- [83] H. Katori, T. Ido, Y. Isoya, and M. Kuwata-Gonokami, “Magneto-Optical Trapping and Cooling of Strontium Atoms down to the Photon Recoil Temperature,” *Physical Review Letters* **82**(6), 1116–1119 (1999).
- [84] K. R. Vogel, T. P. Dinneen, A. Gallagher, and J. L. Hall, “Near-recoil-limited temperatures obtained by laser trapping on the narrow 1S_0 - 3P_1 intercombination transition of neutral strontium,” in *1999 Joint Meeting of the European Frequency and Time Forum and the IEEE International Frequency Control Symposium*, pp. 692–695 (IEEE, 1999).
- [85] T. H. Loftus, T. Ido, A. D. Ludlow, M. M. Boyd, and J. Ye, “Narrow line cooling: finite photon recoil dynamics.” *Physical Review Letters* **93**(7), 073,003– (2004).
- [86] T. Binnewies *et al.*, “Doppler cooling and trapping on forbidden transitions.” *Physical Review Letters* **87**(12), 123,002– (2001).
- [87] R. Maruyama, R. Wynar, M. Romalis, A. Andalkar, M. Swallows, C. Pearson, and E. Fortson, “Investigation of sub-Doppler cooling in an ytterbium magneto-optical trap,” *Physical Review A* **68**(1), 011,403 (2003).
- [88] B. H. Bransden and C. J. Joachain, *Physics of Atoms and Molecules; 2nd ed.* (Prentice-Hall, Harlow, 2003).
- [89] H. Hachisu *et al.*, “Trapping of Neutral Mercury Atoms and Prospects for Optical Lattice Clocks,” *Physical Review Letters* **100**(5), 053,001 (2008).
- [90] M. Petersen, R. Chicireanu, S. Dawkins, D. Magalhães, C. Mandache, Y. Le Coq, A. Clairon, and S. Bize, “Doppler-Free Spectroscopy of the 1S_0 - 3P_0 Optical Clock Transition in Laser-Cooled Fermionic Isotopes of Neutral Mercury,” *Physical Review Letters* **101**(18), 183,004 (2008).
- [91] J. Guest *et al.*, “Laser Trapping of ^{225}Ra and ^{226}Ra with Repumping by Room-Temperature Blackbody Radiation,” *Physical Review Letters* **98**(9), 093,001 (2007).
- [92] Y. Castin, H. Wallis, and J. Dalibard, “Limit of Doppler cooling,” *Journal of the Optical Society of America B* **6**(11), 2046–2057 (1989).
- [93] H. Katori, “Laser cooling of strontium atoms toward quantum degeneracy,” in *XVII international conference ICAP 2000 (Atomic Physics 17)*, pp. 382–396 (AIP, 2001).
- [94] S. Stellmer, B. Pasquiou, R. Grimm, and F. Schreck, “Laser cooling to quantum degeneracy,” arXiv:1301.4776v1 (2013).

- [95] S. Chu, J. Bjorkholm, A. Ashkin, and A. Cable, “Experimental observation of optically trapped atoms.” *Physical Review Letters* **57**(3), 314–317 (1986).
- [96] R. Grimm, M. Weidemüller, and Y. B. Ovchinnikov, “Optical dipole traps for neutral atoms,” *Advances in Atomic, Molecular and Optical Physics* **42**, 95–170 (2000).
- [97] I. Bloch, J. Dalibard, and S. Nascimbène, “Quantum simulations with ultracold quantum gases,” *Nature Physics* **8**(4), 267–276 (2012).
- [98] X. Zhang, C. L. Hung, S. K. Tung, and C. Chin, “Observation of Quantum Criticality with Ultracold Atoms in Optical Lattices,” *Science* **335**(6072), 1070–1072 (2012).
- [99] J. Struck *et al.*, “Quantum Simulation of Frustrated Classical Magnetism in Triangular Optical Lattices,” *Science* **333**(6045), 996–999 (2011).
- [100] Y.-J. Lin, R. L. Compton, K. Jiménez-García, J. V. Porto, and I. B. Spielman, “Synthetic magnetic fields for ultracold neutral atoms.” *Nature* **462**(7273), 628–632 (2009).
- [101] B. Paredes, A. Widera, V. Murg, O. Mandel, S. Fölling, I. Cirac, G. V. Shlyapnikov, T. W. Hänsch, and I. Bloch, “Tonks–Girardeau gas of ultracold atoms in an optical lattice,” *Nature* **429**(6989), 277–281 (2004).
- [102] R. Dicke, “The Effect of Collisions upon the Doppler Width of Spectral Lines,” *Physical Review* **89**(2), 472–473 (1953).
- [103] J. Bergquist, W. Itano, and D. Wineland, “Recoilless optical absorption and Doppler sidebands of a single trapped ion,” *Physical Review A* **36**(1), 428–430 (1987).
- [104] T. Ido and H. Katori, “Recoil-Free Spectroscopy of Neutral Sr Atoms in the Lamb-Dicke Regime,” *Physical Review Letters* **91**(5), 053,001 (2003).
- [105] C. Bordé *et al.*, “Optical Ramsey fringes with traveling waves,” *Physical Review A* **30**(4), 1836–1848 (1984).
- [106] F. Riehle, A. Witte, T. Kisters, and J. Helmcke, “Interferometry with Ca atoms,” *Applied Physics B* **54**(5), 333–340 (1992).
- [107] U. Sterr *et al.*, “The optical calcium frequency standards of PTB and NIST,” *Comptes Rendus Physique* **5**(8), 845–855 (2004).
- [108] D. A. Steck, “Quantum and Atom Optics. Available online at <http://steck.us/teaching> (revision 0.5.11, 28 February 2011),” .
- [109] I. H. Deutsch and P. S. Jessen, “Quantum control and measurement of atomic spins in polarization spectroscopy,” *Optics Communications* **283**(5), 681–694 (2010).
- [110] P. G. Westergaard *et al.*, “Lattice-Induced Frequency Shifts in Sr Optical Lattice Clocks at the 10^{-17} Level,” *Physical Review Letters* **106**(21), 210,801 (2011).
- [111] D. M. Brink and G. R. Satchler, *Angular momentum* (Clarendon Press Oxford, 1968).
- [112] M. Boyd, “High Precision Spectroscopy of Strontium in an Optical Lattice: Towards a New Standard for Frequency and Time,” Ph.D. thesis, University of Colorado (2007).

- [113] G. Jönsson, C. Levinson, and A. Persson, “Natural radiative lifetimes in the $1 P_1$ and $1 F_3$ sequences of Sr I - Springer,” *Zeitschrift für Physik A* **316**, 255–258 (1984).
- [114] A. Ludlow, “The Strontium Optical Lattice Clock: Optical Spectroscopy with Sub-Hertz Accuracy,” Ph.D. thesis, University of Colorado (2008).
- [115] T. Middelmann, S. Falke, C. Lisdat, and U. Sterr, “High accuracy correction of blackbody radiation shift in an optical lattice clock,” arXiv:1208.2848v1 (2012).
- [116] M. Bishof *et al.*, “Inelastic collisions and density-dependent excitation suppression in a ^{87}Sr optical lattice clock,” *Physical Review A* **84**(5), 052,716 (2011).
- [117] X. Xu *et al.*, “Single-Stage Sub-Doppler Cooling of Alkaline Earth Atoms,” *Physical Review Letters* **90**(19), 193,002 (2003).
- [118] T. Mukaiyama, H. Katori, T. Ido, Y. Li, and M. Kuwata-Gonokami, “Recoil-limited laser cooling of ^{87}Sr Atoms near the Fermi Temperature,” *Physical Review Letters* **90**(11) (2003).
- [119] M. M. Boyd *et al.*, “Nuclear spin effects in optical lattice clocks,” *Physical Review A* **76**(2), 022,510 (2007).
- [120] S. Falke, M. Misera, U. Sterr, and C. Lisdat, “Delivering pulsed and phase stable light to atoms of an optical clock,” *Applied Physics B: Lasers and Optics* **107**(2), 301–311 (2012).
- [121] L.-S. Ma, P. Jungner, J. Ye, and J. L. Hall, “Delivering the same optical frequency at two places: accurate cancellation of phase noise introduced by an optical fiber or other time-varying path,” *Optics letters* **19**(21), 1777–1779 (1994).
- [122] C. Degenhardt *et al.*, “Calcium optical frequency standard with ultracold atoms: Approaching 10^{-15} relative uncertainty,” *Physical Review A* **72**(6), 062,111 (2005).
- [123] H. J. Lipkin, “Some simple features of the Mössbauer effect,” *Annals of Physics* **9**(2), 332–339 (1960).
- [124] G. J. Perlow, W. Potzel, R. M. Kash, and H. de Waard, “Application of a Method of Frequency Modulation Mössbauer Spectroscopy in ^{67}Zn to the Precise Determination of the Electric Quadrupole Interaction of ^{67}ZnO ,” *Le Journal de Physique Colloques* **35**(C6), 6–6 (1974).
- [125] M. J. Martin *et al.*, “A quantum many-body spin system in an optical lattice clock,” arXiv:1212.6291v1 (2012).
- [126] S. Blatt *et al.*, “Rabi spectroscopy and excitation inhomogeneity in a one-dimensional optical lattice clock,” *Physical Review A* **80**(5), 052,703 (2009).
- [127] P. Lemonde and P. Wolf, “Optical lattice clock with atoms confined in a shallow trap,” *Physical Review A* **72**(3), 033,409 (2005).
- [128] S. Blatt, “High Precision Spectroscopy of Strontium in an Optical Lattice: Towards a New Standard for Frequency and Time,” Ph.D. thesis, University of Colorado (2007).
- [129] M. Takamoto and H. Katori, “Coherence of Spin-Polarized Fermions Interacting with a Clock Laser in a Stark-Shift-Free Optical Lattice,” *Journal of the Physical Society of Japan* **78**(1), 013,301 (2008).

- [130] H. Uys *et al.*, “Decoherence due to elastic Rayleigh scattering,” *Physical Review Letters* **105**(20), 200,401 (2010).
- [131] J. J. Sakurai, *Advanced quantum mechanics*, Addison-Wesley Series in Advanced Physics (Addison-Wesley, Reading, MA, 1967).
- [132] M. J. Martin, S. M. Foreman, T. R. Schibli, and J. Ye, “Testing ultrafast mode-locking at microhertz relative optical linewidth,” *Optics Express* **17**, 558–568 (2009).
- [133] F. L. Hong *et al.*, “Measuring the frequency of a Sr optical lattice clock using a 120 km coherent optical transfer,” *Optics letters* **34**(5), 692–694 (2009).
- [134] A. Yamaguchi *et al.*, “Stability Transfer between Two Clock Lasers Operating at Different Wavelengths for Absolute Frequency Measurement of Clock Transition in ^{87}Sr ,” *Applied Physics Express* **5** (2012).
- [135] M. D. Swallows *et al.*, “Suppression of Collisional Shifts in a Strongly Interacting Lattice Clock,” *Science* **331**(6020), 1043–1046 (2011).
- [136] T. Akatsuka, M. Takamoto, and H. Katori, “Optical lattice clocks with non-interacting bosons and fermions,” *Nature Physics* **4**(12), 954–959 (2008).
- [137] A. Taichenachev, V. Yudin, V. Ovsiannikov, V. Pal’chikov, and C. Oates, “Frequency Shifts in an Optical Lattice Clock Due to Magnetic-Dipole and Electric-Quadrupole Transitions,” *Physical Review Letters* **101**(19) (2008).
- [138] S. Porsev and A. Derevianko, “Multipolar theory of blackbody radiation shift of atomic energy levels and its implications for optical lattice clocks,” *Physical Review A* **74**(2), 020,502(R) (2006).
- [139] J. Sherman *et al.*, “High-Accuracy Measurement of Atomic Polarizability in an Optical Lattice Clock,” *Physical Review Letters* **108**(15), 153,002 (2012).
- [140] S. Porsev, A. Ludlow, M. Boyd, and J. Ye, “Determination of Sr properties for a high-accuracy optical clock,” *Physical Review A* **78**(3), 032,508 (2008).
- [141] M. Safronova, S. G. Porsev, U. Safronova, M. Kozlov, and C. W. Clark, “Blackbody-radiation shift in the Sr optical atomic clock,” *Physical Review A* **87**(1), 012,509 (2013).
- [142] T. Middelmann *et al.*, “Tackling the Blackbody Shift in a Strontium Optical Lattice Clock,” in *IEEE Transactions on Instrumentation and Measurement*, pp. 2550–2557 (2011).
- [143] A. Quessada *et al.*, “The Dick effect for an optical frequency standard,” in *Journal of Optics B-Quantum and Semiclassical Optics*, pp. S150–S154 (2003).
- [144] M. Aspelmeyer, S. Groeblacher, K. Hammerer, and N. Kiesel, “Quantum optomechanics—throwing a glance [Invited],” *Journal of the Optical Society of America B* **27**(6), A189–A197 (2010).
- [145] J. Chan *et al.*, “Laser cooling of a nanomechanical oscillator into its quantum ground state.” *Nature* **478**(7367), 89–92 (2011).

- [146] R. Rivière *et al.*, “Optomechanical sideband cooling of a micromechanical oscillator close to the quantum ground state,” *Physical Review A* **83**(6), 063,835 (2011).
- [147] B. P. Abbott *et al.*, “LIGO: the Laser Interferometer Gravitational-Wave Observatory,” *Reports on Progress in Physics* **72**(7), 076,901 (2009).
- [148] H. B. Callen and R. F. Greene, “On a Theorem of Irreversible Thermodynamics,” *Physical Review* **86**, 702–710 (1952).
- [149] L. D. Landau and E. M. Lifshitz, *Statistical Physics*; 3rd ed. (Butterworth, Oxford, 1980).
- [150] P. R. Saulson, “Thermal noise in mechanical experiments,” *Physical Review* **D42**, 2437–2445 (1990).
- [151] Y. Levin, “Internal thermal noise in the LIGO test masses: a direct approach,” *Physical Review D* **57**(2), 659–663 (1998).
- [152] A. Gillespie and F. Raab, “Thermally excited vibrations of the mirrors of laser interferometer gravitational-wave detectors,” *Physical Review D* **52**(2), 577–585 (1995).
- [153] M. Bondarescu, O. Kogan, and Y. Chen, “Optimal light beams and mirror shapes for future LIGO interferometers,” *Physical Review D* **78**(8), 082,002 (2008).
- [154] J. D. Jackson, *Classical Electrodynamics*, 3rd ed. (John Wiley and Sons, Inc., 1999).
- [155] T. Kessler, T. Legero, and U. Sterr, “Thermal noise in optical cavities revisited,” *Journal of the Optical Society of America B* **29**(1), 178–184 (2012).
- [156] G. M. Harry *et al.*, “Thermal noise in interferometric gravitational wave detectors due to dielectric optical coatings,” *Classical and Quantum Gravity* **19**(5), 897–917 (2002).
- [157] K. Numata, A. Kemery, and J. Camp, “Thermal-Noise Limit in the Frequency Stabilization of Lasers with Rigid Cavities,” *Physical Review Letters* **93**(25), 250,602 (2004).
- [158] R. Schnabel *et al.*, “Building blocks for future detectors: Silicon test masses and 1550 nm laser light,” *Journal of Physics Conference Series* **228**(1), 012,029 (2010).
- [159] *et al.* Uchiyama T, Tomaru T, “Mechanical quality factor of a cryogenic sapphire test mass for gravitational wave detectors,” *Physics Letters A* **261**, 5–11 (1999).
- [160] R. Nawrodt *et al.*, “High mechanical Q-factor measurements on calcium fluoride at cryogenic temperatures,” *The European Physical Journal Applied Physics* **38**(1), 53–59 (2007).
- [161] I. W. Martin *et al.*, “Effect of heat treatment on mechanical dissipation in Ta₂O₅ coatings,” *Classical and Quantum Gravity* **27**(22), 225,020 (2010).
- [162] G. M. Harry *et al.*, “Thermal noise from optical coatings in gravitational wave detectors,” *Applied Optics* **45**(7), 1569–1574 (2006).
- [163] J. J. Wortman and R. A. Evans, “Young’s Modulus, Shear Modulus, and Poisson’s Ratio in Silicon and Germanium,” *Journal of Applied Physics* **36**(1), 153 (1965).
- [164] S. D. Penn *et al.*, “High quality factor measured in fused silica,” *Review of Scientific Instruments* **72**(9), 3670–3673 (2001).

- [165] V. B. Braginsky and S. P. Vyatchanin, “Thermodynamical fluctuations in optical mirror coatings,” *Physics Letters A* **312**, 244–255 (2003).
- [166] R. Nawrodt, A. Zimmer, T. Koettig, S. Nietzsche, M. Thürk, W. Vodel, and P. Seidel, “High mechanical Q-factor measurements on calcium fluoride at cryogenic temperatures,” *The European Physical Journal Applied Physics* **38**(1), 53–59 (2007).
- [167] G. D. Cole, “Cavity optomechanics with low-noise crystalline mirrors,” in *SPIE NanoScience + Engineering*, K. Dholakia and G. C. Spalding, eds., p. 845807 (SPIE, 2012).
- [168] T. Kessler *et al.*, “A sub-40-mHz-linewidth laser based on a silicon single-crystal optical cavity,” *Nature Photonics* **6**(10), 687–692 (2012).
- [169] D. R. M. Crooks *et al.*, “Excess mechanical loss associated with dielectric mirror coatings on test masses in interferometric gravitational wave detectors,” *Classical and Quantum Gravity* **19**(5), 883–896 (2002).
- [170] G. Rempe, R. J. Thompson, H. J. Kimble, and R. Lalezari, “Measurement of ultralow losses in an optical interferometer,” *Optics letters* **17**(5), 363–365 (1992).
- [171] G. D. Cole, S. Gröblacher, K. Gugler, S. Gigan, and M. Aspelmeyer, “Monocrystalline $\text{Al}_x\text{Ga}_{1-x}\text{As}$ heterostructures for high-reflectivity high-Q micromechanical resonators in the megahertz regime,” *Applied Physics Letters* **92**(26), 261,108 (2008).
- [172] G. D. Cole, W. Zhang, M. J. Martin, J. Ye, and M. Aspelmeyer, “Tenfold reduction of Brownian noise in optical interferometry,” arXiv:1302.6489v1 (2013).
- [173] M. G. Tarallo *et al.*, “Generation of a flat-top laser beam for gravitational wave detectors by means of a nonspherical Fabry-Perot resonator,” *Applied Optics* **46**(26), 6648–6654 (2007).
- [174] V. B. Braginsky, M. L. Gorodetsky, and S. P. Vyatchanin, “Thermodynamical fluctuations and photo-thermal shot noise in gravitational wave antennae,” *Physics Letters A* **264**(1), 1–10 (1999).
- [175] M. Evans, S. Ballmer, M. Fejer, P. Fritschel, G. Harry, and G. Ogin, “Thermo-optic noise in coated mirrors for high-precision optical measurements,” *Physical Review D* **78**(10), 102,003 (2008).
- [176] M. Cerdonio, L. Conti, A. Heidmann, and M. Pinard, “Thermoelastic effects at low temperatures and quantum limits in displacement measurements,” *Physical Review D* **63**, 082,003 (2001).
- [177] V. B. Braginsky and S. P. Vyatchanin, “Thermodynamical fluctuations in optical mirror coatings,” *Physics Letters A* **312**(3-4), 244 – 255 (2003).
- [178] J. Alnis, A. Matveev, N. Kolachevsky, T. Udem, and T. W. Hänsch, “Subhertz linewidth diode lasers by stabilization to vibrationally and thermally compensated ultralow-expansion glass Fabry-Pérot cavities,” *Physical Review A* **77**(5), 053,809 (2008).
- [179] C. J. Numata K, Kemery A, “Thermal-Noise Limit in the Frequency Stabilization of Lasers with Rigid Cavities,” *Physical Review Letters* **93**(25), 250,602 (2004).

- [180] C. J. Hood, H. J. Kimble, and J. Ye, “Characterization of high-finesse mirrors: Loss, phase shifts, and mode structure in an optical cavity,” *Physical Review A* **64**(3), 33,804 (2001).
- [181] H. Kimble, B. Lev, and J. Ye, “Optical Interferometers with Reduced Sensitivity to Thermal Noise,” *Physical Review Letters* **101**(26), 260,602 (2008).
- [182] M. L. Gorodetsky, “Thermal noises and noise compensation in high-reflection multilayer coating,” *Physics Letters A* **372**(46), 6813–6822 (2008).
- [183] V. B. Braginsky, M. L. Gorodetsky, and S. P. Vyatchanin, “Thermo-refractive noise in gravitational wave antennae,” *Physics Letters A* **271**, 303–307 (2000).
- [184] Y. S. Touloukian, ed., Thermophysical properties of matter (IFI/Plenum, 1970).
- [185] J. A. McCauley, V. M. Donnelly, M. Vernon, and I. Taha, “Temperature dependence of the near-infrared refractive index of silicon, gallium arsenide, and indium phosphide,” *Physical Review B* **49**(11), 7408 (1994).
- [186] J. S. Blakemore, “Semiconducting and other major properties of gallium arsenide,” *Journal of Applied Physics* **53**(10), R123 – R181 (1982).
- [187] J. Talghader and J. Smith, “Thermal dependence of the refractive index of GaAs and AlAs measured using semiconductor multilayer optical cavities,” *Applied Physics Letters* **66**(3), 335–337 (1995).
- [188] <http://www.ioffe.rssi.ru/SVA/NSM/Semicond/AlGaAs/thermal.html> .
- [189] G. Cole, Private communication .
- [190] N. Kolachevsky *et al.*, “Measurement of the $2S$ Hyperfine Interval in Atomic Hydrogen,” *Physical Review Letters* **102**(21), 213,002 (2009).
- [191] M. J. Thorpe, K. D. Moll, R. J. Jones, B. Safdi, and J. Ye, “Broadband Cavity Ringdown Spectroscopy for Sensitive and Rapid Molecular Detection,” *Science* **311**(5767), 1595–1599 (2006).
- [192] R. Miller *et al.*, “Trapped atoms in cavity QED: coupling quantized light and matter,” *Journal of Physics B: Atomic, Molecular and Optical Physics* **38**(9), S551 (2005).
- [193] A. Brillet and J. Hall, “Improved Laser Test of the Isotropy of Space,” *Physical Review Letters* **42**(9), 549–552 (1979).
- [194] D. Hils and J. L. Hall, “Improved Kennedy-Thorndike experiment to test special relativity,” *Physical Review Letters* **64**(15), 1697–1700 (1990).
- [195] C. Eisele, A. Y. Nevsky, and S. Schiller, “Laboratory Test of the Isotropy of Light Propagation at the 10^{-17} Level,” *Physical Review Letters* **103**(9), 090,401 (2009).
- [196] S. Blatt *et al.*, “New Limits on Coupling of Fundamental Constants to Gravity Using ^{87}Sr Optical Lattice Clocks,” *Physical Review Letters* **100**(14), 140,801 (2008).
- [197] U. a. Sterr, “The optical calcium frequency standards of PTB and NIST,” *Comptes Rendus Physique* **5**, 845–855 (2004).

- [198] M. Takamoto, F.-L. Hong, R. Higashi, and H. Katori, “An optical lattice clock,” *Nature* **435**(7040), 321–324 (2005).
- [199] A. Ludlow *et al.*, “Systematic study of the ^{87}Sr clock transition in an optical lattice,” *Physical Review Letters* **96**(3), 033,003 (2006).
- [200] R. Le Targat *et al.*, “Accurate optical lattice clock with ^{87}Sr atoms,” *Physical Review Letters* **97**(13), 130,801 (2006).
- [201] S. A. Diddams *et al.*, “An Optical Clock Based on a Single Trapped $^{199}\text{Hg}^+$ Ion,” *Science* **293**(5531), 825 (2001).
- [202] A. A. Madej, J. E. Bernard, P. Dubé, L. Marmet, and R. S. Windeler, “Absolute frequency of the $^{88}\text{Sr}+5s^2S_{1/2}-4d^2D_{5/2}$ reference transition at 445 THz and evaluation of systematic shifts,” *Physical Review A* **70**(1), 012,507 (2004).
- [203] H. S. Margolis *et al.*, “Hertz-Level Measurement of the Optical Clock Frequency in a Single $^{88}\text{Sr}^+$ Ion,” *Science* **306**(5700), 1355–1358 (2004).
- [204] T. Heavner, S. Jefferts, E. Donley, J. Shirley, and T. Parker, “NIST-F1: recent improvements and accuracy evaluations,” *Metrologia* **42**, 411 (2005).
- [205] S. Bize, *et al.*, “Cold atom clocks and applications,” *Journal of Physics B: Atomic, Molecular and Optical Physics* **38**, S449 (2005).
- [206] B. E. A. Saleh and M. C. Teich, *Fundamentals of photonics* (Wiley-Interscience, 1991).
- [207] B. Saleh, M. Teich, and B. Saleh, *Fundamentals of photonics*, vol. 22 (Wiley New York, 1991).
- [208] M. J. Lawrence, B. Willke, M. E. Husman, E. K. Gustafson, and R. L. Byer, “Dynamic response of a Fabry–Perot interferometer,” *Journal of the Optical Society of America B* **16**(4), 523–532 (1999).
- [209] R. W. P. Drever *et al.*, “Laser phase and frequency stabilization using an optical resonator,” *Applied Physics B* **31**, 97–105 (1983).
- [210] T. Day, E. Gustafson, and R. Byer, “Sub-hertz relative frequency stabilization of two-diode laser-pumped Nd:YAG lasers locked to a Fabry-Perot interferometer,” *IEEE Journal of Quantum Electronics* **28**(4), 1106–1117 (1992).
- [211] O. Mor and A. Arie, “Performance analysis of Drever-Hall laser frequency stabilization using a proportional+integral servo,” *Quantum Electronics, IEEE Journal of* **33**(4), 532–540 (1997).
- [212] E. Black, “An introduction to Pound-Drever-Hall laser frequency stabilization,” *American Journal of Physics* **69**, 79–87 (2001).
- [213] E. Bava, G. Galzerano, and C. Svelto, “Amplitude and frequency noise sensitivities of optical frequency discriminators based on Fabry-Perot interferometers and the frequency modulation technique,” *Review of Scientific Instruments* **77**(12), 123,106 (2006).
- [214] D. Hils and J. L. Hall, “Response of a Fabry-Perot cavity to phase modulated light,” *Review of Scientific Instruments* **58**, 1406–1412 (1987).

- [215] C. Salomon, D. Hils, and J. L. Hall, “Laser stabilization at the millihertz level,” *Journal of the Optical Society of America B* **5**, 1576–1587 (1988).
- [216] N. Wong and J. L. Hall, “Servo control of amplitude modulation in frequency-modulation spectroscopy: demonstration of shot-noise-limited detection,” *Journal of the Optical Society of America B* **2**(9), 1527–1533 (1985).
- [217] R. S. Weis and T. K. Gaylord, “Lithium niobate: Summary of physical properties and crystal structure - Springer,” *Applied Physics A* **37**, 191–203 (1985).
- [218] I. P. Kaminow and E. H. Turner, “Electrooptic light modulators,” *Applied Optics* **5**(10), 1612–1628 (1966).
- [219] J. M. Ley, “Low-voltage light-amplitude modulation,” *Electronics Letters* **2**(1), 12–13 (1966).
- [220] L. Chen *et al.*, “Vibration-induced elastic deformation of Fabry-Perot cavities,” *Physical Review A* **74**(5), 053,801 (2006).
- [221] J. Millo *et al.*, “Ultrastable lasers based on vibration insensitive cavities,” *Physical Review A* **79**(5) (2009).
- [222] R. Jason Jones, I. Thomann, and J. Ye, “Precision stabilization of femtosecond lasers to high-finesse optical cavities,” *Physical Review A* **69**(5), 051,803 (2004).
- [223] T. Legero, T. Kessler, and U. Sterr, “Tuning the thermal expansion properties of optical reference cavities with fused silica mirrors,” *Journal of the Optical Society of America B* **27**(5), 914 (2010).
- [224] S. A. Webster, M. Oxborrow, and P. Gill, “Vibration insensitive optical cavity,” *Physical Review A* **75**(1), 011,801(R) (2007).
- [225] J.-P. Richard and J. J. Hamilton, “Cryogenic monocrystalline silicon Fabry-Perot cavity for the stabilization of laser frequency,” *Review of Scientific Instruments* **62**(10), 2375–2378 (1991).
- [226] S. Seel, R. Storz, G. Ruoso, J. Mlynek, and S. Schiller, “Cryogenic Optical Resonators: A New Tool for Laser Frequency Stabilization at the 1 Hz Level,” *Physical Review Letters* **78**(25), 4741–4744 (1997).
- [227] H. Müller, S. Herrmann, C. Braxmaier, S. Schiller, and A. Peters, “Modern Michelson-Morley experiment using cryogenic optical resonators,” *Physical Review Letters* **91**(2), 020,401 (2003).
- [228] R. W. Fox, “Temperature analysis of low-expansion Fabry-Perot cavities,” *Optics Express* **17**(17), 15,023–15,031 (2009).
- [229] G. White, “Reference materials for thermal expansion: certified or not?” *Thermochimica Acta* **218**, 83–99 (1993).
- [230] C. Taylor, M. Notcutt, E. K. Wong, A. Mann, and D. Blair, “Measurement of the thermal expansion coefficient of an all-sapphire optical cavity,” *Instrumentation and Measurement, IEEE Transactions on* **46**(2), 183–185 (1997).

- [231] C. A. Swenson, “Recommended Values for the Thermal Expansivity of Silicon from 0 to 1000 K,” *Journal of Physical and Chemical Reference Data* **12**(2), 179–182 (1983).
- [232] M. G. Littman and H. J. Metcalf, “Spectrally narrow pulsed dye laser without beam expander,” *Applied Optics* **17**(14), 2224–2227 (1978).
- [233] W. B. Dress, P. D. Miller, J. M. Pendlebury, P. Perrin, and N. F. Ramsey, “Search for an electric dipole moment of the neutron,” *Physical Review D* **15**(1), 9–21 (1977).
- [234] M. Takamoto, T. Takano, and H. Katori, “Frequency comparison of optical lattice clocks beyond the Dick limit,” *Nature Photonics* **5**(5), 288–292 (2011).
- [235] S. Vogt *et al.*, “Demonstration of a transportable 1 Hz-linewidth laser,” *Applied Physics B: Lasers and Optics* **104**(4), 741–745 (2011).
- [236] J. E. Gray and D. W. Allan, “A method for estimating the frequency stability of an individual oscillator,” in *Proceedings of the 8th Annual Symposium on Frequency Control*, vol. 2439, pp. 277–287 (1974).
- [237] A. Premoli and P. Tavella, “A revisited three-cornered hat method for estimating frequency standard instability,” *IEEE Transactions on Instrumentation and Measurement* **42**(1), 7–13 (1993).
- [238] D. Hils and J. Hall, “Improved Kennedy-Thorndike experiment to test special relativity,” *Physical Review Letters* **64**(15), 1697–1700 (1990).
- [239] M. Notcutt, L. Ma, A. Ludlow, S. Foreman, J. Ye, and J. Hall, “Contribution of thermal noise to frequency stability of rigid optical cavity via Hertz-linewidth lasers,” *Physical Review A* **73**(3), 031,804(R) (2006).
- [240] C. Benko *et al.*, “Full phase stabilization of a Yb: fiber femtosecond frequency comb via high-bandwidth transducers,” *Optics letters* **37**(12), 2196–2198 (2012).
- [241] S. T. Dawkins, J. J. McFerran, and A. N. Luiten, “Considerations on the measurement of the stability of oscillators with frequency counters,” *IEEE Transactions on Ultrasonics, Ferroelectrics and Frequency Control* **54**, 918–925 (2007).
- [242] T. Rosenband, D. B. Hume, P. O. Schmidt, C. W. Chou, A. Brusch, L. Lorini, W. H. Oskay, R. E. Drullinger, T. M. Fortier, and J. E. Stalnaker, “Frequency ratio of Al⁺ and Hg⁺ single-ion optical clocks; metrology at the 17th decimal place,” *Science* **319**(5871), 1808–1812 (2008).
- [243] T. M. Fortier *et al.*, “Generation of ultrastable microwaves via optical frequency division,” *Nature Photonics* **5**(7), 425–429 (2011).
- [244] C. Hagemann *et al.*, “Providing 10⁻¹⁶ short-term stability of a 1.5 μm laser to optical clocks,” arXiv:1208.1634v1 (2012).
- [245] T. R. Schibli *et al.*, “Optical frequency comb with submillihertz linewidth and more than 10 W average power,” *Nature Photonics* **2**(6), 355–359 (2008).

- [246] I. Hartl, T. R. Schibli, A. Marcinkevičius, and D. C. Yost, “Cavity-enhanced similariton Yb-fiber laser frequency comb: 3×10^{14} W/cm² peak intensity at 136 MHz,” *Optics Letters* **32**(19), 2870–2872 (2007).
- [247] L. Fu, B. K. Thomas, and L. Dong, “Efficient supercontinuum generations in silica suspended core fibers,” *Optics Express* **16**, 19,629–19,642 (2008).
- [248] J. Stenger, H. Schnatz, C. Tamm, and H. Telle, “Ultraprecise Measurement of Optical Frequency Ratios,” *Physical Review Letters* **88**(7), 073,601 (2002).
- [249] S. Foreman, “Femtosecond Frequency Combs for Optical Clocks and Timing Transfer,” Ph.D. thesis, University of Colorado (2007).
- [250] T. Fortier *et al.*, “Phase stabilization of an octave-spanning Ti: sapphire laser,” *Optics Letters* **28**(22), 2198 (2003).
- [251] M. J. Thorpe, L. Rippe, T. M. Fortier, M. S. Kirchner, and T. Rosenband, “Frequency stabilization to 6×10^{-16} via spectral-hole burning,” *Nature Photonics* **5**(11), 688–693 (2011).
- [252] D. Meiser, J. Ye, D. Carlson, and M. Holland, “Prospects for a Millihertz-Linewidth Laser,” *Physical Review Letters* **102**(16) (2009).
- [253] M. Martin, D. Meiser, J. Thomsen, J. Ye, and M. Holland, “Extreme nonlinear response of ultranarrow optical transitions in cavity QED for laser stabilization,” *Physical Review A* **84**(6), 063,813 (2011).
- [254] J. Lodewyck, P. Westergaard, and P. Lemonde, “Nondestructive measurement of the transition probability in a Sr optical lattice clock,” *Physical Review A* **79**(6) (2009).
- [255] K. Gibble and B. Verhaar, “Eliminating cold-collision frequency shifts,” *Physical Review A* **52**(4), 3370–3373 (1995).
- [256] J. Weiner, V. S. Bagnato, S. Zilio, and P. S. Julienne, “Experiments and theory in cold and ultracold collisions,” *Reviews of Modern Physics* **71**, 1–85 (1999).
- [257] H. Suno, B. D. Esry, and C. H. Greene, “Recombination of Three Ultracold Fermionic Atoms,” *Physical Review Letters* **90**(5), 053,202 (2003).
- [258] K. Huang and C. Yang, “Quantum-Mechanical Many-Body Problem with Hard-Sphere Interaction,” *Physical Review Letters* **105**(3), 767–775 (1957).
- [259] A. Derevianko, “Revised Huang-Yang multipolar pseudopotential,” *Physical Review A* **72**(4), 044,701 (2005).
- [260] Z. Idziaszek, “Analytical solutions for two atoms in a harmonic trap: *p*-wave interactions,” *Physical Review A* **79**, 062,701 (2009).
- [261] C. J. Pethick and H. Smith, *Bose-Einstein condensation in dilute gases* (Cambridge University Press, Cambridge, 2002).
- [262] B. DeMarco and D. S. Jin, “Exploring a quantum degenerate gas of fermionic atoms,” *Physical Review A* **58**(6), 4267–4270 (1998).

- [263] W. Ketterle and H. Miesner, “Coherence properties of Bose-Einstein condensates and atom lasers,” *Physical Review A* **56**(4), 3291–3293 (1997).
- [264] D. M. Harber, H. J. Lewandowski, J. M. McGuirk, and E. A. Cornell, “Effect of cold collisions on spin coherence and resonance shifts in a magnetically trapped ultracold gas,” *Physical Review A* **66**, 053,616 (2002).
- [265] G. K. Campbell *et al.*, “Probing Interactions Between Ultracold Fermions,” *Science* **324**(5925), 360–363 (2009).
- [266] Y. Martinez de Escobar, P. Mickelson, P. Pellegrini, S. Nagel, A. Traverso, M. Yan, R. Côté, and T. Killian, “Two-photon photoassociative spectroscopy of ultracold ^{88}Sr ,” *Physical Review A* **78**(6), 062,708 (2008).
- [267] K. Kim *et al.*, “Quantum simulation of frustrated Ising spins with trapped ions.” *Nature* **465**(7298), 590–593 (2010).
- [268] J. W. Britton *et al.*, “Engineered two-dimensional Ising interactions in a trapped-ion quantum simulator with hundreds of spins.” *Nature* **484**(7395), 489–492 (2012).
- [269] S. Taie *et al.*, “Realization of a $\text{SU}(2)\times\text{SU}(6)$ system of fermions in a cold atomic gas,” *Physical Review Letters* **105**(19), 190,401 (2010).
- [270] B. J. DeSalvo, M. Yan, M. P. G., de Escobar. Y. N. M., and T. C. Killian, “Degenerate Fermi gas of ^{87}Sr ,” *Physical Review Letters* **105**, 030,402 (2010).
- [271] H. Hara, Y. Takasu, Y. Yamaoka, J. M. Doyle, and Y. Takahashi, “Quantum degenerate mixtures of alkali and alkaline-earth-like atoms,” *Physical Review Letters* **106**, 205,304 (2011).
- [272] M. K. Tey, S. Stellmer, R. Grimm, and F. Schreck, “Double-degenerate Bose-Fermi mixture of strontium,” *Physical Review A* **82**, 011,608 (2010).
- [273] N. D. Lemke *et al.*, “ p -Wave cold collisions in an optical lattice clock.” *Physical Review Letters* **107**(10), 103,902 (2011).
- [274] A. M. Rey, A. V. Gorshkov, and C. Rubbo, “Many-Body Treatment of the Collisional Frequency Shift in Fermionic Atoms,” *Physical Review Letters* **103**(26), 260,402 (2009).
- [275] K. Gibble, “Decoherence and Collisional Frequency Shifts of Trapped Bosons and Fermions,” *Physical Review Letters* **103**(11), 113,202 (2009).
- [276] Z. Yu and C. J. Pethick, “Clock Shifts of Optical Transitions in Ultracold Atomic Gases,” *Physical Review Letters* **104**(1), 010,801 (2010).
- [277] A. Auerbach, Interacting Electrons and Quantum Magnetism (Springer, 1994).
- [278] A. L. Fetter and J. D. Walecka, Quantum Theory of Many-Particle Systems (Dover, 2003).
- [279] A. Sørensen, L. M. Duan, J. I. Cirac, and P. Zoller, “Many-particle entanglement with Bose-Einstein condensates,” *Nature* **409**(6816), 63–66 (2001).
- [280] M. Kitagawa and M. Ueda, “Squeezed spin states.” *Physical Review A* **47**(6), 5138–5143 (1993).

- [281] D. Wineland, J. Bollinger, W. Itano, F. Moore, and D. Heinzen, “Spin squeezing and reduced quantum noise in spectroscopy,” *Physical Review A* **46**(11), R6797–R6800 (1992).
- [282] M. Steel and M. Collett, “Quantum state of two trapped Bose-Einstein condensates with a Josephson coupling,” *Physical Review A* **57**(4), 2920–2930 (1998).
- [283] J. Esteve, C. Gross, A. Weller, S. Giovanazzi, and M. K. Oberthaler, “Squeezing and entanglement in a Bose–Einstein condensate,” *Nature* **455**(7217), 1216–1219 (2008).
- [284] C. Gross, T. Zibold, E. Nicklas, J. Esteve, and M. K. Oberthaler, “Nonlinear atom interferometer surpasses classical precision limit,” *Nature* **464**(7292), 1165–1169 (2010).
- [285] B. Lücke *et al.*, “Twin matter waves for interferometry beyond the classical limit.” *Science* **334**(6057), 773–776 (2011).
- [286] D. Porras and J. I. Cirac, “Effective quantum spin systems with trapped ions,” *Physical Review Letters* **92**, 207,901 (2004).
- [287] M. D. Swallows *et al.*, “Operating a ^{87}Sr optical lattice clock with high precision and at high density,” *IEEE Transactions on Ultrasonics, Ferroelectrics and Frequency Control* **59**(3), 416–425 (2012).
- [288] M. Bishof, Y. Lin, M. D. Swallows, A. V. Gorshkov, J. Ye, and A. M. Rey, “Resolved atomic interaction sidebands in an optical clock transition,” *Physical Review Letters* **106**(25), 250,801 (2011).
- [289] A. Traverso *et al.*, “Inelastic and elastic collision rates for triplet states of ultracold strontium,” *Physical Review A* **79**(6), 060,702 (2009).
- [290] C. Lisdat, J. S. R. Vellore Winfred, T. Middelmann, F. Riehle, and U. Sterr, “Collisional Losses, Decoherence, and Frequency Shifts in Optical Lattice Clocks with Bosons,” *Physical Review Letters* **103**(9), 090,801 (2009).
- [291] G. Quémener and J. L. Bohn, “Strong dependence of ultracold chemical rates on electric dipole moments,” *Physical Review A* **81**(2), 022,702 (2010).
- [292] M. Takamoto and H. Katori, “Coherence of Spin-Polarized Fermions Interacting with a Clock Laser in a Stark-Shift-Free Optical Lattice,” *Journal of the Physical Society of Japan* **78**(1), 013,301 (2008).
- [293] A. Ludlow *et al.*, “Cold-collision-shift cancellation and inelastic scattering in a Yb optical lattice clock,” *Physical Review A* **84**(5), 052,724 (2011).
- [294] A. Smerzi, S. Fantoni, S. Giovanazzi, and S. R. Shenoy, “Quantum Coherent Atomic Tunneling between Two Trapped Bose-Einstein Condensates,” *Physical Review Letters* **79**(25), 4950–4953 (1997).
- [295] M. Albiez *et al.*, “Direct Observation of Tunneling and Nonlinear Self-Trapping in a Single Bosonic Josephson Junction,” *Physical Review Letters* **95**(1), 010,402 (2005).
- [296] R. Dicke, “Coherence in Spontaneous Radiation Processes,” *Physical Review Letters* **93**(1), 99–110 (1954).

- [297] R. Friedberg and J. T. Manassah, “Dicke states and Bloch states,” *Laser Physics Letters* **4**(12), 900–911 (2007).
- [298] A. Trombettoni and A. Smerzi, “Discrete solitons and breathers with dilute Bose-Einstein condensates.” *Physical Review Letters* **86**(11), 2353–2356 (2001).
- [299] P. R. Johnson, E. Tiesinga, J. V. Porto, and C. J. Williams, “Effective three-body interactions of neutral bosons in optical lattices,” *New Journal of Physics* **11**, 093,022 (2009).
- [300] A. M. Rey *et al.*, Manuscript in preparation (2013).
- [301] A. Polkovnikov, “Phase space representation of quantum dynamics,” *Annals of Physics* **325**(8), 1790–1852 (2010).
- [302] S. Diehl, W. Yi, A. J. Daley, and P. Zoller, “Dissipation-Induced d-Wave Pairing of Fermionic Atoms in an Optical Lattice,” *Physical Review Letters* **105**(22), 227,001 (2010).
- [303] J. T. Barreiro *et al.*, “An open-system quantum simulator with trapped ions,” *Nature* **470**(7335), 486–491 (2011).
- [304] A. J. Daley, J. M. Taylor, S. Diehl, M. Baranov, and P. Zoller, “Atomic three-body loss as a dynamical three-body interaction,” *Physical Review Letters* **102**, 040,402 (2009).
- [305] A. V. Gorshkov *et al.*, “Tunable superfluidity and quantum magnetism with ultracold polar molecules,” *Physical Review Letters* **107**, 115,301 (2011).
- [306] K. R. A. Hazzard, S. R. Manmana, M. Foss-Feig, and A. M. Rey, “Far from equilibrium quantum magnetism with ultracold polar molecules,” arXiv:1209.4076v1 (2012).
- [307] E. L. Hahn, “Spin Echoes,” *Physical Review* **77**(4), 746–746 (1950).
- [308] L. Viola and S. Lloyd, “Dynamical suppression of decoherence in two-state quantum systems,” *Physical Review A* **58**(4), 2733–2744 (1998).
- [309] L. Viola, E. Knill, and S. Lloyd, “Dynamical Decoupling of Open Quantum Systems,” *Physical Review Letters* **82**(12), 2417–2421 (1999).
- [310] G. S. Uhrig, “Exact results on dynamical decoupling by pulses in quantum information processes,” *New Journal of Physics* **10**(8), 083,024 (2008).
- [311] M. J. Biercuk, H. Uys, A. P. VanDevender, N. Shiga, W. M. Itano, and J. J. Bollinger, “Optimized dynamical decoupling in a model quantum memory,” *Nature* **458**(7241), 996–1000 (2009).
- [312] H. Uys, M. Biercuk, and J. Bollinger, “Optimized Noise Filtration through Dynamical Decoupling,” *Physical Review Letters* **103**(4), 040,501 (2009).
- [313] G. De Lange, Z. H. Wang, D. Riste, V. V. Dobrovitski, and R. Hanson, “Universal Dynamical Decoupling of a Single Solid-State Spin from a Spin Bath,” *Science* **330**, 60–63 (2010).
- [314] J. R. Maze *et al.*, “Nanoscale magnetic sensing with an individual electronic spin in diamond,” *Nature* **455**(7213), 644–647 (2008).

- [315] G. Balasubramanian *et al.*, “Ultralong spin coherence time in isotopically engineered diamond,” *Nature Materials* **8**(5), 383–387 (2009).
- [316] S. Kotler, N. Akerman, Y. Glickman, A. Keselman, and R. Ozeri, “Single-ion quantum lock-in amplifier,” *Nature* **473**, 61–65 (2011).
- [317] F. Riehle, *Frequency standards* (Wiley-Vch, 2006).
- [318] M. Bishof, X. Zhang, M. J. Martin, and J. Ye, “An optical spectrum analyzer with quantum limited noise floor,” arXiv:1303.6741v1 (2013).
- [319] M. Takamoto, F.-L. Hong, R. Higashi, and H. Katori, “An optical lattice clock,” *Nature* **435**(7040), 321–324 (2005).
- [320] P. Gill, “When should we change the definition of the second?” *Philosophical Transactions of the Royal Society A: Mathematical, Physical and Engineering Sciences* **369**(1953), 4109–4130 (2011).
- [321] V. I. Yudin *et al.*, “Atomic Clocks with Suppressed Blackbody Radiation Shift,” *Physical Review Letters* **107**(3), 030,801 (2011).
- [322] D. Meiser, J. Ye, and M. J. Holland, “Spin squeezing in optical lattice clocks via lattice-based QND measurements,” *New Journal of Physics* **10**(7), 073,014 (2008).
- [323] D. Chang, J. Ye, and M. Lukin, “Controlling dipole-dipole frequency shifts in a lattice-based optical atomic clock,” *Physical Review A* **69**(2) (2004).
- [324] F. Gerbier and J. Dalibard, “Gauge fields for ultracold atoms in optical superlattices,” *New Journal of Physics* **12**, 033,007 (2010).
- [325] S. Kato, S. Sugawa, K. Shibata, R. Yamamoto, and Y. Takahashi, “Resonant Control of Interaction Between Different Electronic States,” arXiv:1210.2483v3 (2012).
- [326] S. Stellmer, M. K. Tey, B. Huang, and R. Grimm, “Bose-Einstein condensation of strontium,” *Physical Review Letters* **103**(20), 200,401 (2009).
- [327] S. Taie, R. Yamazaki, S. Sugawa, and Y. Takahashi, “An SU(6) Mott insulator of an atomic Fermi gas realized by large-spin Pomeranchuk cooling,” *Nature Physics* **8**, 825–830 (2012).
- [328] I. Reichenbach and I. Deutsch, “Sideband Cooling while Preserving Coherences in the Nuclear Spin State in Group-II-like Atoms,” *Physical Review Letters* **99**(12), 123,001 (2007).
- [329] A. Daley, M. Boyd, J. Ye, and P. Zoller, “Quantum Computing with Alkaline-Earth-Metal Atoms,” *Physical Review Letters* **101**(17) (2008).
- [330] A. Gorshkov *et al.*, “Alkaline-Earth-Metal Atoms as Few-Qubit Quantum Registers,” *Physical Review Letters* **102**(11) (2009).
- [331] D. Meiser and M. J. Holland, “Steady-state superradiance with alkaline-earth-metal atoms,” *Physical Review A* **81**(3), 033,847 (2010).
- [332] M. O. Scully and M. S. Zubairy, *Quantum optics* (Cambridge University Press, 1997).
- [333] J. Geremia, J. Stockton, and H. Mabuchi, “Tensor polarizability and dispersive quantum measurement of multilevel atoms,” *Physical Review A* **73**(4), 042,112 (2006).

Appendix A

Coherent atom-light interactions

In this Appendix, we derive a time-evolution operator approach for finding the time evolution of coherent spectroscopy. We then apply the formalism to derive the lineshapes and Dick sensitivity functions used throughout this Thesis.

A.1 Derivation of the Hamiltonian

We consider a laser with electric field

$$\mathbf{E}(\mathbf{r}, t) = \frac{1}{2} \mathbf{E}_0(\mathbf{r}) e^{-i\phi_L(t)} + \frac{1}{2} \mathbf{E}_0^*(\mathbf{r}) e^{i\phi_L(t)}. \quad (\text{A.1})$$

The Hamiltonian in the dipole approximation is given by [332]

$$\hat{H}(t) = \hbar\omega_a |e\rangle\langle e| + (\mathbf{d}_{ge} |g\rangle\langle e| + \mathbf{d}_{ge}^* |e\rangle\langle g|) \cdot \mathbf{E}(\mathbf{r}, t), \quad (\text{A.2})$$

where \mathbf{d}_{ge} is the dipole between the ground and excited states being considered. Next we write down $|\psi(t)\rangle$ as

$$|\psi(t)\rangle = c_1(t) |g\rangle + e^{-i\phi_L(t)} c_2(t) |e\rangle. \quad (\text{A.3})$$

This represents a change of basis to the frame co-rotating with an angle equivalent to the laser phase. Writing down Schrödinger's equation yields

$$i\hbar \frac{d}{dt} |\psi(t)\rangle = \hat{H}(t) |\psi(t)\rangle \quad (\text{A.4})$$

$$\begin{aligned} &= \hbar\omega_a c_2(t) e^{-i\phi_L(t)} |e\rangle + \mathbf{d}_{ge} \cdot \mathbf{E}(\mathbf{r}, t) e^{-i\phi_L(t)} c_2(t) |g\rangle \\ &\quad + \mathbf{d}_{ge}^* \cdot \mathbf{E}(\mathbf{r}, t) c_1(t) |e\rangle \end{aligned} \quad (\text{A.5})$$

We now project onto $\langle e|$ and $\langle g|$

$$\langle g|i\hbar\frac{d}{dt}|\psi(t)\rangle = i\hbar\dot{c}_1(t) = \mathbf{d}_{ge} \cdot \mathbf{E}(\mathbf{r}, t) e^{-i\phi_L(t)} c_2(t) \quad (\text{A.6})$$

Similarly

$$\langle e|i\hbar\frac{d}{dt}|\psi(t)\rangle = i\hbar[\dot{c}_2(t) - i\omega_L(t)c_2(t)] e^{-i\phi_L(t)} \quad (\text{A.7})$$

$$= \mathbf{d}_{ge}^* \cdot \mathbf{E}(\mathbf{r}, t) c_1(t) + \hbar\omega_a c_2(t) e^{-i\phi_L(t)} \quad (\text{A.8})$$

Here, $\omega_L(t) \equiv \frac{d}{dt}\phi_L(t)$. This results in

$$i\hbar\dot{c}_1(t) = \mathbf{d}_{ge} \cdot \left[\frac{1}{2}\mathbf{E}_0(\mathbf{r}) e^{-i2\phi_L(t)} + \frac{1}{2}\mathbf{E}_0^*(\mathbf{r}) \right] c_2(t) \quad (\text{A.9})$$

We now make the rotating wave approximation. The phase factor $e^{-i2\phi_L(t)}$ is rapidly varying (it is the laser's total phase) so we drop this term. This leaves

$$i\hbar\dot{c}_1(t) = \frac{1}{2}\mathbf{d}_{ge} \cdot \mathbf{E}_0^*(\mathbf{r}) c_2(t) = \frac{1}{2}\hbar\Omega^*(\mathbf{r}) c_2(t), \quad (\text{A.10})$$

where we define the Rabi frequency as

$$\Omega(\mathbf{r}) = \mathbf{d}_{ge}^* \cdot \mathbf{E}_0(\mathbf{r}) / \hbar = e^{-i\phi} |\mathbf{d}_{ge}^* \cdot \mathbf{E}_0(\mathbf{r})| / \hbar \quad (\text{A.11})$$

Similarly, we find

$$i\hbar\dot{c}_2(t) = \frac{1}{2}\hbar\Omega(\mathbf{r}) c_1(t) - \hbar\Delta(t) c_2(t) \quad (\text{A.12})$$

where $\Delta(t) = \omega_L(t) - \omega_a$ so that we can write

$$i\hbar\frac{d}{dt} \begin{pmatrix} c_2(t) \\ c_1(t) \end{pmatrix} = \begin{pmatrix} -\Delta(t) & \frac{1}{2}\Omega(\mathbf{r}) \\ \frac{1}{2}\hbar\Omega^*(\mathbf{r}) & 0 \end{pmatrix} \times \begin{pmatrix} c_1(t) \\ c_2(t) \end{pmatrix} \quad (\text{A.13})$$

Since we don't care about global phase factors, we are free to add and subtract constants from the diagonal. The time evolution finally becomes

$$i\hbar\frac{d}{dt} \begin{pmatrix} c_2(t) \\ c_1(t) \end{pmatrix} = \frac{1}{2}\hbar \begin{pmatrix} -\Delta(t) & e^{-i\phi} |\Omega(\mathbf{r})| \\ e^{i\phi} |\Omega(\mathbf{r})| & \Delta(t) \end{pmatrix} \times \begin{pmatrix} c_2(t) \\ c_1(t) \end{pmatrix} \quad (\text{A.14})$$

For a real rabi frequency

$$i\hbar\frac{d}{dt} \vec{c} = \underbrace{\left[\frac{1}{2}\hbar\Omega(\mathbf{r}) \hat{\sigma}_\phi - \frac{1}{2}\hbar\Delta(t) \hat{\sigma}_z \right]}_{\text{Effective Hamiltonian}} \vec{c} \quad (\text{A.15})$$

where $\hat{\sigma}_i$ is a Pauli matrix with $i \in \{x, y, z\}$ and $\hat{\sigma}_\phi = \cos \phi \hat{\sigma}_x + \sin \phi \hat{\sigma}_y$.

A.2 Time evolution operator for lineshape calculation

We begin with the effective Hamiltonian of Eq. A.15 in the limit of constant detuning and Rabi frequency,

$$\hat{H} = \frac{1}{2}\hbar\Omega_0\hat{\sigma}_\phi - \frac{1}{2}\hbar\Delta_0\hat{\sigma}_z. \quad (\text{A.16})$$

We can make use of the formal solution for the time evolution operator for independent Hamiltonians, such that

$$\hat{U}(t; t_0) = \exp\left[\frac{-i\hat{H}}{\hbar}t\right] = \exp\left[-i\frac{\Omega}{2}\vec{n} \cdot \vec{\sigma}t\right]. \quad (\text{A.17})$$

Here, $\Omega = \sqrt{\Omega_0^2 + \Delta^2}$ and $\vec{n} = \{\Omega_0 \cos(\phi), \Omega_0 \sin(\phi), -\Delta_0\}$. The reader may recognize this operation as an SU(2) rotation about the vector \vec{n} . We can use the properties of the Pauli matrices to simplify Eq. A.17

$$\hat{U}(t; t_0) = \cos\left(\frac{\Omega}{2}t\right)\hat{I} - i\frac{\Omega_0}{\Omega}\sin\left(\frac{\Omega}{2}t\right)(\cos\phi\hat{\sigma}_x + \sin\phi\hat{\sigma}_y) + i\frac{\Delta}{\Omega}\sin\left(\frac{\Omega}{2}t\right)\hat{\sigma}_z. \quad (\text{A.18})$$

The usefulness Eq. A.18 comes from the simplicity with which it allows calculations of the time evolution during spectroscopy sequences.

A.2.1 Rabi lineshape

We now focus on the specific case of spectroscopy. In order to calculate the excited state population, in general we will calculate

$$p_e(t) = |\langle e|\psi(t)\rangle|^2 = \left|\langle e|\hat{U}(t; t_0)|\psi(t_0)\rangle\right|^2. \quad (\text{A.19})$$

We can choose the initial phase such that $\phi \rightarrow 0$, which simplifies the time evolution operator of Eq. A.18. Writing Eq. A.19 in vector representation with $|\psi(t_0)\rangle = |g\rangle$ yields

$$\langle e|\psi(t)\rangle = \begin{pmatrix} 1 & 0 \end{pmatrix} \cdot \hat{U}(t; t_0) \begin{pmatrix} 0 \\ 1 \end{pmatrix} = -i\frac{\Omega_0}{\Omega}\sin\left(t\frac{\Omega}{2}\right). \quad (\text{A.20})$$

Thus,

$$p_e(t; \Delta_0) = \frac{\Omega_0^2}{\Omega^2}\sin^2\left(t\frac{\Omega}{2}\right), \quad (\text{A.21})$$

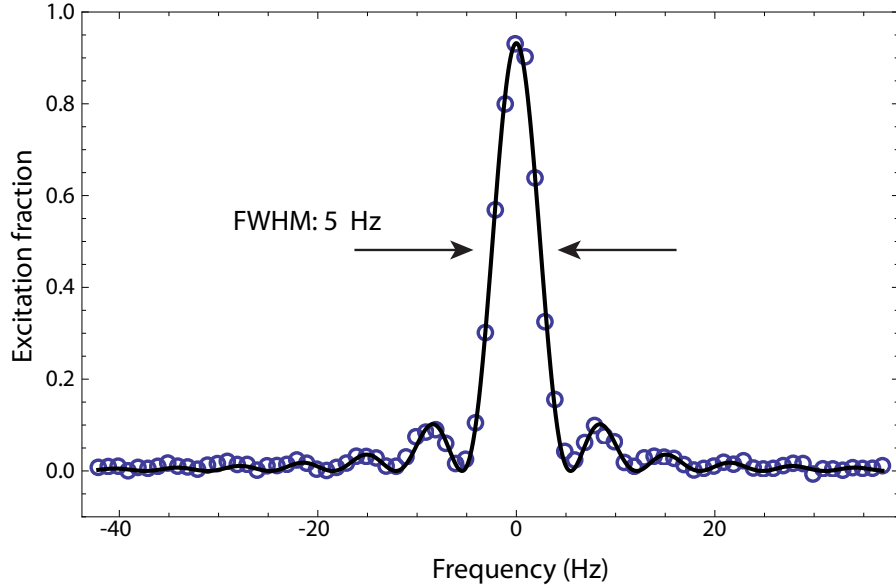


Figure A.1: Rabi spectroscopy lineshape for a π -pulse time of 160 ms (line) fit to experimental data (circles). An overall scaling factor has been applied to account for effects that reduce the peak excitation probability.

where we recall that $\Omega = \sqrt{\Omega_0^2 + \Delta_0^2}$. This is the Rabi result. For the normal spectroscopic sequence used for clock operation, $t = \pi/\Omega_0$ —the π -pulse condition—which yields unity excitation when $\Delta_0 = 0$ and is given by

$$p_e(\Delta_0) = \frac{\Omega_0^2}{\Omega^2} \sin^2\left(\frac{\pi\Omega}{2\Omega_0}\right). \quad (\text{A.22})$$

An example of this function applied to real data is shown in Fig. A.1. An overall scaling factor is applied to account for non-unity excitation due to two-body inelastic losses and slight excitation inhomogeneity.

A.2.2 Ramsey lineshape

In this section, we again use the time evolution operator approach to calculate the lineshape for Ramsey spectroscopy. Unlike Rabi spectroscopy, for Ramsey spectroscopy there are three distinct periods of evolution:

- (1) Initial $\pi/2$ pulse, where Eq. A.18 applies (again we are free to choose $\phi \rightarrow 0$).

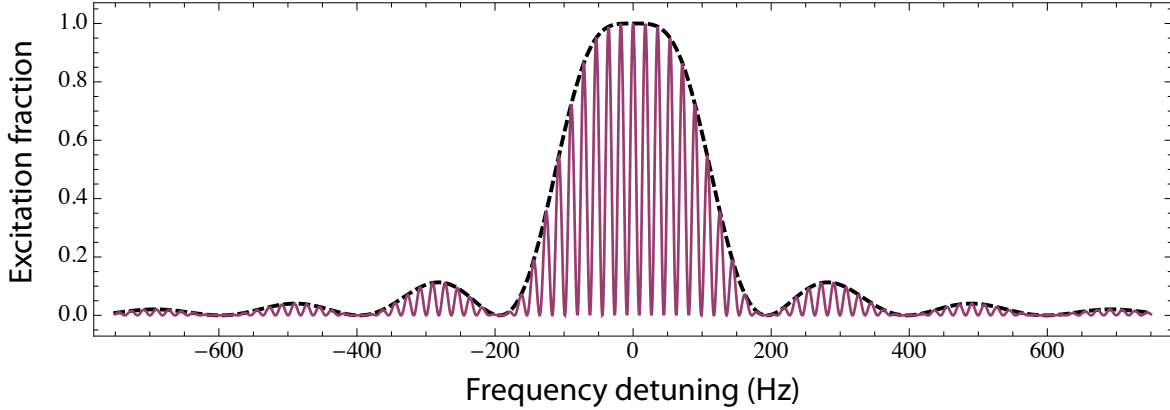


Figure A.2: Ramsey spectroscopy lineshape. The dashed black line shows the envelope of the rapidly-oscillating excitation. The envelope is similar, but not identical, to the Rabi lineshape. Here, the π -pulse time is 10 ms, and the free evolution time, τ is 50 ms; this results in a total spectroscopy time of 60 ms.

- (2) Free evolution time, where the dynamics are described by Eq. A.18 with $\Omega_0 \rightarrow 0$ (and thus $\Omega \rightarrow \Delta_0$). We label the free evolution time τ .
- (3) Final $\pi/2$ pulse. The time evolution operator is the same as in case (1).

Mathematically, we can write this as

$$p_e(t; \Delta_0) = \left| \langle e | \hat{U}_3(t; t_2) \hat{U}_2(t_2; t_1) \hat{U}_1(t_1; t_0) | \psi(t_0) \rangle \right|^2, \quad (\text{A.23})$$

where the subscript indicates case 1–3 listed above. Here, the free evolution time τ is given by $\tau = t_2 - t_1$. We perform the matrix multiplication for the case where the first and last pulses are exactly $\pi/2$ pulses (i.e., $t_1 - t_0 = \pi/(2\Omega_0) = t - t_2$) and find

$$p_e(\Delta_0) = \frac{\Omega_0^2}{\Omega^4} \left[\Omega \cos\left(\frac{\Delta_0 \tau}{2}\right) \sin\left(\frac{\pi \Omega}{2\Omega_0}\right) - 2\Delta \sin\left(\frac{\Delta_0 \tau}{2}\right) \sin^2\left(\frac{\pi \Omega}{4\Omega_0}\right) \right]^2. \quad (\text{A.24})$$

This function is plotted in Fig. A.2 for a π -pulse time of 10 ms and $\tau = 50$ ms. If desired, the envelope (i.e., the outline of the oscillatory part) can be found by summing in quadrature the prefactors of the $\cos\left(\frac{\Delta_0 \tau}{2}\right)$ and $\sin\left(\frac{\Delta_0 \tau}{2}\right)$ terms.

A.2.3 Dick sensitivity function for Rabi spectroscopy

In Chapter 2, we discussed the Dick effect for optical frequency standards. The key element for calculating the Dick effect is the sensitivity function for a given spectroscopic sequence. The sensitivity function relates a given phase error at a specific time to a fluctuation in the final population by [36]

$$\delta p_e = \frac{1}{2} \int_0^{T_0} dt \Delta\omega(t) r(t; \Delta_0), \quad (\text{A.25})$$

where $\Delta\omega(t)$ describes fluctuations in the laser's frequency about the nominal static detuning Δ_0 . Thus, we can calculate the sensitivity function as a response to an infinitesimal phase perturbation, $\delta\phi$ at time t such that [36]

$$r(t) = 2 \frac{\partial \delta p_e}{\partial \delta \phi_t} \quad (\text{A.26})$$

In order to proceed, we split the time evolution into two steps:

- (1) Non-perturbed evolution. We use the time evolution operator of Eq. A.18 with $\phi \rightarrow 0$.
- (2) The phase perturbation occurs at time t_1 . We use the time evolution operator of Eq. A.18 with $\phi \rightarrow \delta\phi$.

This can be written as

$$|\psi(t)\rangle = \hat{U}_{\delta\phi}(t; t_1) \hat{U}_0(t_1; t_0) |\psi(t_0)\rangle. \quad (\text{A.27})$$

Here, the subscript indicates the phase, ϕ of the atom-light interaction. If we carry out the operator multiplication for an infinitesimal phase step we find

$$|\psi(t)\rangle = \left\{ \hat{U}_0(t; t_0) - i\delta\phi \frac{\Omega_0}{\Omega} \sin\left[\frac{\Omega}{2}(t - t_1)\right] \hat{\sigma}_y \times \hat{U}_0(t_1; t_0) \right\} |\psi(t_0)\rangle \quad (\text{A.28})$$

$$= |\psi_0(t)\rangle + \delta\phi |\delta\psi(t; t_1)\rangle, \quad (\text{A.29})$$

where $|\psi_0(t)\rangle = \hat{U}_0(t; t_0) |\psi(t_0)\rangle$, the unperturbed time evolution of wave function. We can then find $\delta p_e(t_1)$ as

$$\delta p_e(t_1) = |\langle e|\psi(t)\rangle|^2 - |\langle e|\psi_0(t)\rangle|^2 \quad (\text{A.30})$$

$$= 2\delta\phi \Re \{ \langle e|\psi_0(t)\rangle \langle \delta\psi(t; t_1)|e\rangle \} + \mathcal{O}(\delta\phi^2) \quad (\text{A.31})$$

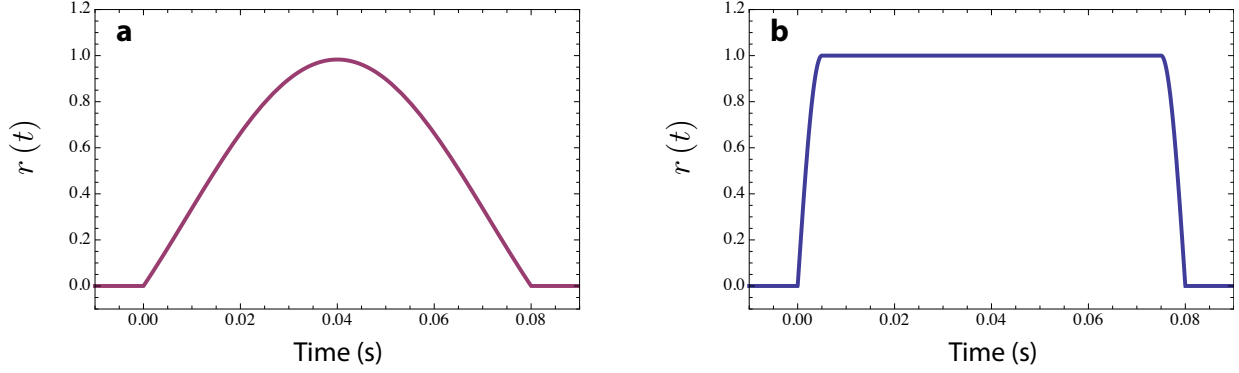


Figure A.3: Rabi Ramsey sensitivity functions. In both cases, the detuning Δ_0 is negative and chosen such that $p_e = 0.5$. **(a)** Sensitivity function for Rabi spectroscopy for an 80 ms spectroscopy time. **(b)** Sensitivity function for Ramsey spectroscopy for an 80 ms spectroscopy sequence with a 10 ms π -pulse time and 70 ms free-evolution time τ .

For the usual case of a π -pulse excitation, we find

$$r(t_1) = 4\Re\{\langle e|\psi_0(t_\pi)\rangle\langle\delta\psi(t_\pi; t_1)|e\rangle\} \quad (\text{A.32})$$

where $t_\pi = \pi/\Omega_0$. When we carry out the operator multiplication we find that

$$r(t) = \frac{\Delta\Omega_0^2}{\Omega^3} \left\{ \sin\left(\frac{\pi\Omega}{\Omega_0}\right) - \sin(\Omega t) - \sin\left[\Omega\left(\frac{\pi}{\Omega_0} - t\right)\right] \right\}. \quad (\text{A.33})$$

A.2.4 Dick sensitivity function for Ramsey spectroscopy

In Chapter 6 we derived the perturbation of the Bloch vector angle Θ due to laser noise. For Ramsey spectroscopy, $\delta p_e \simeq \delta\Theta/2$ for small fluctuations $\delta\Theta$. Thus, the sensitivity function we derived in Chapter 6 is exactly the Dick sensitivity function. We thus find, in the limit where $\Delta_0 \ll 1/\tau$,

$$r(t) = \sin[\theta(t)]. \quad (\text{A.34})$$

Here, as in Chapter 6, $\theta(t)$ is the total pulse area applied to the atoms. The Fourier-domain sensitivity $|R(f)|^2$ is given by Eq. 6.57 with $n = 0$. In the limit that $\Omega_0 \rightarrow \infty$, we recover the Ramsey sensitivity function of Eq. 2.66. We note that in general, the effect of longer $\pi/2$ pulses in Ramsey spectroscopy is to provide an additional pole of low-pass filtration at the Rabi frequency

corresponding to the $\pi/2$ -pulse duration. The time-domain for both Rabi and Ramsey (finite π -pulse case) are shown in Fig. A.3

Appendix B

Calculating the dipole moments from measured atomic lifetimes

In this Appendix, we summarize the method for relating transition dipole moments to experimentally measured lifetimes. The dipole moments are necessary for computing the AC polarizability and the scattering rate, as calculated in Chapter 2.

We begin with the Wigner-Eckert theorem applied to the dipole operator. Simply stated, the theorem relates a dipole moment ($\hat{\mathbf{d}} \equiv e\hat{\mathbf{r}}$) to a scalar quantity modified by a Clebsch-Gordan coefficient. This can be stated mathematically as [111, 108]

$$\langle n, J, m_J | e\hat{r}_q | n', J', m'_J \rangle = \langle nJ || e\hat{\mathbf{r}} || n'J' \rangle (-1)^{J'-1-m_J} \sqrt{2J+1} \begin{pmatrix} 1 & J' & J \\ q & m'_J & -m_J \end{pmatrix}. \quad (\text{B.1})$$

Here, the quantum number n indicates an electronic configuration, J is the total angular momentum, and m_J is the angular momentum projection onto the quantization axis. The term in parenthesis is the Wigner 3- j symbol. This expression is only useful when the reduced matrix element $\langle nJ || e\hat{\mathbf{r}} || n'J' \rangle$ is known. Luckily, it is related to the rate, $\Gamma_{J'J}$, at which an excited fine structure manifold decays to a lower fine structure manifold ($n'J' \rightarrow nJ$) by [108]

$$\Gamma_{n'J' \rightarrow nJ} = \frac{\omega_{n'J' \rightarrow nJ}^3}{3\pi\epsilon_0\hbar c^3} \frac{2J+1}{2J'+1} |\langle nJ || e\hat{\mathbf{r}} || n'J' \rangle|^2, \quad (\text{B.2})$$

where $\omega_{n'J' \rightarrow nJ}$ is the transition angular frequency. However, even this expression is not so useful. The most commonly reported quantities in the literature are the lifetimes (or “total” Einstein A-coefficients given by $A_T(n', J') = 1/\tau$, where τ is the lifetime) of an upper fine structure state with electronic configuration labelled by n' and angular momentum J' decaying to multiple fine structure states below.

In order to attack this problem, there is another fact we need to know. The reduced dipole matrix element $\langle nJ||e\hat{\mathbf{r}}||n'J'\rangle$ for a given J state in an L manifold is related to the L reduced matrix element, $\langle nL||e\hat{\mathbf{r}}||n'L'\rangle$, by [111, 108]

$$\langle nJ||e\hat{\mathbf{r}}||n'J'\rangle = \langle nL||e\hat{\mathbf{r}}||n'L'\rangle \sqrt{(2J'+1)(2L+1)} (-1)^{J'+L+1+S} \left\{ \begin{matrix} L & L' & 1 \\ J' & J & S \end{matrix} \right\}, \quad (\text{B.3})$$

where the term in the curly braces is the Wigner 6- j symbol. Now we're ready to use the published A_T values to actually get somewhere. Using Eqns. B.2 and B.3, we can relate A_T to a sum over all the ground fine structure states by

$$\begin{aligned} A_T(n', J') &= \sum_J \Gamma_{n'J' \rightarrow nJ} \\ &= \frac{|\langle nL||e\hat{\mathbf{r}}||n'L'\rangle|^2}{3\pi\epsilon_0\hbar c^3} \left(\frac{2L+1}{2L'+1} \right) \sum_J \omega_{n'J' \rightarrow nJ}^3 (2J+1) (2L'+1) \left\{ \begin{matrix} L & L' & 1 \\ J' & J & S \end{matrix} \right\}^2. \end{aligned} \quad (\text{B.4})$$

One important fact about Eq. B.4 is that if we ignore the J dependence of $\omega_{J'J}$, we can use the fact that

$$\sum_J (2J+1) (2L'+1) \left\{ \begin{matrix} L & L' & 1 \\ J' & J & S \end{matrix} \right\}^2 = 1 \quad (\text{B.5})$$

to recover an expression identical to Eq. B.2, only this time for a decay $L' \rightarrow L$. However, we choose not to make this assumption, and instead treat the sum as a weighted average of $\omega_{J'J}^3$, such that

$$\tilde{\omega}_{n'J'}^3 \equiv \sum_J \omega_{n'J' \rightarrow nJ}^3 (2J+1) (2L'+1) \left\{ \begin{matrix} L & L' & 1 \\ J' & J & S \end{matrix} \right\}^2. \quad (\text{B.6})$$

This allows us to finally solve for $|\langle nL||e\hat{\mathbf{r}}||n'L'\rangle|^2$, namely

$$|\langle nL||e\hat{\mathbf{r}}||n'L'\rangle|^2 = A_T(n', J') \frac{3\pi\epsilon_0\hbar c^3}{\tilde{\omega}_{n'J'}^3} \left(\frac{2L'+1}{2L+1} \right). \quad (\text{B.7})$$

We note that it is also possible to write the branching ratio between different decay pathways as

$$\frac{\Gamma_{n'J' \rightarrow nJ}}{A_T(n', J')} = \frac{\omega_{n'J' \rightarrow nJ}^3}{\tilde{\omega}_{n'J'}^3} (2J+1) (2L'+1) \left\{ \begin{matrix} L & L' & 1 \\ J' & J & S \end{matrix} \right\}^2. \quad (\text{B.8})$$

The term $\zeta(nJ; n'J') \equiv \omega_{n'J' \rightarrow nJ}^3 / \tilde{\omega}_{n'J'}^3$ has sometimes been called the relativistic correction factor [112], because it corrects the effect of fine structure energy shifts on the dipole elements. For Sr, this term is at most a 10% correction.

With these results, we are finally able to compute the desired matrix element given by Eq. B.1.

The final result is

$$\begin{aligned} \langle n, J, m_j | e\hat{r}_q | n', J', m'_j \rangle &= \sqrt{\frac{3\pi\epsilon_0\hbar c^3 A_T}{\tilde{\omega}_{n'J'}^3}} \sqrt{(2J'+1)(2L'+1)(2J+1)} \times \\ &(-1)^{2J'+L+S-m_j} \times \begin{Bmatrix} L & L' & 1 \\ J' & J & S \end{Bmatrix} \begin{pmatrix} 1 & J' & J \\ q & m'_j & -m_j \end{pmatrix}. \end{aligned} \quad (\text{B.9})$$

For $\phi_i \in \{^3P_0, ^1S_0\}$, the expression for the dipole is particularly simple. It is given by

$$\sum_q |\langle \phi_i | \varepsilon_q d_q | n', 1, -q \rangle|^2 = \frac{3\pi\epsilon_0\hbar c^3 A_T(n', J')}{\tilde{\omega}_{n'J'}^3} (2L'+1) \times \begin{Bmatrix} L & L' & 1 \\ J' & 0 & S \end{Bmatrix}^2, \quad (\text{B.10})$$

where the one remaining complication is the dependence on the relativistic correction factor in $\tilde{\omega}_{n'J'}$. This simplifies for 3P_0 to

$$\sum_q \left| \langle ^3P_0 | \varepsilon_q \hat{d}_q | n', 1, -q \rangle \right|^2 = \frac{3\pi\epsilon_0\hbar c^3 A_T(n', J') (2L'+1)}{\tilde{\omega}_{n'J'}^3} \frac{1}{9}. \quad (\text{B.11})$$

where the polarization can be arbitrary and the result still holds.

An even simpler expression is obtained for 1S_0 , and it is important to note that there is no relativistic correction factor here due to the absence of fine structure in the 1S manifold. In this case, the dipole depends directly on the lifetime and transition frequency as

$$\sum_q \left| \langle ^1S_0 | \varepsilon_q \hat{d}_q | n', 1, -q \rangle \right|^2 = \frac{3\pi\epsilon_0\hbar c^3 A_T(n', J')}{\omega_{n'J'}^3}, \quad (\text{B.12})$$

For both 1S_0 and 3P_0 , as is expected, there is no ε_q dependence of the polarizability, which reflects the isotropic nature of the $J=0$ atomic states.

As discussed in Chapter 2, the hyperfine interaction breaks the symmetry and gives a m_F dependence to the polarizability. This effect is negligible due to the smallness of the hyperfine energy splittings of 3P_0 . Although this is one mechanism by which the clock states can acquire

a vector and tensor polarizability in ^{87}Sr , the hyperfine-induced state mixing between levels [119] with the same principle quantum number F is the biggest contributor to orientation-dependent light shifts [25, 112].

Appendix C

Spherical tensor treatment of the light shift

In this Appendix, we present a detailed derivation of the scalar, vector, and tensor light shifts. We follow the treatments of [108, 109]. It is my hope that the results of this section “take the mystery” out of calculating vector and tensor shifts and to better elucidate the physics of lattice trapping.

We begin our treatment with Eq. 2.12 of the main text (see, e.g., [109])

$$U(\mathbf{r}) = -E_{\mu}^{(-)} E_{\nu}^{(+)} \alpha_{\mu\nu} \quad (\text{C.1})$$

where

$$\alpha_{\mu\nu} = 2 \sum_k \frac{\omega_{ik} \langle \phi_i | \hat{d}_{\mu} | \phi_k \rangle \langle \phi_k | \hat{d}_{\nu} | \phi_i \rangle}{\hbar (\omega_{ik}^2 - \omega^2)}. \quad (\text{C.2})$$

The electric field is now expressed with slightly different parameters such that $\mathbf{E}^{(+)} \equiv \mathbf{E}_0(\mathbf{r})/2 = [\mathbf{E}^{(-)}]^*$. Next, we project the tensorial operator $\hat{d}_{\mu} \hat{d}_{\nu}$ onto states with quantum number n' and angular momenta F' , along with the state for which we wish to calculate the polarizability, labeled by its angular momentum F such that we define an operator [333]

$$\hat{\mathbf{A}}_{n'F'} = \sum_{m,m',m''} |nF m''\rangle \langle nF m'' | \hat{\mathbf{d}} | n'F' m' \rangle \langle n'F' m' | \hat{\mathbf{d}} | nF m \rangle \langle nF m | \quad (\text{C.3})$$

$$\equiv \hat{\mathbf{d}}_{n'F'} \hat{\mathbf{d}}_{nF}, \quad (\text{C.4})$$

where the $\hat{\mathbf{d}}_{n'F'}$ are the dipole operator projected between the ground¹ state and $n'f'$ manifold.

¹ By “ground” state we mean the state for which we intend to calculate the polarizability.

The polarizability projection between these same manifolds is then

$$\hat{\alpha}_{n'F'} = 2 \frac{\omega_{nF \rightarrow n'F'} \hat{\Lambda}_{n'F'}}{\hbar (\omega_{nF \rightarrow n'F'}^2 - \omega^2)}. \quad (\text{C.5})$$

and thus

$$U(\mathbf{r}) = -\mathbf{E}^{(-)} \cdot \underbrace{\sum_{n',F'} \langle nF, m | \hat{\alpha}_{n'F'} | nF, m \rangle}_{\alpha_{\mu\nu}} \cdot \mathbf{E}^{(+)}. \quad (\text{C.6})$$

Since the tensorial operator $\hat{\alpha}_{n'F'}^{(0)}$ is formed by a product of two vector operators, we can decompose it into irreducible components

$$\hat{\alpha}_{n'F'} = \hat{\alpha}_{n'F'}^{(0)} + \hat{\alpha}_{n'F'}^{(1)} + \hat{\alpha}_{n'F'}^{(2)}. \quad (\text{C.7})$$

The goal is to find the contributions of each of these terms to the dipole potential as written in Eq. C.6.

We begin by first finding the j th representations of the operator $\Lambda_{n'F'}$, as it directly relates to $\hat{\alpha}_{n'F'}$. We begin by expressing the product of the vector operators $\mathbf{d}_{n'F'}$ in terms of a spherical tensors [333]

$$\hat{\Lambda}_{n'F'} = \hat{\mathbf{d}}_{n'F'} \hat{\mathbf{d}}_{n'F'} = \sum_{qq'} \mathbf{e}_q^* \mathbf{e}_{q'}^* \hat{d}_q(n'F') \hat{d}_{q'}(n'F') \quad (\text{C.8})$$

$$= \sum_{j,m} \sum_{q,q'} \mathbf{e}_q^* \mathbf{e}_{q'}^* \hat{T}_m^{(j)} \langle 1, q; 1, q' | j, m \rangle. \quad (\text{C.9})$$

Here, \mathbf{e}_q are the spherical unit vectors and are related to Cartesian coordinates by $\mathbf{e}_{\pm 1} = \mp (\mathbf{e}_x \pm i\mathbf{e}_y)$ and $\mathbf{e}_0 = \mathbf{e}_z$ such that

$$\hat{\mathbf{d}}_{n'F'} = \sum_q \mathbf{e}_q^* \hat{d}_q(n'F'), \quad \hat{d}_q(n'F') = \mathbf{e}_q \cdot \hat{\mathbf{d}}_{n'F'}, \quad (\text{C.10})$$

and

$$\hat{T}_m^{(j)} = \sum_{q,q'} \hat{d}_q(n'F') \hat{d}_{q'}(n'F') \langle 1, q; 1, q' | j, m \rangle. \quad (\text{C.11})$$

Thus, we find the j th irreducible component of $\Lambda_{n'F'}$ is [333]

$$\Lambda_{n'F'}^{(j)} = \sum_{q,q'} \mathbf{e}_q^* \mathbf{e}_{q'}^* T_m^{(j)} \langle 1, q; 1, q' | j, m \rangle. \quad (\text{C.12})$$

Since the irreducible components of $\alpha_{nF'}$ connect states with equal m , we can restrict ourselves to consideration of only the $m = 0$ components of the spherical tensor. Thus

$$\alpha_{n',F'}^{(j)} \equiv \langle nF, m | \hat{\alpha}_{n',F'}^{(j)} | nF, m \rangle = \underbrace{\langle nF || \hat{\alpha}_{n',F'}^{(j)} || nF \rangle}_{\alpha_{n',F'}^{(j)}(m)} \langle F, m | F, m; j, 0 \rangle \sum_{q,q'} \mathbf{e}_q^* \mathbf{e}_{q'} \langle 1, q; 1, q' | j, 0 \rangle. \quad (\text{C.13})$$

It can be shown that for the j th irreducible component of the projected operator, $\Lambda_{nF'}^{(j)}$, the reduced matrix element is given by [111, 108]

$$\langle nF || \hat{\Lambda}_{n',F'}^{(j)} || nF \rangle = (-1)^{j+F+F'} \sqrt{(2F+1)(2j+1)} \begin{Bmatrix} 1 & 1 & j \\ F & F & F' \end{Bmatrix} \left| \langle nF || \hat{\mathbf{d}} || n'F' \rangle \right|^2, \quad (\text{C.14})$$

which we can use to compute $\alpha_{n',F'}^{(j)}(m)$ as

$$\alpha_{n',F'}^{(j)}(m) = 2 \frac{\omega_{n'F'} \langle nF || \hat{\Lambda}_{n',F'}^{(j)} || nF \rangle}{\hbar (\omega_{nF \rightarrow n'F'}^2 - \omega^2)} \times \langle F, m | F, m; j, 0 \rangle. \quad (\text{C.15})$$

From Eqns. C.13 and C.15, we can solve for the contributions of the irreducible components of the polarizability tensor as

$$\begin{aligned} \mathbf{E}^{(-)} \cdot \alpha_{n',F'}^{(0)} \cdot \mathbf{E}^{(+)} &= \alpha_{n',F'}^{(0)}(m) \frac{1}{\sqrt{3}} \mathbf{E}^{(-)} \cdot (\mathbf{e}_{-1}^* \mathbf{e}_1^* - \mathbf{e}_0^* \mathbf{e}_0^* + \mathbf{e}_1^* \mathbf{e}_{-1}^*) \cdot \mathbf{E}^{(+)} \\ &= -\alpha_{n',F'}^{(0)}(m) \frac{|\mathbf{E}^{(+)}|^2}{\sqrt{3}} \end{aligned} \quad (\text{C.16})$$

$$\begin{aligned} \mathbf{E}^{(-)} \cdot \alpha_{n',F'}^{(1)} \cdot \mathbf{E}^{(+)} &= \alpha_{n',F'}^{(1)}(m) \frac{1}{\sqrt{2}} \mathbf{E}^{(-)} \cdot (-\mathbf{e}_{-1}^* \mathbf{e}_1^* + \mathbf{e}_1^* \mathbf{e}_{-1}^*) \cdot \mathbf{E}^{(+)} \\ &= \frac{i\alpha_{n',F'}^{(1)}(m)}{\sqrt{2}} \left(\mathbf{E}^{(+)} \times \mathbf{E}^{(-)} \right) \cdot \mathbf{e}_z \end{aligned} \quad (\text{C.17})$$

$$\begin{aligned} \mathbf{E}^{(-)} \cdot \alpha_{n',F'}^{(2)} \cdot \mathbf{E}^{(+)} &= \alpha_{n',F'}^{(2)}(m) \frac{1}{\sqrt{6}} \mathbf{E}^{(-)} \cdot (\mathbf{e}_{-1}^* \mathbf{e}_1^* + 2\mathbf{e}_0^* \mathbf{e}_0^* + \mathbf{e}_1^* \mathbf{e}_{-1}^*) \cdot \mathbf{E}^{(+)} \\ &= \frac{\alpha_{n',F'}^{(2)}(m)}{\sqrt{6}} \left(3 \left| \mathbf{E}^{(+)} \cdot \mathbf{e}_z \right|^2 - \left| \mathbf{E}^{(+)} \right|^2 \right). \end{aligned} \quad (\text{C.18})$$

The dependence on the light polarization comes directly from the sum over Clebsch-Gordan coef-

ficients in Eq. C.13. We also find

$$\alpha_{n'F'}^{(0)}(m) = \frac{2\omega_{n'F'}}{\hbar(\omega_{n'F'}^2 - \omega^2)} \frac{-1}{\sqrt{3}} \left| \langle nF || \hat{\mathbf{d}} || n'F' \rangle \right|^2, \quad (\text{C.19})$$

$$\alpha_{n'F'}^{(1)}(m) = \frac{2\omega_{n'F'}}{\hbar(\omega_{n'F'}^2 - \omega^2)} (-1)^{F+F'+1} \sqrt{\frac{3(2F+1)}{F(F+1)}} \times m \begin{Bmatrix} 1 & 1 & 1 \\ F & F & F' \end{Bmatrix} \left| \langle nF || \hat{\mathbf{d}} || n'F' \rangle \right|^2, \quad (\text{C.20})$$

$$\begin{aligned} \alpha_{n'F'}^{(2)}(m) &= \frac{2\omega_{n'F'}}{\hbar(\omega_{n'F'}^2 - \omega^2)} (-1)^{F+F'} \sqrt{\frac{5(2F+1)}{F(1+F)(2F-1)(3+2F)}} \\ &\quad \times [3m^2 - F(F+1)] \begin{Bmatrix} 1 & 1 & 2 \\ F & F & F' \end{Bmatrix} \left| \langle nF || \hat{\mathbf{d}} || n'F' \rangle \right|^2. \end{aligned} \quad (\text{C.21})$$

Now all that is left is to perform the sum as in Eq. C.6. The result is

$$\alpha(\boldsymbol{\varepsilon}) = \alpha_s + i\alpha_v(\boldsymbol{\varepsilon} \times \boldsymbol{\varepsilon}^*) \cdot \mathbf{e}_z \frac{m}{F} + \alpha_t \frac{(3|\boldsymbol{\varepsilon} \cdot \mathbf{e}_z|^2 - 1)}{2} \left[\frac{3m^2 - F(F+1)}{F(2F-1)} \right]. \quad (\text{C.22})$$

Here, $\boldsymbol{\varepsilon}$ is the light polarization and we have introduced α_s , α_v , and α_t , the ‘‘scalar’’, ‘‘vector’’, and ‘‘tensor’’ polarizabilities, respectively. The normalizations of the vector and tensor shifts are chosen such that the coefficients are maximally unity for both α_v and α_t (e.g., the case of circular polarization and $m = F$ in the tensor case). We find the polarizabilities are (as in [108])

$$\alpha_s = \sum_{n'F'} \frac{2\omega_{nF \rightarrow n'F'} \left| \langle nF || \hat{\mathbf{d}} || n'F' \rangle \right|^2}{3\hbar(\omega_{nF \rightarrow n'F'}^2 - \omega^2)}, \quad (\text{C.23})$$

$$\alpha_v = \sum_{n'F'} (-1)^{F+F'+1} \sqrt{\frac{6F(2F+1)}{(F+1)}} \begin{Bmatrix} 1 & 1 & 1 \\ F & F & F' \end{Bmatrix} \frac{\omega_{nF \rightarrow n'F'} \left| \langle nF || \hat{\mathbf{d}} || n'F' \rangle \right|^2}{\hbar(\omega_{nF \rightarrow n'F'}^2 - \omega^2)}, \quad (\text{C.24})$$

$$\alpha_t = \sum_{n'F'} (-1)^{F+F'} \sqrt{\frac{40F(2F-1)(2F+1)}{(1+F)(2F+3)}} \begin{Bmatrix} 1 & 1 & 2 \\ F & F & F' \end{Bmatrix} \frac{\omega_{nF \rightarrow n'F'} \left| \langle nF || \hat{\mathbf{d}} || n'F' \rangle \right|^2}{\hbar(\omega_{nF \rightarrow n'F'}^2 - \omega^2)}. \quad (\text{C.25})$$

We can relate the reduced matrix element $\langle nF || \hat{\mathbf{d}} || n'F' \rangle$ to $\langle nJ || \hat{\mathbf{d}} || n'J' \rangle$ by [111, 108, 109]

$$\langle nF || e\hat{\mathbf{r}} || n'F' \rangle = \langle nJ || \hat{\mathbf{d}} || n'J' \rangle \sqrt{(2F'+1)(2J+1)} (-1)^{F'+J+I+1} \begin{Bmatrix} J & J' & 1 \\ F' & F & I \end{Bmatrix}. \quad (\text{C.26})$$

The procedure for calculating the reduced matrix elements $\langle nJ || \hat{\mathbf{d}} || n'J' \rangle$ from the measured lifetimes is presented in Appendix B.

Appendix D

The s - and p -wave interaction overlap integrals

In this appendix we derive the mode-dependent overlap integrals that appear in the many-body Hamiltonian for s - and p -wave interactions as presented in Chapter 5.

We begin by inserting the potentials of Eqns. 5.9 and 5.10 into Eq. 5.31, we find that

$$U_{ij}^{eg} = \frac{4\pi a_{eg}^- \hbar^2}{m} \int d^3x |\phi_i(\mathbf{x})|^2 |\phi_j(\mathbf{x})|^2 \quad (\text{D.1})$$

$$V_{ij}^{ss'} = \frac{12\pi b_{ss'}^3 \hbar^2}{m} \int d^3x \left| \phi_i(\mathbf{x}) \vec{\nabla} \phi_j(\mathbf{x}) - \phi_j(\mathbf{x}) \vec{\nabla} \phi_i(\mathbf{x}) \right|^2 \quad (\text{D.2})$$

We consider the specific case where the $\phi(\mathbf{x})$ are harmonic oscillator eigenstates such that

$$\phi_i(\mathbf{x}) = \phi_{n_{x,i}}(x) \phi_{n_{y,i}}(y) \phi_0(z). \quad (\text{D.3})$$

Here it is assumed that all the atoms are in the longitudinal ground state. We can then write

$$U_{ij}^{eg} = \frac{4\pi a_{eg}^- \hbar^2}{\sqrt{2\pi m x_0^z}} S(n_{x,i}, n_{x,j}) S(n_{y,i}, n_{y,j}) \quad (\text{D.4})$$

and

$$V_{ij}^{ss'} = \frac{6\pi b_{ss'}^3 \hbar^2}{\sqrt{2\pi m x_0^z} (x_0^r)^2} [P(n_{x,i}, n_{x,j}) S(n_{y,i}, n_{y,j}) + P(n_{y,i}, n_{y,j}) S(n_{x,i}, n_{x,j})], \quad (\text{D.5})$$

where

$$S(n_{\xi,i}, n_{\xi,j}) = \int d\xi |\phi_{n_{\xi,i}}(\xi)|^2 |\phi_{n_{\xi,j}}(\xi)|^2 \quad (\text{D.6})$$

and

$$P(n_{\xi,i}, n_{\xi,j}) = \int d\xi |\phi_{n_{\xi,i}}(\xi) [\sqrt{n_{\xi,j} + 1} \phi_{n_{\xi,j}+1}(\xi) - \sqrt{n_{\xi,j}} \phi_{n_{\xi,j}-1}(\xi)] - \phi_{n_{\xi,j}}(\xi) [\sqrt{n_{\xi,i} + 1} \phi_{n_{\xi,i}+1}(\xi) - \sqrt{n_{\xi,i}} \phi_{n_{\xi,i}-1}(\xi)]|^2. \quad (\text{D.7})$$

To derive Eq. D.7, we have used the relationship between the harmonic oscillator raising and lowering operators and a spatial derivative.

The quantities $S(n_i, n_j)$ and $P(n_i, n_j)$ are plotted in Fig. D.1. Due to the opposite scaling with n for $S(n_i, n_j)$ and $P(n_i, n_j)$, which characterize the s - and p -wave interaction strengths, respectively, the p -wave interaction energy is insensitive to radial temperature (see Chapter 5, Fig. 5.15).

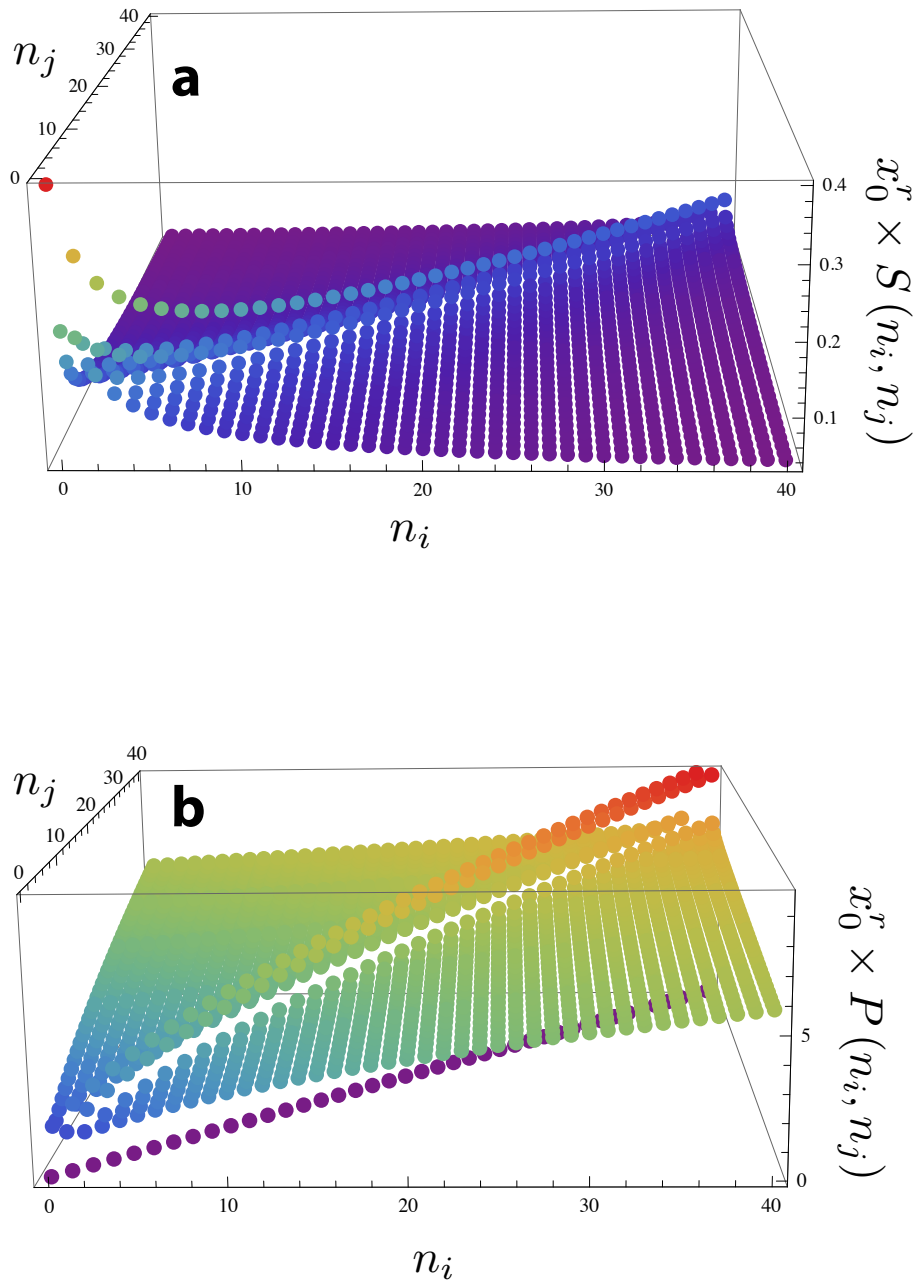


Figure D.1: s - and p -wave mode-dependent interaction strength coefficients. (a) The mode-dependent s -wave interaction strength coefficient. The function $S(n_i, n_j)$ is scaled by the radial harmonic oscillator length, x_0^r , to remove the x_0^r -dependence of $S(n_i, n_j)$. (b) The mode-dependent s -wave interaction strength coefficient. As with the s -wave case, $P(n_i, n_j)$ is scaled with x_0^r .

Appendix E

Site occupancy distribution

In this Appendix, we derive the site occupancy distribution for an optical lattice loaded by a Gaussian-profile atomic cloud. In the computation of density-dependent experimental observables, such as the density shift, lineshapes, and spin noise, we have utilized the occupancy distribution derived here to form a properly-weighted average of the desired quantity.

E.1 Sites with n

We begin by considering the situation depicted in Fig. E.1. A Gaussian-profile MOT is loaded into a 1-D optical lattice during the red MOT stage of the experiment (see Chapter 2). Thus, if a total of N_{tot} atoms are loaded into the lattice, the probability of a given site labelled i having n atoms is given by a Poissonian distribution

$$p_i(n) = \frac{\lambda_i^n e^{-\lambda_i}}{n!}, \quad (\text{E.1})$$

where the mean values λ_i are given by

$$\lambda_i \propto N_{\text{tot}} e^{-\frac{x_i^2}{2\sigma^2}}. \quad (\text{E.2})$$

Here x_i is the position of the i th site with respect to the MOT center and σ is the MOT width. For the ^{87}Sr lattice clock, we estimate that $\sigma \simeq 30 \mu\text{m}$. The loading is depicted schematically in Fig. E.1. The constant of proportionality should be chosen such that the sum of λ_i will be equal to N_{tot} .

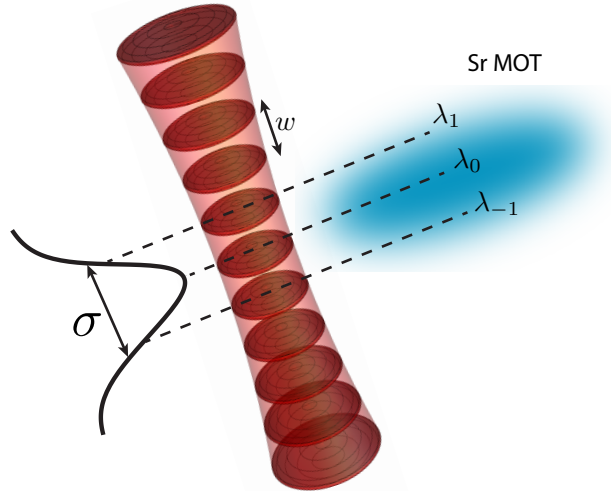


Figure E.1: Lattice loading from the red MOT and longitudinal distribution. The red MOT has longitudinal extent σ , which causes each trap site to have a position-dependent loading, with site-dependent averages $\{\lambda_i\}$. The lattice sites are spaced a distance $w = 813/2$ nm. The figure is not drawn to scale. In the experiment, $\sigma \simeq 30 \mu\text{m}$.

The most important quantity we need to calculate is the distribution of site occupancies (i.e., the average number of sites with n atoms), which we call $S(n)$. This quantity is given by

$$S(N) = \sum_i p_i(n) = \sum_i \frac{\lambda_i^n e^{-\lambda_i}}{n!}. \quad (\text{E.3})$$

We note that this sum can be carried out numerically. We approximate the sum by an integral such that

$$\sum_i \rightarrow \int_{-\infty}^{\infty} \frac{dx}{w} \quad (\text{E.4})$$

where w is the spacing between lattice sites, and in this case $w = \lambda_{\text{lattice}}/2$. It is then obvious that the proper continuous distribution for λ_i , $\lambda(x)$, is given by

$$\lambda(x) = \frac{wN_{\text{tot}}}{\sqrt{2\pi\sigma^2}} e^{-\frac{x^2}{2\sigma^2}} = \epsilon N_{\text{tot}} e^{-\frac{x^2}{2\sigma^2}}, \quad (\text{E.5})$$

where we have made the substitution $\epsilon \equiv w/\sqrt{2\pi\sigma^2}$. We plug this continuous distribution into Eq. E.4 and obtain

$$S(n) = \int_{-\infty}^{\infty} \frac{dx}{w} \frac{[\lambda(x)]^n e^{-\lambda(x)}}{n!}. \quad (\text{E.6})$$

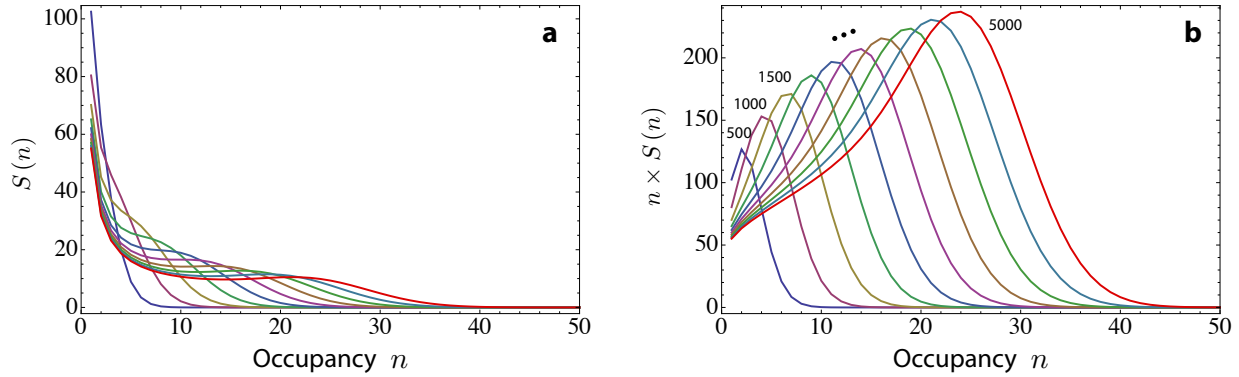


Figure E.2: Distribution of site occupancies. **(a)** The average number of sites containing n atoms. The color scheme is as labeled at right. **(b)** The atom-number-weighted site occupancy distribution. As the total atom number increases, the majority of atoms reside in highly-occupied sites. The numbers label N_{tot} for a given color. The color scheme is the same at left.

Inserting the continuous distribution of Eq. E.5 into Eq. E.6 and performing a Taylor expansion on the exponential yields an infinite sum of Gaussian integrals, each with its own analytical solution. We replace each Gaussian integral in the sum with its analytic solution to finally obtain

$$S(n) = \frac{1}{\epsilon n!} \sum_{j=0}^{\infty} \frac{(-1)^j (\epsilon N_{\text{tot}})^{j+n}}{j! \sqrt{j+n}}, \quad (\text{E.7})$$

where as before $\epsilon \equiv w/\sqrt{2\pi\sigma^2}$. The reader is cautioned that for large N_{tot} and large n , the sum converges **very** slowly, so high numerical precision should be used in evaluating the sum (double precision is woefully insufficient). Finally, we note that the sum can be truncated to a total number of terms given by $\sim 2\epsilon n N_{\text{tot}}$. For typical conditions of $\sigma = 30 \mu\text{m}$ and $N_{\text{tot}} = 5000$, this means that around 100 terms of the sum must be evaluated. We plot the function $S(n)$ in Fig. E.2a. A more useful quantity is the atom-weighted $S(n)$ given by $n \times S(n)$. This quantity gives the total number of atoms that share, on average, a site with n atoms. This quantity is plotted in Fig. E.2b.

E.2 Linearity of the density shift and average occupancy

In this section we show that the Poissonian site occupancy statistics enforce that the total density-dependent shift should be linear in atom number under simplifying assumptions.

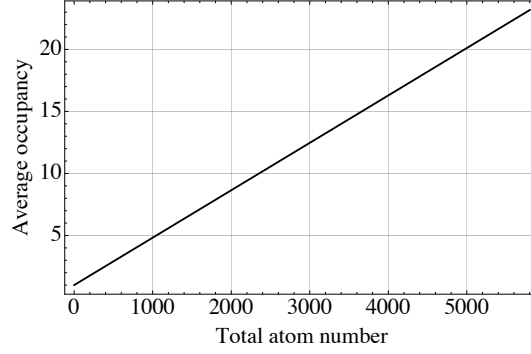


Figure E.3: Average site occupancy as a function of total atom number.

We consider the case where the density shift scales as $n(n-1)$, which will generally be the case for a many-body interaction potential of the form of Eq. 5.45 and in the absence of two-body losses, which are nonlinear. Thus, the average interaction energy per particle when averaged over trap occupancy is proportional to the $S(n)$ -weighted sum of $n(n-1)$ as

$$u \propto \frac{1}{N_{\text{total}}} \sum_n n(n-1) S(n) = \frac{1}{N_{\text{total}}} \sum_n \sum_i n(n-1) \frac{[\lambda_i]^n e^{-\lambda_i}}{n!} \quad (\text{E.8})$$

From the properties of the Poisson distribution, we find that this reduces to

$$u \propto \frac{1}{N_{\text{tot}}} \sum_i \lambda_i^2. \quad (\text{E.9})$$

If we use the approximation of Eq. E.4 combined with the probability distribution function of Eq. E.5 we find

$$\frac{1}{N_{\text{tot}}} \sum_n n(n-1) S(n) = \frac{\epsilon N_{\text{tot}}}{\sqrt{2}}, \quad (\text{E.10})$$

where $\epsilon \equiv w/\sqrt{2\pi\sigma^2}$. It is then also seen then that atom-number weighted average occupancy is given by

$$\bar{N} = \frac{1}{N_{\text{tot}}} \sum_n n^2 S(n) = \frac{\epsilon N_{\text{tot}}}{\sqrt{2}} + 1, \quad (\text{E.11})$$

thus proving its linearity with respect to N_{tot} . The average site occupancy as a function of N_{tot} is plotted in Fig. E.3. Thus, as seen from Eq. E.10, the average interaction energy per particle (and thus the frequency shift) is proportional to N_{tot} .